

ULTIMATE ELASTIC WALL STRESS ENVELOPES FOR (GRE) PIPES

This thesis is submitted with the requirements of the University of
Newcastle upon Tyne for the degree of Doctor of Philosophy

By

Tarak Ahmed Assaleh

Centre for Composite Materials Engineering,
School of Mechanical and Systems Engineering,
University of Newcastle upon Tyne

March-2011

In the name of God, Most Gracious, Most Merciful.

**TO THE LIBYAN MARTYRS WHO SACRIFICED THEIR
LIFE FOR NEW LIBYA.**

ACKNOWLEDGEMENTS

First of all I would like to express my thanks to the Libyan peoples Bureau and Libyan Culture Department in London for providing financial support for my PhD study at University of Newcastle upon Tyne.

I am heartily grateful to Professor A.G. Gibson for his supervision, continued support and invaluable help during the research. I would also like to thank Dr. J.M. Hale for his helpful, discussions and advices. I am also grateful to Future Pipe Team and in particular Mr. Mark Hekman, Mr. K. Rookus and Mr. Jan for their supporting and advising.

I would like to thank all staff member in the School of Mechanical and System Engineering and Centre for Composite Material Engineering at University of Newcastle, specially Dr. George Kotsikos, Mr. Mohd Shukry, Mr Ken Madden, Mr Malcolm Black, Mr Michael Foster, for their help.

Lastly, but not least, Appreciation and many thanks is extended to my parents, my wife (Lutfeya), my son (Ahmed) and my daughters (Nada and Hala) for their continued support, and patience during my study.

ABSTRACT

In this thesis the procedures for qualifying fiberglass pipes are discussed in relation to industry needs. The *ultimate elastic wall stress* (UEWS) test appears to provide an efficient means of rating pressure pipes, and indeed vessels, for cases where weepage failure occurs resulting from the accumulation of matrix cracks. The principle behind the UEWS test is to identify from stress-strain response, a stress level below which damage growth is either negligible or at least sufficiently low to avoid failure within the design life.

An experimental investigation into the UEWS of $\pm 55^\circ$ filament wound composite pipes has been conducted under various load and environmental conditions. The pipes were subjected to biaxial loading, which was achieved by a combination of hoop and axial stress loading. Loads were applied as groups of 10 one-minute pressure cycles, recording the hoop or/and axial strain. These pressure groups were gradually increased until the UEWS had been determined. Various ratios of hoop to axial stress were applied, ranging from pure axial to pure hoop loading at room temperature, 65°C and 95°C. These ratios were investigated by applying different pressures in both the main and small chambers built inside the pipe, and therefore it was unnecessary to add external load to the pipe wall. Tests were stopped at the first observed leakage through the pipe wall.

The UEWS test appears to provide an attractive alternative to the currently used procedure laid down in ISO 14692. This involves an expensive series of long term constant pressure tests described in ASTM 2992, running for over 10,000 hours. It is shown here that the UEWS test reflects the cyclic fatigue behaviour of fiberglass pipe, but further work on the relationship between cyclic and static behaviour is needed.

The test results are presented in the form of UEWS and failure envelopes showing the effects of testing at elevated temperature, and the degradation in pipe properties as the test progressed. Acoustic emission examinations were also conducted to detect damage development in the GRE pipes during the tests, allowing its compatibility

with the UEWS test to be assessed. Four different types of failure mode were observed according to the loading conditions.

It has been shown that a Miner's Law approach is effective in modelling damage due to combined static and cyclic effects, and that damage can be directly related to matrix crack growth. This approach could form the basis of future procedures for describing the lifetime behaviour of GRE pipes under any required combination of static, fatigue, hydrostatic and non-hydrostatic (multi-axial) loading.

TABLE OF CONTENTS

1	CHAPTER 1	1
	INTRODUCTION	1
2	CHAPTER 2	5
	LITERATURE REVIEW	5
2.1	APPLICATIONS OF COMPOSITE MATERIALS	5
2.2	GLASS REINFORCED EPOXY PIPES (GRE) AND THEIR MANUFACTURE	8
2.3	FILAMENT WINDING PROCESS.....	9
2.4	MATERIAL USED IN GRE PIPES.....	10
2.4.1	<i>Glass fibre</i>	10
2.4.2	<i>Aramid fibres</i>	10
2.4.3	<i>Carbon and graphite fibres</i>	11
2.4.4	<i>Boron fibres</i>	11
2.4.5	<i>Other types of fibre</i>	11
2.5	RESIN SYSTEMS	11
2.6	THERMOSETTING RESINS	12
2.6.1	<i>Epoxy resin</i>	12
2.6.2	<i>Polyester resin</i>	13
2.6.3	<i>Vinyl ester resin</i>	14
2.6.4	<i>Phenolic resin</i>	14
2.7	THERMOPLASTIC RESINS	15
2.8	STRESS-STRAIN RELATIONSHIPS IN COMPOSITES	16
2.9	LOADING SYSTEM IN PIPES	16
2.9.1	<i>Bi-axial loading</i>	16
2.9.2	<i>Pure hoop loading</i>	18
2.10	FATIGUE BEHAVIOUR OF COMPOSITE MATERIAL.....	19
2.11	FACTORS INFLUENCING FATIGUE BEHAVIOUR IN COMPOSITES	20
2.11.1	<i>Effect of fibre</i>	20
2.11.2	<i>Effect of matrix</i>	22
2.11.3	<i>Effect of the interface</i>	22
2.11.4	<i>Effect of mean stress and stress ratio</i>	23

2.11.5	<i>Effect of loading frequency</i>	25
2.12	FATIGUE CURVE	25
2.13	FAILURE MODES OF LONG FIBRE COMPOSITES	28
2.14	FAILURE DEVELOPMENT IN GRE PIPES	29
2.14.1	<i>Matrix microcracking</i>	29
2.14.2	<i>Delamination</i>	31
2.14.3	<i>Weepage</i>	32
2.14.4	<i>Fibre breakage</i>	33
2.15	FAILURE DEVELOPMENT OF GRE PIPES UNDER BIAxIAL LOADING	33
2.16	FAILURE CRITERIA	34
2.16.1	<i>Tsai-Hill maximum stress criterion</i>	35
2.16.2	<i>Tsai – Wu Criterion</i>	36
2.17	METHODS OF FAILURE ANALYSIS FOR FILAMENT WOUND COMPOSITE PIPES	37
2.17.1	<i>Ply by ply method</i>	37
2.17.2	<i>Sudden failure method</i>	38
2.18	FAILURE ASSESSMENT	39
2.18.1	<i>Microscopy</i>	39
2.18.2	<i>Acoustic emission</i>	40
2.19	FAILURE ENVELOPES	43
2.20	MODELLING OF THE FAILURE BEHAVIOUR OF COMPOSITES	45
2.20.1	<i>Miner’s law</i>	45
2.20.2	<i>Cumulative damage results and life prediction under cycle loading</i> . 47	
2.21	MODELLING OF MATRIX MICROCRACKING	48
2.22	STIFFNESS REDUCTION IN COMPOSITES.....	49
2.23	PIPE QUALIFICATION AND REQUALIFICATION	52
2.23.1	<i>Biaxial testing according to ASTM D2992 for pipe qualification</i>	52
3	CHAPTER 3	54
	EXPERIMENTAL METHODS	54
3.1	MATERIAL SELECTION.....	54
3.2	RIG DESIGN FOR UEWS TEST	55
3.3	CONSTRUCTION OF THE TEST RIG	57
3.4	END FITTINGS	57
3.4.1	<i>Adhesive bonded end fittings</i>	57

3.4.2	<i>Mechanical end fittings</i>	60
3.5	PISTON AND SHAFT DESIGN	63
3.6	DATA CAPTURE	64
3.7	PRESSURE AND STRAIN MEASURES	65
3.8	PRESSURIZING SYSTEM.....	65
3.9	PRESSURE REDUCER	66
3.10	HEATING DEVICE.....	67
3.11	ACOUSTIC EMISSION EQUIPMENT	68
3.12	THE ULTIMATE ELASTIC WALL STRESS (UEWS) TEST	69
3.13	DEFINITIONS	70
3.13.1	<i>Ultimate elastic wall stress (UEWS)</i>	70
3.13.2	<i>Cycle test pressure (CTP)</i>	70
3.13.3	<i>Cycle</i>	70
3.13.4	<i>Nominal pressure (NP)</i>	70
3.14	TEST PREPARATION	70
3.15	TEST CONDITIONS.....	71
3.16	TEST PROCEDURE	71
3.17	CALCULATION OF THE ULTIMATE ELASTIC WALL STRESS	73
3.18	WALL THICKNESS MEASUREMENTS	74
3.19	ELASTIC MODULUS MEASUREMENTS	75
3.19.1	<i>Axial Young's modulus</i>	75
3.19.2	<i>Hoop elastic modulus</i>	77
3.20	OPTICAL MICROSCOPY TEST	79
4	CHAPTER 4	82
	QUALIFICATION AND LIFETIME MODELLING OF FIBREGLASS PIPE	82
4.1	PIPES QUALIFICATION.....	82
4.2	THE ULTIMATE ELASTIC WALL STRESS (UEWS)	84
4.3	COMPARISON BETWEEN PROCEDURES.....	85
4.4	PREDICTION OF ELASTIC MODULUS CONSTANTS	86
4.5	MINER'S LAW INTERPRETATION OF THE UEWS TEST.....	88
4.6	EFFECTS OF CRACK DENSITY ON PROPERTIES	90
4.7	MODELLING OF THE UEWS AND FAILURE ENVELOPS	94

4.7.1	<i>Model A</i>	94
4.7.2	<i>Model B</i>	95
5	CHAPTER 5	97
	RESULTS AND DISCUSSION	97
5.1	ULTIMATE ELASTIC WALL STRESS (UEWS) TESTS	97
5.1.1	<i>UEWS results under pure axial loading (0:1)</i>	97
5.1.2	<i>UEWS results under 0.5:1 hoop to axial stress</i>	99
5.1.3	<i>UEWS results under 1:1 hoop to axial stress</i>	101
5.1.4	<i>UEWS results under pure hydrostatic pressure (2:1)</i>	103
5.1.5	<i>UEWS results under 4:1 hoop to axial stress</i>	105
5.1.6	<i>UEWS results under pure hoop loading (1:0)</i>	107
5.2	AXIAL AND HOOP YOUNG’S MODULUS MEASUREMENTS	109
5.3	FAILURE MODES	112
5.3.1	<i>Mode I</i>	113
5.3.2	<i>Mode II</i>	114
5.3.3	<i>Mode III</i>	116
5.3.4	<i>Mode IV</i>	117
5.4	MICROSCOPIC ANALYSIS	120
5.5	UEWS AND FAILURE ENVELOPES.....	123
5.5.1	<i>UEWS and failure envelopes at room temperature</i>	123
5.5.2	<i>UEWS and failure envelopes at 65°C</i>	124
5.5.3	<i>UEWS and failure envelopes at 95°C</i>	125
6	CHAPTER 6	128
	ACOUSTIC EMISSION AND MODELLING RESULTS	128
6.1	ACOUSTIC EMISSION (AE) OBSERVATION.....	128
6.1.1	<i>AE results of GRE pipes under pure internal pressure</i>	129
6.1.2	<i>AE results for GRE pipes under pure axial loading</i>	134
6.1.3	<i>AE results for GRE pipes under pure hoop loading</i>	138
6.2	MODELLING RESULTS.....	143
6.2.1	<i>Prediction of pipe elastic modulus</i>	143
6.2.2	<i>The UEWS test based on Miner’s law sum</i>	145
6.2.3	<i>Effects of crack density on pipe properties</i>	146

6.2.4	<i>Stress-strain behaviour</i>	148
6.2.5	<i>Modelling of the UEWS and failure envelopes</i>	150
7	CHAPTER 7	155
	CONCLUSIONS AND FUTURE WORK	155
7.1	CONCLUSIONS	155
7.2	FUTURE WORK	157
	REFERENCES	158
	APPENDIX A:	171
	APPENDIX B:	173
	APPENDIX C:	176
	APPENDIX D:	178

LIST OF FIGURES

<i>Figure 1 Offshore Platform Holly, South Ellwood Field, CA.....</i>	<i>5</i>
<i>Figure 2 Use of GRE pipes in the petrochemical industries.....</i>	<i>7</i>
<i>Figure 3 Use of composites for pipe repair</i>	<i>8</i>
<i>Figure 4 filament winding machine</i>	<i>9</i>
<i>Figure 6 Chemical structure of a typical isophthalic polyester.....</i>	<i>13</i>
<i>Figure 5. Chemical reaction to produce diglycidyl ether.....</i>	<i>13</i>
<i>Figure 7 Chemical reaction to produce novolac</i>	<i>14</i>
<i>Figure 8 Chemical reaction to produce resole phenolic</i>	<i>15</i>
<i>Figure 9 Biaxial loading arrangement for pure pressure loading</i>	<i>17</i>
<i>Figure 10 Biaxial loading arrangement for pure hoop loading</i>	<i>18</i>
<i>Figure 11 Effect of glass fibre size on transverse cracking</i>	<i>21</i>
<i>Figure 12 Modes of fatigue crack growth in fibre</i>	<i>23</i>
<i>Figure 13 The influence of mean stress on fatigue strength.....</i>	<i>24</i>
<i>Figure 14 S–N curve for a carbon-epoxy laminate.....</i>	<i>26</i>
<i>Figure 15 Data scatter showing the difficulty of establishing the S-N curve</i>	<i>27</i>
<i>Figure 16 Possible failure modes in laminate</i>	<i>28</i>
<i>Figure 17 Buckling, fracture and bending in fibres.....</i>	<i>29</i>
<i>Figure 18 Buckling mode shapes for a delaminated composite</i>	<i>32</i>
<i>Figure 19 Formation of weepage path through the pipe wall.....</i>	<i>34</i>
<i>Figure 20 Matrix micro-cracks in lamina.....</i>	<i>39</i>
<i>Figure 21 Crack propagation in resin</i>	<i>41</i>
<i>Figure 22 Characteristic tensile and amplitude curves of a PE composite.....</i>	<i>41</i>
<i>Figure 23 Determination of historic index (HI) from AE records.....</i>	<i>42</i>
<i>Figure 24 Failure envelopes for IPD epoxy and PSX phenolic±55° GRP pipes</i>	<i>44</i>
<i>Figure 25 Failure envelopes for multi-angle tubes.....</i>	<i>45</i>
<i>Figure 26 Temperature cycling test between 80 C⁰ and 95 C⁰</i>	<i>46</i>
<i>Figure 27 Constant pressure regression curves generated from Wellstream ramp experiments at 60°C</i>	<i>47</i>
<i>Figure 28 Elastic modulus reduction ratios as a function of transverse crack.....</i>	<i>51</i>
<i>Figure 29 regression line indicating pressure at design lifetime of 20 years.....</i>	<i>53</i>
<i>Figure 30 Pipe spool with straight and tapered reinforced ends</i>	<i>54</i>

<i>Figure 31 Test rig for carrying out biaxial loading tests</i>	56
<i>Figure 32 Pipe spool with tapered reinforced ends</i>	58
<i>Figure 33 Adhesive bonded end fitting</i>	59
<i>Figure 34 Pipe spool with adhesive bonded end fittings</i>	59
<i>Figure 35 Adhesive cap dismantling procedure</i>	60
<i>Figure 36 Pipe spool with straight reinforced ends</i>	61
<i>Figure 37 Mechanical end fitting</i>	61
<i>Figure 38 Pipe spool with mechanical end fittings</i>	62
<i>Figure 39 Piston heads screwed to shaft</i>	63
<i>Figure 40 Data capture system used in the UEWS test</i>	65
<i>Figure 41 Air driven pump</i>	66
<i>Figure 42 Pressure reducer</i>	67
<i>Figure 43 Environmental chamber</i>	68
<i>Figure 44 AE equipment</i>	69
<i>Figure 45 Definition of test cycles and cycle groups</i>	73
<i>Figure 46 Coating layer measurements</i>	75
<i>Figure 47 Pipe samples for tensile test</i>	76
<i>Figure 48 Pipe sample set up in the tensile machine</i>	76
<i>Figure 49 Ring specimens for the 100 seconds hoop Young's modulus test</i>	78
<i>Figure 50 sample set up for hoop Young's modulus measurements</i>	79
<i>Figure 51 Specimens for microstructure analysis</i>	80
<i>Figure 52 Moulded sample in epoxy resin</i>	80
<i>Figure 53 Determination of the hydrostatic design basis (HDB)</i>	83
<i>Figure 54 Matrix micro-cracks in a filament wound $\pm 55^\circ$ glass epoxy tube</i>	91
<i>Figure 55 Dimensionless change in 'hydrostatic/axial modulus' and 'hydrostatic/hoop modulus'</i>	93
<i>Figure 56 Stress-strain relationships, strain plot and UEWS points under pure axial loading</i>	98
<i>Figure 57 Stress-strain relationships, strain plot and UEWS points under 0.5:1 stress ratio</i>	100
<i>Figure 58 Stress-strain relationships, strain plot and UEWS points under 1:1 stress ratio</i>	102
<i>Figure 59 Stress-strain relationships, strain plot and UEWS points under 2:1 stress ratio</i>	104

<i>Figure 60 Stress-strain relationships, strain plot and UEWS points under 4:1 stress ratio.....</i>	<i>106</i>
<i>Figure 61 Stress-strain relationships, strain plot and UEWS points under pure hoop loading</i>	<i>108</i>
<i>Figure 62 Test set ups to measure Young’s modulus.....</i>	<i>110</i>
<i>Figure 63 Degradation in axial elastic modulus for conditioned pipes under 2:1 stress ratio.....</i>	<i>111</i>
<i>Figure 64 Degradation in hoop elastic modulus for conditioned pipes under 2:1 stress ratio.....</i>	<i>111</i>
<i>Figure 65 Axial and hoop elastic modulus degradation in different conditions.....</i>	<i>112</i>
<i>Figure 66 Weepage mode.....</i>	<i>113</i>
<i>Figure 67 Mode II a helical delamination</i>	<i>115</i>
<i>Figure 68 Mode III, local leakage</i>	<i>116</i>
<i>Figure 69 Pipe buckled under pure hoop loading</i>	<i>118</i>
<i>Figure 70 Mode IV, rupture due to buckling</i>	<i>119</i>
<i>Figure 71 local leakage occurred under pure hoop loading at 95°C.....</i>	<i>120</i>
<i>Figure 72 Micrograph of a cross-section of $\pm 55^{\circ}$ GRE pipe tested under a 2:1 biaxial loading</i>	<i>121</i>
<i>Figure 73 Crack path across pipe wall.....</i>	<i>122</i>
<i>Figure 74 Transverse microcracks initiated in the void pocket and propagated through the ply thickness.....</i>	<i>122</i>
<i>Figure 75 Failure envelope for $\pm 55^{\circ}$ GRE pipes at room temperature.....</i>	<i>123</i>
<i>Figure 76 Failure envelope for $\pm 55^{\circ}$ GRE pipes at 65 °C.....</i>	<i>125</i>
<i>Figure 77 Failure envelope for $\pm 55^{\circ}$ GRE pipes at 95 °C.....</i>	<i>126</i>
<i>Figure 78 Summering of failure and UEWS envelopes for $\pm 55^{\circ}$ GRE pipes at room temperature, 65 °C and 95 °C.....</i>	<i>127</i>
<i>Figure 79 AE counts vs. time and hoop stress for $\pm 55^{\circ}$ GRE pipes under 2:1 stress ratio.....</i>	<i>130</i>
<i>Figure 80 AE energy release rate vs. time and wall stress for $\pm 55^{\circ}$ GRE pipes under 2:1 stress ratio</i>	<i>131</i>
<i>Figure 81 AE absolute dB versus position of channel and AE duration versus amplitude for $\pm 55^{\circ}$ GRE pipes</i>	<i>132</i>
<i>Figure 82 AE amplitude vs. time for the $\pm 55^{\circ}$ GRE pipe under 2:1 stress ratio</i>	<i>133</i>

<i>Figure 83 AE events vs. time for the $\pm 55^{\circ}$ GRE pipe under 2:1 hoop to axial stress ratio</i>	134
<i>Figure 84 AE counts vs. time and hoop stress for $\pm 55^{\circ}$ GRE pipes under pure axial loading</i>	135
<i>Figure 85 AE energy release rate vs. time and wall stress for $\pm 55^{\circ}$ GRE pipes under pure axial loading</i>	136
<i>Figure 86 AE amplitude vs. time for the $\pm 55^{\circ}$ GRE pipe under pure axial loading.</i>	136
<i>Figure 87 AE absolute dB versus position of channel and AE duration versus amplitude for $\pm 55^{\circ}$ GRE pipes under pure axial loading</i>	137
<i>Figure 88 AE events vs. time for the $\pm 55^{\circ}$ GRE pipe under pure axial loading</i>	138
<i>Figure 89 AE counts vs. time and hoop stress for $\pm 55^{\circ}$ GRE pipes under pure hoop loading</i>	139
<i>Figure 90 AE energy release rate vs. time and wall stress for $\pm 55^{\circ}$ GRE pipes under pure hoop loading</i>	140
<i>Figure 91 AE amplitude vs. time for the $\pm 55^{\circ}$ GRE pipe under pure hoop loading.</i>	140
<i>Figure 92 AE absolute dB versus position of channel and AE duration versus amplitude for $\pm 55^{\circ}$ GRE pipes under pure hoop</i>	142
<i>Figure 93 AE events vs. time for the $\pm 55^{\circ}$ GRE pipe under pure hoop loading</i>	143
<i>Figure 94 Axial and hoop elastic modulus function in winding angle</i>	144
<i>Figure 95 Miner's Law sum at each hoop stress level in UEWS test</i>	145
<i>Figure 96 Dimensionless change in elastic constants vs. crack density</i>	146
<i>Figure 97 Dimensionless change in 'hydrostatic/axial modulus' and 'hydrostatic/hoop modulus'</i>	147
<i>Figure 98 Dimension less change in elastic modulus as the UEWS test progressed</i>	148
<i>Figure 99 Miner's Law-based simulation of strain response in UEWS test at room temperature</i>	149
<i>Figure 100 Miner's Law-based simulation of strain response in UEWS test at 65°C</i>	149
<i>Figure 101 Miner's Law-based simulation of strain response in UEWS test at 95°C</i>	150
<i>Figure 102 Modelling of UEWS and failure envelopes for GRE pipe, at 20°C</i>	151
<i>Figure 103 Modelling of UEWS and failure envelopes for GRE pipe, at 65°C</i>	152

Figure 104 Modelling of UEWS and failure envelopes for GRE pipe, at 95°C..... 152

Figure 105 Modelling of the UEWS envelope based on maximum stress criterion. 154

CHAPTER 1

INTRODUCTION

Filament wound glass fibre reinforced epoxy (GRE) pipes are being increasingly used in a wide range of applications, such as high pressure containers and long distance piping. GRE pipes are used in the petrochemical and oil industries due to their superior corrosion resistance and high strength to weight ratio [1]. The use of GRE composite pipes has supplanted that of steel casings in many cases due to the former's relatively low cost. This has encouraged researchers to develop and carry out experimental and theoretical investigations in order to understand their mechanical and failure behaviour under a variety of load and environmental conditions[2].

The structure of filament wound composite pipes is mainly based on fibre and resin. Fibres are used as a reinforcing material and resin bonds the fibres together and keeps them in the proper position. Resins furthermore protect the fibres from mechanical and chemical damage such as abrasion and chemical corrosion. The most common reinforced fibres are made of glass, carbon, and aramid due to their low cost and good strength. Other types of fibre used in industry include those made of nylon, polyester and polyethylene.

The most common polymers used in filament wound composite pipes are vinyl ester and phenolic resins, which are cheap and exhibit good durability. Vinyl ester is preferred in many applications due to its advantages of water resistance and high mechanical strength, but it is about twice as expensive as polyester and therefore is used only when high performance is required. Epoxy resin is superior in term of durability, but the relatively high cost limits their use. Other types of resins, such as polyethersulphones and polyetherimides are also used in industry where toughness and stability at high temperature are required.

The stress-strain relationships of composite materials are predominately linear and then non-linearity occurs close to final failure. The non-linearity is significantly

increased by damage such as matrix cracking, delamination and yielding . Nahas and et al (1984) [3] reviewed several methods for the analysis and modelling of the non-linear behaviour of laminated reinforced composite materials, and Sun and Tao (1998) [4] modelled the stress-strain behaviour of composite laminate by considering both the material's non-linearity and progressive matrix cracking. Roberts et al (2002) [5] modified laminate theory by introducing the influence of matrix microcracking on stiffness and strain. J. Wang et al (2007) [6] simulated the stress-strain curve of non-tube composites under cycle loading conditions and found that the non-linear elasticity of samples under compression cycles showed local deformations which occurred before global buckling is recovering upon first unloading.

The endurance of filament wound pipes under biaxial loading has been investigated by many researchers in order to understand the failure mechanisms and modes under a variety of load and environmental conditions. The most common type of failure is due to fatigue. This occurs when alternating loads are applied to the component, and it can plotted against the number of cycles up to failure in order to build up a fatigue curve. This graph is also called S-N curve, and is usually plotted in a logarithmic scale.

Owen et al (1972) [7] was one of the earliest studies of the fatigue behaviour of glass reinforced plastic under tensile and fatigue loading. Smith et al (1989) [8] implemented a number of experiments testing glass/polymer cruciform specimens. They found that failure was based on three modes; rectangular cracking, shear failure, and mixed mode failure. Fujii and et al (1996) [9] proposed a model based on stiffness degradation for multiaxial life prediction. Adden and Horst (2009) [10] introduced a model based on ply-by-ply stiffness degradation to evaluate fatigue damage under multiaxial loading.

In fact there are many methods available used to analyse the fatigue and failure mechanisms of composites, the most common being the ply by ply and sudden failure methods. In terms of composite pipes, weepage is the definitive type of failure, and complete failure is rarely noted when pipes are exposed to pressure loading.

The behaviour of fibre reinforced composites is quite complicated because it is not only anisotropic but also exhibits non-homogeneity. This leads to a variety of failure mechanisms in composites. For example, GRE pipes subjected to pure hydrostatic pressure can develop matrix cracks, and then the plies may delaminate or fibres can debond from the matrix, whereas fibres under pure hoop loading will debond from the matrix and then break due to buckling [6]. Pipes tested under a variety of biaxial loading conditions failed at different strengths in the axial and hoop directions; consequently a symmetrical biaxial failure envelope will be constructed which shows the pipe stiffness at these load ratios. The biaxial failure envelope is a graph of axial failure strength versus hoop failure strength, and the envelope's shape is significantly affected by winding angle and temperature. Hale et al (2000) [11] investigated the effect of hot and wet conditions on the behaviour of the failure envelope for fibre/glass tubes under biaxial loading.

Since the use of GRE pipes has extended to the inshore and offshore applications, the qualification and requalification of products to define the working pressure for long periods of time has become a primary concern for researchers. Currently, the ISO ASTM D2992 standard is used to predict the maximum service pressure for GRE pipes. The standard describes the method used to establish a regression line to predict long term allowable stress [12]. The hydrostatic design basis (HDB) is a method used to reconfirm the product, and is needed when any change is made to materials, manufacturing processes, construction, and liner thickness or fitting design. In the HDB test, the product is subjected to 1,000 hours of hydrostatic pressure based on the 1,000 hour lower prediction limit (LPL) of the regression line obtained from ASTM D2992.

While acknowledging the benefits of the current HDB reconfirmation method based on regression analysis, the need among manufacturers for more rapid and effective method of monitoring changes in product quality has become imperative. The ultimate elastic wall stress (UEWS) method currently provides an attractive alternative method due to its advantages of test speed. The UEWS test takes only a few hours to perform compared with the 1,000 hour HDB reconfirmation procedure, and the UEWS appears to be very sensitive to changes in key manufacturing and raw material parameters.

The main purpose of the present work is to establish a new method for pipe requalification in rapid. The UEWS test enables the stress-strain response of the pipes under biaxial loading to be studied, allowing the maximum stress level in the elastic zone to be defined. Furthermore, the UEWS test provides a realistic statistical approach to establishing a long-term pressure rating when there is a slow deterioration of properties.

The present study conducts a series of UEWS tests for $\pm 55^\circ$ filament wound composite pipes under biaxial loading with a variety of load conditions. The results are then presented in the form of a UEWS envelope showing the effects of testing at elevated temperatures. This is the first time that the strength envelope of GRE pipes has been fitted in term of the elastic limit.

The relevant literature is thoroughly reviewed in chapter two of this thesis, which starts with a discussion of fibre and resin types and composite applications. The second part explains the stress-strain relationship and the failure behaviour of composites, as well as the factors influencing the fatigue behaviours. Failure assessment is discussed in the third part of this chapter, including microscopy and acoustic emission monitoring techniques. Finally the modelling of failure behaviour and failure envelopes are reviewed.

In the third chapter, the experimental procedure is described including pipes specification rig design and UEWS test, as are the tensile and 100s creep tests. The acoustic emission and microscopy analysis conducted then is explained. Fibreglass pipe qualification and lifetime modelling are the main topics of chapter four, including the modelling of the stress-strain relationship and elastic modulus degradation. In chapter five the UEWS results, tensile and creep test results, microscopy analysis of the failed sample, and UEWS envelopes are presented. Chapter six presents the acoustic emission results of GRE pipes under pure hydrostatic, pure axial and pure hoop loading. Modelling results are also included in chapter six and show the approach of using Miner's law to predict the stress-strain relationships, elastic modulus degradation due to increasing matrix crack density, and failure envelopes. Finally, the conclusions of the study and recommendations for future work are discussed in chapter seven.

CHAPTER 2

LITERATURE REVIEW

2.1 Applications of composite materials

Composites offer a wide range of characteristics suitable for many design requirements due to their advantages of cost, weight to strength ratio and chemical resistance. Thus composites have found many applications, such in the transportation, marine, civil infrastructure, and petrochemical industries. Moreover, composites are used in onshore and offshore applications both topside and subsea. Figure 2.1 shows the Holly, South Ellwood Field offshore platforms where composites are used [13].



Figure 2.1. The use of composites in offshore applications. Offshore Platform Holly, South Ellwood Field, CA.

The most common polymers used in industrial applications are vinyl ester and phenolic resins, due to their low cost and good durability. Vinyl ester is preferred in many applications due to its advantage of water resistance and high mechanical properties. However, vinyl ester is about twice as expensive as polyester resin, and therefore it is used only for specific high performance requirements. Other types of resins, such as epoxies, polyethersulphones and polyetherimides are also used in industry. Table 2.1 compares the most common resins available in the industrial use.

Table 2.1 The most common types of resins in terms of mechanical and fire performance properties as well as cost, source Gibson (1989) [14].

Resin	Mechanical integrity	Low smoke & toxicity in fire	Cost
Polyester	****	*	***
Vinyl ester	*****	*	*****
Epoxies	*****	*	*****
Phynolic	*****	****	****
Mod.Acrylic	****	*****	****

One of the most important fields where composites are widely used is transport and storage fluid applications. Glass reinforced epoxy (GRE) is the most common composite used in low and high pressure piping for a wide variety of fluids. However, in onshore applications, GRE pipes used to carry oil and fresh and sea water over long distances, due to not only the advantages mentioned above, but also due to their ease of handling and repair. Figure 2.2 shows the use of GRE pipes in the petro chemical industries. Tanks and vessels are one of the useful usages of their composite due to its excellent manufacturability.

Composites have also recently been used in lining metal pipes in order to minimize the effect of the surrounding media, as well as to prevent possible corrosion from taking place. Until a decade ago the main method of pipeline repair was based on welding or the complete replacement of damaged pipes with new ones. This takes a huge amount of effort and long operational periods starting from excavating the ground before the replacement process. However, composites can now be applied as thin cross section liners made from resin impregnated glass fibre woven so as to cover particular damaged areas, in a technique called ‘cure in place pipe’ (CIPP) [15]. CIPP is preferred due to the advantages of low cost, ease of installation and the

fact that repairs can be conducted without shutting down the plant. Figure 2.3 shows the repair process for a steel pipeline.



Figure 2.2 Use of GRE pipes in the petrochemical industries



Figure 2.3. Clockspring being applied offshore to externally corroded pipe. Application involves first cleaning the surface and filling external pits or damage, to allow stress to be transmitted from the pipe to the repair. Following this, the clockspring laminate is wound around the pipe while being coated with adhesive which is allowed to cure.

2.2 Glass reinforced epoxy pipes (GRE) and their manufacture

The use of GRE composite pipes has supplanted that of steel casings in many cases due to their low cost. Filament winding is the method most commonly used to produce GRE pipes. The reason for this relates to high fibre constants and hence high levels of mechanical properties can be achieved. Filament winding is an accurate process, ideally suited to the precise and consistent production of the pipes. Furthermore, the winding angle can be adjusted to give the required balance of hoop and axial properties. Depending on the assumptions made, the optimum winding

angle for pipes subjected to pure hydrostatic pressure is $\pm 55^\circ$ according to Natting's analysis [16].

2.3 Filament winding process

The pulled fibres are impregnated with a resin and wound on to rotating mandrel, which should be coated with a wax release agent before the winding process. The winding angle Φ is achieved by the relative speed of the lateral movement of the winding head and mandrel. Fibre bundles should be wound in such a way that the mandrel is completely covered and the product has constant wall thickness. After finishing the winding process, the compound on the mandrel is allowed to cure and post-cure at the lowest possible temperature to release the thermal and residual stresses. In the final stage of the manufacturing process the cured pipe is removed from the mandrel. Figure 2.4 shows a schematic diagram of a filament winding machine.

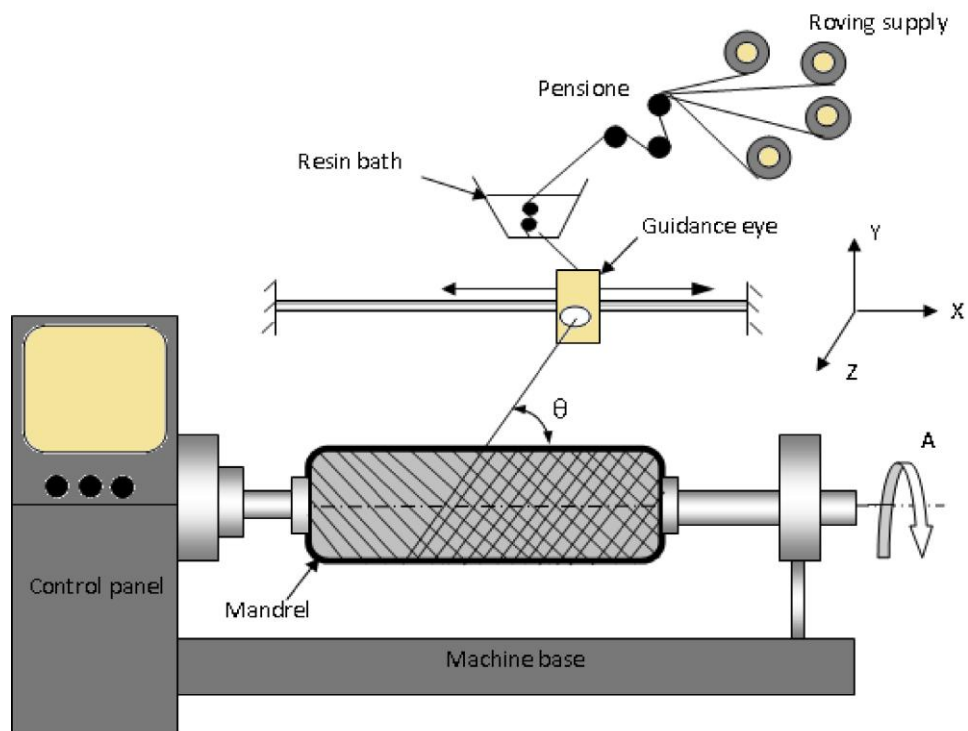


Fig. 2.4. Schematic diagram of a filament winding machine. Fibres are drawn from a roving supply through a resin bath. The wetted roving is led through the guidance eye and laid on the rotating mandrel at a precisely predetermined angle.

2.4 Material used in GRE pipes

The composition of filament wound pipes is mainly based on fibre and resin. There are many types of fibres used as reinforcing material, the most common being glass, carbon, and aramid. Other types of fibre are used in industry, including those made of nylon, polyester, and polyethylene.

2.4.1 Glass fibre

Glass fibres are normally produced by the melting of silica sand, limestone fluorspar, boric acid, and clay. Other types of fibre can be produced with significant variations in properties by using different processes and varying the properties of the raw material. For example, electric grade glass fibre (E-glass) has good electrical, mechanical and chemical properties. Furthermore, E-glass fibres are available at very low cost compared with other products, and therefore, E-glass is commonly used in many applications. On the other hand, carbon glass (C-glass) has high chemical and corrosion resistance; and therefore it is often preferred for the inner resin-pipe lining in the manufacturing of GRE pipes. Silica (S-glass) has higher mechanical properties than C and E-glass fibres, and for this reason is used in high pressure pipes, but is not preferred for low or medium pressure pipes because of its relatively high expense[17].

2.4.2 Aramid fibres

Aramid fibres are basically formed from aromatic polyamides. The polymers are spun from a strong acid solution (concentrated H_2SO_4), by a dry jet wet spinning process. The polymer is produced by adding acid chloride to an amine solution in cool media, and then, the clean polymer is mixed with strong acid at an elevated temperature to form the filament. Several types of aramid fibres are available, with different names such as Kevlar, Twaron, and Technora. Three types of modified Kevlar fibres are also available: Kevlar 29, 49, and 149. Although Kevlar fibres have excellent scraping resistance, their usage is still limited due to low compression performance.

2.4.3 Carbon and graphite fibres

The term graphite is used to describe fibres that have a carbon content in excess of 99%, whereas, carbon fibres have a carbon content of 80-95%. The technology for producing carbon fibre is based on thermal decomposition of various organic precursors. Carbon and graphite fibres are the predominant high-strength high-modulus reinforcements.

2.4.4 Boron fibres

Boron fibres are produced by chemical vapour deposition (CVD) from the reduction of boron trichloride (BCL₃) with hydrogen on a tungsten or carbon monofilament substrate [17]. By heating up the substrate to an elevated temperature of 1260°C, it is pulled through the reactor to obtain the desired thickness of boron coating. Today boron filaments are produced with diameter 100, 140, and 200µm. Boron-tungsten filaments have good tensile strength, which can be increased by etching away part of the outer portion of the filament.

2.4.5 Other types of fibre

The high-temperature reinforced fibres can be produced by developing ceramic fibres, which have high strength and high elastic modulus with high temperature capability. Among the most important ceramic fibres are aluminium and silicon carbon fibres. Another fibre introduced by the Allied Chemical Corporation (ACC) is named organic spectra 900 fibre. This is an ultra high molecular weight fibre produced by solution and gel spinning. This fibre's most important property is that it can have a very small diameter of 30 µm. However, the melting point of 150°C is a major limitation in most applications [17] .

2.5 Resin systems

The resin system or matrix in composite materials has several tasks. Firstly to bond the fibres together and keep them in the proper position are the main tasks of the resin. Secondly, it is used to transfer and distribute loads to the fibres as well as

protect them from mechanical and chemical damage such as abrasion, and chemical corrosion.

Therefore, such a resin should have specific properties to carry out these tasks which can be listed as follows:

High adhesive strength to the fibres.

Enough elasticity to be able to transfer loads to the fibres

Good mechanical and chemical properties.

Good heat conductivity, and moisture resistance.

Polymers are classified into two main types, thermosetting and thermoplastic, according to the effect of heat on their processing and properties.

2.6 Thermosetting resins

Thermosetting polymers are formed from a chemical reaction between resin and a hardener (catalyst) in a non reversible molecular cross-linking process to form tightly bound rigid products. The behaviour of the molecular structure of thermosetting resins is changing from solid glassy polymer to amorphous polymer. The majority of filament wound composite pipes are made from four main resin types: epoxy, polymer, vinyl ester, and phenolic ester resins.

2.6.1 Epoxy resin

Different types of epoxy resins are available for industrial use. The most commonly used in filament wound pipes is diglycidyl ether of bisphenol A (DGEBA), which is produced by the reaction of epichlorohydrin with bisphenol A in the presence of sodium hydroxide as shown in figure 2.5 [18].

For filament winding purposes, polymers with low viscosity are preferred, while polymers with higher viscosities are used as adhesives due to their high stability. The properties of cured epoxy resin depend on the chemical composition of its epoxy polymer, which could be improved as well as the curing agent molecule. Epoxy resins are superior to other polymers with regard to their adhesive properties and chemical and moisture resistance.

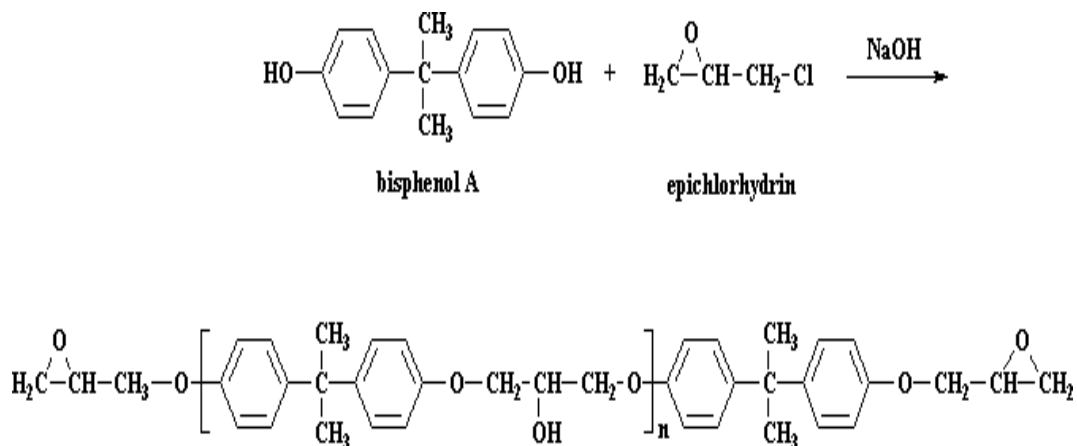


Figure 2.5. Reaction of epichlorohydrin with bisphenol A in the presence of sodium hydroxide to produce diglycidyl ether

2.6.2 Polyester resin

The two general types of polymer resins are orthophthalic and isophthalic. The latter is frequently preferred in industrial applications, such as the marine and oil industries due to its high water and chemical resistance, figure 2.6 shows its chemical structure. Orthophthalic polymer resins are used as standard inexpensive resins for general purposes, because of their low cost compared with other resins. It is therefore preferred in structural applications where corrosion resistance is not a priority.

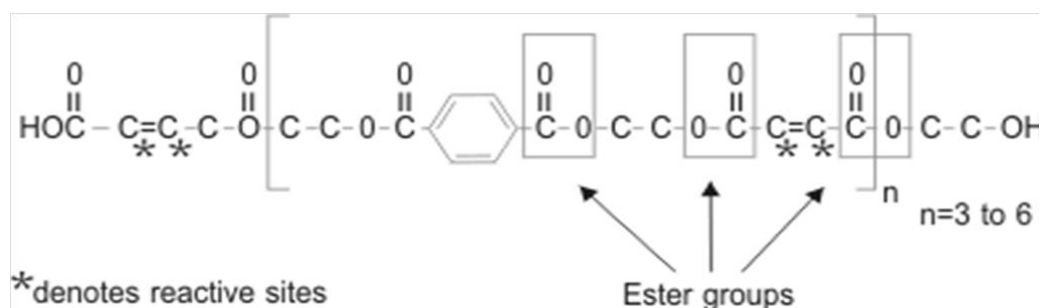


Figure 2.6 Idealised chemical structure of a typical isophthalic polyester [19].

This reaction is achieved at 160°C with the blending of hexamethylene and tetramine. This makes the bond decompose and form the formaldehyde to novolac [23].

Resole phenolic resin is formed by the chemical reaction of phenol and an excess of formaldehyde in a rich alkaline catalyst. The cross-linking via the methylol group occurs by heating up the resin to a certain temperature as illustrated in figure 2.8.

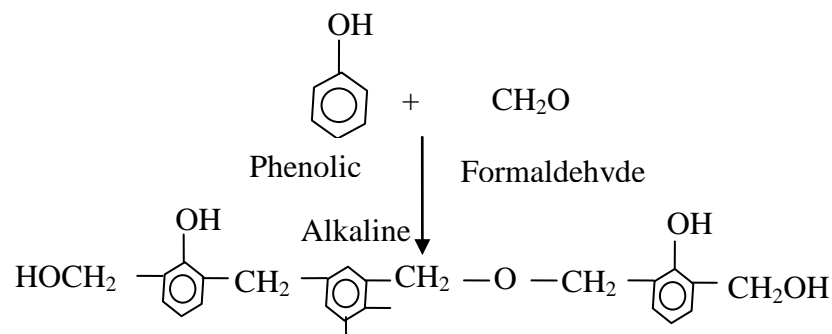


Figure 2.8. Reaction of phenol with an excess of formaldehyde in the presence of an alkaline catalyst.

2.7 Thermoplastic resins

Thermoplastic resins are not cross-linked, as are thermosetting resins. They derive their strength from the inherent properties of their monomer units and high molecular weight, which act as cross-links due to high molecule concentration. Thermoplastic resins are soft and melt upon heating, and returning to hard condition again with cooling. They could also be classified as anisotropic materials, depending on conditions during solidification. In addition to their high failure strains, they also have good chemical resistance. On the other hand, the processing of thermoplastic composites is more difficult than that of the thermosetting type, because of their high viscosity [16]. There are several types of thermoplastic resins classified according to their chemical structure into a number of groups, such as styrenics, vinyls, polyolefines, polyamides, sulphur-containing thermoplastic [24].

Most of these types are classified as amorphous polymers. The use of thermoplastic matrices in filament wound pipes is sharply increasing in many industrial applications. A number of theoretical and experimental studies have been carried out on filament wound thermoplastic pipes by Gibson and Fahrer (2000) [25], in order to determine their behaviour under a variety of load and environmental conditions.

2.8 Stress-strain relationships in composites

The stress-strain relationship of composites is predominately linear up to close to final failure, and then non-linearity occurs in the very last stage of loading [26]. A number of studies have investigated and modelling the relationship between the stress and strain of composites, such as Petit (1969) [27] and Hahn (1978) [28]. The latter introduced analytical techniques to predict the behaviour of laminate reinforced composite materials. Abu-Farsakh et al (1997) [29] investigated the effect of the material's non-linearity on deflected beams. They found that the deflection is more prominent for the shear which dominated core failure. Sun and Tao (1998) [4] also investigated the effect of progressive matrix cracking on the stress-strain behaviour.

Roberts et al (2002) [5] modified laminate theory by introducing the influence of matrix microcracking on the stiffness and strain. More recently, J.Wang et al (2007) [6] simulated the stress-strain curve of non-tube composites under cyclic loading conditions. Reporting, non-linear elasticity, they interpreted their observations by suggesting that under a compression cycle a local deformation occurred in the sample before global buckling is recovering upon first unloading.

2.9 Loading system in pipes

2.9.1 Bi-axial loading

Biaxial loading is a combination of two or more loads acting at the same time, which could be present as tension and pressure loading, tension and torsion loading, torsion and pressure loading and so on. The type of biaxial loading examined in this study consists of tension and internal hydrostatic pressure. A typical arrangement for biaxial loading is illustrated in figure 2.9. When the composite pipe is arranged as

closed-ended, and then hydrostatic pressure is applied, axial, hoop, and radial stresses will all be generated. However the radial stress is negligible compared with axial and hoop stresses in cases of $L/D < 20$. Hoop stress can be calculated by:

$$\sigma_H = \frac{P D}{2 t} \quad (2.1)$$

where: σ_H is hoop stress, P is applied pressure, D is the inner diameter of the pipe, and t is the pipe wall thickness.

Since the hoop stress generated is equal to twice the axial stress in the case of the closed-ended arrangement, this particular type of load called is 2Hoop:1Axial, (2:1) loading, and as a result the axial stress could then be written as:

$$\sigma_A = \frac{\sigma_H}{2} = \frac{P D}{4 t} \quad (2.2)$$

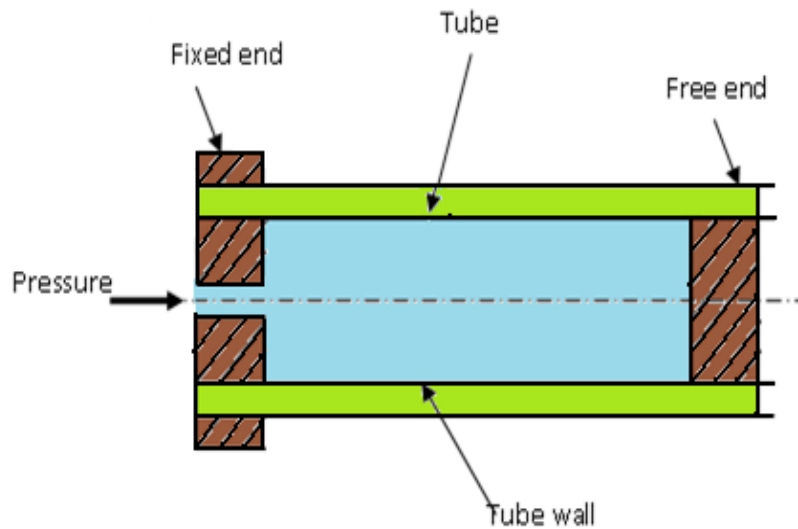


Figure 2.9. Typical arrangement for biaxial loading, pure pressure loading.

2.9.2 Pure hoop loading

Figure 2.10 shows a sketch of an open-ended arrangement, where two end fittings of the pipe are free to slip on rubber O-rings. Therefore the axial stress will extend to the shaft which is connected between two pistons; consequently the axial stress in the pipe wall will be about zero.

Several methods for testing filament wound pipes have been carried out using different types of loading. Soden et al (1978) [30] suggested a method of testing which involved loading the filament wound pipe by internal pressure with axial tension or compression applied simultaneously. Hull et al (1978) [31] presented three methods of tests : mode I closed-ended, applying internal pressure to restrain the ends (axial strain = 0); mode II for biaxial loading, where the ratio of hoop to axial stress is 2:1; and a mode III open-ended setting with internal pressure where axial stress = 0. Soden et al (1993) [32] and Kaddour et al (1998) [33] introduced a method to carry out uniaxial and biaxial loading by applying internal pressure with axial tension or compression at the same time. Mistry et al (1992) [34] designed a new test rig enabling them to study the buckling behaviour of composite pipe under external pressure and axial loading.

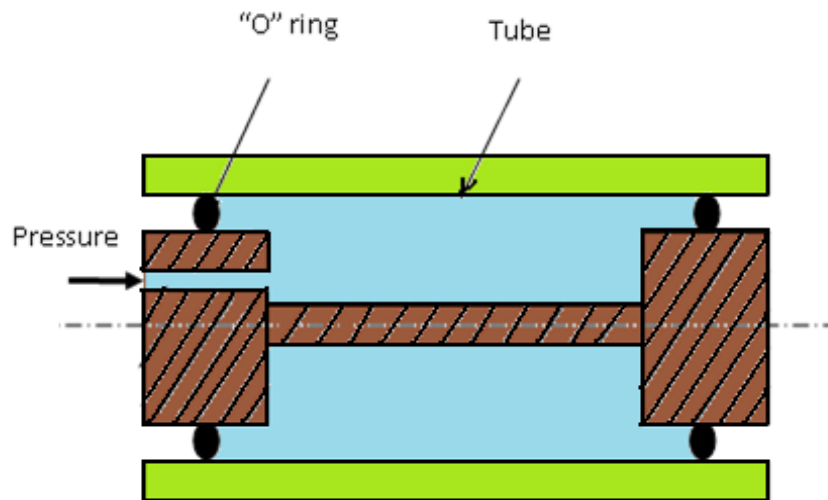


Figure 2.10. Typical arrangement for biaxial loading, Pure hoop loading.

2.10 Fatigue behaviour of composite material

The behaviour of composite materials under uniaxial and multiaxial load conditions has been extensively studied by a number of researchers in order to understand and develop methodologies for safe fatigue and failure evaluation. The earliest study to attempt the systematic investigation of fatigue behaviour through extensive experimentation was by Owen (1972) [7]. Fujii et al (1995) [35] also contributed significantly aspects to the study of fatigue behaviour for composites. All these researchers refer to testing conditions which was a combination of external loads (global loads) and internal loads (local loads). The latter is mainly, however, generated by material anisotropy for off-axis laminates under uniaxial external and multiaxial loads [36]. Smith et al (1989) [8] implemented a number of experimental tests of glass/polymer cruciform specimens. They assumed that failure is mainly based on three modes: rectangular cracking, shear failure and mixed mode failure. They used a homogenised quadratic polynomial function to account for strain energy based on cracking and maximum shear stress for shear failure to establish the mixed mode of failure. A stiffness degradation model for multiaxial life prediction was suggested by Fujii et al (1996) [9], and ratios for both tension and shear were used to express the damage variables. Adden and Horst (2009) [10] introduced a model based on ply-by-ply stiffness degradation to evaluate fatigue damage under multiaxial loading.

Fatigue failure generally occurs locally and is driven by local stress fields causing a sequence of failure mechanisms. There are five main failure mechanisms in unidirectional glass/fibre composite material: interfacial debonding; matrix cracking; weepage; delamination; and fibre breakage. Delamination occurs as a result of matrix cracking and interfacial debonding. This causes debonding between the adjacent layers of the reinforcement.

The fatigue mechanism in unidirectional composites using different type of fibres has been widely discussed in terms of fibre deformation characteristics and matrix resin fatigue limit relations. Several experiments on GRE and carbon fibre reinforced plastic (CFRP), have been carried out by Curtis and Moor (1983) [37] and Lorenzo and Hahn (1987) [38]. They note that the damage is in the form of matrix cracking and longitudinal splitting which is initiated by interfacial debonding, and matrix

cracking. They also observed that glass fibre composites show more extensive damage than carbon fibre composites.

The most common type of failure is fatigue. This occurs when alternating loads are applied to the component, which can be plotted against number of cycles up to failure to build up a fatigue curve called the S-N curve, usually plotted in a logarithmic scale.

2.11 Factors influencing fatigue behaviour in composites

There are several factors influencing the fatigue behaviour of composites, which can be summarised as follows.

2.11.1 Effect of fibre

Many investigations have been conducted on the effects of fibre construction and orientation on the fatigue behaviour of composites. Although unidirectional composites have a maximum tensile strength when loads are applied parallel to fibre direction, this is not the case in fatigue resistance because of splitting in the fibre direction due to relatively low transverse strength. Many investigations have claimed fatigue strength is better in cross-ply non-woven unidirectional 0° and 90° , because the fibres are straight and parallel and do not get crimped [17].

Godara (2007) [39] used digital image correlation (DIC) to study the influence of fibre orientation on global mechanical behaviour and mesoscale strain localization in short glass-fibre reinforced composites. DIC is a method for the determination of the heterogeneity of elastic-plastic deformation and strain fields in materials with heterogeneous microstructures and is based on the recognition of geometrical changes in colour scale. Two different angle sets of composite plates were tested (cross ply $0^\circ/90^\circ$ and $\pm 45^\circ$). The results showed that a strong influence of fibre orientation was observed on anisotropic mechanical behaviour and the failure mechanism. Furthermore, a good correlation was noted between the distribution of deformation at mesoscale and material microstructure. Staking sequence also has a strong influence on fatigue life. Foye and Baker (1970) [40] reported that a

significant difference in fatigue strength was observed when the positions of the plies in a $\pm 15^\circ$ and $\pm 45^\circ$ laminate were changed .

A number of studies into the performance of carbon fibre reinforced composites have been carried out by Owen et al (1974) [41], Curtis et al (1983) [37] and Harris (1986) [42]. These found that a high modulus carbon fibre composite gave the best fatigue performance among the composites tested. Curtis and Dorey (1986) [43] also reported Kevlar fibre reinforced plastic composites had a fatigue performance intermediate between carbon and glass fibre composites. On the other hand other factors which influence fatigue behaviour relate to the fibre characteristic, such as fibre volume fraction, the interfacial bond between the fibres and the matrix, and the fibre size (short or long fibres).

Fernberg et al (2000) [44] studied the effect of glass fibre size on transverse cracking using two different fibre types with epoxy and vinylester matrix. They observed that the size of coating of the glass fibre has a strong effect on the cracking behaviour of cross-ply laminates, which has been shown to affect the slope of crack density versus strain, as illustrated in figure 2.11.

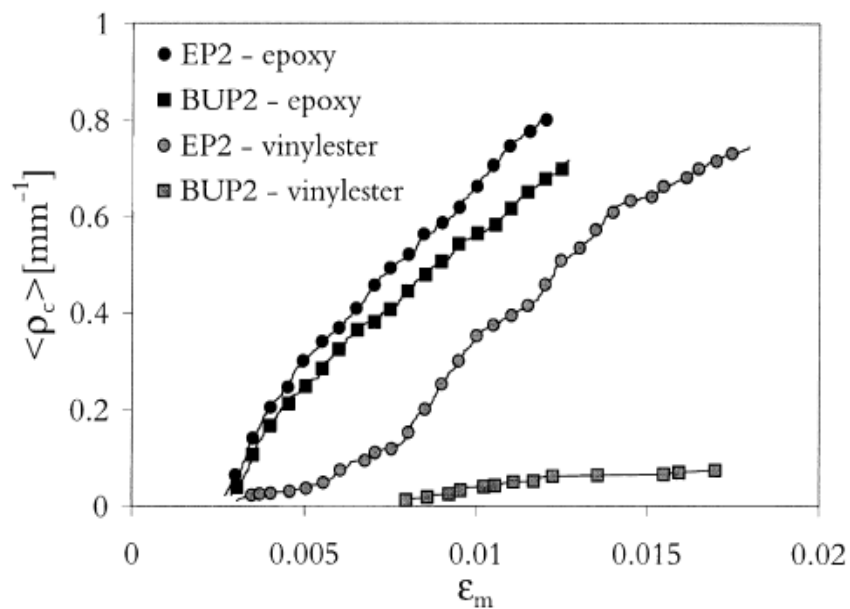


Figure 2.11. Crack density (ρ_c) as a function of applied mechanical strain ϵ_m . Comparison between laminates with the same fibre but different matrices. Two types of fibre, BUP2 and EP2, are compared [44].

2.11.2 Effect of matrix

Interfacial matrix will usually determine the performance of composite materials under load. Incompatible matrices could cause a premature failure of the composite due to physical or chemical unsuitability. For example, poor wettability between ultrahigh molecular weight polyethylene fibres and epoxies results in weak bonding strength [45]. A large number of studies have been carried out on the effect of matrix properties on the failure performance of composites. Boller (1969) [46] found that the fatigue performance of epoxy matrix composites is superior to that of polymer vinyl ester, phenolic, and silicon resins, due to high strength, good bonding to the fibres, and low shrinkage. This results in smaller residual stress, less exposure, and higher strain without cracking. It has also been reported that composites with vinyl ester resins have a higher fatigue resistance than polymer resin under cyclic loading. Scholte (1993) [47] mentioned that isophthalic polymers have better fatigue performance than polyester resin, whereas only a negligible difference was noted between vinyl ester and a new pre-accelerated thixotropic vinyl ester.

2.11.3 Effect of the interface

The interface is the point where the local properties begin to change from those of the most of the fibre to those of the matrix. Studies by Shih and Ebert (1987) [48] and Curtis (1987) [49] have reported that there are significant effects on crack initiation and propagation depending on the bonding strength of the interface as well as fibre orientation and principal stresses. A weak interface and strong fibres leads to deviations the cracks parallel to the fibre direction, as shown in figure 2.12.a. On the other hand, strong interface bonding and ductile fibres are sensitive to crack tip stresses, and as a result cracks may grow into the fibre causing rapid fatigue failure, as in figure 2.12.b [17].

Sekercioglu et al (2005) [50] have studied the effects of bonding clearance and interfacial fit on the strength of cylindrical composites. Significant decreases were observed in static and cyclic strength as the bonding clearance increased. Gan et al (2009) [45] modelled the progressive damage of interfacial debonding in composites using nonlinear models due to the complexity of the failure mechanisms.

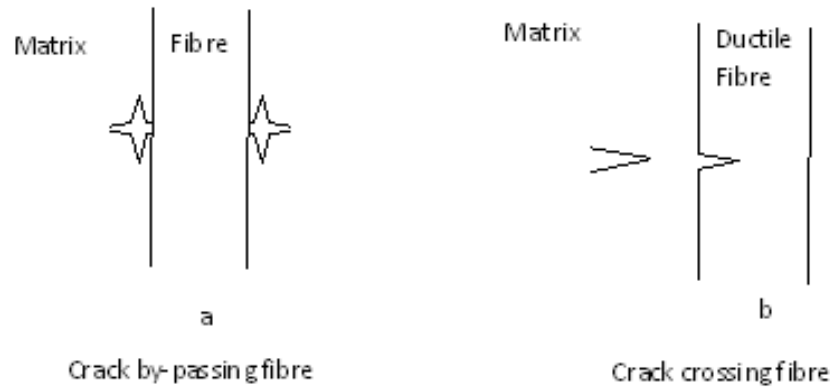


Figure 2.12 Modes of fatigue crack growth in fibre reinforced material.

2.11.4 Effect of mean stress and stress ratio

The influence of mean stress on fatigue behaviour cannot be clearly recognised in the fatigue (S-N) curve. However, for design purposes this information may be essential, and so S-N curves for mean stresses are needed. These curves help in constructing the Smith diagram or master diagram, in which the stress amplitude S_A is plotted against mean stress S_m for the chosen life, as shown in figure 2.13. It can be easily recognised that the allowable stress amplitude decreases when mean stress increases. The influence of mean stress on the fatigue behaviour of composites is similar to that of metallic material due to the linear relationship between stress amplitude S_A and mean stress S_m . The relationship between fatigue strength S_E at zero mean stress for a given life and the stress rupture strength for the life cycle S_C of the material suggested by Goodman [17] is:

$$S_E = \frac{S_A}{1 - \frac{S_m}{S_C}} \quad (2.3)$$

Many investigations have been carried out by a number of researchers in order to study the effect of mean stress on the fatigue behaviour of composite materials. El Kadi and Ellyin (1994) [51] implemented an off-axis fatigue test on unidirectional

glass/fibre composites under different stress ratios R (the ratio of minimum stress to maximum stress). They found fatigue strengths were lowest at $R = -1$ than ratios of 0 and 0.5. Miyano et al (1995) [52] investigated the effect of the stress ratio on fatigue behaviour for unidirectional carbon fibre reinforced plastic (CFRP). They found that fatigue strength becomes lower as the stress ratio decreases from 1 to 0. Kawai et al (2004) [36] modelled the fatigue behaviour of an off-axis unidirectional T800H/2500 system over the range of non-negative mean stresses, showing the independence of fibre orientation and stress ratio.

More recently Talreja et al (2010) [53] studied the effect of stress ratios on fatigue performance referring to material axis other than geometrical axis. They concluded that the ratio of shear stress to longitudinal stress has a much stronger effect than the ratio of transverse stress to longitudinal stress on the fatigue strength of composites.

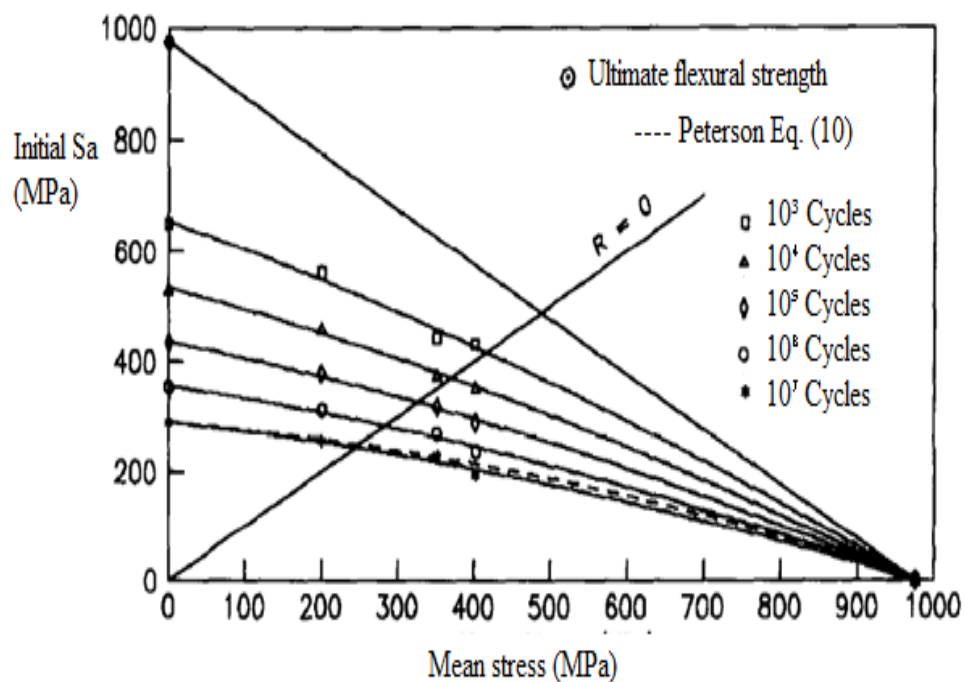


Figure 2.13. Master diagram of GFRP showing influence of mean stress on fatigue strength [54].

2.11.5 Effect of loading frequency

Loading frequency significantly influences the fatigue of composite materials, due to temperature rise with the specimen during fatigue tests. As a result the fatigue life decreases when load frequency is increased. For all stress levels, the number of cycles to final failure increases when loading frequencies are increased due to the decrease in time under load. Curtis and Moore (1983) [37] claimed that the effect of frequency on fatigue life is due to creep/fatigue interaction. They also reported that damage development is strongly dependent on the stress ratio.

In fact the effect of loading frequency is relatively complex, since it acts at two levels. The first level concerns the viscoelastic behaviour of glass/epoxy composite. High frequency loading leads to rises in temperature in the specimen, and in this case the life expectancy depends on the material's geometry and ability to dissipate the heat. The second level relates to the interaction between fatigue and creep. Low loading frequency means a higher load time, which can influence component life time by increasing the creep rate. So the load frequency should be chosen to minimize resin temperature and avoid any significant creep taking place. Joon et al (2009) [55] investigated the effect of loading frequency on the fatigue behaviour of a silicon carbide fibre reinforced glass ceramic composite at room temperature. They reported that the fatigue life decreases as load frequency increases, according to their investigations by analysis of microscopic characterisation using electron microscopy.

In addition to the factors mentioned above which affect the fatigue behaviour of composites, several additional factors also influence fatigue, such as environmental conditions, the shape and structure of the specimen, and stress concentrations such as holes, notches, and other imperfections in the composite structure.

2.12 Fatigue curve

The fatigue life is defined as the total number of cycles at a given stress level to cause failure. Failure in the field of composite pipes occurs when liquid leaks through the pipe wall (weepage). Generally the method used to evaluate the fatigue life of materials starts by subjecting the component to static or cyclic loading of a constant amplitude and then recording the number of cycles to cause failure at a

given stress level in the case of cyclic loading, or the time required to fail in the case of static loading. By applying different stress levels and recording the corresponding number of cycles, the fatigue curve (S-N curve) can be then built up. S-N curve can be defined as a curve showing mean stress against number of cycles to failure (N). Figure 2.14 shows S-N curve obtained from real data for reinforced laminate composite epoxy under cyclic loading [56].

The mean and average stresses can be defined as:

$$\sigma_m = \frac{\sigma_{max} + \sigma_{min}}{2} \quad (2.4)$$

$$\sigma_a = \frac{\sigma_{max} - \sigma_{min}}{2} \quad (2.5)$$

where, σ_m is mean stress, σ_a is average stress, σ_{max} and σ_{min} is the maximum and minimum loads within one cycle.

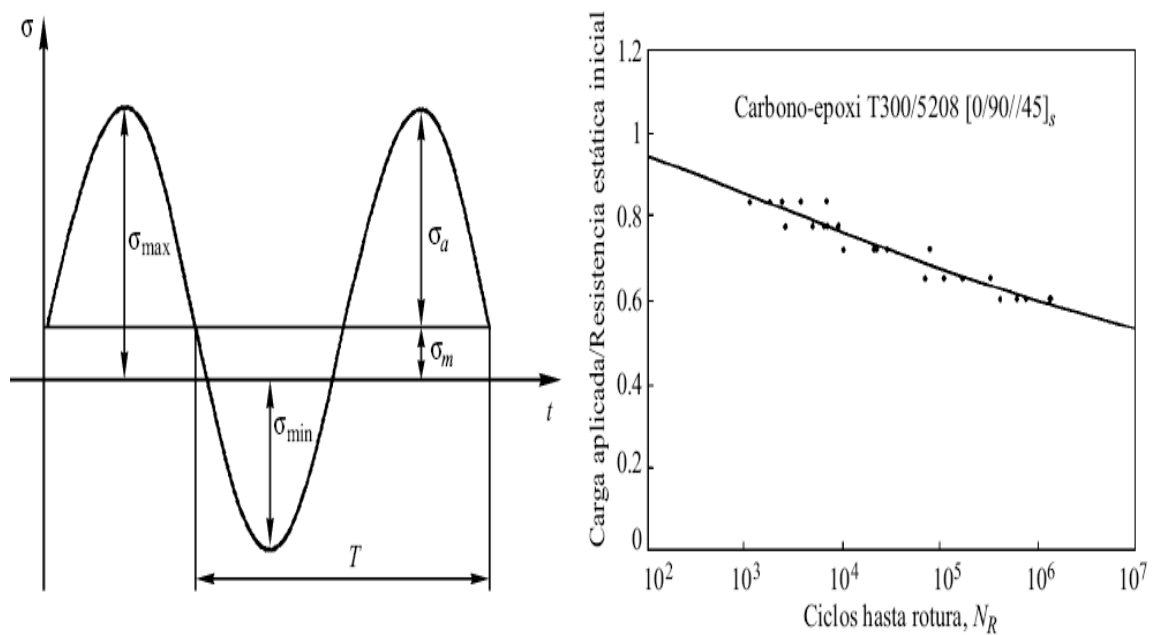


Figure 2.14. S-N curve for a carbon-epoxy laminate T300/5208 [0/90/±45] and typical sinusoidal shape of a load function generated by a fatigue testing machine [56].

The prediction of fatigue curves in composites is difficult for many reasons, the main one being the variations in failure modes under different stress ratios. A number of studies have investigated fatigue in glass/fibre reinforced composites. Hashin (1981) [57] has published extensive fatigue data for glass fibre reinforced material, and found it difficult to establish the fatigue curve for multi direction laminates due to large scatter in the data as shown in figure 2.15 which are not usually observed in metals.

To date a large number of fatigue studies have been conducted, due to the importance of fatigue curves of defining the long-term behaviour of composites. Although the most appropriate method of prediction has not yet emerged, the American Standard ASTM D-2992 provides an acceptable guide for designing and testing fibre glass reinforced composites based on the regression line from the fatigue curve. Its procedure and criticisms of it are discussed later in this chapter.

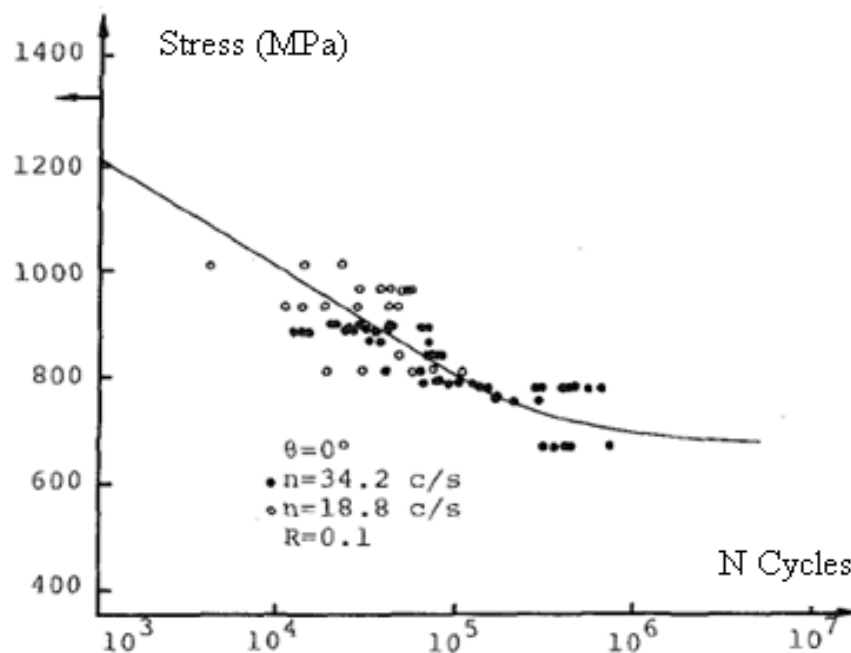


Figure 2.15. Data scatter showing the difficulty of establishing the S-N curve for multidirectional laminates [57].

2.13 Failure modes of long fibre composites

There are three most important types of failure modes in composites, as illustrated in figure 2.16: (a) axial tensile failure; (b) transverse tensile failure; and (c) shear failure. Tensile failure occurs when a large axial stress applied to the lamina causes fibre and matrix fracture, with the fracture line normal to fibre direction. Lower transverse and shear loads could lead to transverse and shear delamination with the fracture path parallel to fibre direction. In this case the fracture occurs within the matrix at the fibre/matrix interface [16].

The behaviour of composites under compression loading is different from cases of tensile and shear loading. Fibres under axial compression will buckle, resulting in compression and tensile stresses across different parts of the fibre section, leading eventually to fibre fracture. Figure 2.17 shows a carbon fibre reinforced composite failed under compressive load.

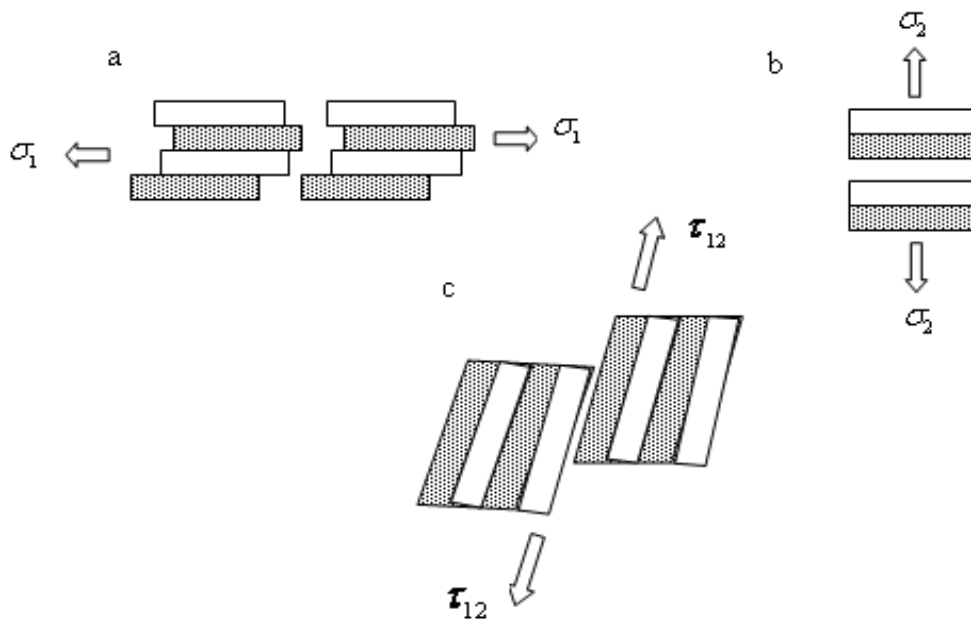


Figure 2.16. Possible failure modes in a laminate.

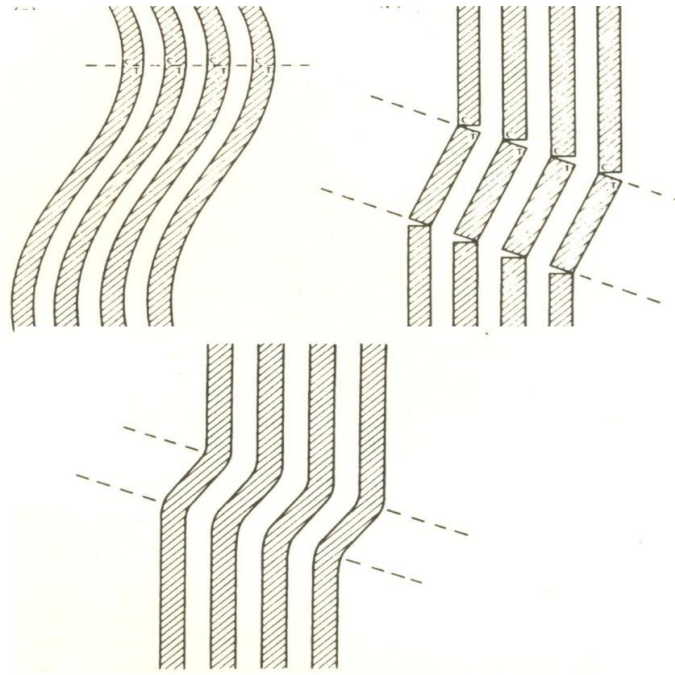


Figure 2.17. Tensile and compressive load in a fibre due to in-phase buckling, fracture and bending [16].

2.14 Failure development in GRE pipes

Filament wound composite pipes exhibit a complex sequence of damage which eventually leads to final failure. It has been noted that glass/fibre reinforced plastic (GRP) pipes subjected to biaxial loading fail due to a sequence of damages starting with matrix microcracking and then delamination, weepage and finally fibre breakage.

2.14.1 Matrix microcracking

A number of studies suggest that the most widely observed failure mechanism in filament wound composite pipes is matrix microcracking. The immediate effect of the microcracking is to cause significant degradation in mechanical and thermal properties, as represented by Young modulus, Poisson ratio, and thermal

conductivity. In addition, matrix microcracking may lead to weepage or even fibre breakage [58].

Avesten and Kelly (1973) [59] found that composites which failed under low strain have multiple cracks of that under high strain, and they derived a method to calculate interfacial stress called multiple fracture theory. This theory has been developed by Garrett and Bailey (1977) [60]. Studying the ply thickness effect on matrix transverse cracking in cross-ply laminates, they found that transverse cracks decreased as thickness increased up to 0.4 mm, then the strain became constant at around 0.4%.

Based on microscopic examination, Jones and Hull (1979) [61] classified the matrix microcracks into two main types: parallel and oblique transverse cracks. Transverse cracks can be found parallel or interlaminar to the fibres. Parallel transverse cracks form through the thickness of the laminate in response to the strain normal to the fibre, whereas interlaminar cracks formed in the longitudinal direction of the laminate in response to shear strain. Oblique transverse cracks usually propagated in the diagonal direction of the laminate in response to both tensile and shear strain.

Scanning electron microscopy (SEM) was used by Smith et al (1985) [62] to observe the development of matrix microcracking using a small tensile rig. They noted that cracks initiated near to the centre of the transverse ply at the fibre/matrix interface where the strain concentration was high.

Nairn et al (2000) [63] reported a correlation between an energy analysis of the composite and prediction of microcracking under a variety of load conditions. The microcracking properties of any laminate could then be predicted if microcracking fracture toughness was shown.

Recently, Talreja et al (2010) [64] evaluated and modelled cracks in multidirectional laminates of $[0_m, 90_n, \mp\theta_p]_s$. They reported that “In general, the damage initiation and progression in an off axis orientation depend on the local constraint on the crack opening displacement imposed by the plies immediately surrounding the cracking plies. The total thickness of the unseparated plies in an off-axis orientation is also found to be important in the damage evolution process”.

2.14.2 Delamination

Delamination or interlaminar cracking occurs when two adjacent plies or the matrix-fibre bonding separate, and it occurs under various load conditions [31]. The most common interlaminar cracks occur as consequence of transverse matrix cracking as well as from manufacturing defects [65]. Delamination can also be defined in terms of material strength under compressive loading due to mixed buckling, which could be local or global as shown in figure 2.18 [66]. Jones and Hull (1979) [61] examined filament wound pipes under biaxial loading and found that delamination usually occurred on the compressed side of the pipe, and was associated with transverse cracks.

In fact there are four types of delamination: strip, circular, elliptical and square. The elliptical delamination of laminate plates was considered by Chai and Babcock (1981) [67] using analytic method based on energy release rate, whereas a three dimensional finite element analysis was used by Whitcomb (1992) [68] in examining postbuckled embedded circular delamination. Aboudi (1994) [69] used a modification of laminate theory to find a suitable model to depict delamination in composite pipes. A Continuous analysis method was used by Wang et al (1995) [70] to determine the local buckling load of delaminated beams and plates with single or multiple delamination. A non-linear finite element analysis was also used by Hwang and Mao (1999) [71] to study of buckling loads and modes as well as critical loads for delamination development in carbon/epoxy composites.

Ozdil and Carlsson (2000) [72] presented a model to predict delamination growth in filament wound pipes. Rasheed et al (2002) [65] then investigated the delamination buckling of composite rings under external pressure. They concluded that the thick delaminated layers were found to have no tendency to snap-buckle inwards until pipe failure, whereas thin delaminated layers were found to be more likely to buckle inwards locally prior to pipe collapse. Zor et al (2005) [66] tested plates with square shaped holes in order to investigate delamination behaviour under buckling load using the three dimensional finite element method. They concluded that two important factors affecting critical delamination width are fibre orientation and the boundary conditions of the plate.

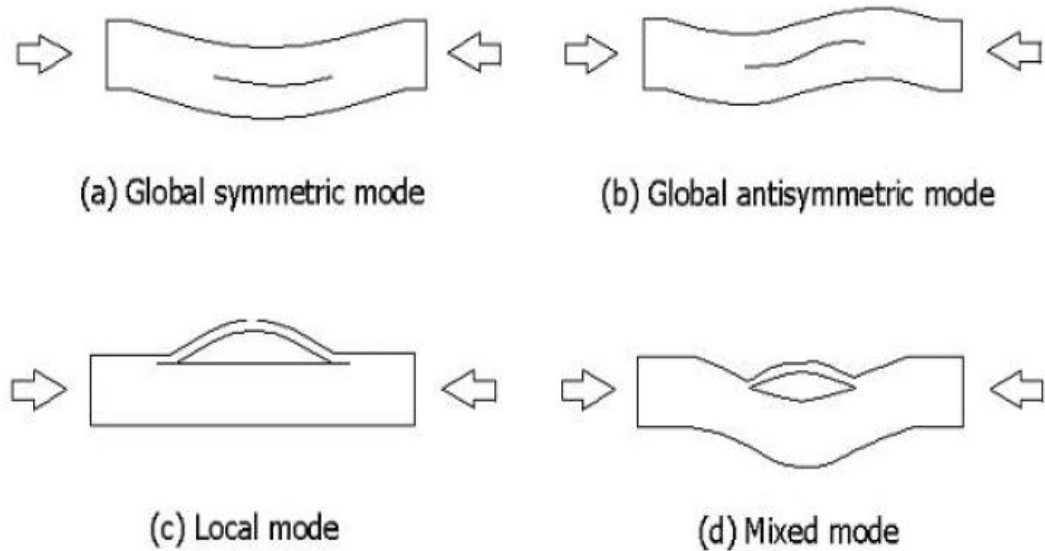


Figure 2.18. Buckling mode shapes for a delaminated composite[66].

2.14.3 Weepage

Weepage is a penetration or leakage of fluid through the pipe wall. When loads are applied cracks will initiate in the matrix and with continued loading these multi cracks will develop which could affect stiffness properties and more critically, fluid will eventually find pathways to cause weepage. Hull et al (1979) [31] found that filament wound pipes under pure hydrostatic pressure failed due to weepage which was associated with transverse cracking of the resin-fibre interface. Rosenow et al (1984) [73] also reported that pipes subjected to biaxial loading start to weep due to longitudinal and circumferential cracks. Soden et al (1993) [32] observed that filament wound composite pipes usually failed by weepage at stresses much lower than fracture stress. Mertiny et al (2007) [74] quantified leakage damage in high pressure fibre-reinforced polymer composite tubes, and found a clear correlation between matrix damage and fluid leakage due to stress-strain and leakage. Moreover, load rates had a significant influence on leakage stress and strain levels.

2.14.4 Fibre breakage

The last stage of failure in composites is fibre breakage, which usually occurs when stresses exceeds the fibre strength. Hull et al (1978) [31] reported that filament wound composite pipes at winding angles of 35°, 45°,55°,65° and 75° subjected to internal pressure showed matrix microcracking up to weepage. After that the fibre angle rotated towards the ideal angle of 55°, and then the fibres started to buckle and eventually failed.

Many investigations have evaluated the breakage of either short or long fibres. Schürhoff et al (2004) [75] performed an experimental test to determine the effect of creep loading on short fibre reinforced metal matrix composite. They found that fibre damage depended on load orientation, where the earlier fibre damage occurred when load acted perpendicular to fibre direction.

2.15 Failure development of GRE pipes under biaxial loading

The behaviour of filament wound composite pipes under biaxial loading is different from that under pure internal pressure due to variations in failure mode under different stress ratios. Carroll et al (1995) [76] observed that pipes exposed to axial dominated loading exhibit positive strain. In this case cracks develop parallel to fibre direction as the loading increases and final failure depends on the applied stress rate. For low stress rates, matrix cracks develop and final failure occurs as weepage, whereas complete matrix failure occurs at high stress rates. This facilitates a saturation of microcracking throughout the wall thickness; and consequently fibres delaminate from the matrix and then fail.

Pipes under hoop dominated loading showed more than one mode of failure, since the negative axial strain prevented microcracking in the matrix from being observed. Visible whitening, which may have been caused by matrix microcracks, was noted and failure could have occurred inside the pipe due to the highest hoop stress through the pipe wall. The second failure mode was delamination, which occurred as a result of crack propagation. In the case of compression the final failure involved matrix shear with an angle parallel to the fibre direction through the wall thickness.

2.16 Failure criteria

The main purpose of analysing failure criteria is to determine composite strength and possible failure modes under combined stresses. In composite pipes failure mode is related to weepage with transverse matrix cracking and the debonding of the fibre/matrix interface. A number of failure criteria have been suggested by researchers to identify the range of failure strengths and modes. For example, Hashin et al (1973) [77] modified mechanical fatigue criteria so as to cover for fibre failure and matrix failure modes. Jones and Hull (1979) [61] microscopically examined the failure mechanisms of GRP pipes and found that weepage in mode II was governed by the occurrence and interaction of transverse cracks, as shown in figure 2.19, while in mode III weepage occurred at high stress levels due to delamination.

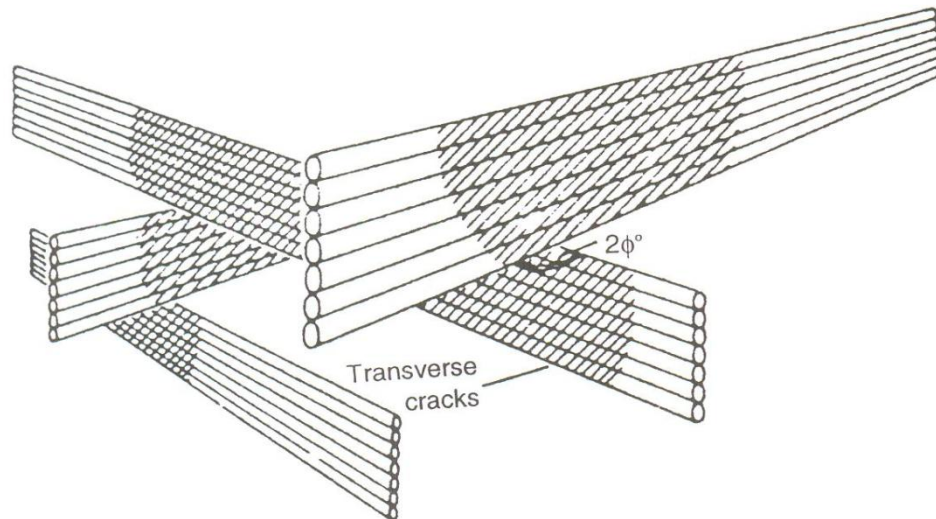


Figure 2.19. Formation of weepage path through the pipe wall by the intersection of transverse cracks. The flow of liquid is restricted to three contact points [61].

Frost and Cervenka (1994) [78] applied axial tensile and hoop loading to GRP pipes, and found that matrix cracks ran through the ply thickness parallel to the fibres, thus helping to keep them intact. They proposed a failure criterion to fit the experimental data for $\pm 45^\circ$, $\pm 55^\circ$ and $\pm 75^\circ$ GRP pipes as the follows:

$$\left(\frac{\sigma_t}{\sigma_{t,\text{fail}}}\right)^2 + \left(\frac{\tau}{\tau_{\text{fail}}}\right)^2 + C \left(\frac{\sigma_t \tau}{\sigma_{t,\text{fail}} \tau_{\text{fail}}}\right) = 1 \quad (2.6)$$

where σ_t , τ are the stress and shear at the given load, $\sigma_{t,\text{fail}}$, τ_{fail} and C are the material constants.

The majority of criteria suggested so far are suitable for two dimensional stress states, although some have also considered three dimensional stress states.

2.16.1 Tsai-Hill maximum stress criterion

The maximum stress criterion in composite laminate is generalized for tensile and compression loads. This criterion assumes that failure occurs when the stress parallel or normal to the fibre axis reaches the appropriate critical value, when the following is satisfied [16]:

$$\sigma_1 \geq \sigma_1^*, \quad \sigma_2 \geq \sigma_2^*, \quad \tau_{12} \geq \tau_{12}^*.$$

The magnitude of σ_x necessary to cause failure in cases of applied uniaxial tension can be plotted as a function of the angle ϕ between the stress and fibre axes, for each of the three failure modes.

$$\sigma_x^* = \frac{\sigma_1^*}{\cos^2 \phi} = \frac{\sigma_2^*}{\sin^2 \phi} = \frac{\tau_{12}^*}{\cos \phi \sin \phi} \quad (2.7)$$

The strains in axial and hoop directions are expressed as:

$$\varepsilon_x = \frac{\sigma_x}{E_x} - \nu_{yx} \frac{\sigma_y}{E_y}, \quad \varepsilon_y = \frac{\sigma_y}{E_y} - \nu_{xy} \frac{\sigma_x}{E_x}, \quad \gamma_{xy} = \tau_{xy} = 0 \quad (2.8)$$

Strains parallel and perpendicular to fibre direction respectively are:

$$\begin{bmatrix} \varepsilon_1 \\ \varepsilon_2 \\ \gamma_{12} \end{bmatrix} = [\mathbf{T}'] \begin{bmatrix} \varepsilon_x \\ \varepsilon_y \\ \gamma_{xy} \end{bmatrix}, \quad [\mathbf{T}'] = \begin{bmatrix} c^2 & s^2 & cs \\ s^2 & c^2 & -cs \\ -2cs & 2cs & c^2 - s^2 \end{bmatrix} \quad (2.9)$$

where: $\varepsilon_1, \varepsilon_2$, are the strains in fibre direction and transverse direction respectively, γ_{12} is the shear strain, and c, s are abbreviations of $\cos\varphi$, $\sin\varphi$.

Axial failure is typically expected only for very small loading angles, but the predicted transition from shear to transverse failure may occur anywhere between 20° and 50° depending on the values of τ_{12}^* , and σ_2^* . In practice, there is likely to be some interaction between failure modes [16]. For instance, shear failure is expected to occur more easily when shear stress dominates.

The most commonly used model taking account of this effect is the Tsai-Hill criterion, which can be expressed mathematically as:

$$\left(\frac{\sigma_1}{\sigma_1^*}\right)^2 + \left(\frac{\sigma_2}{\sigma_2^*}\right)^2 - \left(\frac{\sigma_1\sigma_2}{\sigma_1^{*2}}\right) + \left(\frac{\tau_{12}}{\tau_{12}^*}\right)^2 = 1 \quad (2.10)$$

where:
$$\begin{bmatrix} \sigma_1 \\ \sigma_2 \\ \tau_{12} \end{bmatrix} = [C_{ij}] \begin{bmatrix} \varepsilon_1 \\ \varepsilon_2 \\ \gamma_{12} \end{bmatrix}, \text{ and } C_{ij} \text{ is the matrix stiffness.}$$

2.16.2 Tsai – Wu Criterion

The Tsai–Wu criterion includes the coupling with shear deformation for yielding, which is not considered in the Tsai-Hill criterion. This method is one of the most common criteria used for composite materials, composite strength enabling to be predicted without any experimental data. Moreover, the Tsai–Wu criterion is capable of being applied to two or three-dimensional stresses, by expanding the stress tensor and reducing the second order terms to give [79]:

$$F_i\sigma_i + F_{ij}\sigma_i\sigma_j \leq 1 \quad (2.11)$$

where σ is the applied stress and F_i, F_j are strength parameters and the notation is used where $i, j = 1, 2, 3, \dots, 6$

For axi-symmetric cases the theory can be written as:

$$F_1\sigma_x + F_2\sigma_y + F_3\sigma_z + F_{11}\sigma_x^2 + F_{22}\sigma_y^2 + F_{33}\sigma_z^2 + F_{66}\tau_{xy} + 2(F_{12}\sigma_x\sigma_y + F_{13}\sigma_x\sigma_z + F_{23}\sigma_y\sigma_z) = 1 \quad (2.12)$$

The strength terms can be determined from a properties test using

$$F_1 = \frac{1}{\sigma_{XT}^f} - \frac{1}{\sigma_{XC}^f}, \quad F_{11} = \frac{1}{\sigma_{XT}^f \cdot \sigma_{XC}^f}$$

$$F_{66} = \frac{1}{(\sigma_{XY}^f)^2}, \quad F_{12} = \frac{1}{2} \sqrt{F_{11} \cdot F_{22}}$$

where σ_{XT}^f : longitudinal tensile strength, and σ_{XC}^f : longitudinal compressive strength.

However the main criticism of the Tsai–Wu criterion is that it appears as more mathematical than physical concept.

2.17 Methods of failure analysis for filament wound composite pipes

As mentioned above weepage is the definitive failure mode in composite pipes. Complete failure is rarely noted when pipes have been exposed to any level of pressure loading. It has been discussed earlier in this chapter that stress-strain responses in composites are assumed to be linear up to the point when first damage starts to appear, after which non-linearity is the rule. But in fact composite laminates can last well beyond the first failed ply, and only eventually fail after continuing loading. This resistance depends on the nature of the multidirectional laminate lay-ups. As a result of the sequence of ply failures, the composite exhibits significant degradation in its properties. This can be represented as a decline in elastic modulus, Poisson's ratio changes and weakening of thermal conductivity. This degradation continues up to the last ply failure and then the composite laminate fails completely. The two most common techniques used in failure analysis here are the ply by ply and sudden failure methods.

2.17.1 Ply by ply method

The ply by ply method for failure analysis is generally based on laminate theory, which is used initially to estimate the elastic constants of the lamina. The second step

is to obtain the equivalent stiffness in the laminate direction by applying a transform matrix. By calculating the stiffness matrix in the laminate direction (x, y) and applying a mechanical load to the lamina, the stress and strain in this coordinate system ($\sigma_x, \sigma_y, \varepsilon_x, \varepsilon_y$) will consequently be easy to determine. Finally, the failure criterion is applied to the resulting stress and strain values, and these are compared with the criterion condition. If failure has not been reached under this load, the applied load needs to be increased until the criterion condition has been achieved. This procedure can be repeated for the next layer until the stiffness matrix of the laminate becomes singular.

Many studies have deployed the ply by ply method in analysing failure in composites. Eckold et (1978) [80] built up a strength envelope for different composite tubes based on the ply by ply method with a maximum stress criterion. Sun and Tao (1998) [4] also used the ply by ply method with the assistance of the Hashin- Rotem criterion to predict the failure envelope of unidirectional composite laminate. More recently Adden and Horst (2009) [10] introduced a model which was also based on ply by ply stiffness degradation to evaluate fatigue damage in GFRP tubes under multiaxial loading.

2.17.2 Sudden failure method

Unlike the ply by ply method, the sudden failure method does not consider the stiffness degradation of the lamina. This method is generally based on fibre failure rather than progressive matrix failure in the lamina. To carry out this analysis, the load required for fibre failure in the dominant lamina is calculated, and then the chosen failure criterion for the material is applied. In fact the laminate strength predicted by Sudden et al [30] using this method is higher than that predicted by the ply by ply method.

Another method used for the failure analysis of fibre dominated laminate, where failure can be due to the shear failure of the fibres, is called the Hart-Smith criterion [81].

2.18 Failure Assessment

Several methods and techniques have been developed in order to monitor and evaluate damage mechanisms and failure modes. The most commonly used techniques are microscopy and acoustic emission. Other techniques used in failure assessment in composite materials by many researchers include X-ray examination, ultrasonic and infra-red techniques.

2.18.1 Microscopy

The most common tools used to observe the microstructure of composites are the optical and electron microscopes. In order to proceed with the microscopic examination of a sample a specific sequence of actions needs to be taken first.

The selected sample specimens are sectioned, grinded and polished. Microscopy is useful in viewing specific areas of damage, providing a detailed view of any section. Figure 2.20 shows the cross sectional scan of a $\pm 55^\circ$ filament wound glass epoxy pipe. Transverse cracks formed under loading can be observed.

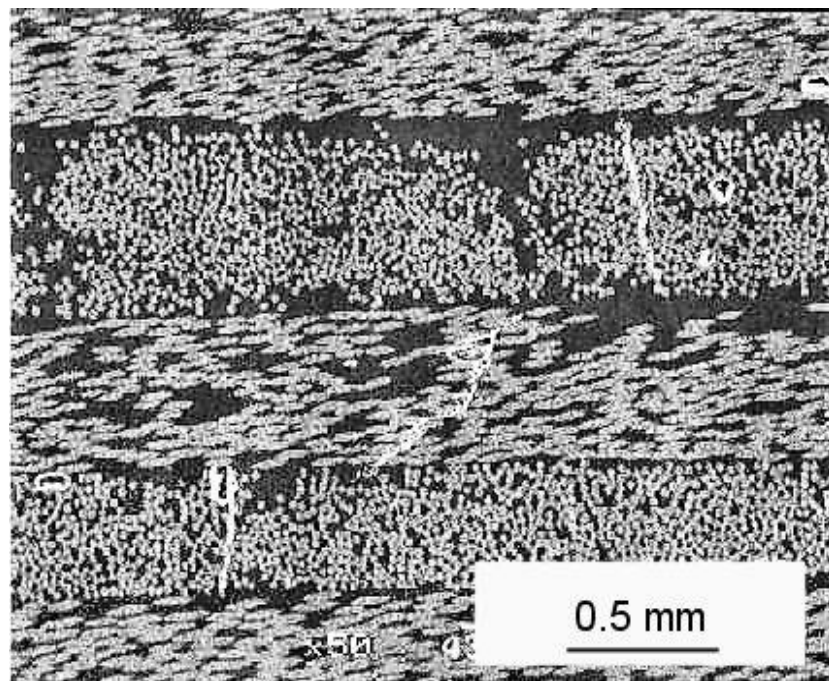


Figure 2.20. Matrix micro-cracks in a filament wound $\pm 55^\circ$ angle ply glass epoxy tube.

On the other hand, microscopy has only a limited ability to follow damage propagation as loading increases. Furthermore, microscopy is an unsuitable tool for evaluating large test specimens.

2.18.2 Acoustic emission

Recently acoustic emission AE analysis has been widely used in monitoring and evaluating the failure modes of materials in many applications. Acoustic emission techniques have been developed for use at the locations of areas and types of damage, based on recorded acoustic signals [82]. A number of studies have been carried out using acoustic emission techniques in order to evaluate failure mechanisms in polymer composite reinforced glass fibre.

Benmedakhene et al (1998) [83] tested a double-cantilever beam specimen under monotonic pure mode (I) conditions with various displacement speeds. They installed the acoustic emission equipment so as to detect crack initiation and to study mechanisms of crack growth. They reported that the strain energy release rate under cyclic loading increased as the applied load rate increased up to final failure. Furthermore, they found that the delamination process is a consequence of several types of damage, such as matrix cracking, interface debonding and fibre fracture. Combining acoustic emission analysis with enhanced microscopic observation helps to observe the crack paths, which appear to propagate through the resin along the fibre/matrix interface at high loading rate, as shown in figure 2.21.

Dogossy and Czigany (2006) [84] tested maize hull composites with applied tensile loads, in order to analyse and follow the failure process by acoustic emission observations. They reported that, it was possible to distinguish acoustic emission from the presence of three failure modes during the tests, which can be classified as matrix deformation (below 25 dB), maize hull pull-out (26-40dB), and maize hull breakage (over 41dB), as shown in figure 2.22.

Guillermo et al (2006) [85] presented a method for determining the endurance limit of fibre glass pipes under internal pressure using acoustic emission technology. They applied static and cyclic loads to 22 samples with 200 mm diameter and 1.5 m

length. Pipes were tested to failure, which was defined as the weepage of liquid through the pipe wall.

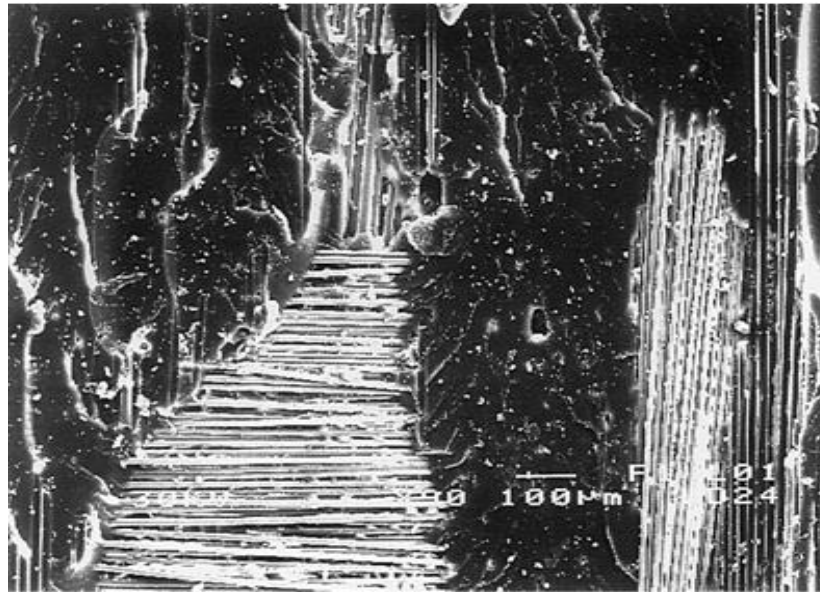


Figure 2.21. Crack propagation in the resin and the interface ($v=100$ mm/mn)[83].

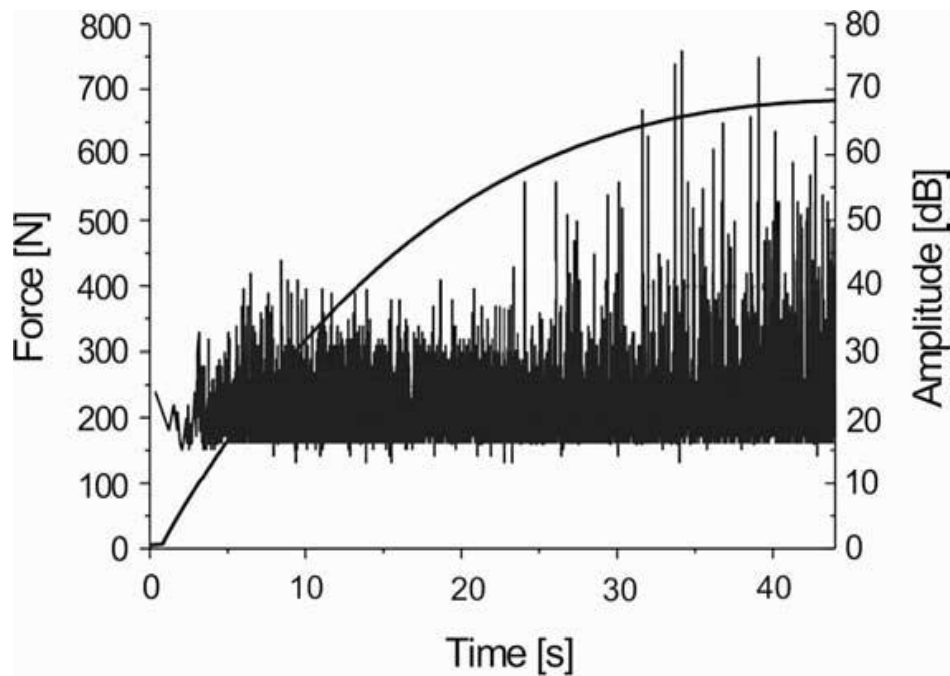


Figure 2.22. Characteristic tensile and amplitude curves of a PE composite containing 30 wt% MH [84].

They used the recorded data to plot cumulative signal strength versus time and also showed the estimated pressure at the acoustic emission ‘knee’, as in figure 2.23. They concluded that, there are correlations between the acoustic emissions during the first loading of the specimens and the ultimate life under cycle loading. Moreover, they claimed that the collected results from acoustic emissions can be used to predict the long term cycle loading performance of reinforced fibreglass pipes. They also concluded that acoustic emission can be used to evaluate the effect on fatigue performance of factors such as changes in materials, fabrication, and methods.

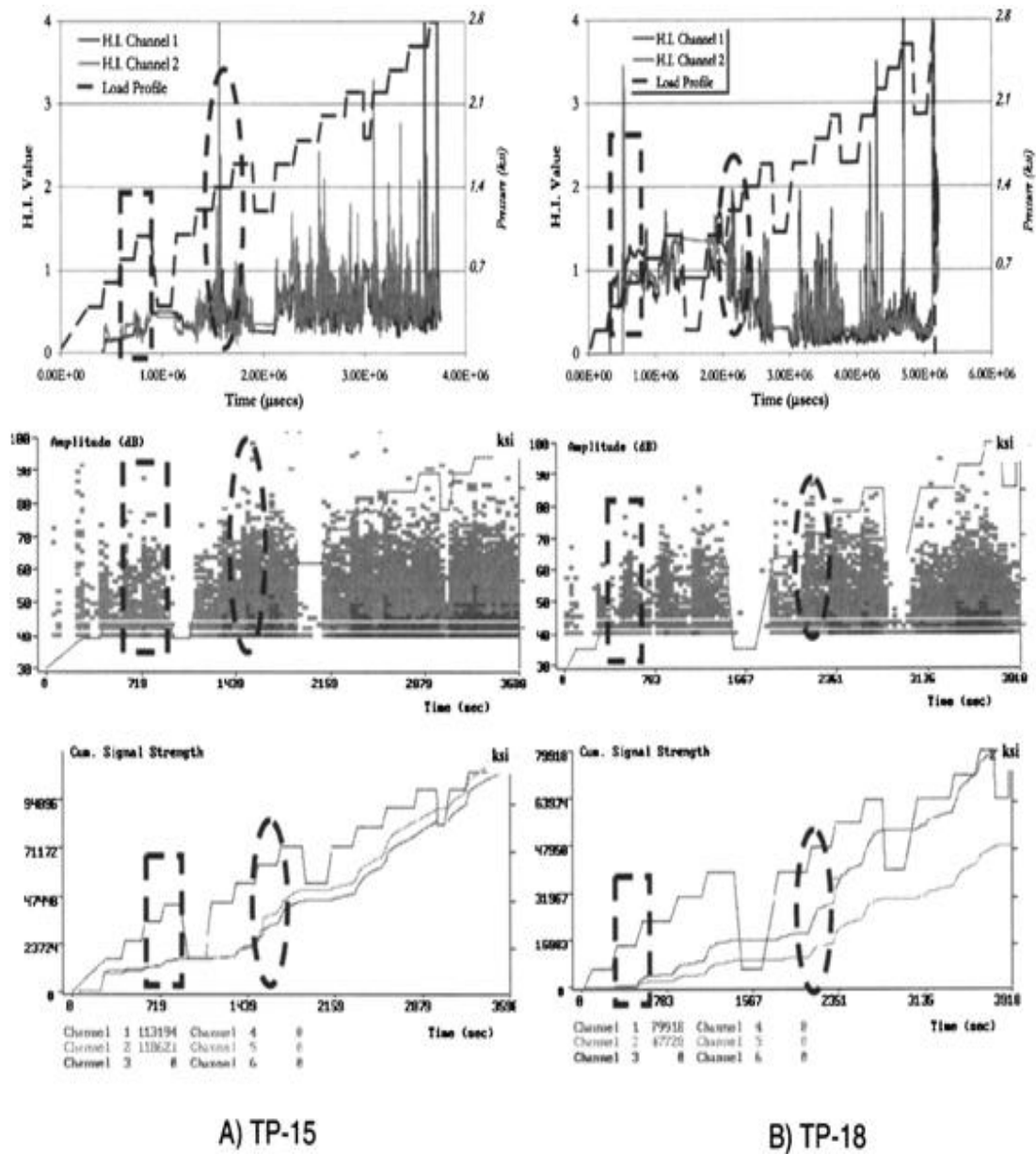


Figure 2.23. Determination of historic index (HI) from AE records [85].

Finkenstadt et al (2007) [86] tested polylactic acid (PLA) oil seed composites, and claimed that three different stages of deformation could be clearly discerned from acoustic emission evaluation. At first the debonding of fibres from the matrix was recognized, and then the yielding of the matrix occurred as a second stage, followed finally by the ductile fracture of the matrix.

2.19 Failure envelopes

A failure envelope graphically shows the failure strength of composite pipes under various hoop to axial stress ratios, where the coordinates of the curve indicate the hoop and axial strength of the pipes in these directions. The shape of the failure envelope depends on the mechanical properties of the GRE pipes, and it is significantly influenced by changing parameter such as winding angle, fibre and resin type and load conditions. Winding angle has a profound effect on the shape of the envelope; for example, when this angle starts to deviate from the axial to the hoop direction, a noticeable change in shape occurs which can be represented as an increase in hoop strength and decreased strength in the axial direction, so that the curve subsequently becomes narrower.

Hale et al (2000) [11] investigated the effect of hot and wet conditions on the behaviour of failure envelopes for fibre/glass tubes under biaxial loading. They found that its shape decreased and becomes narrower to original point of the axis as temperature increased, as shown in figure 2.24.

Ellyin et al (2000) [87] tested $\pm 66^\circ$ filament wound pipe under cycle loading with various stress ratios, and concluded that there is a noticeable regression in the elastic modulus with cycle loading which depends on both applied stress and stress ratio. Furthermore, they found that the largest decline in the pipe's stiffness was under pure axial loading, whereas less degradation was observed in the case of pure hoop loading where the failure mode was defined as fibre rupture.

Mertiny et al (2003) [88] investigated the effect of multi-angle filament winding on the strength of the tubular composite structure. Three pipes with different angle combinations of $[\pm 60^\circ]$, $[\pm 45^\circ, \pm 60^\circ]$, and $[\pm 30^\circ, \pm 60^\circ]$ were tested with various stress ratios. They concluded that the winding angle and applied stress ratios strongly

influenced the failure envelopes. For example, pipes with $[\pm 30^\circ, \pm 60^\circ]$ winding angle exhibited high performance under pure axial loading, whereas those with a $[\pm 60^\circ]$ winding angle showed the highest ability in the case of hoop loading. Figure 2.25 shows the effect of multi-angle filament winding on the failure envelope.

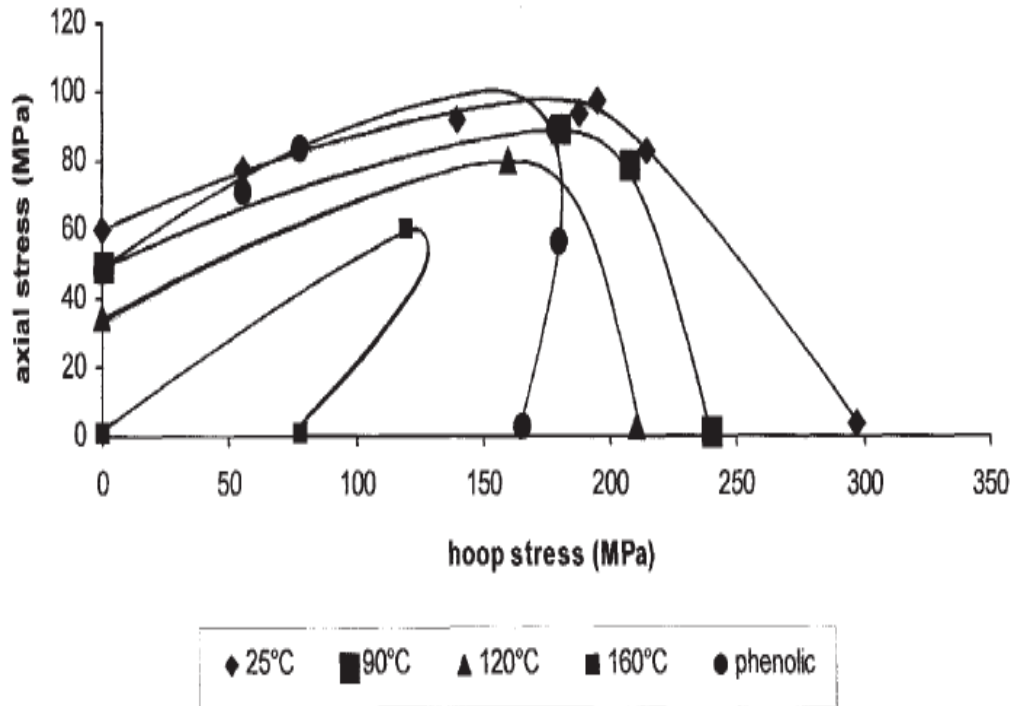


Figure 2.24. Failure envelopes for IPD epoxy and PSX phenolic $\pm 55^\circ$ filament wound pipes at 20 C° , 90 C° , 120 C° and 160 C° under biaxial loading [11].

Meijer et al (2008) [89] tested $\pm 60^\circ$ filament wound composite pipes with an inside diameter of 50.4 mm under a range of stress ratios with positive hoop stress and both tensile and compressive axial loads. Fourteen hoop to axial stress ratios were applied to these pipes, and they found that the maximum strength provided was by ratios below 7:1. They also claimed that five distinct failure modes were observed: axial tensile structural failure under the 0:1 and 1:1 ratios; weepage with the 2:1 ratio, local leakage under ratios of 4:1, 4.5:1, and 5:1, bursting with the 7:1, 1:0, and 7:-1 ratios, and axial compressive structural failure under the 0:-1 stress ratio.

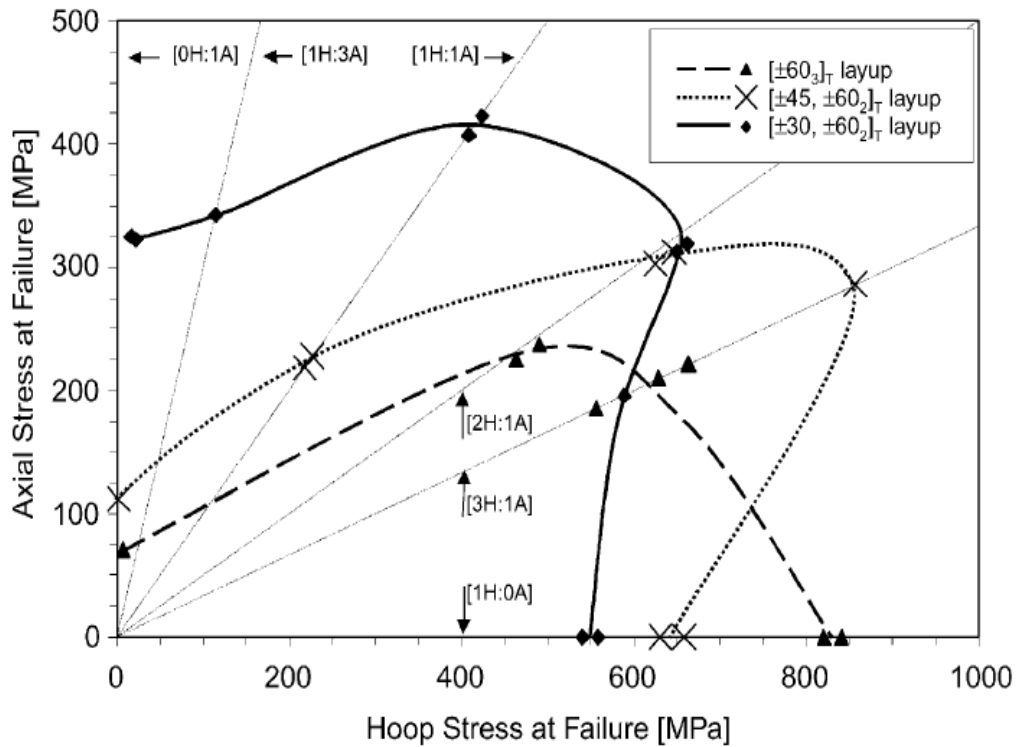


Fig2.25 Experimental structural failure envelopes and points of failure for of $[\pm 60^\circ]$, $[\pm 45^\circ, \pm 60^\circ]$, $[\pm 30^\circ, \pm 60^\circ]$ tube specimens [88].

2.20 Modelling of the failure behaviour of composites

2.20.1 Miner's law

Miner's law was associated by applying various stress levels to aluminium alloy test samples. Fatigue life is generally presented in the form of S-N curves and related to constant amplitude fatigue tests. Miner's law is the theory used to predict the fatigue life under conditions of varying loads. Equation 2.13 describes the application of Miner's rule with respect to cycle loading.

$$\sum_0^i \frac{N_i}{N_{fi}} = 1 \quad (2.13)$$

where N_i is the number of cycles at stress i , and N_{fi} is the number of cycles at the failure point.

Ifwarson et al (1998) [90] applied Miner's rule with regard to time spent at particular stresses and temperatures rather than number of cycles at a given stress. The method was investigated by applying stress to composite pipes with cycle loading at 80°C, and 95°C; see figure 2.26. They found that failure time based on Miner's law at a variety of test temperatures and stress cycles at 1.5 MPa at 100°C was about one-third of that with 2.5 MPa at 90°C. They also claimed that the test results were in agreement with the calculated failure time.

Miner's law has been also applied to reinforced thermoplastic pipes by Gibson (1999) [91] in order to predict the pipe regression curve. Two different pipe samples were subjected to internal pressure at different low speed loadings (LSL). These loads were uniformly applied up to failure. Equation 2.14 shows the modified form of Miner's law which was used in this investigation:

$$\int_0^{t_f} \frac{t_i}{t_{fi}} = 1 \quad (2.14)$$

The derived regression line was expressed as:

$$\sigma_t = A - B \ln(t) \quad (2.15)$$

where t_f is the time to failure at the given pressure P_i , σ_t is the applied stress, and A and B are regression constants.

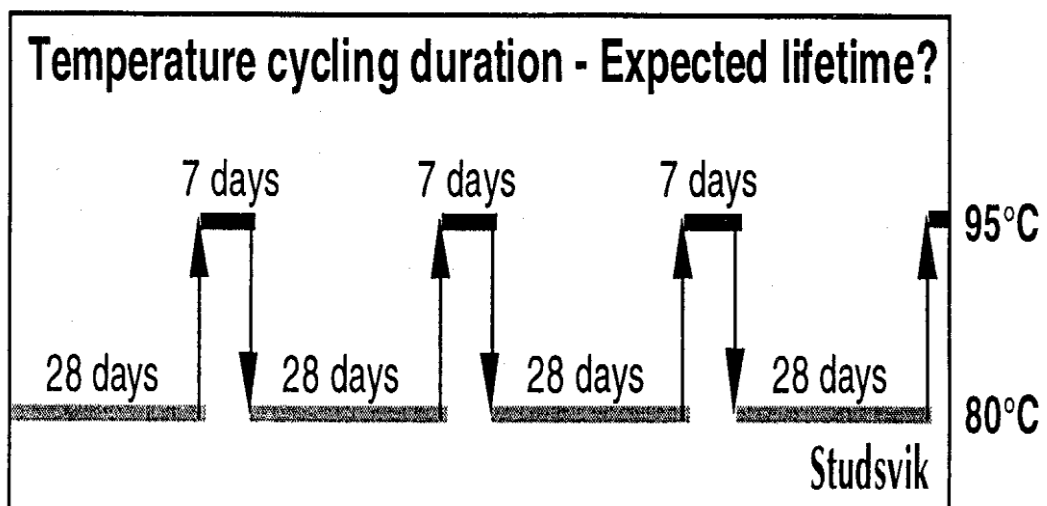


Figure 2.26. Illustration of temperature cycling test between 80°C and 95°C [90].

Integration was applied to Miner's law to give the failure stress σ_t and time to failure as a function of A, B as illustrated in equations 2.16:

$$\sigma_f = A + B \ln\left(\frac{\sigma_t}{B}\right), \quad t_f = \frac{B}{\sigma_t} \ln\left(\frac{\sigma_t}{B}\right) + \frac{A - \sigma_0}{\sigma_t} \quad (2.16)$$

Figure 2.27 shows a comparison of the curves generated from a Wellstream ramp experimental set up at 60°C with the regression curve plotted using the modified Miner's equation [91].

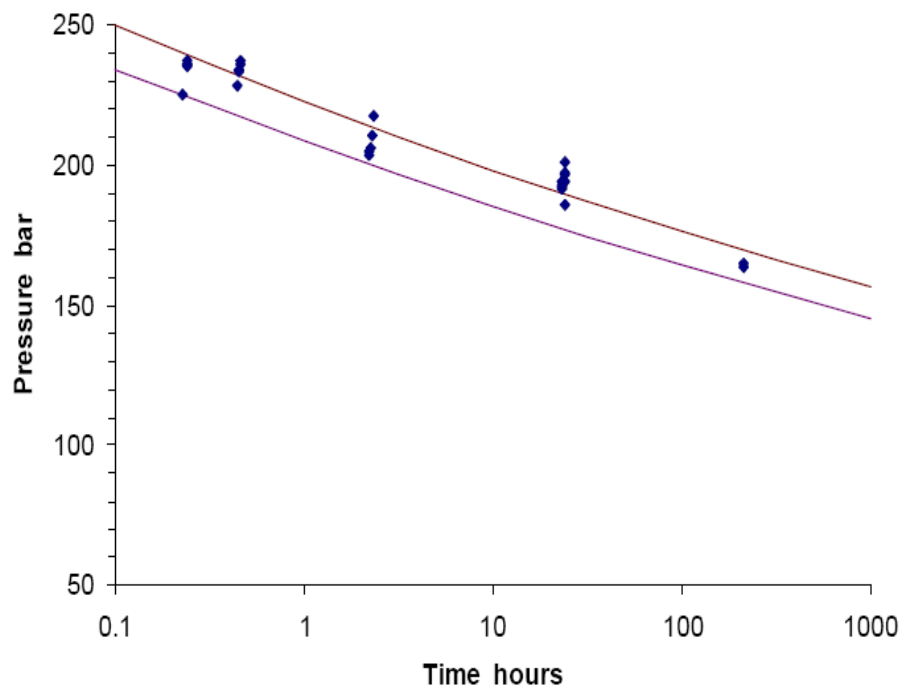


Figure 2.27. Constant pressure regression curves generated from Wellstream ramp experiments at 60°C. Mean line and LPL are shown [91].

2.20.2 Cumulative damage results and life prediction under cycle loading

Even though the accumulation of fatigue damage in fibre reinforced plastic is non-linear, Miner's law plots a linear regression, which is hence stress-independent and free from stress interactions. Owen and Howe [7] (1972) found good results for fibre reinforced plastic laminate when subjected to fatigue loading by improving equation 2.13:

$$\sum_0^i \left[A \left(\frac{n_i}{N_{if}} \right) - B \left(\frac{n_i}{N_{if}} \right)^2 \right] = 1 \quad (2.17)$$

where A, B are material constants.

The cumulative damage expression of the same form may also be related to initial fibre debonding, matrix cracking and fibre breakage.

2.21 Modelling of matrix microcracking

A number of studies have been conducted to estimate matrix microcracking using several methods in order to predict the degradation in mechanical properties. The matrix microcracking prediction can be grouped into fracture, variation, and continuous methods.

The fracture method is based on information about cracking obtained from micrographic analysis, such as crack spacing and width. This method considers the stress distributions in cracked laminate in regions of transverse cracks, which can be estimated by shear-lag variation and elasticity regression. Cox (1952) [92] has formulated a shear-lag theory in order to evaluate the stress in fibre entrenched in elastic matrix. Aveston and Kelly(1973) [59] derived their theory of multiple fracture using shear-lag theory.

A two-dimensional shear-lag model for progressive damage in composites was introduced by Henaff et al (1996) [93] to estimate the stress distributions and elastic constants of the damaged layers and laminate. Jiad Dharani (1998) [94] developed the method in terms of minimum potential energy by studying the effect of interface friction force on the fracture mode of a composite containing non-axisymmetric transverse matrix cracking and interface debonding. Robert et al (2003) [5] modified the method to evaluate the crack density of cracked angle ply laminate. Hui Zhang et al (2006) [95] also modified the variation method to study the effects of transverse cracking and local delaminations in symmetric composite laminates. Ogi et al (2009) [96] used this method with the assistance of the Weibull distribution and Paris law to predict a fatigue model for transverse cracking in CFRP cross-ply laminates under static fatigue loading. Strong correlations were found between crack density and both applied stress and load time.

With regards to the continuous damage method, the composite laminate is treated as a continuum of damage based on the stress-strain relationship. The life of the composite can be predicted by determining the damage level that reduces its mechanical properties below critical values. Several researchers have modelled the matrix cracking in composite laminates accordingly. Won-Lee et al (1989) [97] applied a second tensor to model crack damage in composite laminate. Schipperen (2001) [98] developed an anisotropic damage model to describe the transverse matrix cracking of laminates. A non-linear relationship was found in the stress-strain behaviour in the shear direction, by using the secant stiffness of 50% of the ultimate strain level in the investigation. More recently, Maimi (2008) [99] used a three-dimensional continuum damage model to predict the interlaminar failure mechanism.

2.22 Stiffness reduction in composites

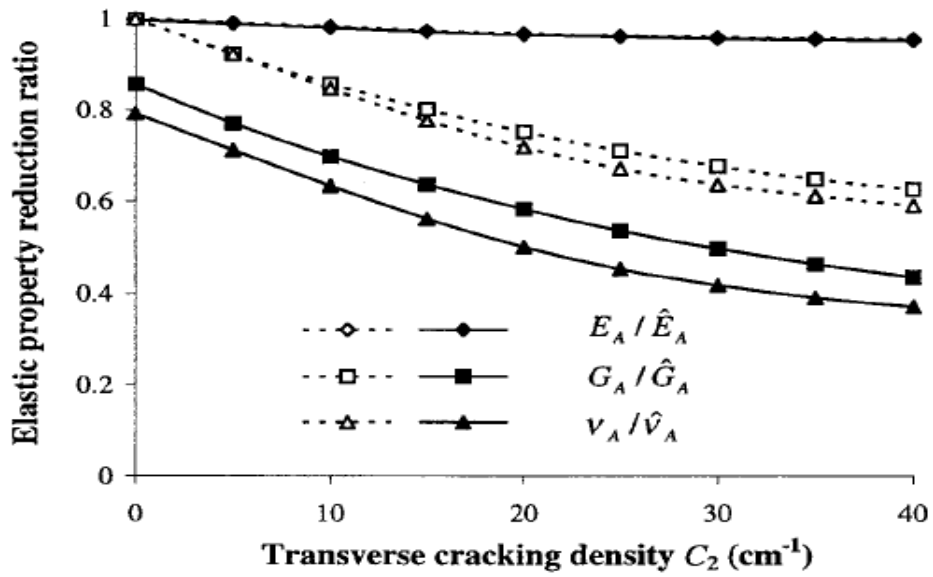
The stress-strain curve of composites is predominantly linear, and then strong non-linearity occurs close to final failure. The non-linear behaviour occurs as a result of degradation in the stiffness of the composite which is usually due to transverse matrix cracks. Transverse matrix cracking is generally the first damage noted when composites are subjected to any type of loading. As mentioned above many theories have been established to predict and follow the degradation in properties in composites, the most important of which are the variation principles [100], continuum damage mechanisms [101], approximate elasticity theory solutions [102] and shear-lag theory [103]. These models were developed to study the behaviour and degradation in stiffness of cross-ply laminates. However, more recently, several studies have investigated the effect of transverse cracking on the degradation in properties of multi directional laminates under biaxial loading. These have examined matrix cracking in off-axis plies [104], the interaction of transverse cracking with edge and local delaminations [105], and matrix cracking in quasi-isotropic laminates [106].

Shear-lag modelling provides an attractive method to calculate reduction in stiffness associated with transverse cracking, and this method has been modified to be suitable for the analysis of cross-ply laminates in various stacking sequences. On the other hand, the behaviour of cross-ply laminates under biaxial loading is different from that under uniaxial loading due to the possibility of matrix cracking occurring in the

transverse 90° and 0° directions (splitting). This type of failure is called multilayer matrix cracking, and it is mathematically more complex to analyse. Highsmith and Reifsnider (1986) [107] have examined cross-ply laminates damaged by matrix transverse cracking and splitting. These studies were based on the evaluation of stresses and involved extensive numerical analysis.

M. Kashtalyan (1999) [108] has evaluated the stiffness degradation of $[0_m, 90_n]_s$ laminates considering both matrix transverse cracking in 90° and 0° splitting plies. They also modified the 2-D shear-lag analysis in order to determine the stress field in cracked lamina, and found that a reduction in stiffness was clearly noted and increased as crack density increases. They also concluded that the significant degradation in Poisson's ratio and shear modulus were due to splitting in the 0° ply. Figure 2.28 shows the elastic and shear modulus and Poisson ratio degradation for cross-ply lamina due to splitting.

Tounsi et al (2006) [109] have modified the shear-lag theory in order to evaluate the effect of transverse cracks on stiffness reduction in angle ply laminates. They plotted the degradation of the elastic modulus against crack density and found that stiffness reduction was significantly influenced by fibre orientation.



(a)

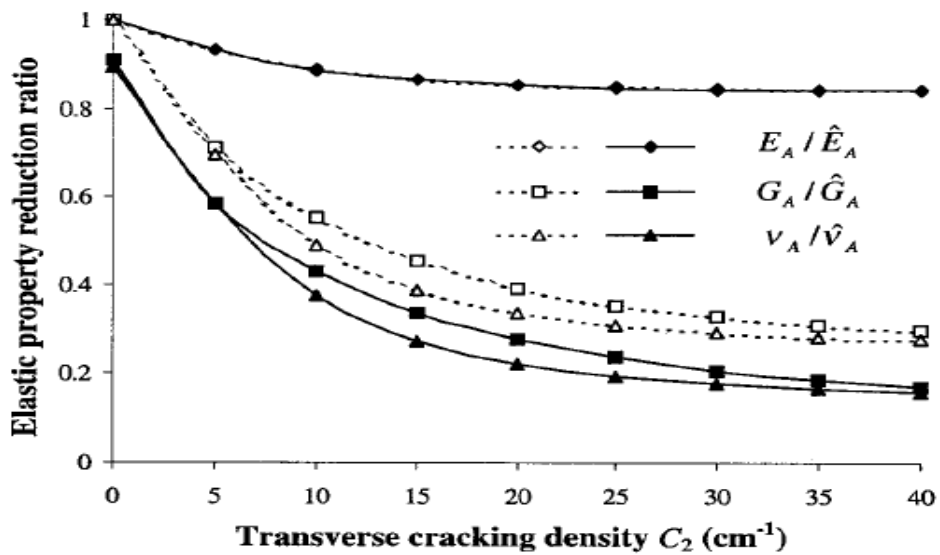


Figure 2.28. Elastic modulus reduction ratios as a function of transverse crack density $C_2 = (2S_2)^{-1}$ (cm⁻¹) for transversally cracked CFRP laminates with (solid lines) and without (hatched lines) splitting: (a) [0/90]_s; (b) [0/90₃]_s. Splitting density 10cm⁻¹.

2.23 Pipe qualification and requalification

2.23.1 Biaxial testing according to ASTM D2992 for pipe qualification

The ISO 14692 standard is currently used to predict the maximum service pressure for GRE pipes under different load conditions. The standard describes the method used to establish a regression line to predict long term allowable stress [12]. This method is based on pressurising the GRE pipes statically or cyclically to derive at least 18 points in order to establish an acceptable regression line, with at least one sample providing a point in excess of 10,000 hours. A graph with log-log format is plotted in terms of stress versus time to failure. By extrapolating the lower confidence limit (LCL) from the regression line, the rating for a design lifetime of 20 or 50 years can be obtained. The expected failure mode of this test is weepage, which is generally due to the presence of a network of matrix cracks which form over time. The regression line obtained from this procedure gives important information that qualifies the product for manufacture and defines the pressure rating to be used in the pipe's system design.

The hydrostatic design basis (HDB) is a method used for the reconfirmation of the product using a regression line built from the ASTM D2992 method. This is needed when any change is made to materials, manufacturing processes, construction, and liner thickness or fitting design. In the HDB test, the product is subjected to 1,000 hours of hydrostatic pressure based on the 1,000 hour lower prediction limit (LPL) of the regression line obtained from ASTM D2992. If there is no weepage or bursting at 1,000 hours, this means that the product is considered safe for the same design lifetime of 20 or 50 years. Figure 2.29 illustrates the regression line of the pipe using ASTM D2992.

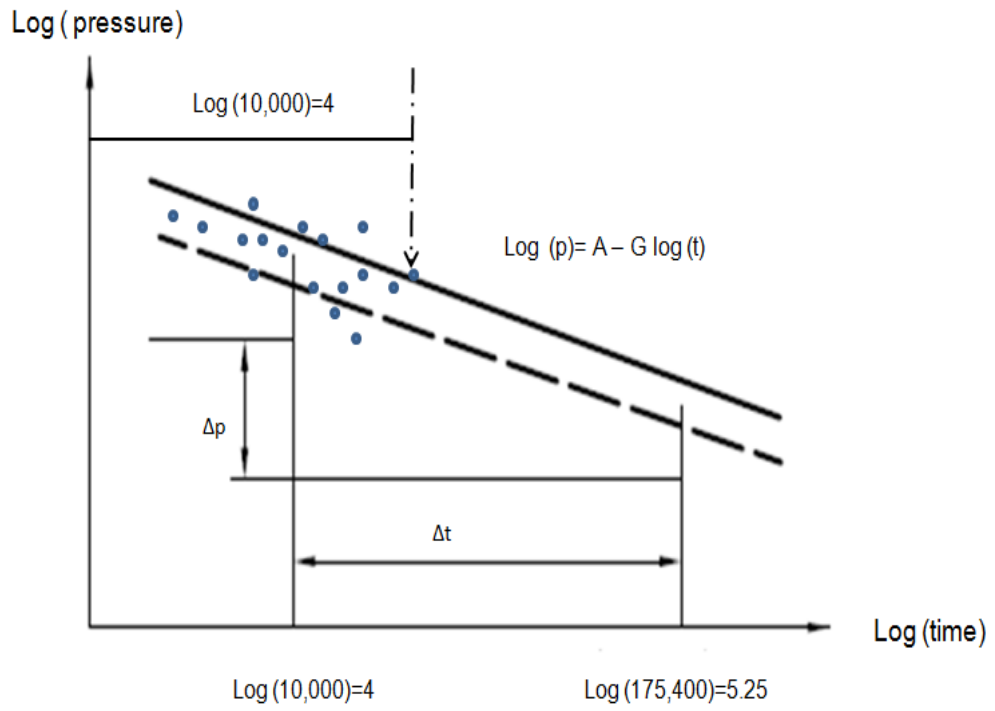


Figure 1: Example of regression line indicating pressure at design lifetime of 20 years and the pressure at the 1000 hours reconfirmation test [12].

CHAPTER 3

EXPERIMENTAL METHODS

This chapter describes the various experimental tests performed on filament wound composite glass/fibre reinforced epoxy pipes. These tests were conducted to study the failure behaviour of GRE pipes over short periods for the purpose of their qualification for official standards. The ultimate elastic wall stress (UEWS) test rig and procedure are described in the first part of the chapter. The second part then considers procedures to measure the tensile and creep Young's modulus, acoustic emission and the examination of microstructure.

3.1 Material selection

All of the MDA epoxy/E-glass filament wound pipes used were manufactured by Future Pipe Industries (FPI). Their reinforced tapered and straight ends are suitable for end caps for adhesive and mechanical fittings, as shown in figure 3.1.

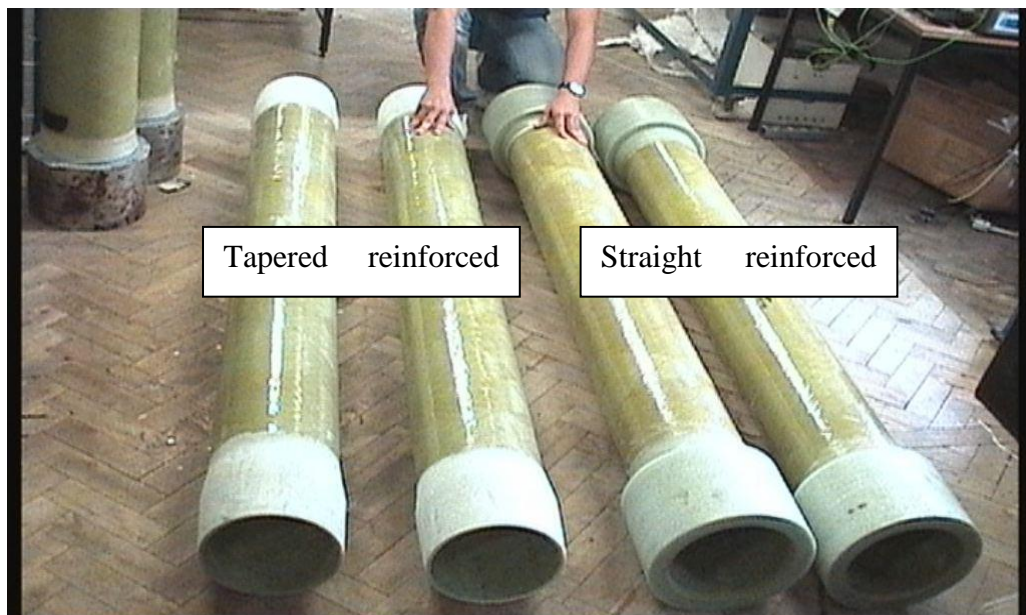


Figure 3.1. Pipe spool with straight and tapered reinforced ends.

All of the pipes were geometrically similar with an inside diameter of 200 mm, length of 2000 mm, 6 mm wall thickness and $\pm 55^\circ$ winding angle. This angle is commonly encountered since the Netting analysis suggests that this is the optimum angle to use in piping systems where the ratio of applied hoop to axial stress is 2:1.

The main component of the pipes is glass fibre impregnated with an aromatic or cycloaliphatic amine epoxy resin. This thermosetting resin is chosen because of its superior corrosion resistance and good mechanical and thermal properties. Table 3.1 shows the physical and mechanical properties of the pipes.

Table 3.1. Physical and mechanical properties of the pipe.

Materials	Test method	
Internal diameter		200 mm
Wall thickness		6 mm
Pipe length		2 000 mm
Epoxy Density		1.8 g/ml
Volume fraction (%)		59%
Axial Young's modulus (E_x)	ASTM D 2105	12 GPa
Axial strength	ASTM D 2105	75 MPa
Hoop Young's modulus (E_y)	ASTM D 2290	20 GPa
Hoop strength	ASTM D 2290	210 MPa
Shear modulus (E_s)		11.5 GPa
Thermal conductivity		0.29 W/m.K
Poisson ratio axial/hoop	N_{xy}	0.65
Poisson ratio hoop/axial	N_{yx}	0.38

3.2 Rig design for UEWS test

In order to carry out the UEWS test with different stress levels and environmental conditions, a rig has been designed and built comprising of on a hollow aluminium shaft, two pistons and two end caps. The UEWS test generates both the UEWS and final failure envelopes under a variety of load and environmental conditions.

Figure 3.2 shows a simple schematic diagram of the biaxial loading test rig. This rig enables additional axial stress to be applied up to pure axial loading. Axial stress up to pure hoop loading could be also minimized by controlling the pressure in both the

main and small chambers inside the pipe. Therefore, it was unnecessary to add any external loads to the pipe wall to perform the test.

This rig was designed to perform the tasks involved in the biaxial tests under a variety of load and environmental conditions. The following criteria needed to be satisfied:

- Maximum working pressure inside the pipe is approximately 250 bar.
- Maximum working temperature is 95^o C
- Shaft and pistons are move freely inside the pipe.
- Pipe failure is expected to be away from the pipe ends.
- Two synchronised pressure loads were to be applied in the main and small chambers to investigate the desired stress ratio.

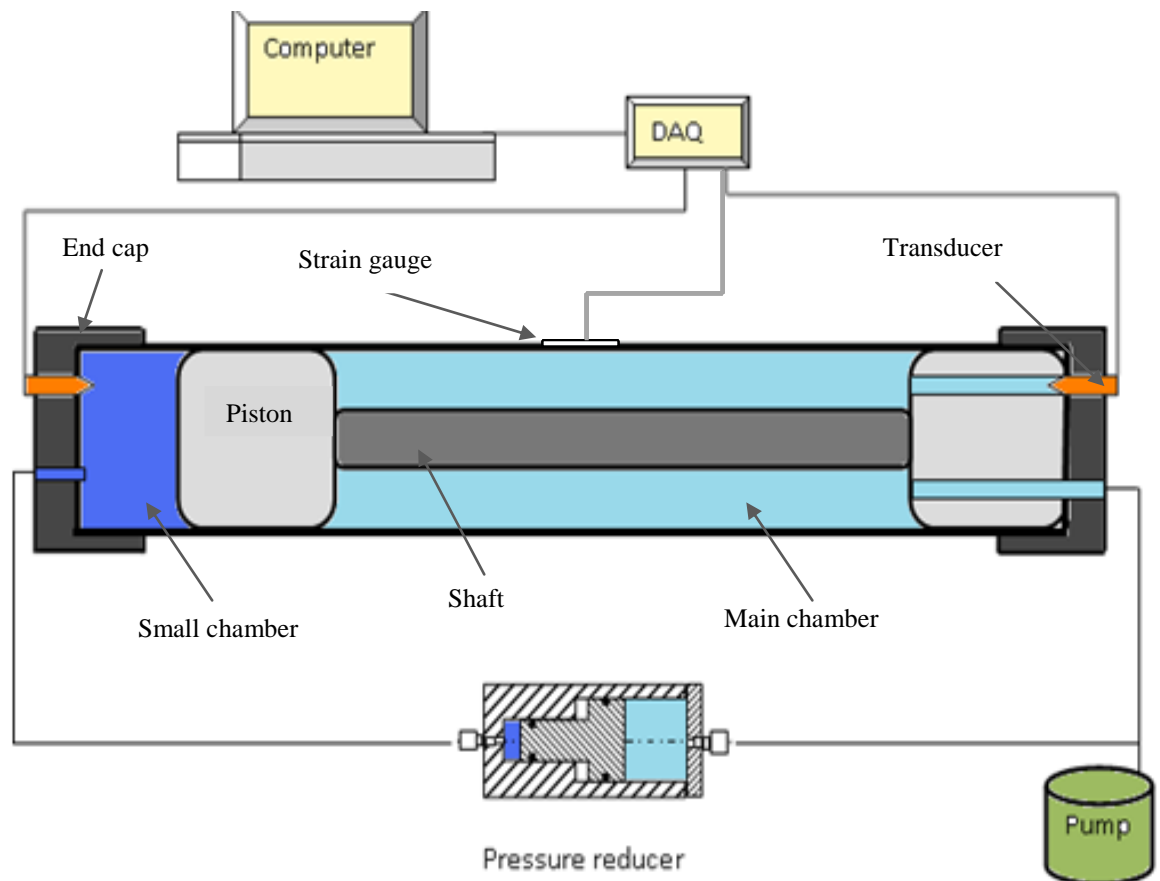


Figure 3.2. Schematic diagram of the rig for carrying out biaxial loading tests.

3.3 Construction of the test rig

3.4 End fittings

For the purpose of conducting experimental tests on pipe specimens subjected to internal pressure, it was necessary to fit end grips at both pipe ends. This type of test is also called the closed-ended test. A strong joint was needed to carry axial loads generated by pressure applied inside the pipe. Furthermore, the construction of seals between the pipes and end fittings had to be carefully considered to prevent any possible leakage at low or high pressure.

Pipes were produced with reinforced layup ends to avoid any possible failure near the end fittings. Good contact and a tight fit between the end caps and pipe ends were necessary. Two types of end fittings were designed and manufactured for carrying out the UEWS tests at room temperature, 65⁰C and 95⁰C.

3.4.1 Adhesive bonded end fittings

Figure 3.3 shows a schematic diagram of a pipe spool with details of the pipe sample. As the pipes were reinforced with E-glass fibre and epoxy resin, the reinforced layer length was carefully calculated to avoid any failure in the bonding media. This design was based on the maximum pressure used by Saied (2002) for ±55⁰ GRE pipes, which was about 18 MPa. The bond length was determined as follows:

$$\text{Bonding length } L = \frac{P r}{2\tau} \quad (3.1)$$

where P is the internal pressure (assumed to be 18 MPa), r is the pipe radius (100 mm) and τ is the allowable shear stress of the epoxy adhesive (7 MPa). From this calculation the bonded length was about 120 mm. However, a length of 140 mm was decided upon to give a safety factor of 1.2.

This kind of fitting was used to perform UEWS tests at room temperature and 65⁰C. However, instability of the bonded fittings was noted at higher temperatures, where the adhesive failed at 95⁰C. At this temperature a shear failure occurred at the bonded caps during the UEWS test at about 120 bar. Figure 3.4 shows a schematic

diagram of the adhesive end fittings (a), and a pipe spool with adhesive bonded end fittings (b).

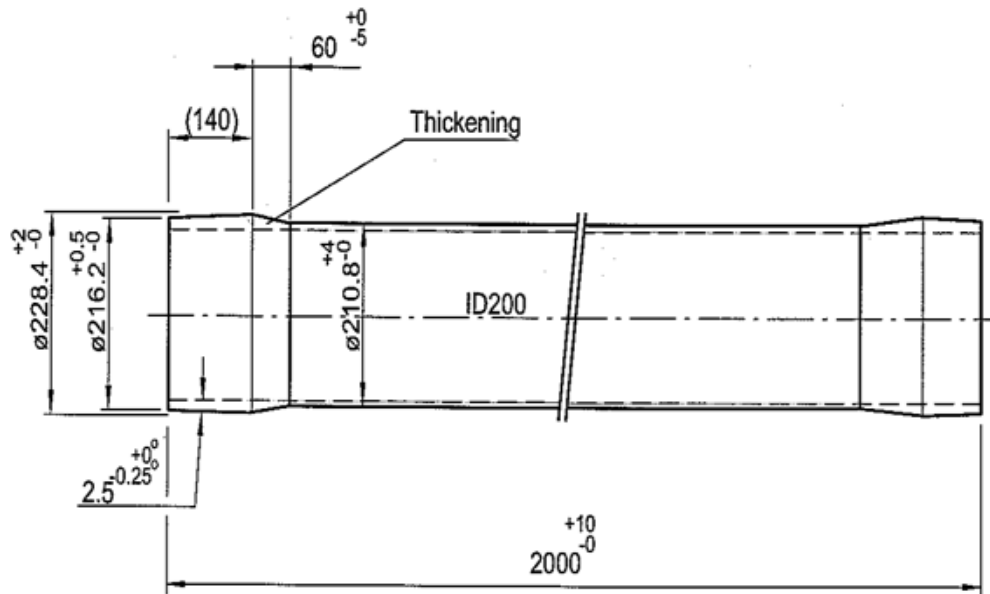
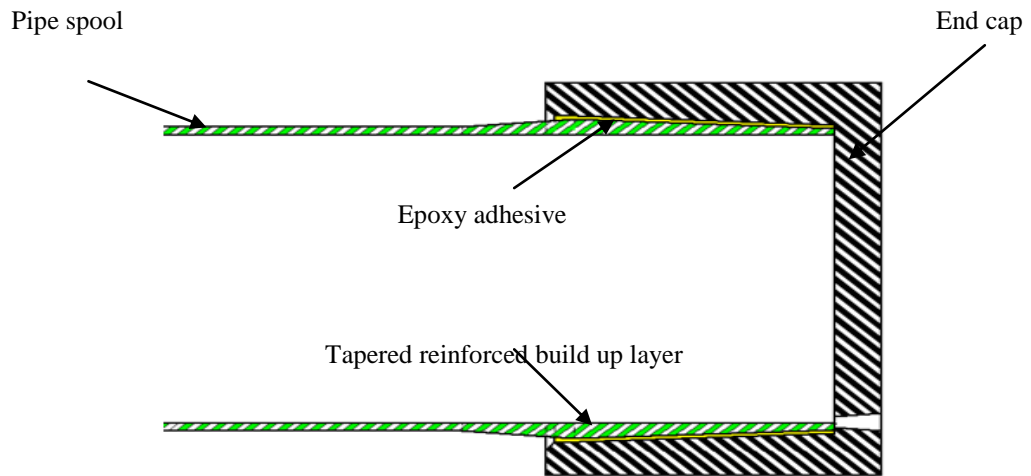


Figure 3.3. Schematic diagram of pipe spool with specifications of the tapered reinforced ends.

After testing, the steel caps were dismantled and cleaned ready for use in the next test. The dismantling procedure was achieved in a sequence of stages. Firstly the bonded pipe end was heated up to about 260⁰C by the heater band. Then axial force was applied to create enough shear stress so that the bonded adhesive would fail using a conventional car jack as illustrated in figure 3.5. Finally the dismantled caps were cleaned at high temperature, removing any remaining adhesive by using a steel brush.

The main advantages of the use of adhesive bonded end fittings are as follows:

- Good sealing over the entire loading range, where the maximum pressure applied to this sort of fitting was 16 MPa.
- Low stress concentration
- Ease of manufacturing and handling.
- Reusable and low cost.



(a)



(b)

Figure 3.4. Schematic diagram of adhesive bonded end fittings (a) and pipe spool with adhesive bonded end fittings (b).

The main drawbacks observed were that the fittings are relatively difficult to install and the bond strength is dramatically reduced at high temperature.

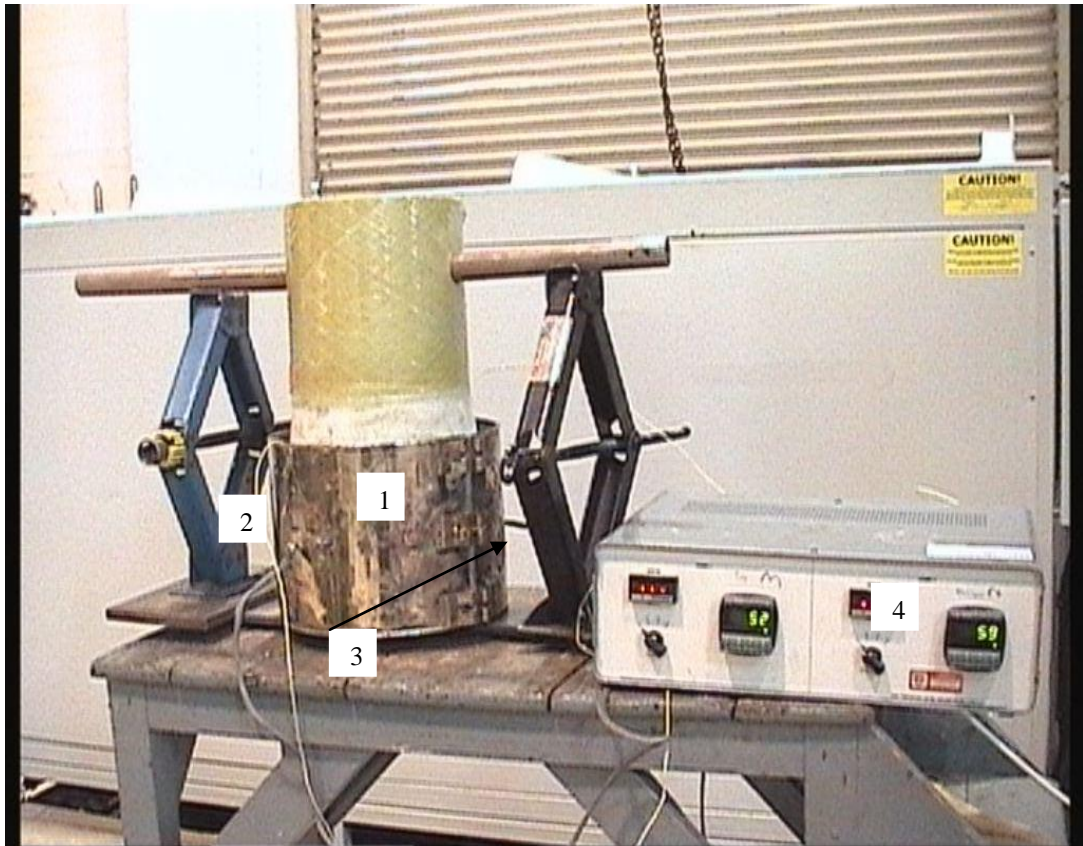


Figure 3.5. Adhesive cap dismantling procedure: (1) heater band, (2) car jack, (3) metal plate fixed to the end cap, (4) heat controller.

3.4.2 Mechanical end fittings

The need for mechanical fittings arose because the adhesively bonded end fittings failed at high temperature. Therefore new mechanical fittings were designed and manufactured for carrying out the test at 95⁰C. In this case pipes were produced with straight 22 mm built up reinforced ends, as illustrated in figure 3.6.

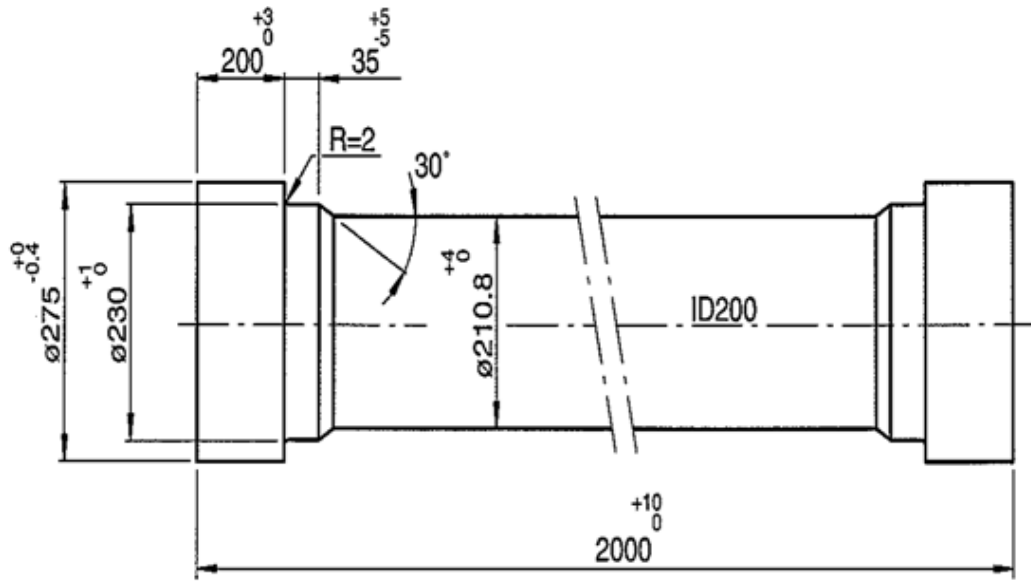


Figure 3.6. Schematic diagram of pipe spool with specifications of the straight reinforced ends.

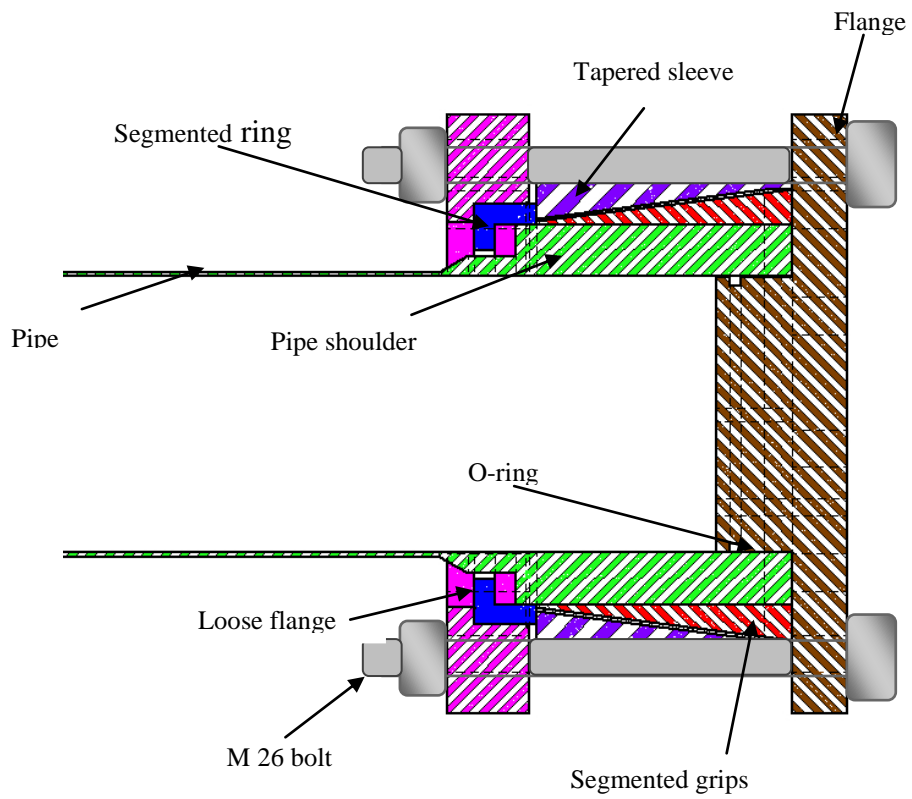


Figure 3.7 Schematic diagram of the mechanical end fittings attached to the pipe.

Figures 3.7 and 3.8 are show a schematic diagram of the mechanical end fittings, and a photo of pipe spool with the mechanical end fittings in place respectively. The mechanical fittings consisted of a rigid tapered sleeve, segmented grips, a segmented ring, a flange and a loose flange. The purpose of the tapered sleeve and grips is to prevent any swelling in the hoop direction which might cause leakage through the O-ring. However, in the case of the pure hydrostatic pressure test, it was unnecessary to use the grips since no pistons and O-rings were fitted. These grips were used only when hoop loading dominated. The working principle of the grips is based on them tightening onto the tapered surface. The sleeves become tight as the bolts are tightened in turn tightening the grips in the hoop direction, due to the pipes tapered ends. This prevented any possible swelling in the hoop direction, and ensured that no leakage occurred through the O-ring.



Figure3.8 Pipe spool with mechanical end fittings.

3.5 Piston and shaft design

In order to create two different pressure loads in the chambers built inside the pipes, two pistons with O-rings were screwed onto a hollow aluminium shaft as shown in figure 3.9. The threaded ends of the shaft join the pistons together and balance the axial loads in the system by carrying undesired loads. The shaft dimensions and thickness were chosen according to considerations of tensile strength, buckling resistance, availability and ease of handling.

The shaft end thread was designed to be able to withstand high pressure loading, and the following calculation was conducted to evaluate thread length and specification.

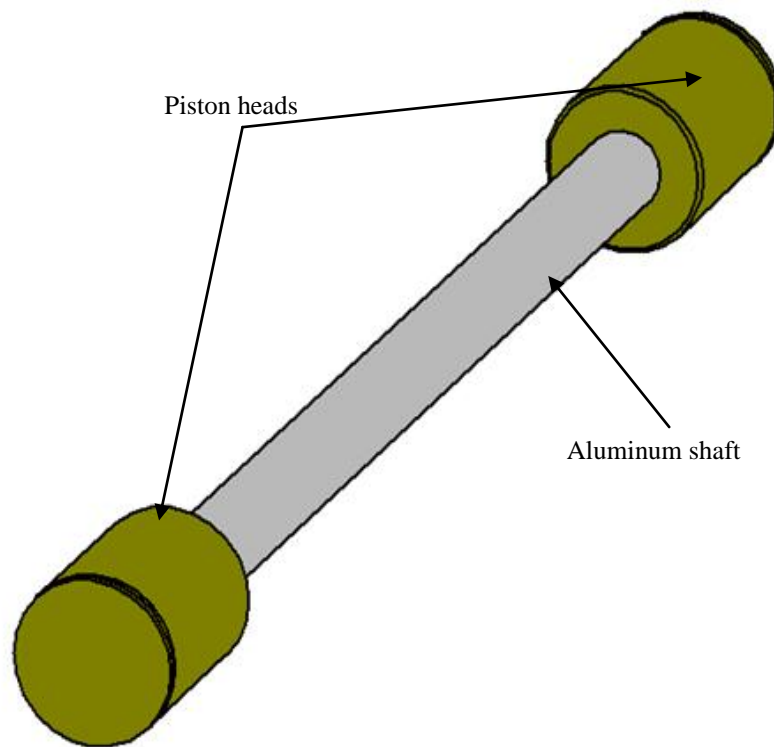


Figure 3.9. Schematic diagram of the piston heads screwed to the aluminium shaft.

The maximum pressure was assumed to be 250 bars and the pipe diameter is 200 mm, so the axial force can then be calculated as:

$$F = P * A \tag{3.2}$$

where, A is the pipe cross section.

$$F = 25 * 10^6 * \pi (0.1^2) \cong 800 \text{ KN}$$

The yield strength of the aluminium is about 150 MPa, but it was taken to be 100 MPa, with a 1.5 safety factor for use at high temperature.

From the standard thread for 80 mm outside diameter of the shaft, M 80 × 6 was selected. Then the required number of turns was calculated as:

$$\tau = \frac{F}{P * \pi * D * n} \tag{3.3}$$

where, n is the number of turns.

$$100 * 10^6 = \frac{800 * 10^3}{\frac{7}{8} * 6 * 10^{-3} * \pi * 0.08 * n} \Rightarrow n \cong 7 \text{ turns}$$

The thread length can then be calculated to be around 60 mm.

The design was based on a safety factor of 2, and so the actual thread length was finally decided to be 120 mm.

The O-Rings were carefully chosen with an outer diameter of 202 mm, 2 mm bigger than the pipe's inside diameter, to ensure a tight contact for maximum sealing. Suitable grooves were machined on the piston heads for these O-Rings.

3.6 Data capture

A data acquisition system supplied by National Instruments (NI) was used to receive signals from the transducers and strain gauges and logged on a personal computer. The data acquisition system consisted of universal analog input NI 9219 with full-bridge supports for the strain gauges, voltage and current excitation, thermocouple, voltage and current measurements, and a capability for 100 reading per second. The system had four channels; two were used for the transducers and the others for the strain gauges. Figure 3.10 shows the data acquisition system used for measuring the parameters during the UEWS tests.

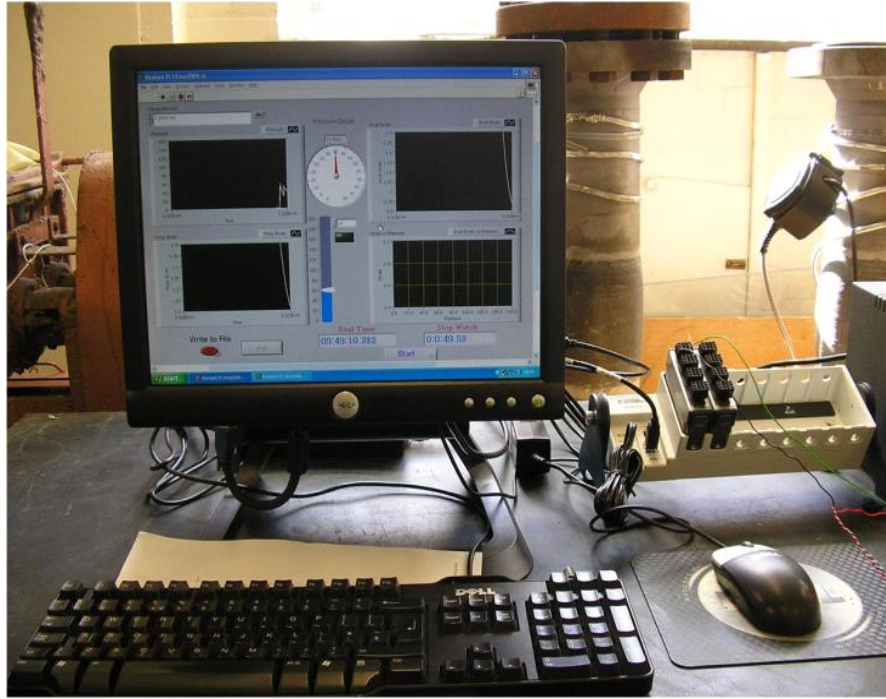


Figure 3.10. Data capture system used in the UEWS test.

3.7 Pressure and strain measures

Two standard industrial transducers manufactured by Swagelok Fluid System Technologies with a capacity of 0 - 400 bar were used to measure pressure levels in the main and small chambers. These transducers were extended by 1/8" tubing to be distant from the test rig.

Two PL-60-11-3LT strain gauges with three meters of lead wire were attached in the hoop and axial directions to detect the pipe's response under loading. These strain gauges were set in quarter bridge configuration. A strain gauge length of 60 mm was recommended by Future Pipe Industries (FPI) in order to cover as long of a pipe surface as possible.

3.8 Pressurizing system

Figure 3.11 shows the SC10-5000 W030 air driven pump used in the UEWS tests to pressurize water media into the main and small chambers. The pump was driven by

compressed air, which was supplied from the main container at 7 bars. The output water flow rate was controlled by an air regulator set up with an air line from the air source to the pump.



Figure 3.11 SC10-5000 W030 air driven pump used in the UEWS tests.

3.9 Pressure reducer

To investigate two different synchronised pressure levels from a single pressure source, an intensifier needed to be connected to the system. This pressure reducer consists of stepped pistons moving freely inside two cylinders, which are called the high and low pressure chambers as shown in figure 3.12.

From the geometry of the cylinders, two different output pressures can be used in inverse proportion to the cylinder areas as follows:

$$\frac{P_1}{P_2} = \frac{A_2}{A_1} \quad (3.4)$$

where: P_1 , P_2 are the high and low pressures in the respective chambers, and A_1 , A_2 are the areas of the high and low pressure cylinders.

Two separate intensifiers were constructed to perform the UEWS tests under hoop to axial stress ratios of, 0.5:1, 1:1 and 4:1.

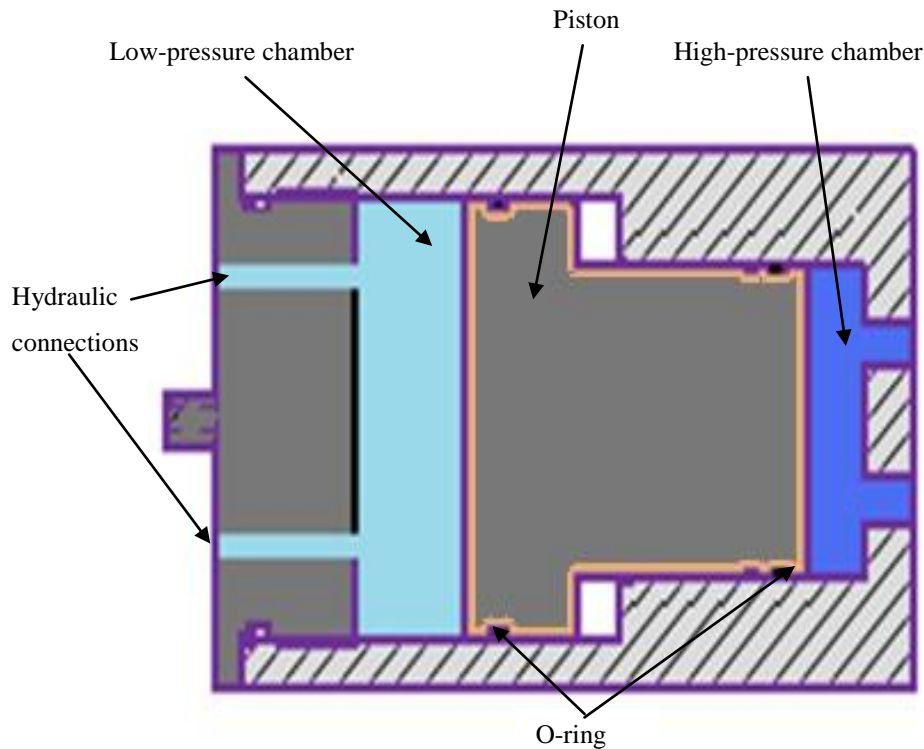


Figure 3.12 Schematic diagram of the pressure reducer used to investigate two different pressure levels.

3.10 Heating device

Figure 3.13 shows the environmental chamber (oven) used to heat up the surrounding media and enable the UEWS test to be carried out at elevated temperatures. Suitable dimensions of 2.5m × 1.5m × 1m for the inner size permitted the easy placing and handling of the pipe. A coil heater and an air blower fan for the uniform distribution of the generated heat are the main components of the oven, in addition to a control box. This oven enabled the surrounding media to be heated up to 150⁰C, whereas the UEWS tests were conducted at room temperature, 65⁰C and 95⁰C.



Figure 3.13. Environmental chamber in open lid condition.

3.11 Acoustic emission equipment

Acoustic emission (AE) can be defined as a transient elastic wave generated from the rapid release of energy from a material [110]. Acoustic emission tests can be performed in applications both in the field and the laboratory. The AE system typically consists of piezoelectric sensors, filters, an amplifier and data storage equipment (personal computer).

Two sensors were attached to the pipe sample during the UEWS test in order to detect damage initiation and propagation through the test stages. The acoustic signal threshold was set at 40dB in cases pure hydrostatic and pure hoop loading, whereas, it was 20dB in pure axial loading. Figure 3.14 shows the AE equipment attached to the pipe spool during the test.

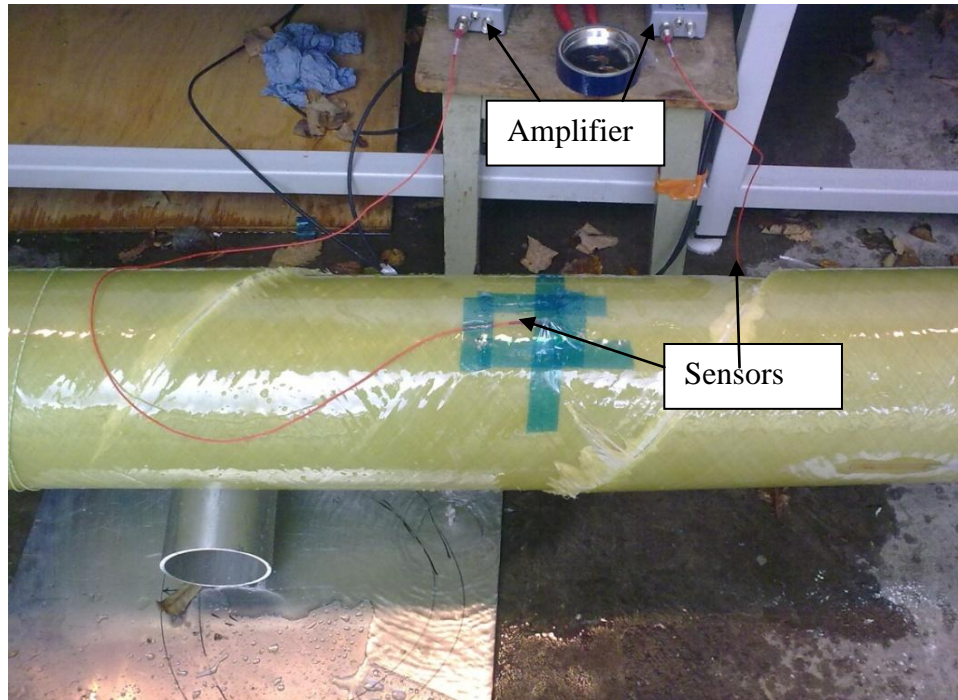


Figure 3.14 AE equipments attached to the pipe spool during the UEWS test.

It is sometimes difficult to separate the AE signals from background noise, which may contaminate the AE readings. One of the available solutions to minimize this interference is to place the amplifiers as close as possible to the sensors, and further filtering or amplification may be needed to be attached. Another difficulty noted is the large volume of data acquired, and so high PC capacity is needed as UEWS tests are usually performed over 6-10 hours.

3.12 The ultimate elastic wall stress (UEWS) test

This section describes the procedure used for the determination of the ultimate elastic wall stress for glass/fibre reinforced epoxy pipes under a variety of load conditions. The UEWS can be used as a criterion for the determination of the working pressure for GRE pipes. This method is generally based on the notion that the failure of GRE pipes starts with glass/fibre interface debonding.

3.13 Definitions

3.13.1 Ultimate elastic wall stress (UEWS)

The UEWS can be defined as the maximum stress (N/mm²) resulting from internal hydrostatic pressure or axial loads that produces an elastic deformation in any direction. In many cases in composite investigations, the UEWS indicates the start of non-linear deformation behaviour [111].

3.13.2 Cycle test pressure (CTP)

The CTP is the maximum pressure applied during a cycle group, which usually starts at 10% of the expected UEWS pressure.

3.13.3 Cycle

The cycle is the time needed to pressurize the system from zero to the CTP pressure, then to hold at the CTP pressure for one minute before a releasing time of one minute at the zero pressure.

3.13.4 Nominal pressure (NP)

The NP is the maximum pressure that water can exert continually with a high degree of certainty that failure will not occur within the design lifetime.

3.14 Test preparation

The reinforced pipe ends were machined to a shallow angle of 2.5° in order to fit tapered steel caps tightly. Then the pipe ends and end caps were cleaned with acetone to remove any remaining grease or oil and then dried. Wavistrong EASY-FIT adhesive was used to bond the caps to both pipe ends which were then cured at 125°C for 90 minutes with a heater band. Once the pistons were attached to the shaft, mounted in the pipe spool and prepared with the end fittings, the pipe was

placed in the oven with rolled supports to minimize any axial reaction generated from the supports.

Two strain gauges were attached to the middle of the pipe to measure any strain during the test in the axial and hoop directions. The strain gauges were connected to the data acquisition system in order to detect the strain signal and then transform it to Excel readable data. Two transducers were also assembled onto the main and small chambers to measure the pressure in them.

An intensifier was then connected between the main and small chambers in some of the tests conducted. This was unnecessary in the pure hydrostatic pressure, pure axial and pure hoop loading tests. Finally all the supply and release tubes and valves were connected and the pipe was filled with pure water, making sure any air bubbles were removed from the system.

3.15 Test conditions

In the case of elevated temperature tests, the pipes were filled with water and placed in an oven maintained at the test temperature (65°C or 95°C) for 24 hrs until temperature equilibrium was reached. This period of time is much longer than that required for conditioning, which can be calculated as follows:

$$30 \text{ minutes} \times 6 \text{ mm wall thickness} = 180 \text{ minutes}$$

where 30 minutes is the required time for conditioning the pipes of wall thickness of 1 mm [111].

3.16 Test procedure

Once the set up was completed, either at room temperature or an elevated temperature, the UEWS tests were performed through a series of procedures as follows:

- 1- First the nominal pressure rating (P_N) was determined, as well as the design load condition.

2- Secondly, the cycle test pressure (CTP) was determined, starting at 10% of the expected UEWS as follows:

$$CTP_1 = 0.1 * P_{UEWS \text{ exp.}} \quad (3.5)$$

3- The pipe was then filled completely with drinking water as mentioned above, and the air bubbles were released to ensure that there was no air trapped inside the pipe.

4- The pump was then attached to the system.

5- The required bridge voltage was applied to the strain gauges due to the DAQ system.

6- The first cycle test pressure was applied with pressure increment from zero to the CTP_1 of wall stress of 5-10 MPa/ minute. Ten cycles were applied under CTP_1 holding for one minute at the given pressure and one minute at conditions of zero pressure.

7- The pressure was then uniformly increased to the second group of cycles, which can be determined by adding 10% of the expected UEWS as follows:

$$CTP_{i+1} = CTP_i + 0.1 * P_{UEWS \text{ exp.}} \quad (3.6)$$

where: CTP_i is the cycle test pressure of the current group (MPa), CTP_{i+1} is the next cycle group of ten cycles (MPa), and $P_{UEWS \text{ exp.}}$ is the test pressure corresponding to the expected UEWS (MPa)

8- The procedure in stage 7 was repeated until one of the follow conditions was met:

a- Weeping or failure of the pipe.

b- The completion of two cycle groups after the UEWS point.

9- Strain measurements as well as pressure readings were taken at the end of the first and tenth cycles.

10- The UEWS was investigated when the difference in strains between the 1st and 10th cycles of the same cycle group exceeds 5%.

$$\varepsilon_{10i}/\varepsilon_{1i} > 1.05 \quad (3.7)$$

where: ε_{1i} , ε_{10i} are the strains at the end of the first and tenth cycles respectively.

11- The test was continued for two cycle groups after the UEWS point using the same procedure. Figure 3.15 shows pressure versus time and cycle group definition.

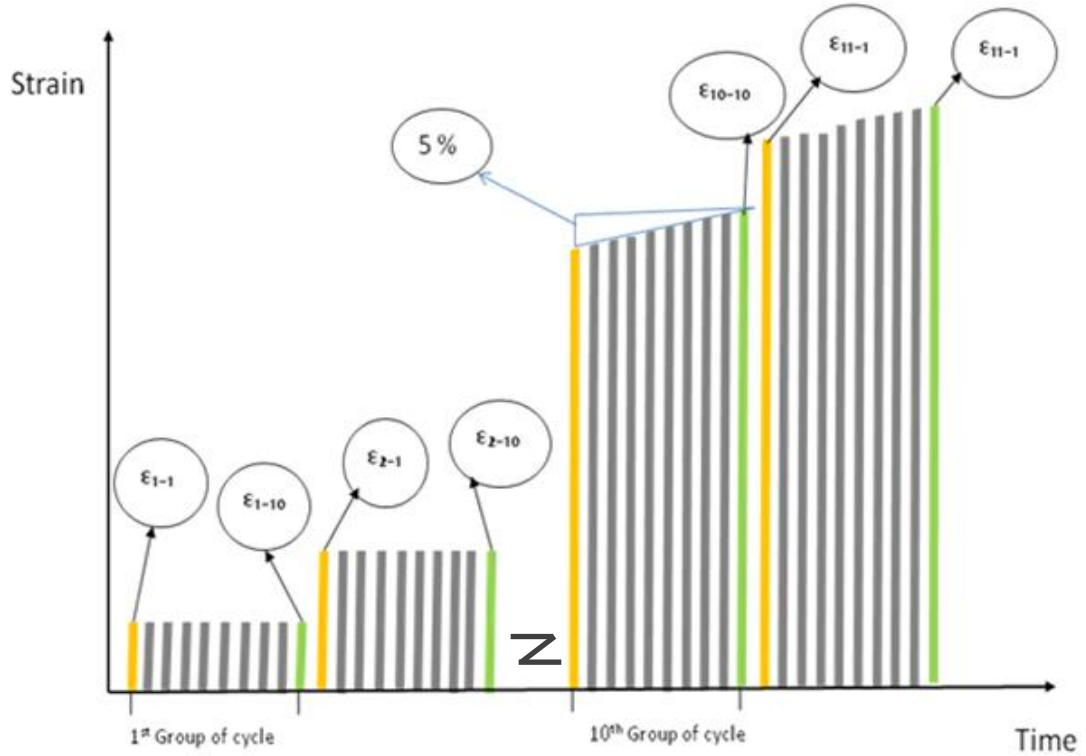


Figure 3.15. Definition of test cycles and cycle groups.

3.17 Calculation of the ultimate elastic wall stress

The UEWS calculation was based on the results of the strain measurements taken in the axial direction when axial loading was predominant, whereas hoop strain was considered when hoop loading dominated.

The calculation began with the determination of the pressure at which $\Delta\varepsilon_c$ exceeds 5%:

$$\Delta \varepsilon_c = 100 \left(\frac{\varepsilon_{10} - \varepsilon_1}{\varepsilon_{10}} \right) \quad (3.8)$$

where $\Delta \varepsilon_c$ is the difference in strain between the first and tenth cycles, $\varepsilon_{10}, \varepsilon_1$ are the strains in the tenth and first cycles respectively in the same cycle group.

$\Delta \varepsilon_p$ is the difference between the measured strain at the tenth cycle and the calculated strain. The latter was calculated from the previous points (strain at tenth cycle) by linear regression.

The strain in the first cycle can be inaccurate, since no previous point has been defined.

$$\Delta \varepsilon_p = 100 \left(\frac{\varepsilon_{10,m} - \varepsilon_{10,p}}{\varepsilon_{10,m}} \right) \quad (3.9)$$

where: $\varepsilon_{10,m}$ is the measured strain in the tenth cycle, and $\varepsilon_{10,p}$ is the predicted strain at the tenth cycle.

The UEWS was then investigated when $\varepsilon_{10,p}$, $\Delta \varepsilon_c$ exceeds 5%, and the UEWS was finally calculated as:

$$UEWS = \left(\frac{P_{UEWS} (D_i + T_r)}{2 T_r} \right) \quad (3.10)$$

where: P_{UEWS} is the internal pressure corresponding to UEWS, D_i is the inner diameter of the tested pipe at the location of the strain gauge, and T_r is the reinforced wall thickness at the location of the strain gauge.

3.18 Wall thickness measurements

The actual pipe wall thickness was measured by cutting a ring of 10 mm width from the middle of the failed pipe. Eight circumference marks were taken to determine the average wall thickness including the coating layer, because inconsistent thickness around the circumference was observed.

The next step was to measure the coating layer. A digital microscope was used to show that the coating layer's thickness was also variable around the circumference of the ring. The average coating thickness was then taken from eight measurements, and finally the actual reinforced wall thickness was determined as:

$$T_{real} = T_{total} - T_{coating} \quad (3.11)$$

Figure 3.16 shows the ring sample under magnification and a coating layer measurement.

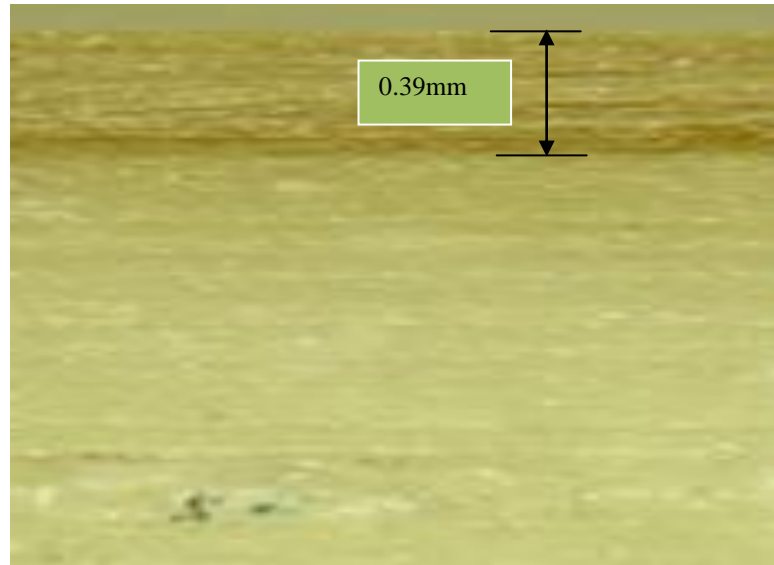


Figure3.16. Coating layer measurement.

3.19 Elastic modulus measurements

The main purpose of carrying out this sort of test is to determine the elastic modulus degradation of the pipes in the axial and hoop directions in different stages of loading. Simple tensile and 100 second creep tests were conducted with the pipes under a variety of load conditions. In order of investigate the effect of UEWS on pipe stiffness, several samples in different conditions were tested on virgin pipes, those halfway to UEWS (50% of UEWS), 100% of UEWS and weeping pipes. For 50% and 100% of UEWS, the tests were stopped at the corresponding stress levels.

3.19.1 Axial Young's modulus

A pull test was carried out with the specimen in order to determine the elastic modulus in the axial direction under each condition. Figure 3.17 shows a pipe sample, and figure 3.18 shows pipe samples set up in the Instron 4505 tensile machine.



Figure 3.17. Preparation of pipe samples for tensile test.



Figure 3.18. Pipe sample set up in the Instron 4505 tensile machine.

A pipe sample of one meter in length was firstly cut from the middle of a tested sample, and then pinned and supported at each end in the machine. The strain gauge was initially attached to the middle of the sample to record the pipe's response under loading in the axial direction and data acquisition system then transformed the data into the personal computer.

The test procedure was started by placing the pipe sample in the machine and then different loads were applied separately (these loads were carefully chosen to be in the elastic zone and far away from the yield point). Each load held constant for a while to ensure that stable readings from the strain gauge were recognised, whereupon a strain reading was taken. The applied load was then released to return to the unloaded condition.

The next load was defined by increasing the previous load by about 15% of the maximum suggested load. The new load was again held for a while for the strain reading to become stable, and the next strain reading was then taken. This procedure was then repeated for the rest of the planned loads, which were totalled eight starting from 2kN up to 16kN with load increments of 2kN.

The collected data of loads and strain reading were analyzed as follows:

$$\sigma_A = \frac{F}{\pi(D_o^2 - d_i^2)} \quad (3.12)$$

where: F is the applied load (N), and D_o , d_i are the pipe outside and inside diameters respectively.

The axial stress was fitted versus axial strain to derive a linear relationship. The slope of the line was defined as the axial elastic modulus. The whole test was conducted for samples under different conditions as stated earlier.

3.19.2 Hoop elastic modulus

100 second creep tests were carried out to determine the elastic modulus in the hoop direction for the tested pipes in the conditions mentioned above. Uniform rings were cut from the middle of the pipes of 20 mm width as illustrated in figure 3.19.

Ring samples were placed in the Instron 4505 pull machine as in figure 3.20, and then four different loads were applied in the hoop direction. The loads applied were much lower than the pipe's hoop elastic limit, for two reasons. The main reason was to ensure that no plastic deformation could occur in the rings. The second reason was to prevent the circular ring from deforming into an oval shape which might disturb the displacement reading. These loads were held for 100 seconds, and then the corresponding vertical displacement was recorded and fitted against the applied loads. After a linear relationship was recognized between the loads and displacements, the creep hoop modulus was then calculated as:

$$E_H = \frac{0.1484 W R^3}{I \delta} \quad (3.13)$$

where: W is the applied load (N), R is the pipe radius (m), I is the moment of inertia (mm), and δ is the vertical displacement (m).

$$I = \frac{b d^3}{12} \quad (3.14)$$

where: b is the ring width and d is the pipe inner diameter.



Figure 3.19 . Photograph of ring specimens for the 100 seconds hoop Young's modulus test.



Figure 3.20. Photograph of the test rig for measuring the creep hoop Young's modulus.

3.20 Optical microscopy test

Optical microscopic examinations were conducted with the failed pipes, in order to evaluate the cumulative damage, damage modes, and crack density. In the final stage of the UEWS test when weepage started to appear, the leakage location was marked and then cut into small pieces $25 \text{ mm} \times 20 \text{ mm}$ for microstructure analysis as shown in figure 2.21. These pieces were cut with a bonded diamond cutter to minimize any possible damage during the preparation.

Each specimen was labelled for identification and then mounted in an epoxy resin in a small mould in order to protect the sample and improve the handling of small samples, as shown in figure 2.22. A grinding machine was used to remove the rough edges from the moulded sample and to flatten the surface. The grinding procedure is listed in table 3.3.

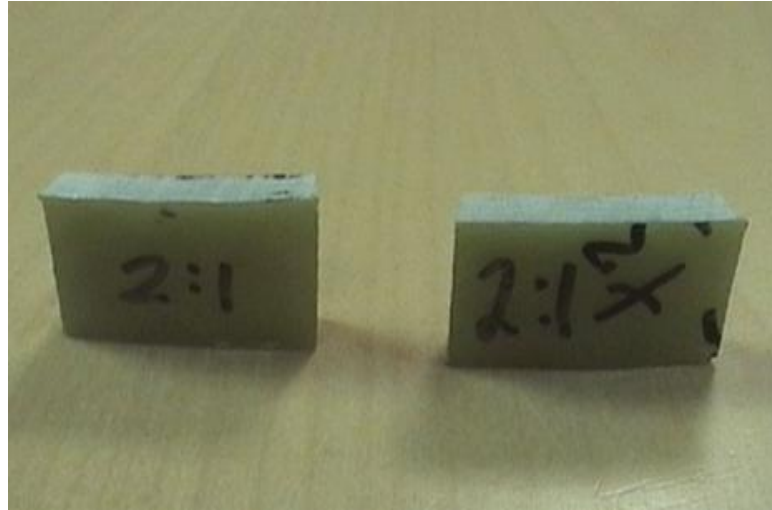


Figure 3.21. Cut specimens for microstructure analysis.



Figure 2.22. Moulded sample in epoxy resin to improve handling for the grinding process.

Table 3.3. Grinding procedure for polymer matrix composites.

Surface	Abrasive size	Load/sample (N)	Base speed rpm	Time (min.)
CarbiMet 2Abrasive discs Water proof paper	320(P400) grit Sic Water cooled	18	150	3.00×2
Ultra Pol, Ultra Pad Cloth	6 μ m MetaDi. Supreme Diamond Suspension	18	150	3.00×2
Tri Dent cloth Text Met Pad	3 μ m Meta Di Supreme Diamond Suspension	22	150	3.00×2
ChemoMet Pad	0.05 μ m MasterMet Colloidal Silica	27	150	3.00×2

CHAPTER 4

QUALIFICATION AND LIFETIME MODELLING OF FIBREGLASS PIPE

This chapter describes the ultimate elastic wall stress (UEWS) modelling for the purposes of pipe's qualification. This including the prediction of elastic modulus constants and the stress-strain relationships of the $\pm 55^\circ$ GRE pipes, based on laminate theory and Miner's low approach. The degradation of elastic modulus in the concepts of crack density evaluation is discussed. Tsai-Hill criterion is also modified to include the combination of stresses interaction in the principle direction to predict the UEWS envelopes.

4.1 Pipes qualification

The qualification standard for fibreglass pipe, ISO 14692, is currently being revised. The procedure by which GRE pipes are rated in the standard, ASTM 2992, covers both cyclic and static pressure loading. Weepage is the only failure mode permitted. End users should note that there are other classes of fibre reinforced pipe where weepage is suppressed by means of a ductile liner, so fibre failure occurs. These pipes are covered by different norms, such as API RP15S. The discussion here relates solely to GRE pipes that fail by weepage.

The ASTM2992 procedure involves hydrostatic pressurisation tests under either cyclic or long term static loading, depending on the loading condition of interest. In each case the method of treating failure data is the same, as summarised in Figure 4.1.

Both the cyclic and static failure processes can be described, respectively, by empirical power law expressions:

$$\sigma = HN_f^{-J} \quad \text{and} \quad \sigma = Ft_f^{-G} \quad (4.1)$$

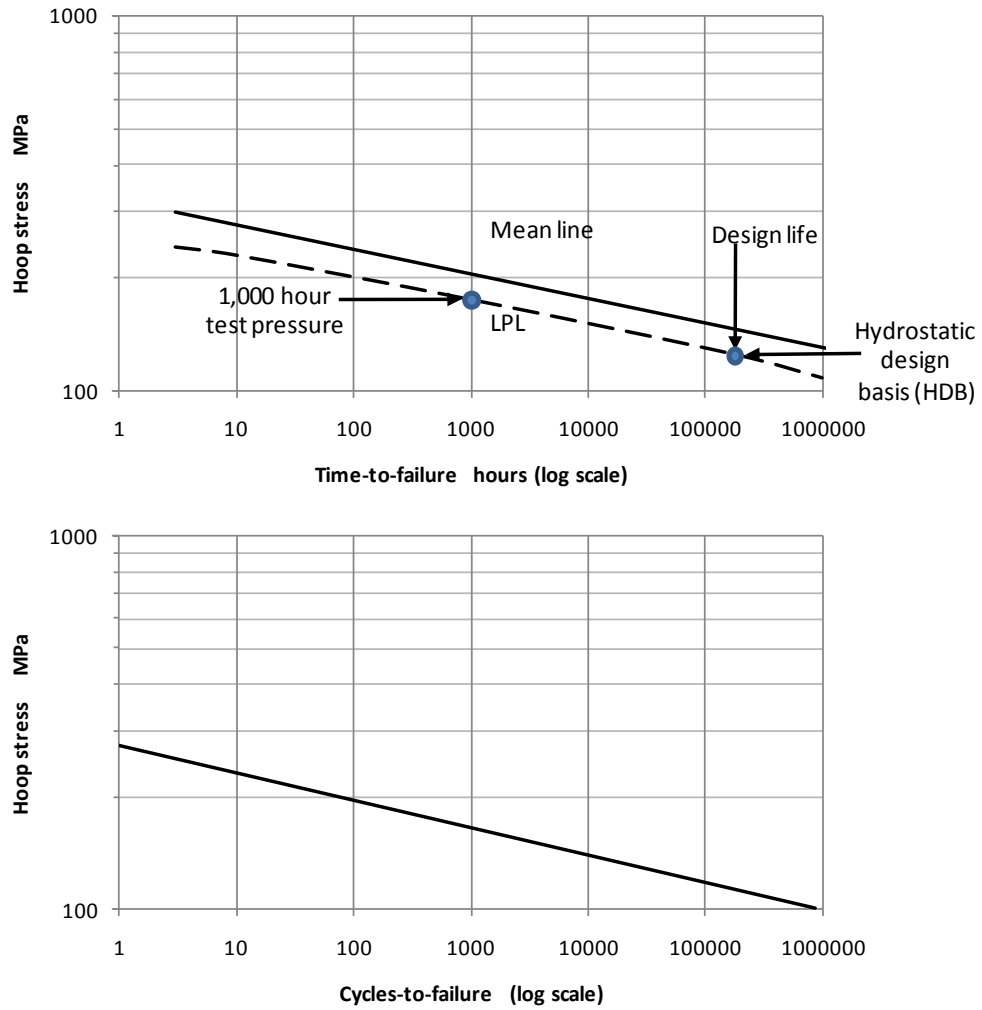


Figure 4.1. Static (upper) and cyclic (lower) Future Pipe test results at 65°C from ISO 14692 and ASTM D2992. Upper figure shows the 97.5% lower predictions limit (LPL) and the procedure for determining the hydrostatic design basis (HDB).

Here, σ is the hydrostatic pressure, N_f is the number of fatigue cycles to failure, t_f is the failure time under static loading, and H , J , F and G are the constants of the relationships in Figure 4.1. These equations can be re-arranged to give the number of cycles, or the time to failure, so:

$$N_f = \left(\frac{\sigma}{H}\right)^{\frac{1}{J}} \quad \text{and} \quad t_f = \left(\frac{\sigma}{F}\right)^{\frac{1}{G}} \quad (4.2)$$

To allow for product variability and testing errors it is necessary to calculate a *lower prediction limit* (LPL) for the results. The LPL line in Figure 4.1 represents the line above which 97.5% of newly determined results are predicted to lie. For static loading the pressure rating for the pipe, known as the *hydrostatic design basis* (HDB) is determined by extrapolating the LPL line to the design life, usually 20 years for oilfield products, as shown. The HDB, combined with a number of other factors, is used to determine the allowable working pressure in the pipe.

As well as giving the pressure rating it is also necessary for a qualification standard to provide methods of deciding whether changes to the materials or manufacturing process have affected the product. This is necessary since it would be expensive to repeat the full qualification procedure every time a small product change was made. The solution offered to this problem is the procedure for ‘reconfirmation of the HDB’. This is a survival test which involves holding samples under hydrostatic pressure at the 1,000 hour LPL value for 1,000 hours. As per the standard, survival in this test indicates that the samples tested are at least as good as those originally qualified.

4.2 The ultimate elastic wall stress (UEWS)

UEWS is the maximum circumferential wall stress resulting from internal hydrostatic pressure or axial loads that produce an elastic deformation in any direction[111]. In this study UEWS tests are suggested and introduced as a short term requalification tests for glass/fibre reinforced pipes.

While acknowledging the benefits of the current reconfirmation method HDB based on regression analysis providing an acceptable life prediction, the need among manufacturers for a rapid and effective method of monitoring changes in product quality has become imperative. The UEWS test appears to provide an attractive alternative to this method. Frost and Cervenka [78] observed that ‘damage involving matrix cracking in composite materials is associated with observable non-linearities in elastic behaviour. Procedures have been described and reported to a limited extent in the public domain for use with vinyl ester-based pipe as well as PVC’.

The main purpose of the UEWS test is to study the stress-strain response, and defining the maximum stress level in elastic zone [111]. The main advantage of

UEWS is that the test takes only a few hours per sample to perform, compared with the 1,000 hour HDB reconfirmation procedure. The UEWS has been found to be sensitive to changes in key manufacturing and raw material parameters such as the quality of the 'size' on the glass fibre, which influences the bond with the resin. These effects are not easily picked up in the ASTM2992 tests, and indeed the HDB reconfirmation procedure provides no product information other than a yes/no outcome. The sensitivity of the test to material and quality parameters has also been found to be superior to tests such as interlaminar shear and through-thickness strength .

In practice the UEWS has been found to correlate well with the long term of lower confidence limit (LCL) value obtained from regression tests. However, assessment of this approach is that the exact significance of the measured quantity is not fully defined.

4.3 Comparison between Procedures

The main advantage claimed for procedures based on cyclic and static fatigue is that they provide a realistic statistical approach to establishing a long-term pressure rating when there is a slow deterioration of properties. For this reason it makes them attractive in connection with statistically-based design. The ASTM2992 confirmation test appears to have significant drawback due to the time needed to achieve the full qualification of new products (10,000 hours ~14 months).

For new piping products, where the regression line slope is not identifiable in advance, this requires significant trial and error to determine the pressures to be used, which often results in a qualification period that exceeds two years. Although it is generally agreed that proof of long term stability is desirable, long term static fatigue measurements may not be the best method of achieving this. Table 4.1 compares the main issues between the regression based on ISO 14692 and the UEWS procedure.

Table 4.1 Compares the regression-based ISO 14692 method and the UEWS procedure.

	ASTM2992 procedures	UEWS tests
Time, expense and convenience.	Expensive procedure requiring ~2 years to achieve qualification.	Simple procedure, which can be carried out in less than day.
Ability to define a long-term pressure rating.	Provides the basis for a 20 year design rating.	Identifies a stress level, below which the rate of damage progression is very low. This stress corresponds approximately to the stress determined by long term regression.
Ability to quantify changes due to process and materials.	HDB reconfirmation procedure is adequately sensitive to these effects, but takes a minimum of 1,000 hours to perform and only provides a yes/no answer.	Very sensitive to these effects.
Ability to quantify effects of chemical environment.	Limited.	Limited.

4.4 Prediction of elastic modulus constants

The main aim of this model was to predict the elastic moduli constants using the classic laminate theory by the rule of the Halpin-Tsai equation.

$$E_{11} = E_f V_f + E_m V_m \quad (4.3), \quad E_{22} = E_m \frac{(1 + \xi_e \eta_e V_f)}{(1 - \eta_e V_f)} \quad (4.4)$$

$$\nu_{12} = \nu_f V_f + \nu_m V_m \quad (4.5), \quad G_{12} = G_m \frac{(1 + \xi_s \eta_s V_f)}{(1 - \eta_s V_f)} \quad (4.6)$$

$$\eta_e = \frac{\left(\frac{E_f}{E_m} - 1\right)}{\left(\frac{E_f}{E_m} + \xi_e\right)} \quad (4.7), \quad \eta_s = \frac{\left(\frac{G_f}{G_m} - 1\right)}{\left(\frac{G_f}{G_m} + \xi_s\right)} \quad (4.8)$$

$$\nu_{21} = (V_f \nu_f + V_m \nu_m) \frac{E_{22}}{E_{11}} \quad (4.9)$$

where: E is the Young's Modulus, V is volume fraction, ν is Poisson ratio, and G is the shear modulus. Subscripts (f, m), (1, 2), and (e, s) represent fibre, matrix, fibre direction and transverse direction of the ply, and elastic, shear respectively.

The laminate theory was used to calculate the elastic moduli, and then converted to derive the reduction of stiffness constants.

$$[C_{ij}] = \begin{bmatrix} C_{11} & C_{12} & 0 \\ C_{12} & C_{22} & 0 \\ 0 & 0 & C_{66} \end{bmatrix} \quad (4.10)$$

$$\text{where: } C_{11} = \frac{E_{11}}{1 - \nu_{12}\nu_{21}} \quad (4.11)$$

$$C_{22} = \frac{E_{22}}{1 - \nu_{12}\nu_{21}} \quad (4.12)$$

$$C_{12} = \nu_{12} C_{22} \quad (4.13)$$

$$C_{66} = G_{12} \quad (4.14)$$

The above reduced stiffness constants were transformed to obtain the corresponding values in the coordinate system of the pipe wall, equivalent to a rotational of ϕ .

Therefore, the transformed reduced stiffness constants are obtained by:

$$[\bar{C}_{ij}] = [T][C_{ij}] \quad (4.15)$$

$$\text{where: } [T] = \begin{bmatrix} c^2 & s^2 & 2s c \\ s^2 & c^2 & -2s c \\ -s c & s c & c^2 - s^2 \end{bmatrix} \quad (4.16)$$

This leads to:

$$\begin{aligned}
\bar{C}_{11} &= C_{11}c^4 + 2(C_{12} + 2C_{66})s^2c^2 + C_{22}s^4 \\
\bar{C}_{12} &= (C_{11} + C_{22} - 4C_{66})s^2c^2 + C_{12}(s^4 + c^4) \\
\bar{C}_{22} &= C_{22}c^4 + 2(C_{12} + 2C_{66})s^2c^2 + C_{11}s^4 \\
\bar{C}_{66} &= (C_{11} + C_{22} - 2C_{12} - 2C_{66})s^2c^2 + C_{66}(s^4 + c^4)
\end{aligned} \tag{4.17}$$

where: c, and s, are abbreviations for $\cos \phi$, and $\sin \phi$ respectively, and \bar{C}_{ij} is the matrix of deformed stiffness constants. Finally, the elastic constants of the pipe wall are calculated using equation 4.15. The stiffness matrix is plotted as:

$$[\bar{C}_{ij}] = \begin{bmatrix} \bar{C}_{11} & \bar{C}_{12} & 0 \\ \bar{C}_{12} & \bar{C}_{22} & 0 \\ 0 & 0 & \bar{C}_{66} \end{bmatrix} \tag{4.18}$$

Axial and hoop elastic modulus in the single lamina can be calculated as:

$$E_{Axial} = \bar{C}_{11}(1 - \nu_{yx}\nu_{xy}), \quad E_{Hoop} = \bar{C}_{22}(1 - \nu_{yx}\nu_{xy}), \quad G_{xy} = \bar{C}_{66} \tag{4.19}$$

where:

$$\nu_{xy} = \bar{C}_{12} / \bar{C}_{22}, \quad \nu_{yx} = \bar{C}_{12} / \bar{C}_{11} \tag{4.20}$$

4.5 Miner's law interpretation of the UEWS test

Miner's Law, an empirical law, was originally proposed to describe the development of cyclic fatigue damage in metals. It provides a method of summing the damage produced by fatigue cycles of different magnitude, and can be extended to model and sum the effects of other types of damage. When cycles of different magnitude are present, end of life is reached when

$$\frac{N_1}{N_{1f}} + \frac{N_2}{N_{2f}} + \frac{N_3}{N_{3f}} + \dots + \frac{N_i}{N_{if}} + \dots = \sum \frac{N_i}{N_{if}} = 1 \tag{4.21}$$

This expression applies where N_1 stress cycles occur at stress σ_1 ; N_2 cycles occur at stress σ_2 , and, in general, N_i cycles occur at stress, σ_i . $N_{1f}, N_{2f} \dots N_{if}$ etc are the corresponding numbers of cycles that would cause failure in a fatigue test at a

constant repeated stress of , $\sigma_1, \sigma_2 \dots \sigma_i$, etc. The expression in equation 4.21 is known as the Miner's Law sum and represents one possible way of adding up the damage that occurs at different stress levels. This approach has been widely used in the design of metallic structures from offshore platforms to aircraft. Miner's Law has been extended to non-metallic materials and it can be generalised to cover static as well as cyclic fatigue [91]. In static fatigue the numbers of cycles at different stress are replaced by periods of time, so equation 4.21 becomes:

$$\frac{t_1}{t_{1f}} + \frac{t_2}{t_{2f}} + \frac{t_3}{t_{3f}} + \dots + \frac{t_i}{t_{if}} + \dots = \sum \frac{t_i}{t_{if}} = 1 \quad (4.22)$$

In this case, $t_1, t_2 \dots t_i$ etc. are the times at a particular stress of $\sigma_1, \sigma_2 \dots \sigma_i$ and $t_{1f}, t_{2f} \dots t_{if}$, are the corresponding times to failure at constant values of these stresses.

Little work has been carried out for the case where both static and cyclic fatigue effects are present at the same time. Often, it is sufficient simply to compare the Miner's Law sums for the two cases, when one will usually be seen to dominate. It has also been proposed [78] that the sums of the two effects simply be added, so that failure is predicted to occur when

$$\sum \frac{t_i}{t_{if}} + \sum \frac{N_i}{N_{if}} = 1 \quad (4.23)$$

It may be reasonable to add these two sums, and it will be shown that the results thus obtained make good sense. It is interesting to briefly consider the possibility that the cyclic fatigue effect may be solely due to the long term effect of the applied stress on the sample during the test. A quick numerical check, involving neglecting the second term in the relationship above shows that this cannot be the case: there is indeed a significant cyclic effect, which must be taken into account in relevant situations. It is interesting to determine whether the existing regression behaviour can be determined in terms of this relationship. Combining equations 4.2 and 4.23 allows the failure state to be predicted for loading histories containing both static and fatigue loading:

$$\sum \left(\frac{\sigma_i}{F} \right)^{\frac{1}{G}} t_i + \sum \left(\frac{\sigma_i}{H} \right)^{\frac{1}{J}} N_i = 1 \quad (4.24)$$

This can be applied to the UEWS test. For a stress increment, $\Delta\sigma$, the usual conditions of a cyclic loading period one minute and groups of 10 cycles, this is given by:

$$\begin{aligned} & \frac{10}{60} F^{-\frac{1}{G}} \left(\sigma^{\frac{1}{G}} + (2\sigma)^{\frac{1}{G}} + (3\sigma)^{\frac{1}{G}} + \dots \right) \\ & + 10H^{-\frac{1}{J}} \left(\sigma^{\frac{1}{J}} + (2\sigma)^{\frac{1}{J}} + (3\sigma)^{\frac{1}{J}} + \dots \right) = 1 \end{aligned} \quad (4.25)$$

The terms in the first bracket relate to static loading, while those in the second are due to cyclic loading.

4.6 Effects of crack density on properties

An improved method of looking at pressure rating and lifetime modelling for GRE will probably require considerations of the crack density and the way it affects measurable quantities such as the elastic constants of the pipe and possibly acoustic emission. Furthermore, a damage growth law is required to relate the change in properties with the loading history. The parameter normally used to describe the damage state is the crack density, ρ , measured in the ply transverse direction as shown in Figure 4.2. ρ is dimensionless, being defined as the ply thickness divided by the average distance between the cracks. This provides a means of taking into account the well-known effect of ply thickness on crack growth. It will be assumed that weepage occurs at a critical value of crack density, $\rho_{weepage}$, and that this value is the same regardless of how the weepage state is reached (i.e. by different combinations of static and cyclic loading or different combinations of internal pressure and axial load).

Several authors have published papers on the effects of cracking in laminates, concluding that cracking results in a significant and measureable decline in elastic properties. The work of Gudmudson and Zhang [112] (1993) is useful, as they modelled the changes due to matrix cracks in thermoplastic properties of angle ply laminates, as used in pipes.

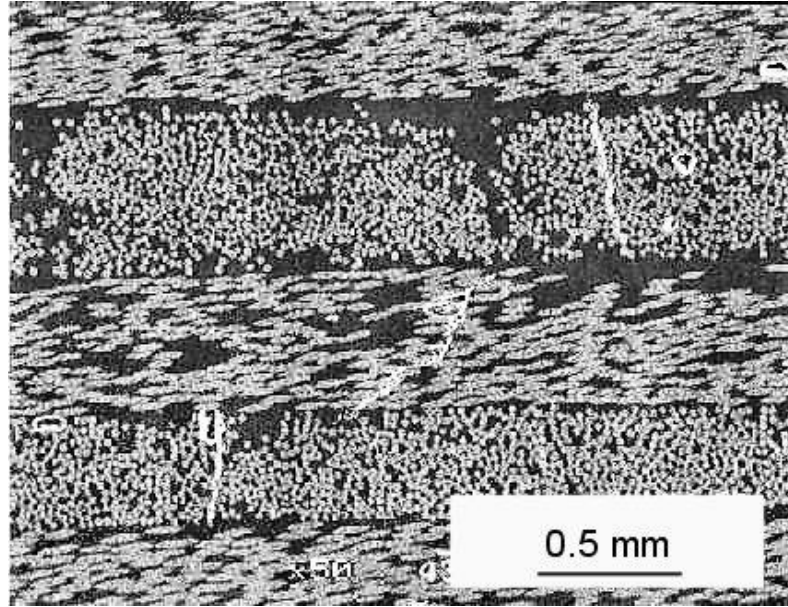


Figure 4.2. Matrix micro-cracks in a filament wound $\pm 55^\circ$ angle ply glass epoxy tube [5].

As there is relatively little crack growth resistance in the fibre direction, the cracks, once initiated, grow rapidly in this direction. The rate-determining process in damage propagation, therefore, is crack initiation, rather than growth. Frost and Cervenka [78] (1994) proposed a damage growth model for GRE pipe using a relationship similar to the Paris Law for crack growth in metals. The modified Paris Law describes the rate of change of crack density, rather than the growth of a single crack so, for the case of cyclic fatigue

$$\frac{d\rho}{dN} = A\sigma^n \quad (4.26)$$

If this can be generalised to consider the effects of static as well as cyclic fatigue, then:

$$d\rho = A\sigma^n dt + B\sigma^m dN \quad (4.27)$$

This provides a further method of summing the damage that occurs in the material. The use of power law relationships has no particular justification, other than the fact that power law-based relations have been used previously to describe crack growth.

It is interesting, however, that the form of the crack growth law, equation 4.27, is analogous to Equation 4.23 above, which resulted from Miner's Law. This lends support to both types of model. The constants, n and m in equation 4.27 are equivalent to I/G and I/J in equation 4.24. One interpretation of the Miner's Law Sum, therefore, is that it is not just an empirical measurement of damage accumulation, but a real quantity related to the crack density within the laminate.

As mentioned above, it is usual in the UEWS test, to measure either the axial or the hoop strain during the application of the hydrostatic pressure cycles. These strains are given by

$$\varepsilon_A = \frac{\sigma_H}{2E_A} - \nu_{HA} \frac{\sigma_H}{E_H} = \frac{\sigma_H}{E_A} (0.5 - \nu_{AH}) \quad (4.28)$$

For the case where axial strain is measured, and

$$\varepsilon_H = \frac{\sigma_H}{E_H} - \nu_{AH} \frac{\sigma_H}{2E_A} = \frac{\sigma_H}{E_H} (1 - 0.5\nu_{HA}) \quad (4.29)$$

for hoop strain measurement.

Noting that the quantities σ_H/E_A and σ_H/E_H are elastic properties with the units of modulus it is possible to define effective UEWS test-related Young's moduli, so that:

$$E_A^{UEWS} = \sigma_H/\varepsilon_A = \frac{E_A}{0.5 - \nu_{AH}} \quad (4.30)$$

$$E_H^{UEWS} = \sigma_H/\varepsilon_H = \frac{E_H}{1 - 0.5\nu_{HA}} \quad (4.31)$$

These quantities are easy to measure in a pressure test, whereas the conventional axial and hoop Young's moduli would require a different type of experiment. The measured values of these UEWS quantities in the undamaged state for Future Pipe GRE are 12 GPa and 20 GPa, respectively.

Values for the dimensionless analogues of E_A^{UEWS} and E_H^{UEWS} can be calculated from the results of Gudmudson and Zhang [112]. In terms of the debate about which quantity, axial or hoop strain, should be used for the UEWS test this appears to

suggest that the axial strain is most sensitive to changes, by a factor of about 4. However, it should be borne in mind that, as mentioned above, E_A^{UEWS} is 4 times larger than E_H^{UEWS} , so, in practice there should be little difference between the observed strain levels in the test. It is useful to have a numerical model for the obtained data which can provide the crack density level up to weepage and described by linear approximations figure (4.3), so that

$$\frac{E_A^{UEWS}}{E_{A_0}^{UEWS}} = 1 - 1.66\rho \quad (4.32)$$

And

$$\frac{E_H^{UEWS}}{E_{H_0}^{UEWS}} = 1 - 0.16\rho \quad (4.33)$$

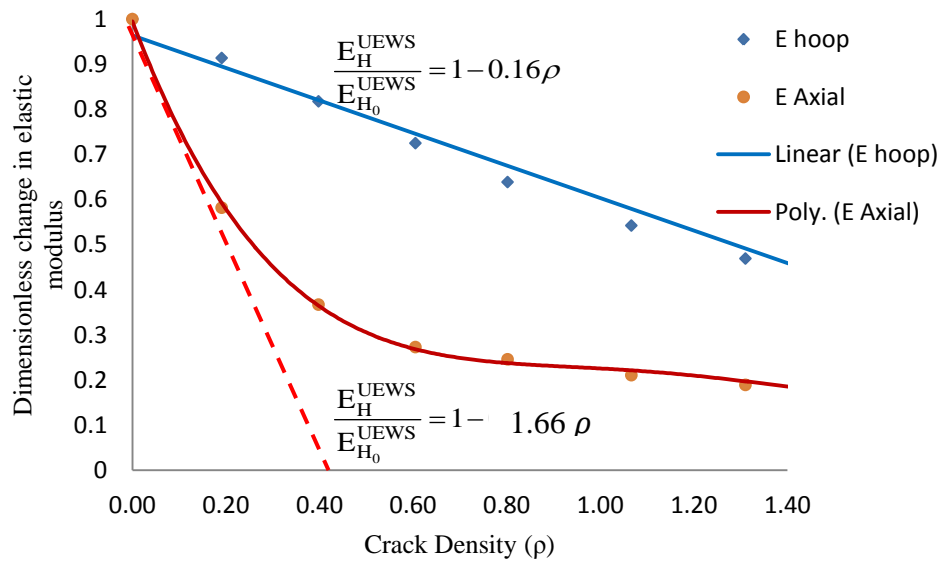


Figure 4.3. Dimensionless change in 'hydrostatic/axial modulus' (hoop stress divided by axial strain) and 'hydrostatic/ hoop modulus' (hoop stress divided by hoop strain) with increasing crack density. Calculated from the results of Gudmudson and Zhang for angle ply laminate.

If, as proposed above, the crack density is related to the Miner's Law Sum, as defined in equation 4.25 then it may be possible to express this relationship in the form:

$$\Phi = k\rho \quad (4.34)$$

It should therefore be possible to use the Miner's Law Sum to deduce the variation in elastic constants. Substituting equation 4.34 into equation 4.32 gives the change in elastic behaviour, so that

$$\frac{E_A^{UEWS}}{E_{A_0}^{UEWS}} = 1 - 1.66 \frac{\Phi}{k} \quad (4.35)$$

Strain in both 1st and 10th cycles can be then estimated from the conventional stress strain relationship as follows:

$$\varepsilon_A = \frac{\sigma_A}{E_A^{UEWS}}$$

4.7 Modelling of the UEWS and failure envelopes

4.7.1 Model A

Since each ply is constrained by plies of different orientation above and below it, as in figure 4.2, cracks only spread, at least initially, within each ply. The initiation of these cracks is governed by the stress (or strain) state in the ply. The crack initiation process is driven by an interactive combination of stresses on the ply which is probably best described by a 'polynomial' expression, similar to the widely used polynomial failure criteria, which takes into account these stresses and their interactions:

$$\Phi = \sqrt{\left(\frac{\sigma_1^2}{\sigma_1^{*2}}\right) + \left(\frac{\sigma_2^2}{\sigma_2^{*2}}\right) + k_1\sigma_1\sigma_2 + k_2\sigma_2\tau_{12} + \left(\frac{\tau_{12}^2}{\tau_{12}^{*2}}\right)} \quad (4.36)$$

And since,
$$\begin{bmatrix} \sigma_1 \\ \sigma_2 \\ \tau_{12} \end{bmatrix} = [T] \begin{bmatrix} \sigma_x \\ \sigma_y \\ \tau_{xy} \end{bmatrix}$$

Then,

$$\sigma_1 = \sigma_H(r \cos^2\phi + \sin^2\phi) \quad (4.37)$$

$$\sigma_2 = \sigma_H(r \sin^2\phi + \cos^2\phi) \quad (4.38)$$

$$\tau_{12} = \sigma_H(r \sin\phi \cos\phi + r \sin\phi \cos\phi) \quad (4.39)$$

The subscripts, 1,2 and 12 denote, respectively, tensile stresses parallel and perpendicular to the ply, and the shear stress and r is the hoop to axial stresses ratio. The starred terms refer to stresses at failure. k_1 and k_2 are fitted parameters that describe, respectively, the importance of the interactions between the two tensile stresses and between σ_2 and τ_{12} .

The stresses in equation 4.36 can be expressed in terms of the pipe wall stresses. This enables the damaging effects of all stresses to be expressed in a single relationship. Since equation 4.36 takes into account the effect of all the stresses acting on the ply, it can be used to model lifetime behaviour under a range of different stress conditions, including those involving axial loads on the pipe, in addition to hydrostatic ones.

4.7.2 Model B

In model B, the maximum stress criterion was considered to predict the UEWS envelope for GRE pipes. It is assumed that failure will start and develop when stresses parallel and perpendicular to the fibres exceed the appropriate critical value. This can be mathematically written as:

$$\sigma_1 \geq \sigma_1^*, \quad \sigma_2 \geq \sigma_2^* \quad , \quad \tau_{12} \geq \tau_{12}^* \quad (4.40)$$

Failure will occur when any of the conditions in equation 4.40 has investigated depends on the associated failure modes. This criterion involves interactions between the modes, since each mode is presented independently. The stress condition parallel to the fibres is rarely used, because the pipe usually fails due to matrix cracking or shearing. In this model, σ_2 , τ_{12} and interaction between them are considered for UEWS envelope modelling.

Equations 4.38, 4.39 were used to evaluate the stresses in shear and transverse directions in terms of hoop stress. Then both transverse and shear stresses are divided by the corresponding critical value as below:

$$\frac{\sigma_2}{\sigma_2^*}, \quad \frac{\tau_{12}}{\tau_{12}^*} \quad (4.41)$$

Since

$$\sigma_H = \sigma_2^* / (r \sin^2 \phi + \cos^2 \phi) \quad (4.42)$$

When, failure dominated by matrix cracking (axial dominated loading).

$$\sigma_H = \tau_{12}^* / (r \sin \phi \cos \phi + r \sin \phi \cos \phi) \quad (4.43)$$

When, shear failure is dominant (hoop dominated loading).

CHAPTER 5

RESULTS AND DISCUSSION

The experimental results of the testing of glass/fibre reinforced epoxy (GRE) pipes are presented in this chapter. The ultimate elastic wall stress and stress-strain results are presented in the first part of the chapter in relation to a range of biaxial loading of 0:1, 0.5:1, 1:1, 2:1, 4:1, 1:0 hoop to axial stress ratio. Next, the plots of tensile and flexural 100s creep modulus are discussed before the failure modes observed in the UEWS tests, and micro structural examinations of the failed samples are considered. Finally the UEWS and failure envelopes at different temperatures are presented.

5.1 Ultimate elastic wall stress (UEWS) tests

As mentioned in the previous chapter the UEWS test reflects the cyclic fatigue behaviour of glass/fibre reinforced pipes under biaxial loading. The main outcomes of the test are a definition of the elastic limit zone in the form of an envelope and the stress-strain response.

5.1.1 UEWS results under pure axial loading (0:1)

Figure 5.1 shows the stress-strain responses and UEWS points of the MDA $\pm 55^\circ$ GRE pipe at room temperature (a), 65°C (b), and 95°C (c) as well as the pipe strain history during UEWS test at room temperature (d). The axial strain was positive in the range of surrounding temperature tests. Most of the stress-strain curves exhibited linear behaviour until the UEWS point, and then significant non-linearity occurred up to final failure due to permanent deformation beyond the elastic limit. This non-linearity was possibly attributed to a combination of matrix microcracking and matrix plasticity. At room temperature the UEWS test yielded an axial stress of about 53MPa and an axial strain response of about 0.48%. These values were reduced by 20% and 5% respectively at 65°C. At 95°C the UEWS and axial strain failed by

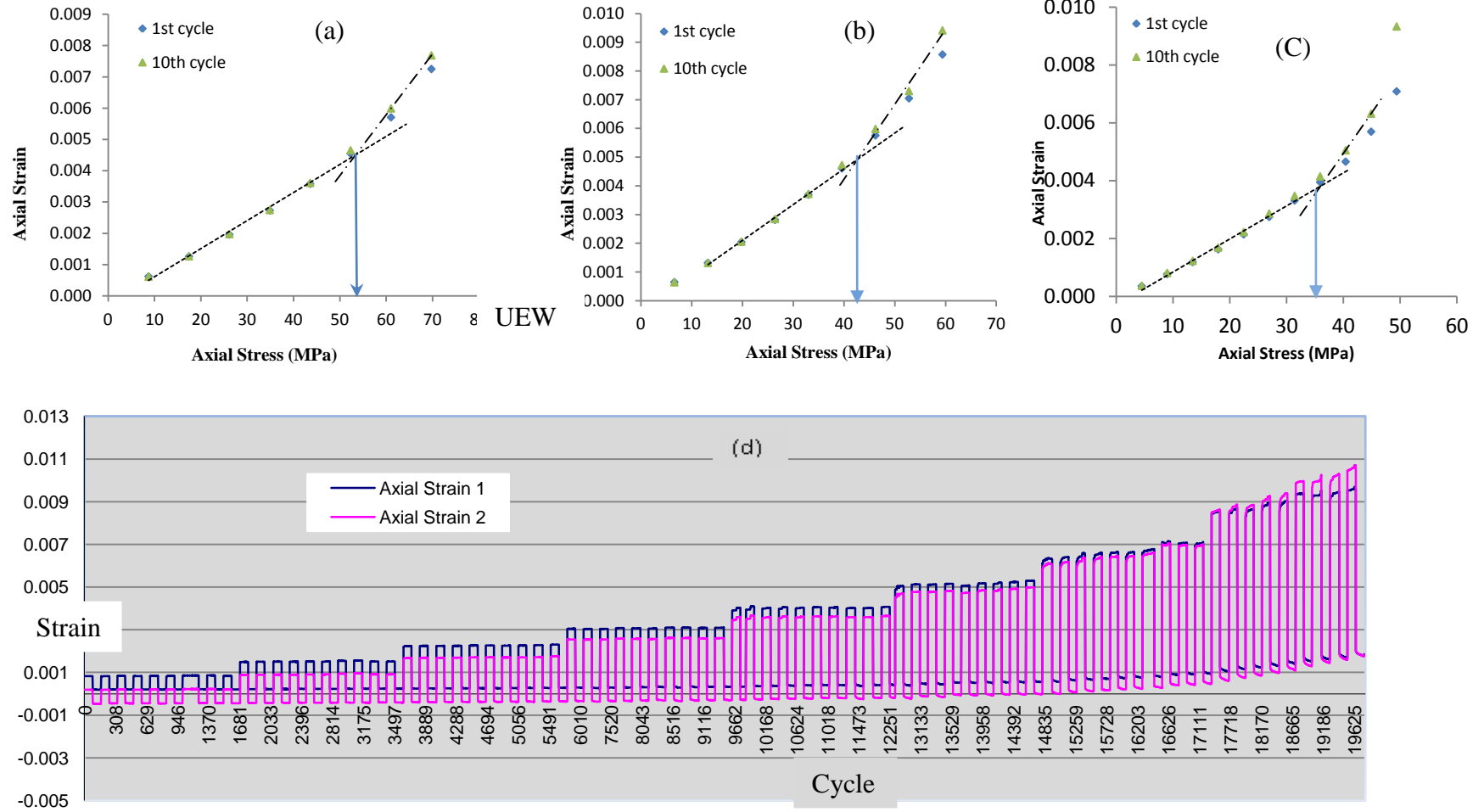


Figure 5.1 Stress-strain relationships and UEWS points under pure axial loading for $\pm 55^\circ$ fibre/glass epoxy pipes (a) at room temperature, (b) at 65°C , and (c) at 95°C . (d) is the axial strain plot during the UEWS test at room temperature.

28%, 27% respectively comparing with those at room temperature. Figure 5.1 (c) shows the non-linearity started slightly before the UEWS point. This could be due to the viscoelastic behaviour of the matrix at elevated temperatures. After the UEWS point there is significant deviation from a linear path in the stress-strain curve, possibly due to the high interaction between shear and transverse stresses.

Final failure was noted as a helical delamination following fibre direction, with a maximum axial stress of 70MPa at room temperature. This could have occurred as a result of the high stress applied in the axial direction in order to produce final failure, where the pressure applied inside the pipe was zero. The failure stress fell by 15% and 28% at 65°C and 95°C respectively. An only slight reduction in pipe strength was noted as the temperature increased.

5.1.2 UEWS results under 0.5:1 hoop to axial stress

In order to investigate this ratio, the pressure inside the small chamber was four times higher than that in the main chamber. Figure 5.2 shows the stress-strain response and UEWS points at room (a), 65°C (b), and 95°C (c), as well as the strain plots at 95°C (d). At room temperature, the stress-strain relationship was linear until about 31MPa. The curves then slowly deviated from linearity beyond the UEWS level up to final failure at 40MPa. The UEWS fell to 26 MPa at 65°C, with a percentage of 35% failing. However, at 95°C, only a slight reduction of 8% was noted in the pipe strength comparing to those at 65°C. Over the range of temperatures the axial strains at weepage level were positive between 0.5-0.7%.

The slow deviation in the stress-strain curve after the UEWS point could be due to the low shear stress and little debonding was taking place. Final failure was associated with the weepage of liquid resulting from a cumulative matrix cracking over time.

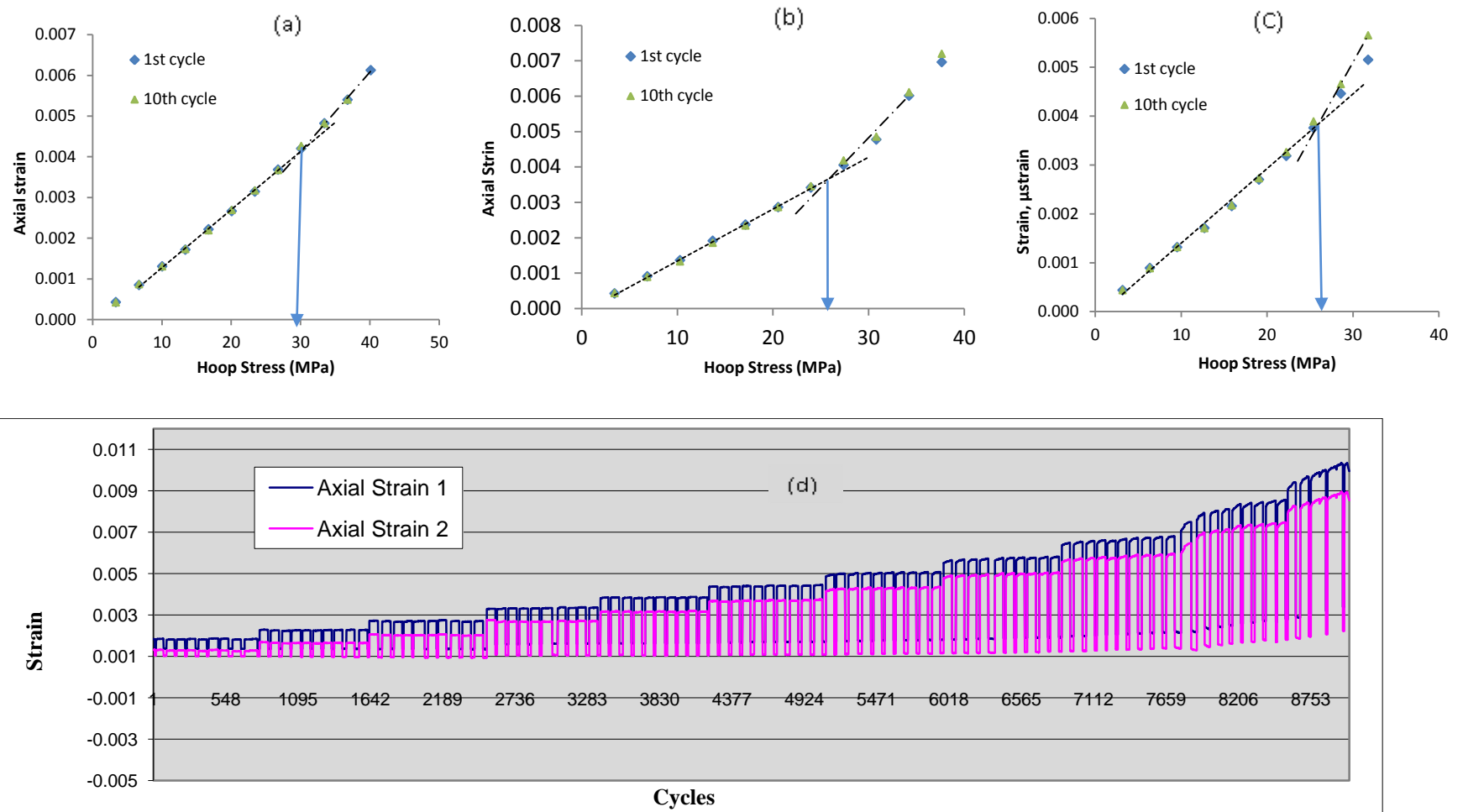


Figure 5.2 Stress-strain relationships and UEWS points at 0.5:1 hoop to axial stress for $\pm 55^\circ$ fibre/glass epoxy pipes (a) at room temperature, (b) at 65°C, and (c) at 95°C. (d) is the axial strain plot during the UEWS test at 95°C.

5.1.3 UEWS results under 1:1 hoop to axial stress

Equal levels of hoop and axial stresses were investigated by applying pressure in the small chamber twice that in the main chamber. Figure 5.3 shows the pipe's stress-strain response in the tests, the UEWS points at room temperature (a), 65⁰C (b), and 95⁰C (c) and the strain plots of the pipe at 65⁰C (d). Linear stress-strain behaviour was observed up to the UEWS point at about 75MPa and 67MPa at room temperature and 65⁰C respectively. Then the curves became dramatically non-linear up to final failure at 92MPa for room temperature and 82MPa for 65⁰C. Nevertheless, the pipe strength at 95⁰C was 3% greater than that recorded at room temperature. This increment was possibly due to the residual stresses generated during pipe manufacture and curing and being released with loading.

On the other hand, the elastic limit achieved for the range of temperatures was between 66-76MPa. The positive axial strain in this case enables cracks to develop in the matrix parallel to the fibre direction, with weepage eventually occurring as a result of saturation from cumulative matrix microcracking.

At 95⁰C viscoelasticity also disrupted the linearity of the stress-strain relationships in the two cycle groups before the UEWS point. Figure 5.3 (d) shows that permanent deformation started in the eighth cycle group, conforming to the point in the stress-strain diagram when curvature occurred.

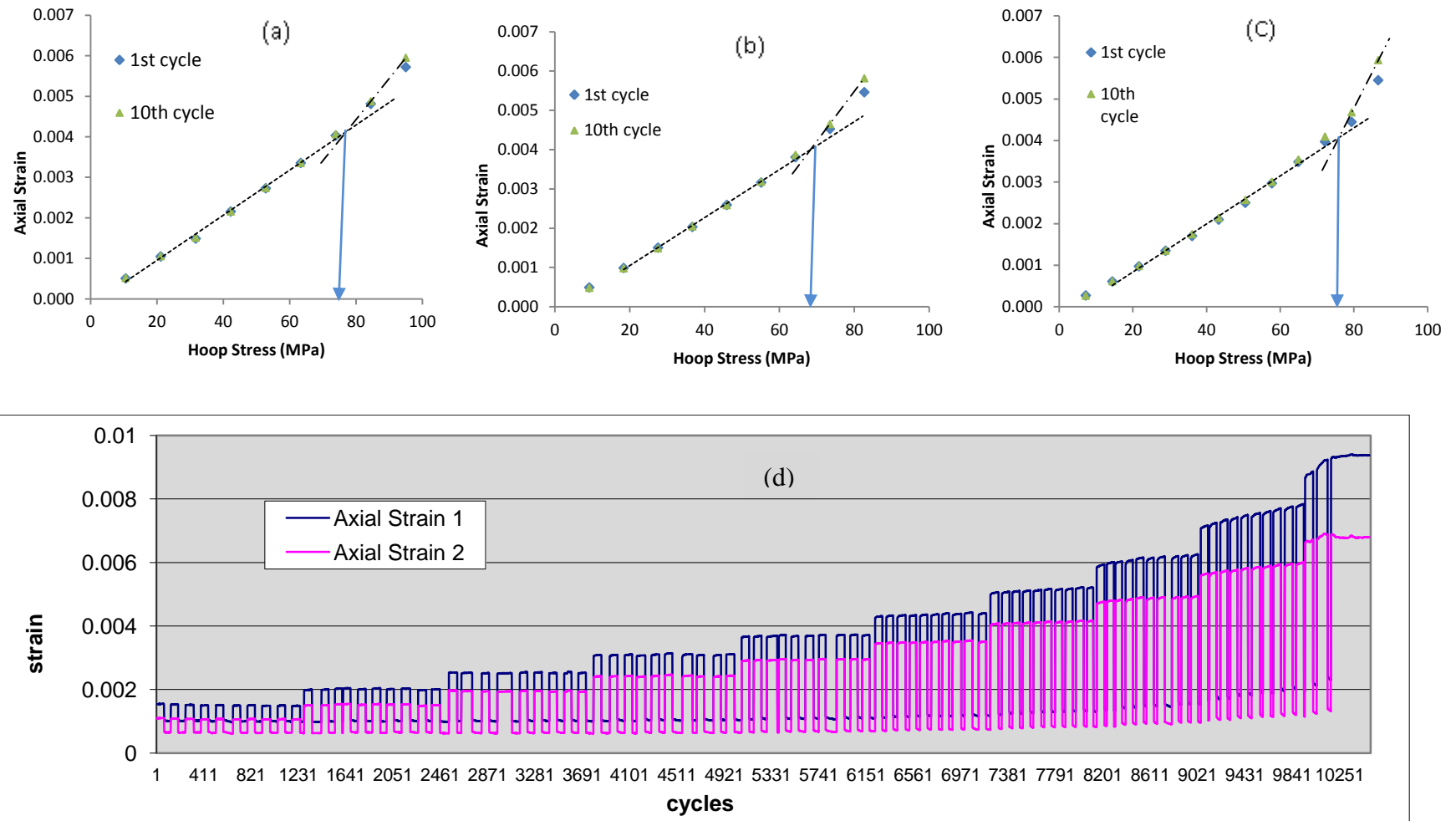


Figure 5.3 Stress-strain relationships and UEWS points at 1:1 hoop to axial stress for $\pm 55^\circ$ fibre/glass epoxy pipes (a) at room temperature, (b) at 65°C , and (c) at 95°C ., (d) is the axial strain plot during the UEWS test at 65°C .

5.1.4 UEWS results under pure hydrostatic pressure (2:1)

Figure 5.4 shows the pipe performance under pure hydrostatic pressure at room temperature (a), 65°C (b), and 95°C (c). The applied stress and corresponding strain are represented in hoop and axial directions respectively. The relationship is shown to be linear, and both hoop and axial strains are positive. However, at pressures above 170MPa a well defined transition to non-linear behaviour occurred up to final failure at about 220MPa. The departure from linearity in the stress-strain curve is due to the interaction of transverse and shear stresses and by exceeding the critical value of these stresses.

The UEWS increased by 10% at 65°C and 95°C, possibly due to the presence of residual stresses from pipe manufacture and cure. Weepage was observed after the formation of lines of very small droplets parallel to the fibre direction, associated with the matrix microcracks developing in the transverse direction as well as delamination.

Pipes under loading of 2:1 hoop to axial stresses provided the longest-lasting linear behaviour before plasticity was observed among all the conducted stress ratios. This level of performance found agreement with netting analysis, assuming that the principle stresses generated in the ply are parallel to fibre direction and transverse stress is zero. It is difficult to compare the results observed here with those of Hull (1975) [31], who conducted UEWS testing on glass/fibre reinforced $\pm 55^\circ$ pipes, since different materials and technology were used then. However, the ratio of UEWS to weepage stress appears to be promising in terms of both the comparison and modelling. The current results give a ratio of 75% UEWS to weep stress, compared with 76% reported by Hull. This indicates that the linear response represents about 75% of the load history from zero to weepage, whereas, non-linearity occurs during only 25%. A noticeable drop in the strain reading occurred for the unloading condition after the fifth cycle group as figure 5.4 (d). This reduction was possibly due to the loss of mass as the cracks were initiated and propagated in the elastic zone indicating that cracks started before the UEWS point.

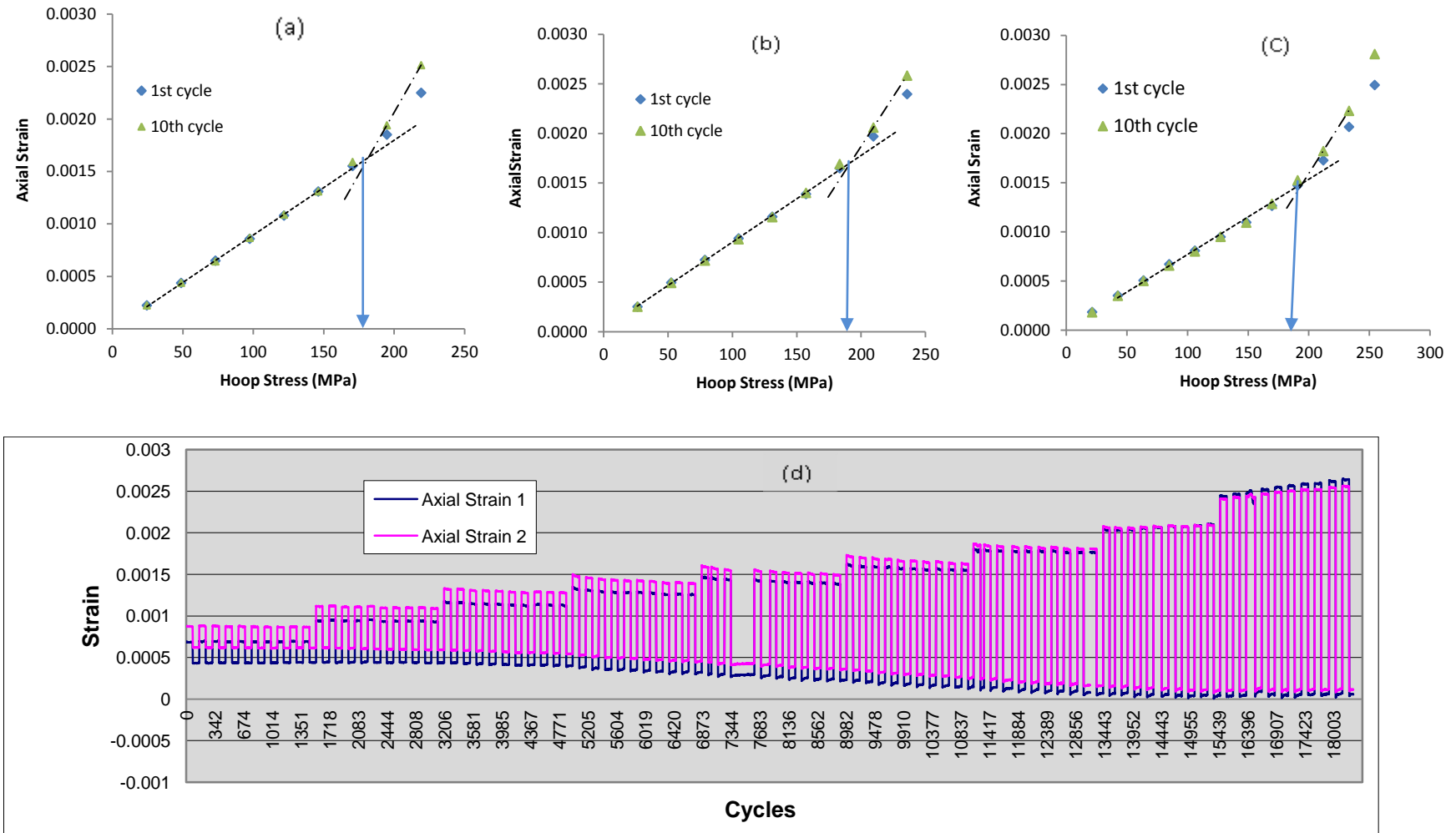


Figure 5.4 Stress-strain relationships and UEWS points at 2:1 hoop to axial stress for $\pm 55^\circ$ fibre/glass epoxy pipes (a) at room temperature, (b) at 65°C , and (c) at 95°C . (d) is the axial strain plot during the UEWS test at 65°C .

5.1.5 UEWS results under 4:1 hoop to axial stress

Figure 5.5 shows pipe performance under a 4:1 stress ratio at room temperature (a), 65°C (b), and 95°C (c) and the strain plots of the test conducted at room temperature (d). This ratio was investigated by applying half the level of pressure in the small chamber compared to that in the main chamber. At the 4:1 stress ratio the pipe appear to provide the highest performance of all the ratios tested in terms of failure. Leakage occurred at 420MPa with a high strain response of 2.5% at room temperature. The pipe strength failed by approximately 12% at 65°C, whereas, the hoop strain showed only negligible decrease. This could be due to the pipe becoming more ductile as the temperature increases. At 95°C the leakage occurred at 320MPa with failing of about 25% from those at room temperature, and again the hoop strain did not decline.

Permanent deformation began to influence the linearity of the stress-strain curve at early stage of loading as shown in figure 5.5 (d). An irreversible strain was noted after the fifth cycle group as the load increased. The stress-strain response was linear for only 35% of the load history, and then a massive plastic deformation took place up to final failure. This explains the observed high levels of strain in the hoop direction. Final failure was noted as small jet leakage, which occurred within a few millimetres of a single location near to the pipe's reinforced end, and was due to stress concentration.

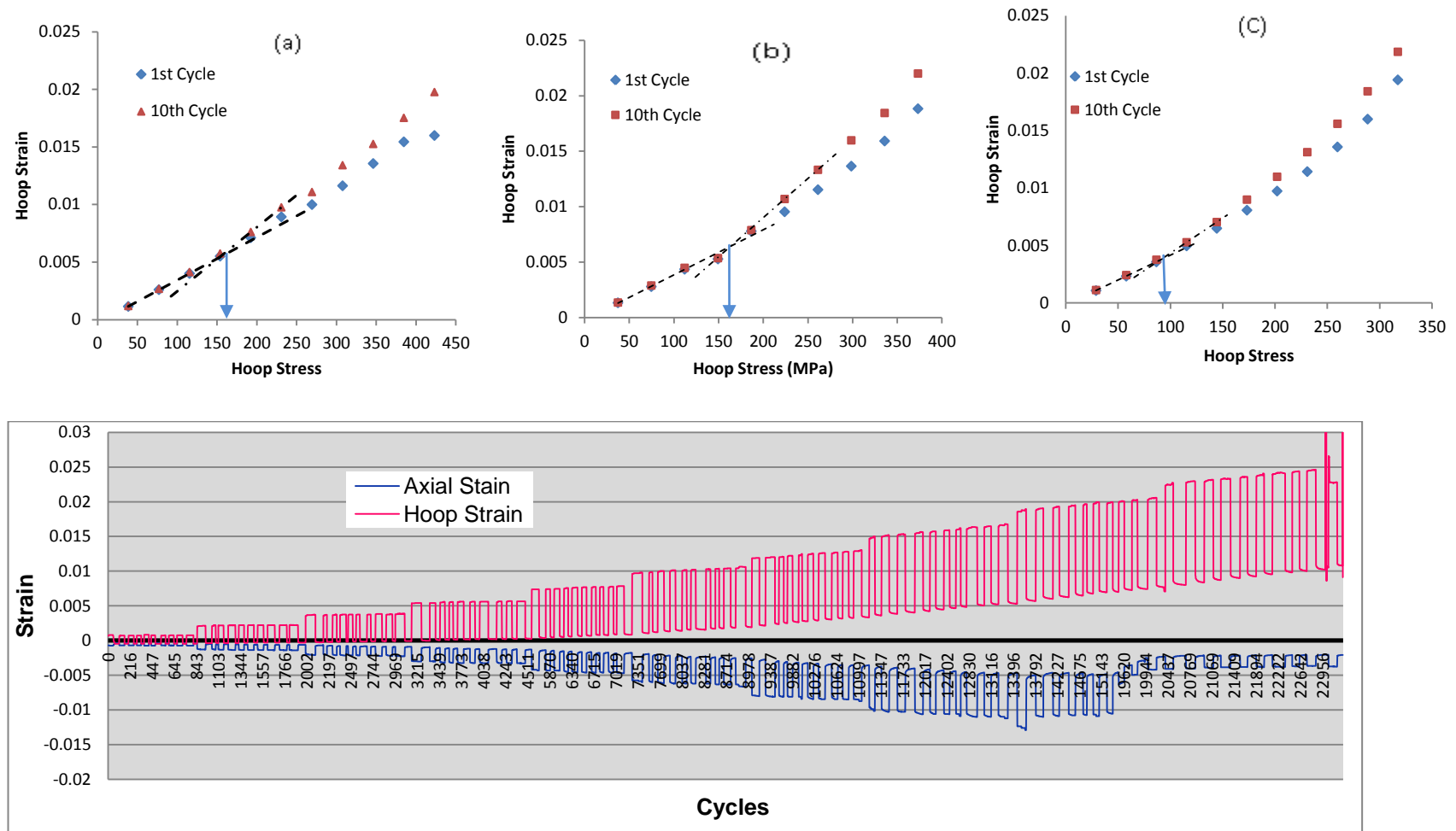


Figure 5.5 Stress-strain relationships and UEWS points at 4:1 hoop to axial stress for $\pm 55^\circ$ fibre/glass epoxy pipes at (a) at room temperature, (b) at 65°C , and (c) at 95°C . (d) is the axial strain plot during the UEWS test at room temperature.

5.1.6 UEWS results under pure hoop loading (1:0)

In this arrangement the pipe ends were free to slide on the O-ring and therefore the axial stresses were transmitted to the shaft attached the pistons. As a result axial stress would be zero in the pipe wall. Figure 5.6 shows the UEWS results and stress-strain of the pipe under pure hoop loading at room temperature (a), 65°C (b), and 95°C (c). When the pipe was pressurized with wall stress increments of about 5MPa/minute, a linear elastic response was observed. This linearity continued until hoop stress of 95MPa at room temperature, 85MPa at 65°C, and 60MPa at 95°C. The curve then slowly deviated from linearity after the UEWS point up to final failure, as shown in figure 5.6 (d). When the pressure was increased above the UEWS, both axial and hoop strains developed smoothly up to the equivalent strain to 200MPa. At these stress level white lines parallel to the fibres appeared along the pipe wall, showing high levels of strain developing up to final failure.

The hoop strain was positive with maximum percentages of 1.8-2% over the range of temperatures. Since the pipe had free ends, the positive hoop strains were followed by a negative axial strain of about 1.7-1.9%. The negative strain in the axial direction prevented the matrix from developing cracks along the pipe wall. Delamination eventually caused between fibres wound at different angles, and appeared as patches of uniformly white regions on the pipe wall. However, at high pressure corresponding to 300MPa in the case of room temperature conditions, leakage occurred suddenly in the form of fine jet through macro cracking near to the pipe end. This was due to massive buckling at high levels of stress which eventually caused rupture. The fibres failed near to the pipe end where the stress may have become most concentrated.

Despite pipe performance decreasing by 10% at 65°C, the hoop strain remained at 2.0% due to the pipe's ductility at high temperatures. At 95°C the pipe showed marked reduction in strength of 30%, recording 210MPa and an axial stain of -1.9%.

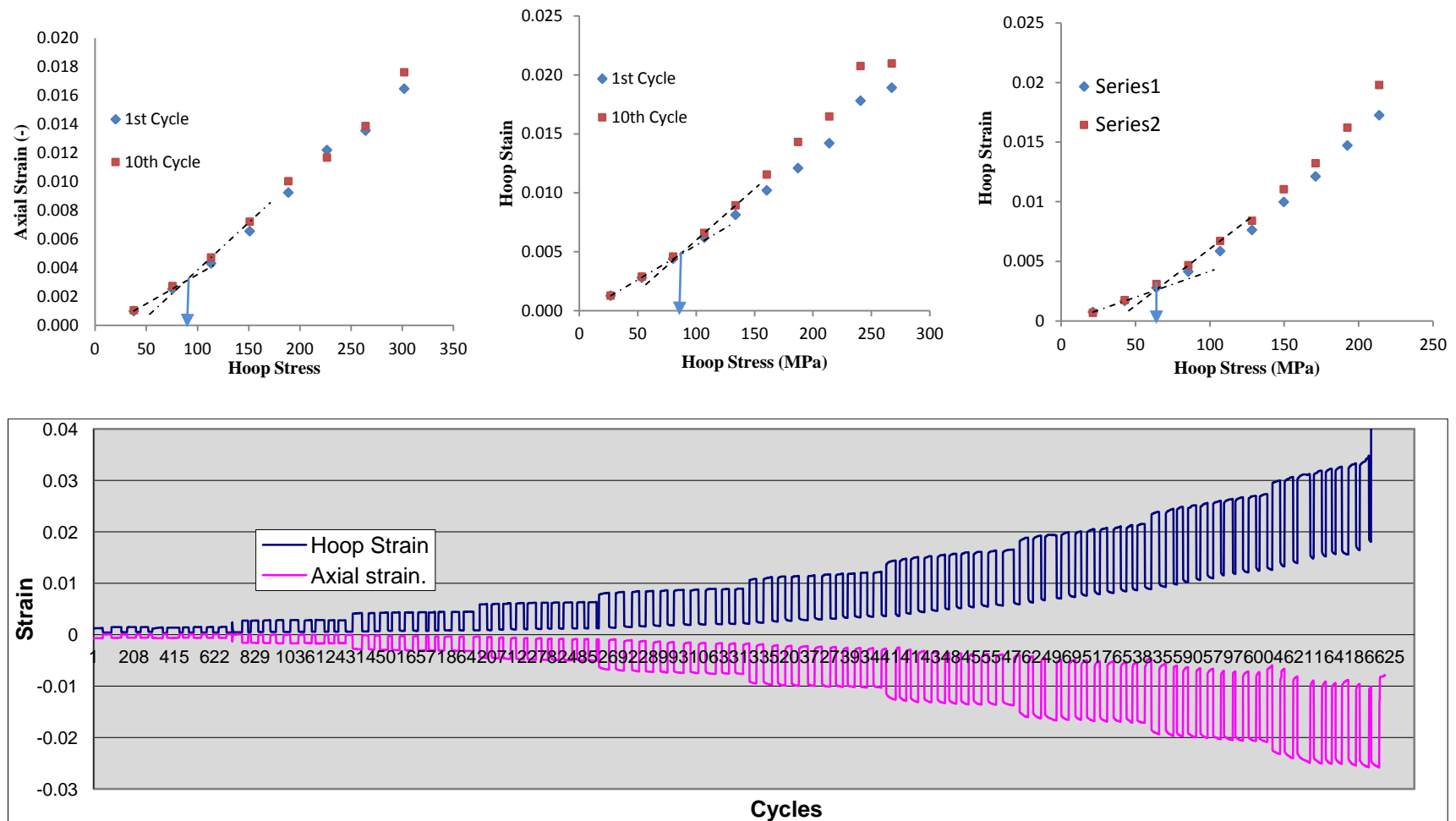


Figure 5.6 Stress-strain relationships and UEWS points under pure hoop loading for $\pm 55^\circ$ fibre/glass epoxy pipes at (a) at room temperature, (b) at 65°C, and (c) at 95°C. (d) is the axial strain plot during the UEWS test at 95°C.

Table 5.1 listed the transverse σ_2 and shear stresses τ_{12} at weepage stress level. These were obtained from the multiplication of axis stresses (σ_x, σ_y) and transformation matrix [T]. Transverse and shear stresses enables to compare and recognise failure modes for the conducted stress ratio tests. For example, final failure for $\pm 55^\circ$ GRE pipes under pure axial load was associated with a combination of shear and transverse stress, which caused transverse cracking and delamination, and governed by transverse stress. While neither transverse nor shear stresses had reached the critical values of about 60MPa. Also failure in case of 1:1 stress ratio was dominated by pure transverse stress, and damage started when σ_2 exceeded the critical value of transverse stress at stress level compatible with the UEWS point.

Table 5.1. Transverse and shear stresses at failure point for $\pm 55^\circ$ GRE pipes.

Stress ratio (H:A)	UEWS (MPa)	Failure stress (MPa)	Transverse stress (MPa)	Shear stress (MPa)
0:1	53	70	47	-32
0.5:1	32	42	67	-19
1:1	75	95	94	0
2:1	180	220	145	51
4:1	160	420	208	148
1:0	95	300	97	141

5.2 Axial and hoop Young's modulus measurements

Simple 100s pull tests were carried out on the conditioned pipe specimens to determine the axial and hoop modulus. Figure 5.7 shows the test setup arrangements for both hoop and axial modulus measurement. The 100s axial and hoop moduli tests were conducted for two separate packages of pipes each in different conditions: virgin, halfway to UEWS, at the UEWS, and weeping pipes.

The main purpose of carrying out these tests was to define and follow the decline in pipe stiffness at different load levels. Figure 5.8 shows the stress-strain diagram of the pipes of different conditions under a 2:1 hoop to axial stress ratio. The elastic modulus was determined in the axial direction from the linear regression of the stress-strain curve as the average of line slope. Figure 5.8 also shows the initial reduction in the axial modulus, which stabilized with a negligible reduction at 50%

of the UEWS at 90MPa. Subsequently a notable reduction of approximately 14% occurred at the UEWS point, when serious damage possibly started to develop. Weeping pipes showed a total reduction of 33% compared to those in virgin condition. Non-linear behaviour in the stress-strain responses was noted even at low levels of loading at UEWS and weeping condition. The non-linearity might be due to exceeding the elastic limit under these test conditions, and the pipes did not appear to achieve linearity afterwards.

Figure 5.9 shows the stress-strain responses of the pipe in the hoop direction under a 2:1 hoop/axial stress ratio. The elastic modulus was determined in this direction from equation 3.13 based on the linear regression. From the regression line the hoop elastic modulus is about 18GPa in the case of virgin pipe. The degradation in pipe properties started at quite an early stage of loading compared with those in axial direction. At 50% UEWS the hoop elastic modulus failed at 17.5GPa with a reduction of approximately 4%. At the UEWS point, the hoop elastic modulus failed by 8% compared to those at virgin condition. The weeping pipes showed a total reduction in hoop elastic modulus of about 18% at 14.8GPa.



Figure 5.7. 100s ring and axial test set ups to measure the elastic modulus of $\pm 55^\circ$ GRE pipe specimens.

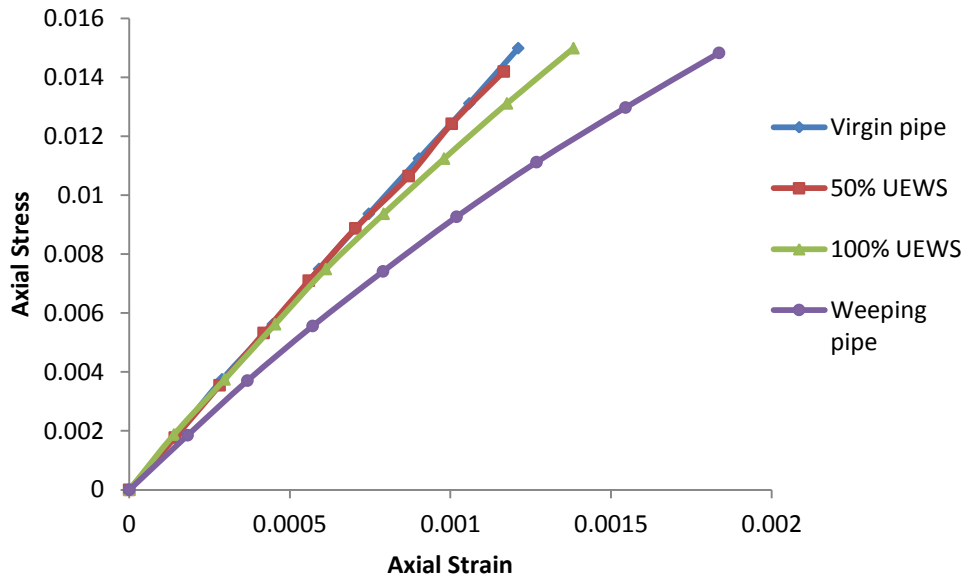


Figure 5.8. Stress-strain response in axial direction of the conditioned $\pm 55^\circ$ glass/fibre epoxy pipe under 2:1 hoop/axial stress ratio.

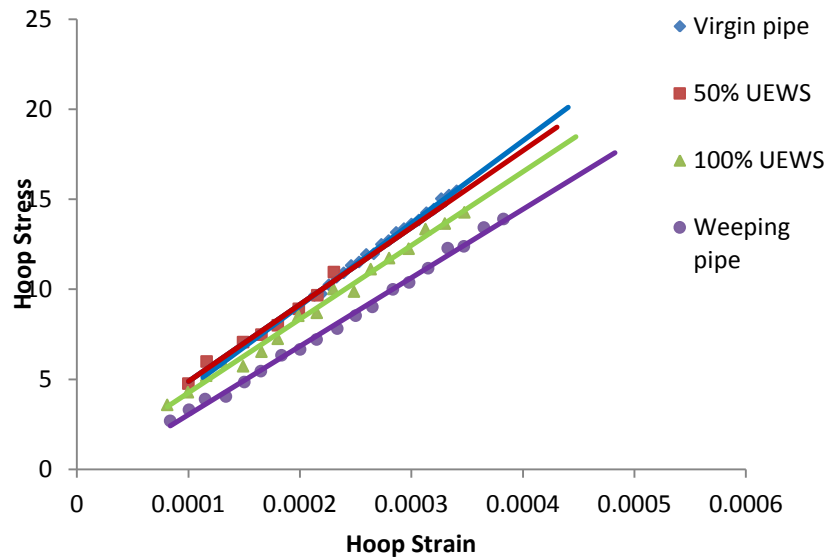


Figure 5.9 Stress-strain responses in hoop direction of the conditioned $\pm 55^\circ$ GRE pipes under a 2:1 stress ratio.

It can be concluded that under the 2:1 stress ratio the hoop elastic modulus of the pipes tested showed a smooth reduction throughout the load history, whereas the axial elastic modulus dramatically fell after the UEWS limit. Figure 5.10 shows the elastic modulus degradation as the UEWS test progressed.

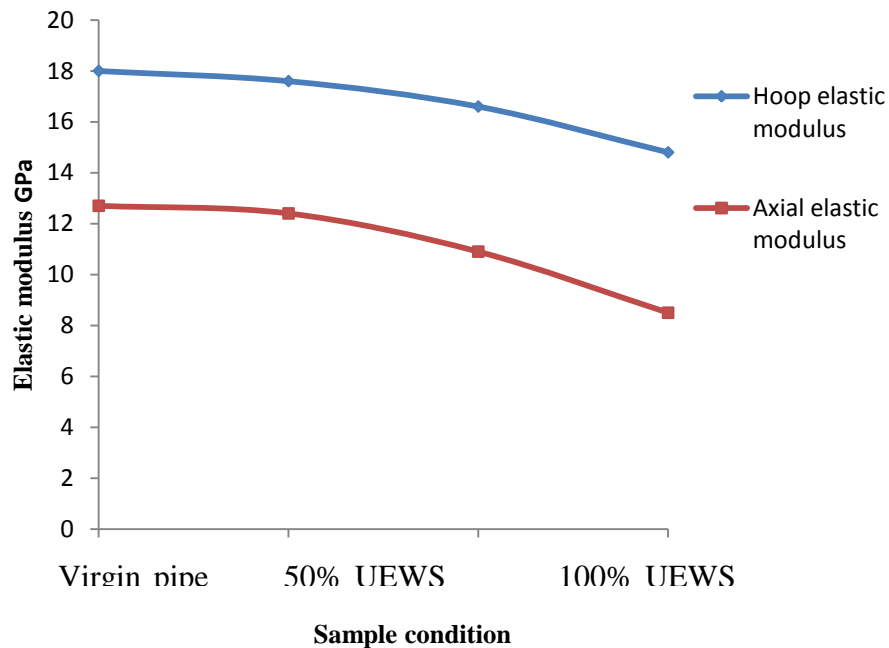


Figure 5.10 Axial and hoop elastic modulus degradation in different conditions.

5.3 Failure modes

Since glass/fibre reinforced composites exhibit anisotropic structures, various failure mechanisms may be noted depending on stress state. Some published studies have defined final failure in composite pipes as complete bursting. In this study, however, the first failure that caused leakage through the pipe wall is considered to be final failure. The failure modes in this investigation are classified into four modes depends on the pipe wall stress state, as follows.

5.3.1 Mode I

Mode I involves weepage at high pressure levels, where small droplets leak through the pipe wall. Weepage was frequently observed in the pipes under hoop to axial stress ratios of 2:1, 0.5:1, and 1:1, and it generally occurs due to the presence of a network of transverse matrix cracks which form over time. Figure 5.11 shows a photograph of a glass/fibre epoxy pipe which failed in weepage mode at room temperature.

The earliest stage of weepage starts with cracks initiated in the transverse direction, and these then propagate in terms of size and number. These are then followed by nose up to a stage when the liquid can find pathways to spread on to the pipe surface. Even though weepage occurs at different stress levels at different stress ratio, water droplets found along the pipe length were common in all cases. For example, weep

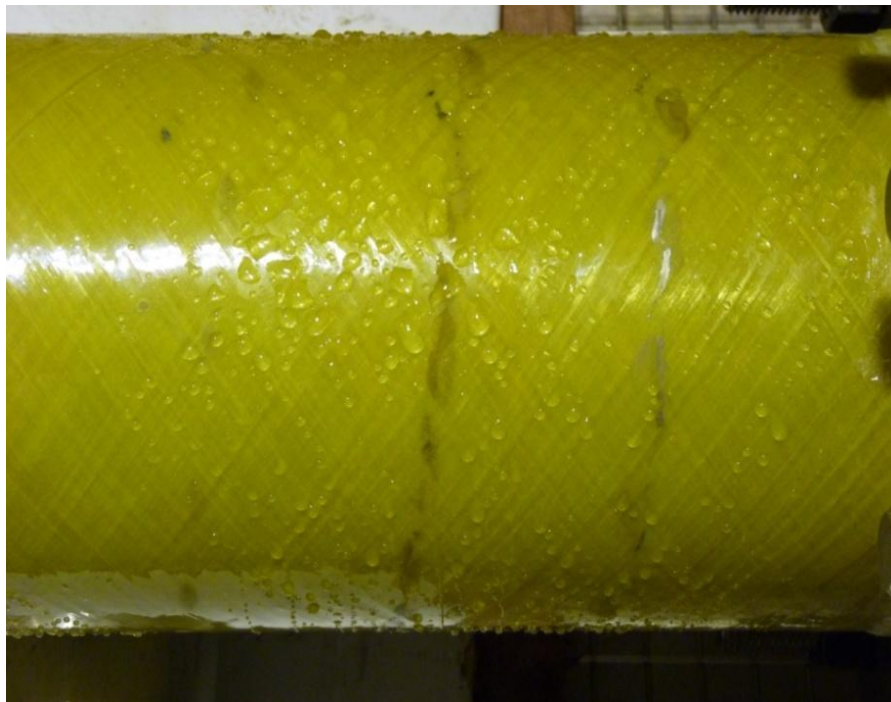


Figure 5.11 Glass/fibre reinforced epoxy pipe with $\pm 55^\circ$ winding angle which failed by weepage (mode I) under a 2:1 hoop to axial stress ratio at room temperature.

stresses were 40MPa, 92Mpa, and 220MPa for the stress ratios of 0.5:1, 1:1, and 2:1 respectively. This indicates that failure mechanisms in this mode have similar behaviour depending on the direction of stress. Elevated temperatures have no effect on the failure mechanism itself, but do influence the stress level where weepage occurs.

5.3.2 Mode II

Pipes failing under pure axial loading in mode II (delamination) develop macro helical cracks following the fibre direction which tend to occur along the pipe's circumference. This type of failure is dominated by matrix cracking and occurs when a critical axial strain is reached. Since the matrix strength is much lower than that of fibres, the pipes subsequently fail at relatively low stresses having formed extensive matrix cracks parallel to the fibres. As shown in figure 5.12 cracks initiated in the matrix between the fibres and then propagate parallel to the winding angle along the pipe length. The reinforced layer parallel to the crack remains intact, whereas complete fracture takes place in the opposite reinforcement.

As mentioned above, final failure for $\pm 55^\circ$ GRE pipes under pure axial loading occurs at different stress levels depending on temperature. For example, pipes failed suddenly and rapidly at room temperature at 70MPa, this stress level failed by 15%, 28% at 65°C and 95°C respectively. The failure mechanism remains the same as temperature increases, but the only strain increases due to resin ductility, so that the strain reaches a critical value at lower stress level. This observation has also been reported by Soden (1993) [32], Ellyin (1997) [113], Hale (2000) [11], and Garret (2008) [2].



(a)



(b)

Figure 5.12 Glass/fibre reinforced epoxy pipe with $\pm 55^\circ$ winding angle which failed by delamination (mode II) under pure axial loading at 25°C (a) and at 65°C (b).

5.3.3 Mode III

Local leakage occurring near to the pipe end is classified as mode III, and is significantly different from the weepage described in mode I. It is observed when pipes are subjected to the 4:1 hoop to axial stress ratio, and appears as a small single jet of water spraying from a macro crack of 20-30mm in length. This crack usually occurred near to the pipe end due to stress concentration there, as shown in figure 5.13. The water jet started with a small amount of leakage and then the magnitude of the jet increased as the test progressed. Eventually a macro crack becomes prominent on the pipe surface.

However, along the pipe length the fibres take on an opaque appearance due to the coarse striations parallel to the reinforcement. This has been observed to indicate the presence of delamination, according to Jones and Hull (1979) [61]. This is also called whitening which usually happens in cases where hoop loading is dominant. Whitening occurs as a result of delamination and shearing in the fibre/matrix interface. The shear starts in an earlier stage of loading, but the low levels of axial strain limit any matrix microcracking from developing and causing premature failure.

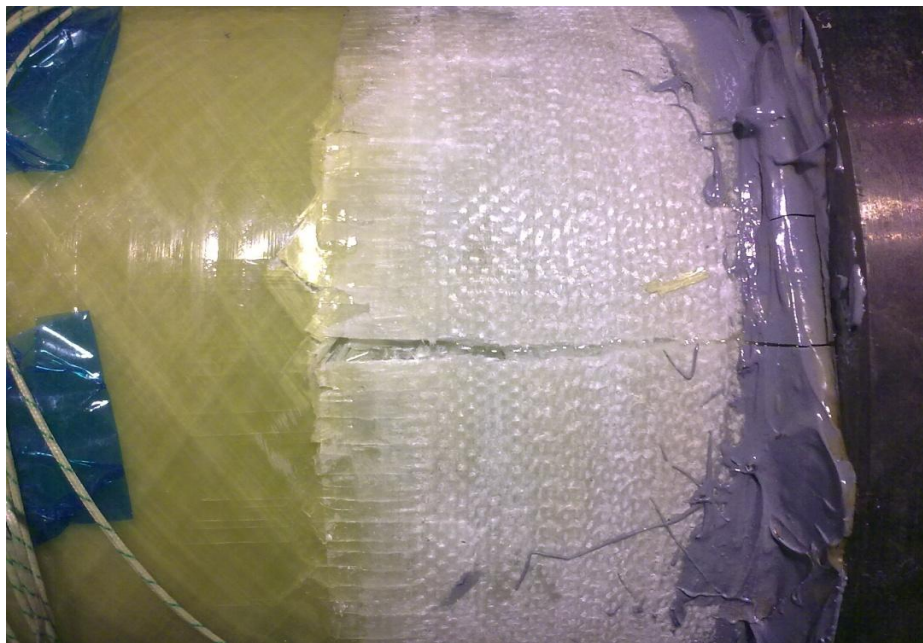


Figure 5.13. $\pm 55^\circ$ glass/fibre pipe tested under 4:1 hoop to axial stress which failed by mode III.

5.3.4 *Mode IV*

As mentioned above, when the pipe ends were free to slide on the O-ring, axial load would transmit from the pipe wall to the shaft. This allows stresses to be developed only in the hoop direction causing positive tensile strain in this direction accompanied by negative axial strain. In these strain conditions, pipes eventually exhibit a marked increase in diameter, decreasing in length and with fibre orientation changing.

The negative axial strain limits the development of matrix cracking which would cause weepage along the pipe length. However, the high positive hoop strain leads to high interlaminar shear strain. This concentrates the transverse compressive stress in the matrix, causing a massive shear in the fibre/matrix interface. As the test progresses whitening appeared in the room temperature and 65°C tests at stress levels between 180-200MPa.

In the very last stage of loading, failure occurred suddenly without any warning or visible development. At high stress levels the pipes started to buckle, as shown in figure 5.14, and rapid ruptures caused fractures in the fibres and complete destruction of the matrix. This fracture was noted near to the pipe end where the stresses may have become concentrated, as illustrated in figure 5.15. Small local jets in the specific areas of failure were classified as final failure.

At 95°C the pipe failed in a different way, where small local jets were found near to the pipe ends but without rupture or buckling as shown in figure 5.16. This was noted also by Saied (2004) [114], who reported that “the tubes exhibited extensive deformation leading to catastrophic failure at the gauge length. This is probably related to the plasticization of the resin which may allow the matrix to accommodate the interlaminar shear strain without failure. Furthermore, the localised compression of the fibre bundles would tend to reduce the flow of the matrix under the influence of the internal pressure and would hence militate against liquid penetration”.



Figure 5.14. Buckling of glass/fibre $\pm 55^\circ$ winding angle pipe under pure hoop loading at 65°C.



Figure 5.15. Rupture in glass/fibre $\pm 55^\circ$ winding angle pipe under pure hoop loading at room temperature, due to buckling.

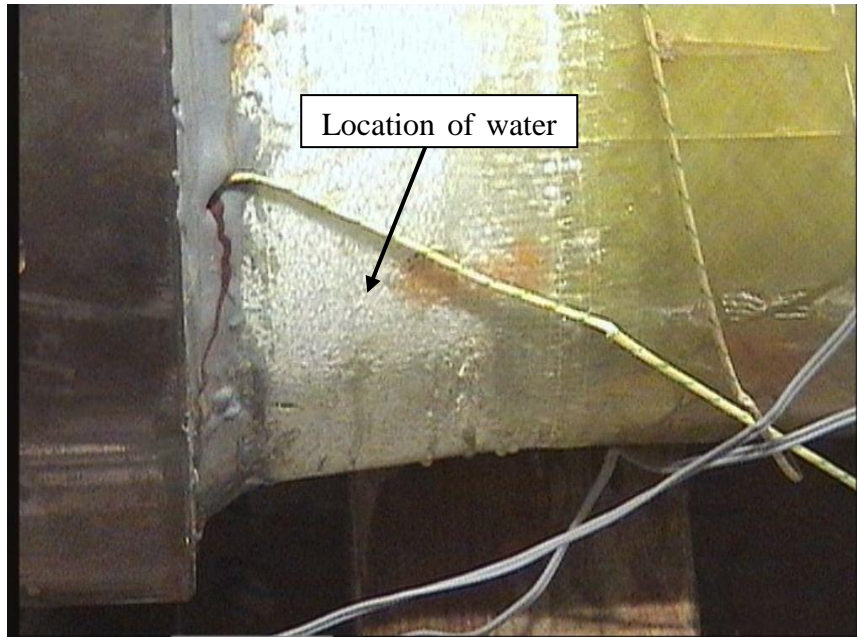


Figure 5.16. Small local jet as the failure mode of $\pm 55^\circ$ glass/fibre pipe tested under pure hoop loading at 95°C .

5.4 Microscopic analysis

The different failure modes lead to variety of types of cracks and shapes of delamination, which can be distinguished by microscopic analysis and observations. The evaluation of crack shape and density causing weepage are the main outcomes of such analysis. After the sequence of polishing and grinding procedures described in chapter three, failed samples were examined by electronic microscopy. Failed pipe samples under the 2:1 stress ratio were cut from the centre of the gauge length with an angle parallel to the fibre orientation of 55° . Each sample was then magnified so as to clearly recognise the -55° ply with fibres of circular shape and longitudinal fibres of $+55^\circ$ ply as in figure 5.17. The visible black spots are voids formed during the pipe manufacturing and curing process.

As the load increases the fibres start to debond from the matrix, initiating cracks in the fibre/matrix interface. These cracks then grow in the matrix and join together as horizontal cracks between the plies, as illustrated in figure 5.18. Figure 5.19 shows that the cracks are apparently initiated from the voids and then propagate parallel to

fibres, being restricted by neighbouring ply interference. This processing relates stress concentration at the voids. Fibres tend to lie at an angle of $\pm 55^\circ$ to the main pipe axis, and the cracks propagate in the resin between the fibres. As a result the fibres remains intact and delamination between the plies then takes place appearing as cracks.

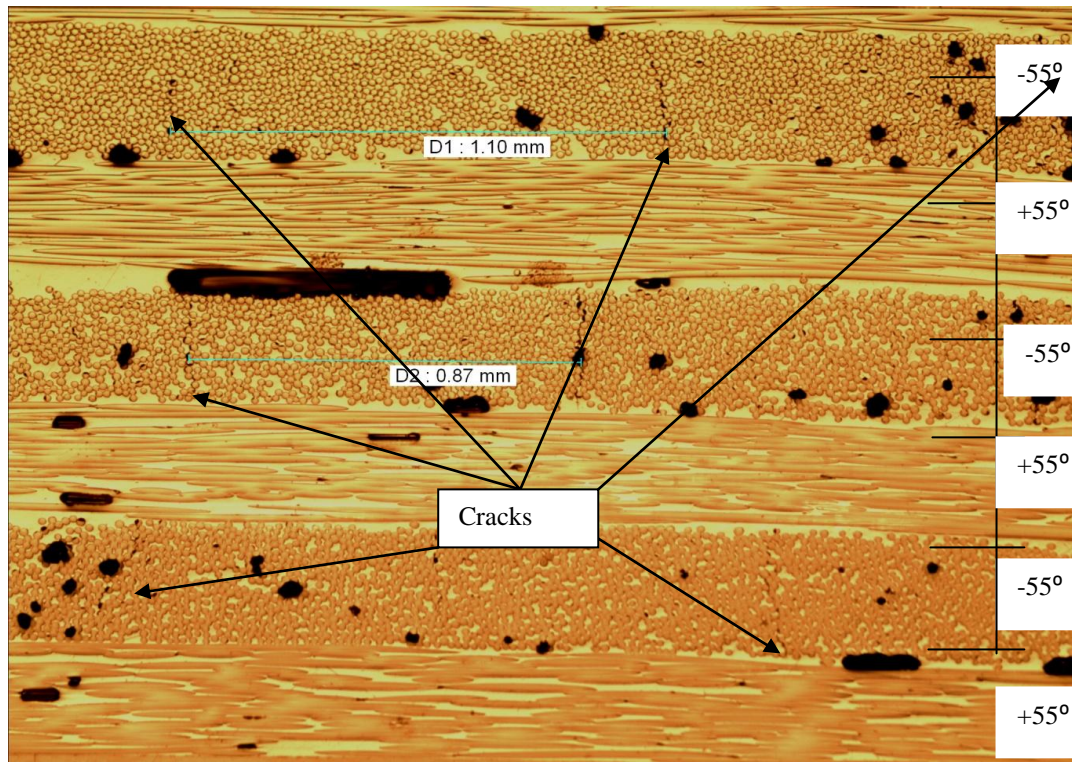


Figure 5.17. Photo-micrograph of a cross-section of $\pm 55^\circ$ glass/fibre epoxy pipe under a 2:1 biaxial loading at room temperature. Crack spacing and ply thickness are measured.

As discussed in chapter 2, composites exhibit a sequence of damage lead to final failure either by weepage, delamination or rupture. Weepage is caused by matrix cracking which depends on matrix strength. The crack density was estimated from the measured crack length and ply thickness, dividing the latter by crack spacing. Ply thickness among the samples examined was between 0.33-0.43mm, whereas crack spacing measured in the range between 0.84 and 1.15 mm. Weepage then occurred with crack density between 0.3-0.4. Saturated crack density was found to be consistent with the predictions of Gudmundson (1993) [112] and Saeid (2004)[114].

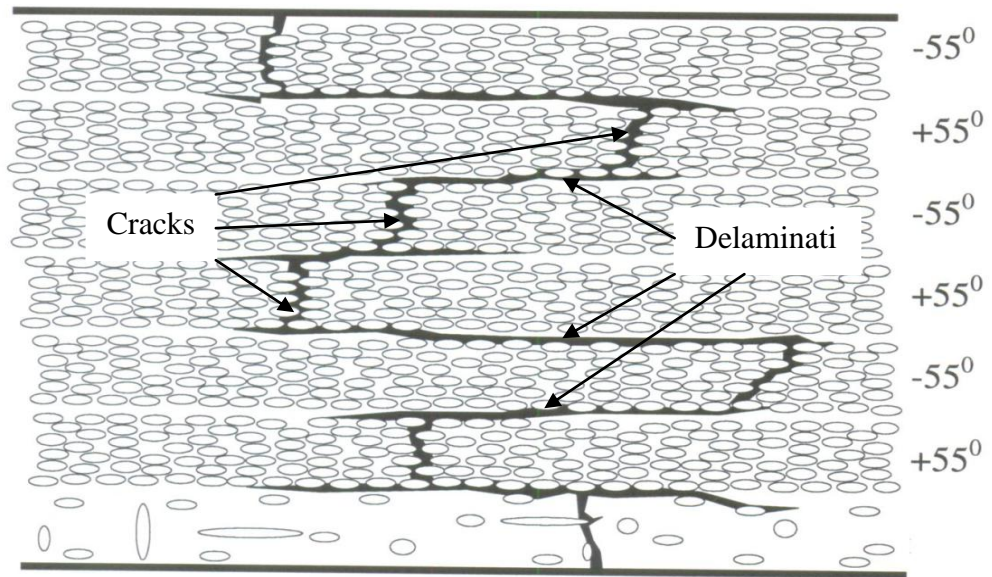


Figure 5.18. Typical crack path across the pipe wall. Cracks are initiated at the fibre/matrix interface followed by matrix cracking, and delamination between plies.

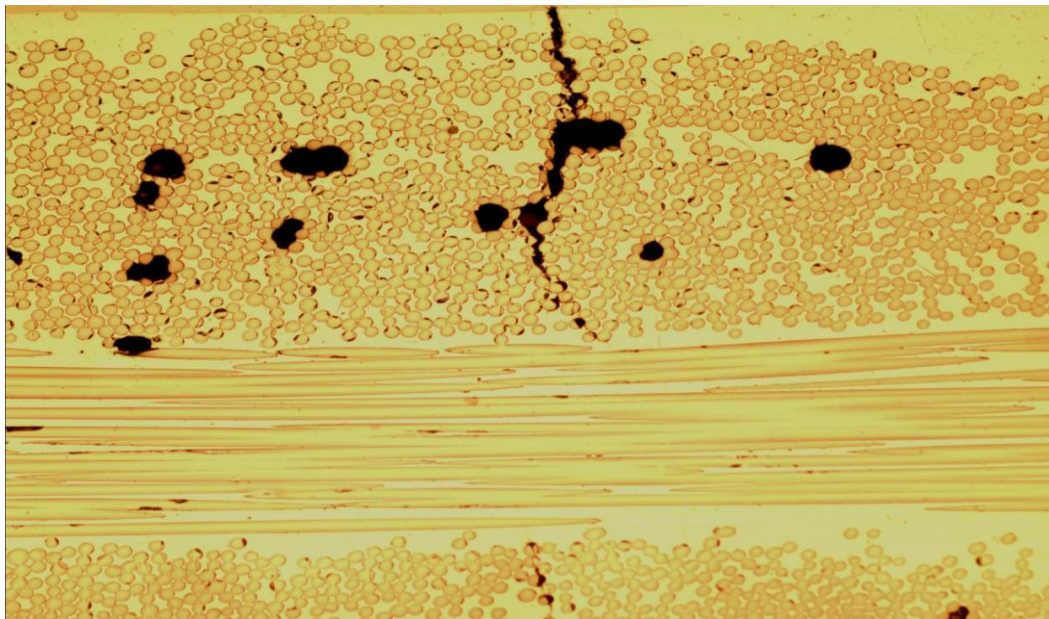


Figure 5.19. Optical micrographs of polished samples from $\pm 55^\circ$ glass/fibre epoxy pipe, with transverse microcracks initiated in the void pocket and propagated through the thickness of the lamina.

5.5 UEWS and failure envelopes

All the envelopes provided by previous researchers in the field of filament wound composite pipes refer to the final failure state. However the UEWS and final failure envelopes were found at positive internal pressure in this study of $\pm 55^\circ$ GRE pipes. The envelopes are plotted as biaxial principle stress (hoop stress versus axial stress). The slope of the line connecting the original points to each data point indicates the stress ratio of biaxial loading. These envelopes can indicate product strength under different loading conditions, and appear to be sensitive to changes in parameters such as temperatures. The collected UEWS and failure stresses are fitted in the form of envelopes showing the effects of testing at elevated temperatures.

5.5.1 UEWS and failure envelopes at room temperature

Figure 5.20 shows the UEWS and failure envelopes for the $\pm 55^\circ$ glass reinforced pipes at room temperature. These pipes were tested under six biaxial load conditions with axial-dominating and hoop-dominating loads.

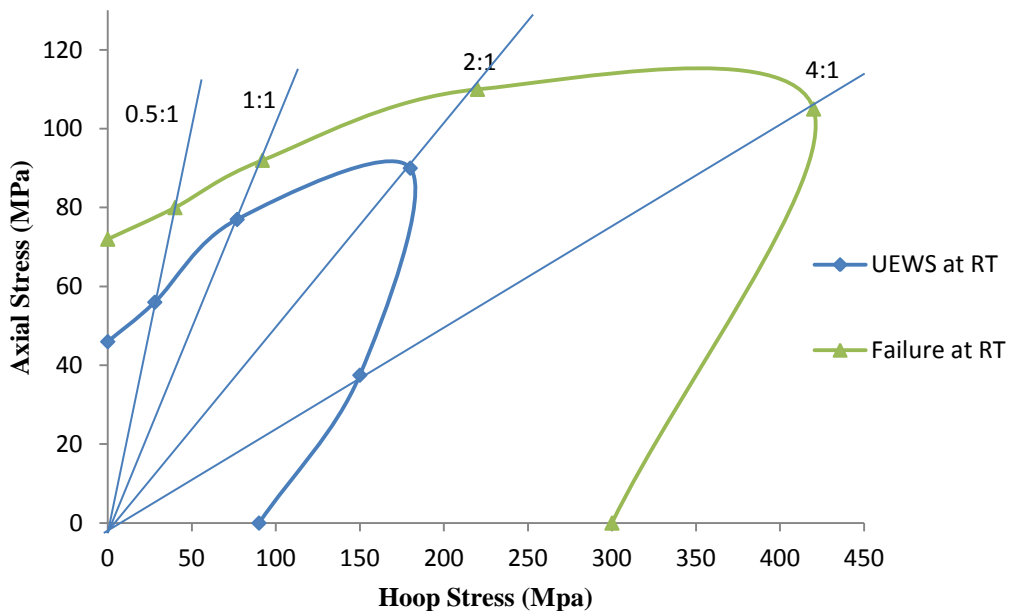


Figure 5.20. Failure envelope for $\pm 55^\circ$ glass reinforced pipes at room temperature.

The general form of the failure envelope is as might be expected, showing high strength over the full range from pure axial to pure hoop loading. The graph appears to show that the maximum strength up to weepage provided by the pipes was under the 4:1 stress ratio at about 420MPa. The pipe strength failed by 28% under pure hoop loading (300MPa) comparing with those at 4:1. Pipes dominated by axial loading are low in strength, being only 70MPa under pure axial loading. Strength then gradually increases at about 80MPa at 0.5:1, 90MPa at 1:1 and 220MPa at 2:1 stress ratio. The strength tends to increase as the hoop stress is dominate due to the deviation of principle stresses to the ideal angle of 55° to be taken by the fibres.

On the other hand, the UEWS envelope seems to be narrower than that for failure, where the highest linear relationship between stress and strain was under the 2:1 stress ratio at 180MPa. This agrees with the interpretation of the Netting analysis, where the ideal angle to carry loads at the ratio 2:1 before any observed damage is 55° . The UEWS is then reduced under the other of stress ratios to be 50MPa and 95MPa at pure axial and pure hoop loading respectively. Marked permanent deformation was also noted in the hoop dominating load sector. This might clearly indicate the presence of shear and delamination which caused final failure at high strain levels. Also, the negative strain in the axial direction is keeping the cracks close and limits matrix cracking from developing so that no weepage at earlier stages of loading.

5.5.2 UEWS and failure envelopes at 65°C

Generally at 65°C , both the failure and UEWS envelopes become narrower compared with those at room temperature. At elevated temperatures the water acts as a plasticiser which eventually lowers the glass transition temperature of the resin. This can change the matrix material into an amorphous state; a conversion influencing material stiffness by decreasing the elastic modulus. In addition, the changes in state allow the passage of liquid between the fibres even though the pipe remains intact in most cases, although eventually causing failure by weeping. However, the pipes appear to be more stable under the 2:1 stress ratio, recording UEWS of 190MPa and 220MPa for final failure. This could be due to the pipe's

ductility at elevated temperatures or the possibility residual stresses after the manufacturing and currying processes.

The UEWS at axial dominated sector failed with the range of 5-15 % at 65°C from those at room temperature, whereas, it is failed by 5-10% at the cases where hoop stress is dominated. Failure strength has a maximum failing of 15 % under the 4:1 stress ratio, and between 5 to 10% for the other stress ratios as illustrated in figure 5.21.

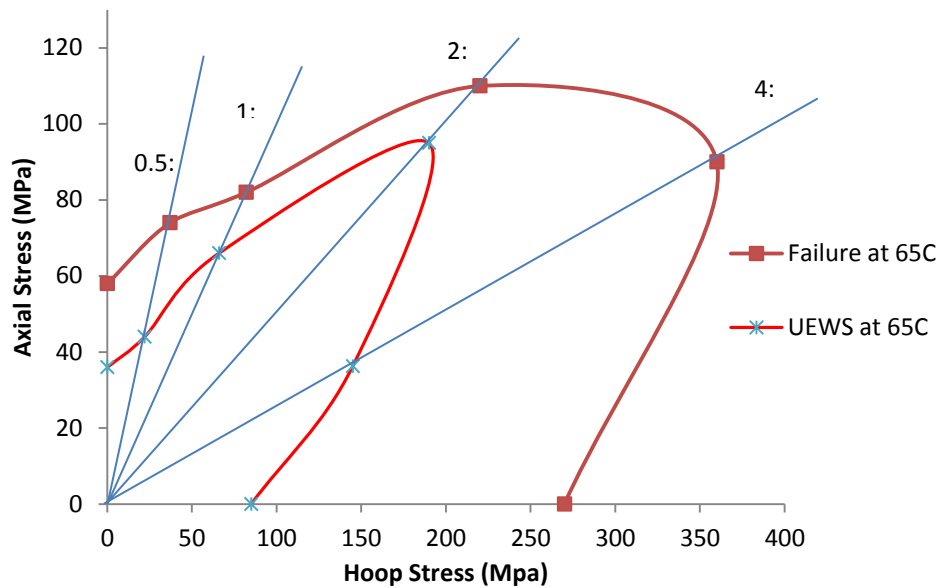


Figure 5.21. Failure envelope for $\pm 55^\circ$ glass reinforced pipes at 65°C.

5.5.3 UEWS and failure envelopes at 95°C

Glass reinforced pipes exhibited less strength over the full range of loading conditions at 95°C. This result is consistent with those previous obtained by Hale et al (2000) [11] and Saied (2004) [114]. This reduction was considerable under pure axial and pure hoop loading, recording 38MPa and 210MPa respectively. Under the 4:1 stress ratio, the pipe's strength failed by 42% compared to those at room temperature. This indicates that the pipe strength is sensitive to the elevated

temperatures due to resin mutability. The stress ratios of 0.5:1 and 1:1 led to reductions in pipe strength between 20-25%.

Although the pipe failure stresses have a reduction in all stress ratios at 95°C, this is not true of the UEWS envelope. The latter has sharp narrowing forward to the original point as shown in figure 5.22.

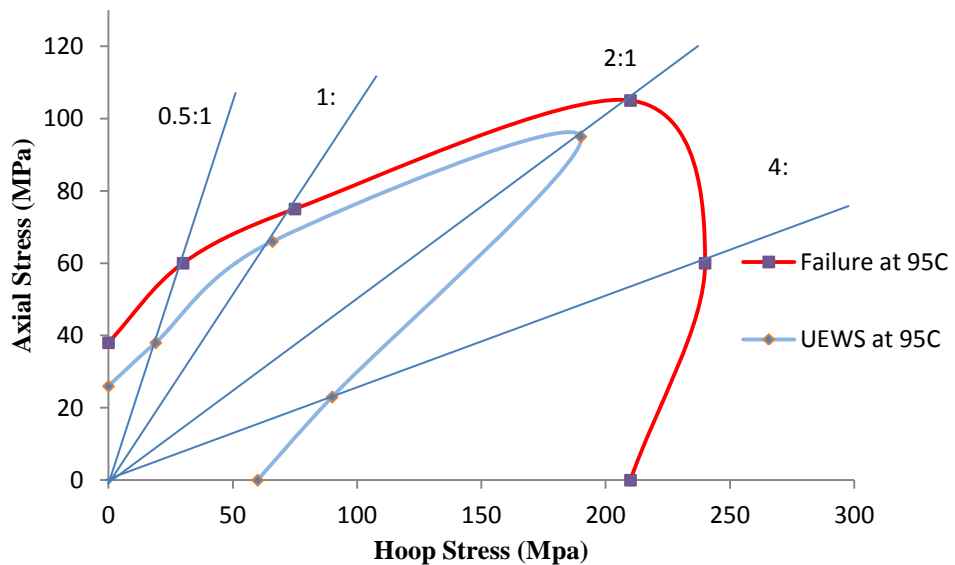


Figure 5.22. Failure envelope for $\pm 55^\circ$ glass reinforced pipes at 95°C.

The narrowing of the envelopes with increasing temperature could be due to the high susceptibility of the resin component to the water absorption effects compared to the fibre. However, the UEWS at 2:1 stress ratio remains the same as those at 65°C, possibly again due to the presence of residual stresses. Figure 5.23 summarises all of the UEWS and failure envelopes at room temperature, 65°C, and 95°C for $\pm 55^\circ$ glass fibre reinforced epoxy.

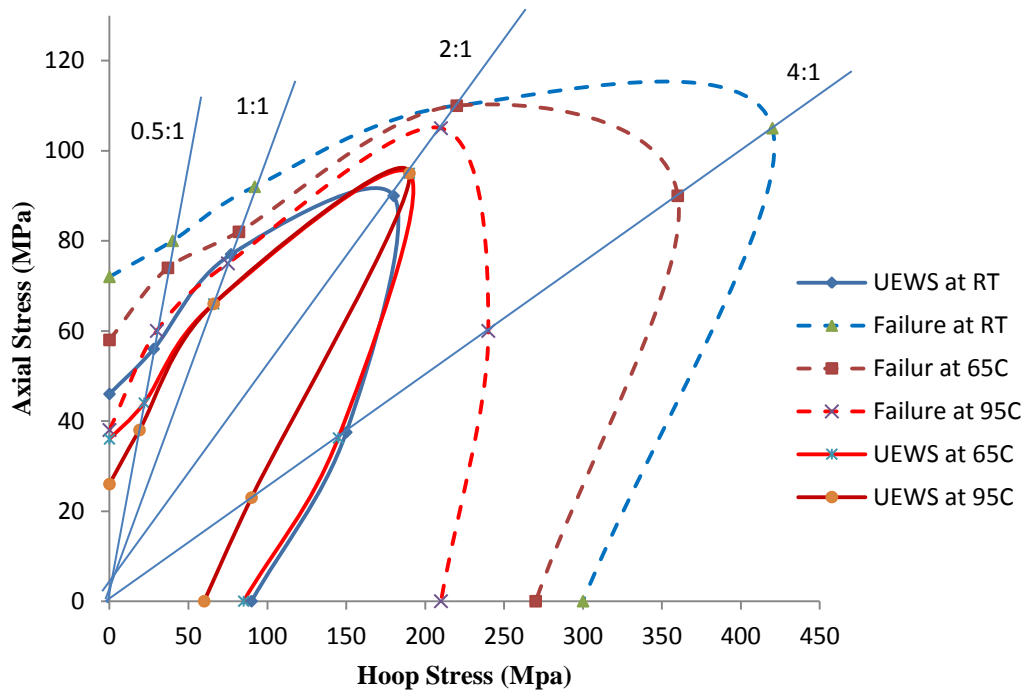


Figure 5.23. Summering of failure and UEWS envelopes for $\pm 55^\circ$ glass reinforced pipes at room temperature, 65°C and 95°C .

CHAPTER 6

ACOUSTIC EMISSION AND MODELLING

RESULTS

This chapter presents the acoustic emission observations made for the purpose of enhancing the UEWS results for $\pm 55^\circ$ glass fibre reinforced pipes. The acoustic emission tests were implemented under three different loading modes, pure hydrostatic pressure, pure axial and pure hoop loading. Furthermore, modelling results showing stress-strain relationships, elastic modulus degradation due to increasing matrix crack density, and failure envelopes are discussed in this chapter.

6.1 Acoustic emission (AE) observation

The main purpose of implementing acoustic emission examinations was to devise a methodology for assessing the detected damage development in the GRE pipes during the UEWS tests. The AE technique is used extensively in monitoring damage evolution in composite materials and has been accepted as a quality control tool for composite structures. This is because AE has the ability of providing reliable information of damage initiation and accumulation.

Most failures encountered in test samples involved either transverse or shear stress, because the strength of the laminate in the direction of fibres is relatively high. The UEWS tests were implemented in the presence of AE equipment under three different conditions. These were:

Pure axial loading 1:0 (mode II), giving a negative transverse to shear ratio.

Pure internal pressure 2:1 biaxial loading (mode I) with a high transverse to shear ratio.

Pure hoop loading 0:1 (mode IV) giving a relatively low shear to transverse ratio.

Two sensors were attached on opposite positions one-third of the pipe length from each end. Both channels were supplied with high pass filters of 100 KHz, and the amplifiers were set with a 40dB threshold level. In this investigation the classical parameters of acoustic emission were plotted, which are:

- AE counts vs. time and wall stress.
- AE absolute energy vs. time vs. wall stress.
- AE signal amplitude vs. time for each sensor.
- AE absolute dB vs. position vs. channel.
- AE duration vs. amplitude.
- AE events vs. time

6.1.1 AE results of GRE pipes under pure internal pressure

In this test the pipe ends were both sealed with steel end caps which were not constrained from movement resulting in the hoop stress being twice the axial stress. The pressure was gradually increased up to the cycling test pressure (CTP1), was held there for one minute and then released for another minute. This was repeated ten times and then the cycle test pressure was increased to the level of the subsequent cycle group, as explained in chapter three. The distinction between cycle groups was manually marked in order to analyse independently the AE signals for each group.

Figure 6.1 illustrates the AE counts as a function of both time (seconds) and pipe wall stress in MPa. The loading was halted at a stress level of 223MPa, when intensive leakage made it difficult for any further increase in pressure to be applied. The amplifier sensitivity was set at 40dB, and therefore any AE signals lower than 40dB were filtered out.

AE events started at quite an early stage of loading, suggesting that matrix microcracking took place as a result of the stress being increasingly taken up by the fibre reinforcement. These events increased up to the corresponding wall stress of 74MPa and then stabilized with negligible subsequent increase of AE event rate detected, indicating that a constant rate of damage occurred up to the eighth cycle at a wall stress of 149MPa. At this stress level progressive development and a sudden increase in acoustic events were noted. It is likely that, as load increases transverse

cracking and delamination have initiated. After that there were only slight decreases in AE events during crack propagation compared to those generated due to their initiation. At a wall stress of 204MPa an increase in acoustic events indicated that debonding was occurring opening a pathway for liquid to weep.

This is also clearly noted in figure 6.2 when cumulative energy is plotted against time and wall stress (MPa). A noticeable release of energy was observed starting at 74MPa, the “first knee” due to matrix microcracks, whereas a significant release being initiated at the eighth cycle group (149MPa), the “second knee”. At this stress level a massive amounts of energy continued to be released due to increases in crack length and number parallel with delamination. At 204MPa the “third knee” indicates debonding occurred and makes pathway for water to weep.

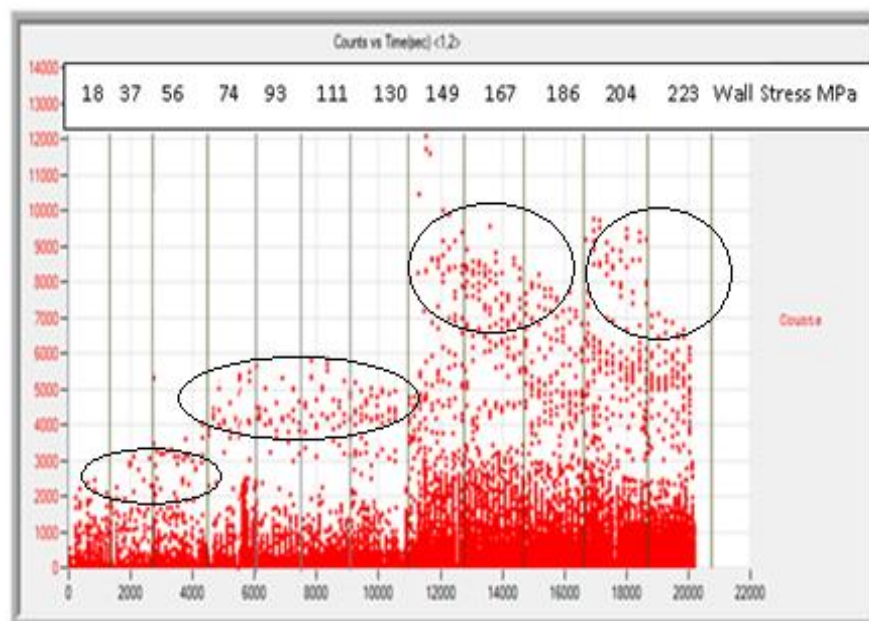


Figure 6.1. AE counts vs. time and hoop stress, for $\pm 55^\circ$ GRE pipes under 2:1 stress ratio.

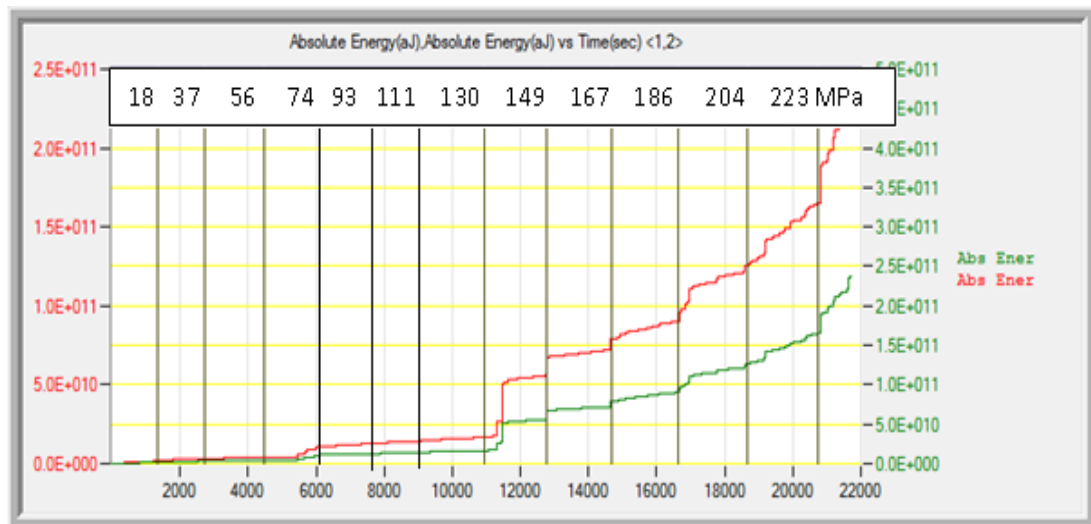
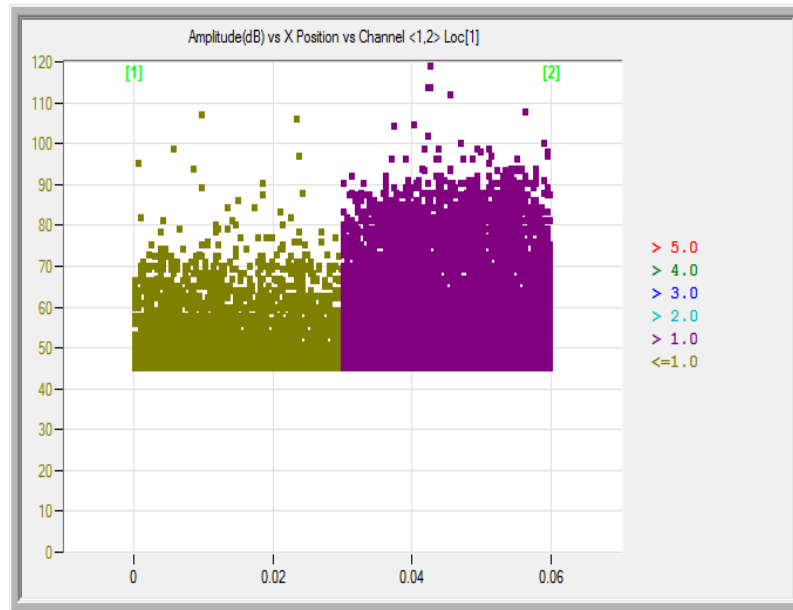
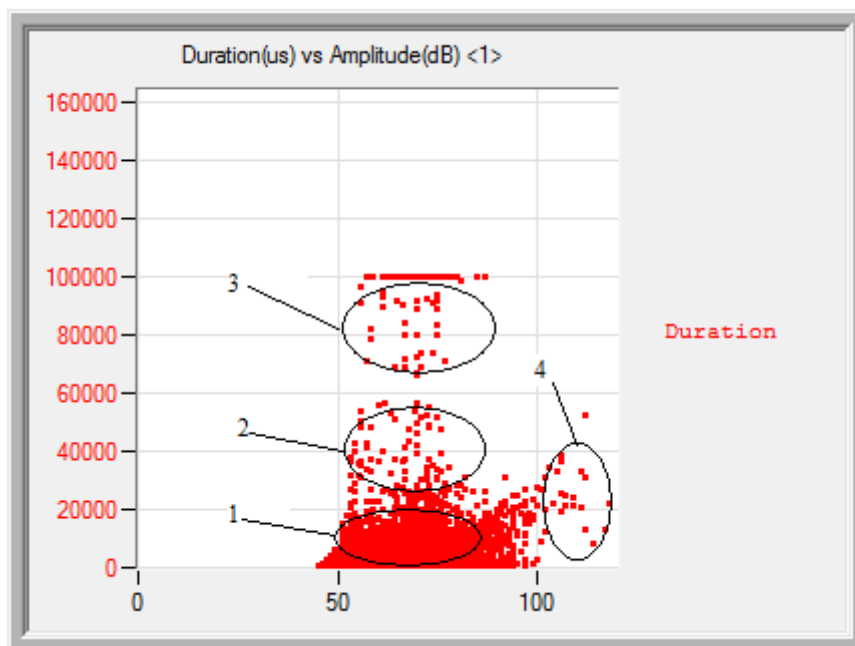


Figure 6.2. AE cumulative energy release rate vs. time and wall stress, for $\pm 55^\circ$ GRE pipes under 2:1 stress ratio.

Figure 6.3(a) suggests that the failure is taking place closer to channel 2 probe. Most of the acoustic emission was low duration events between 40db and 80db amplitude (zone 1 in Figure 6.3(b)). Such behaviour is normally associated with matrix cracking and indicates that matrix cracking was taking place throughout the test. There are also three other distinct zones of events evident. Zones 2 and 3 are intermediate and high duration events with amplitude between 50db and 80db. High duration events are normally associated with friction and therefore could arise from fibre pull-out. Intermediate duration events could be attributed to delamination. Zone 4 is characterised by high amplitude low duration events which is associated with debonding and the possible of presence of fibre fracture.



(a)



(b)

Figure 6.3. AE absolute dB versus position of channels 1 and 2 (a), and AE duration versus amplitude dB (b) for $\pm 55^\circ$ GRE pipes under 2:1 stress ratio.

Figure 6.4 is a record of the AE amplitude vs time, from both channels, for the pipe sample tested to failure. The plot shows that up to 130MPa there is a low amplitude activity associated with matrix cracking. There is also a small burst of activity at around 74MPa of events with amplitude between 60db and 70db that could be attributed to matrix microcracking. Above 130MPa there is a higher amount of AE activity and a distinct band of events is recorded between 70db and 90db amplitude. This suggests that a second failure mechanism is developing, in addition to matrix cracking, which seems to involve delamination and debonding. There are some events of high amplitude (100db) that are normally associated with fibre fracture. Undoubtedly some fibre fracture is taking place but this is very limited. The latter statement is supported by the fact that the failure of the pipe took place by weepage and not bursting which would have involved substantial fibre failures.

More events noted in figure 6.5 from the tenth cycle group up to weepage indicated that significant debonding in the fibre/matrix interface took place. This debonding occurred alongside rapid transverse cracking in the later stages of loading, eventually resulting in weepage.

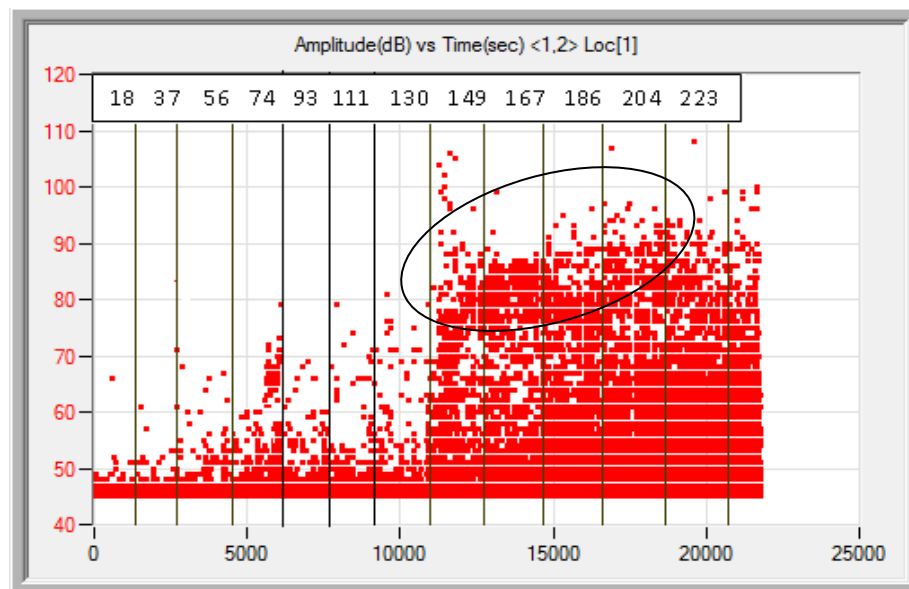


Figure 6.4. Signal amplitude vs. time for the $\pm 55^{\circ}$ GRE pipe under 2:1 hoop to axial stress ratio.

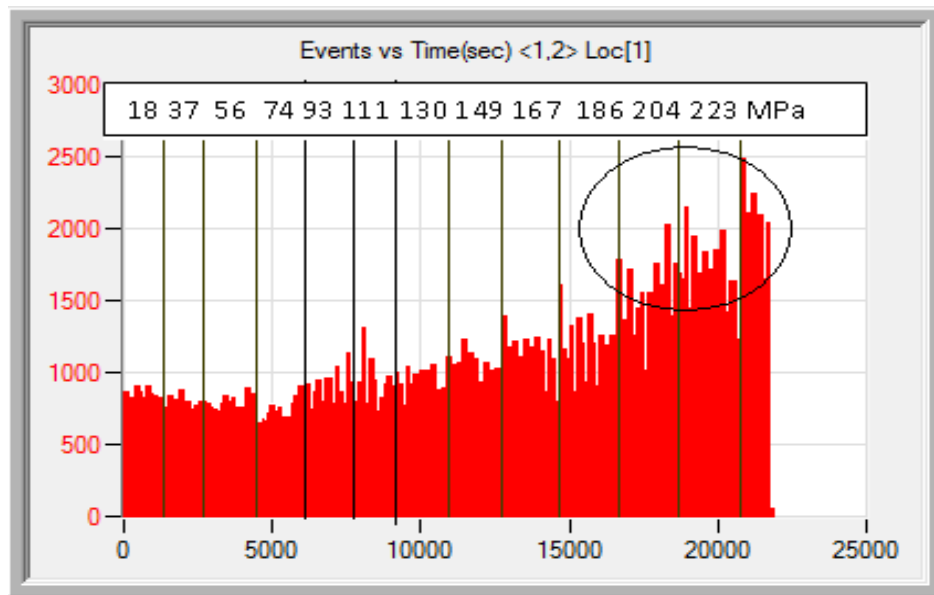


Figure 6.5. AE events vs. time for the $\pm 55^\circ$ GRE pipe under 2:1 hoop to axial stress ratio.

6.1.2 AE results for GRE pipes under pure axial loading

In this test the amplifier was set with a 20dB threshold in order to increase the sensitivity of the AE signal detection. Figure 6.6 shows the AE signal counts versus time for the $\pm 55^\circ$ GRE pipe under pure axial loading. The counts are also represented as a function of cycle groups and axial stress. AE events appeared from the first load condition from stress release up to 35MPa. Steady damage growth then occurred afterwards indicates matrix microcracks are growth with about constant rate up to about 52MPa where a noticeable increment in the AE events was recorded. This was found to be compatible with the UEWS level and indicates the presence of delamination. A massive increase then occurred in the final stage of loading due to debonding and intensive fibre fracture. As discussed in chapter five, massive debonding is followed by macro helical cracks in pipes under pure axial loading.

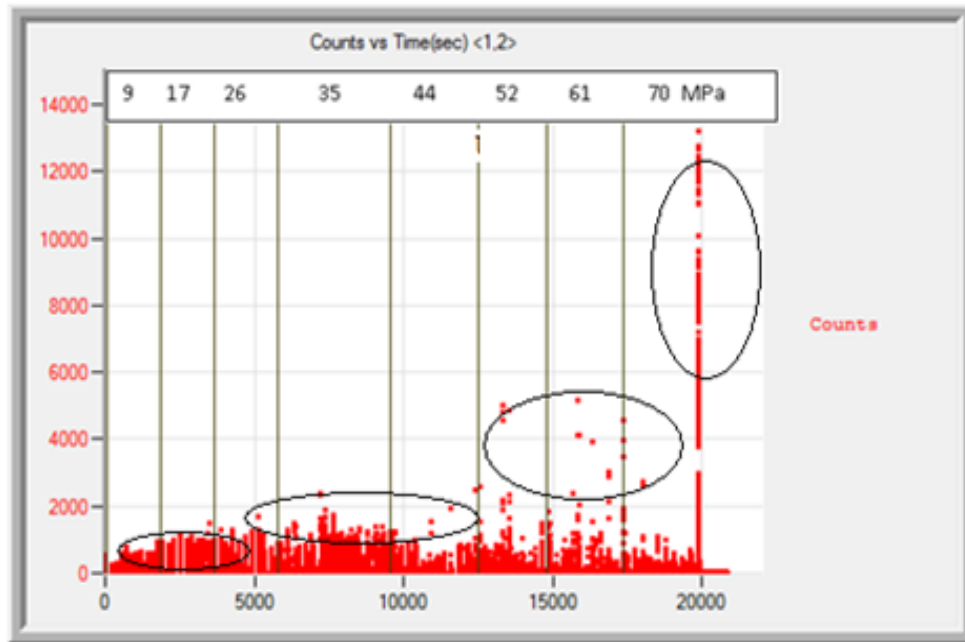


Figure 6.6. AE counts vs. time and axial stress, for $\pm 55^\circ$ GRE pipes under pure axial loading.

Figure 6.7 shows the cumulative absolute energy released as a function of time and wall stress. It can be clearly noted that the first recognisable release of energy was at the load corresponding to 35MPa. This can also be clearly seen in figure 6.8, when there is more AE activity between 50-80dB from the fourth cycle onwards. At stress level of 52MPa delamination may occurred with AE amplitude between 70 to 90dB, and then debonding took place for short time and eventually caused fibre fracture.

Based on all these results, it seems that pipe failure might be associated with matrix microcracking, delamination and then debonding followed by fibre breakage. Matrix microcracking first appeared to cause energy release increments from the fourth cycle group at (35MPa). Then the “first knee” occurred due to delamination at the sixth cycle, corresponding to the UEWS at 52MPa.

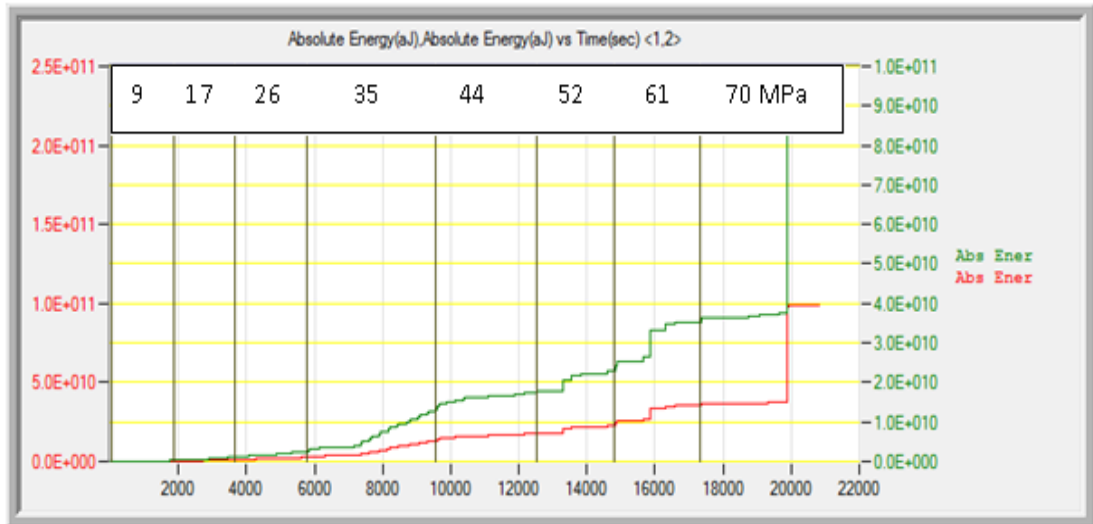


Figure 6.7. AE energy release rate vs. time and hoop stress, for $\pm 55^\circ$ GRE pipes under pure axial ratio.

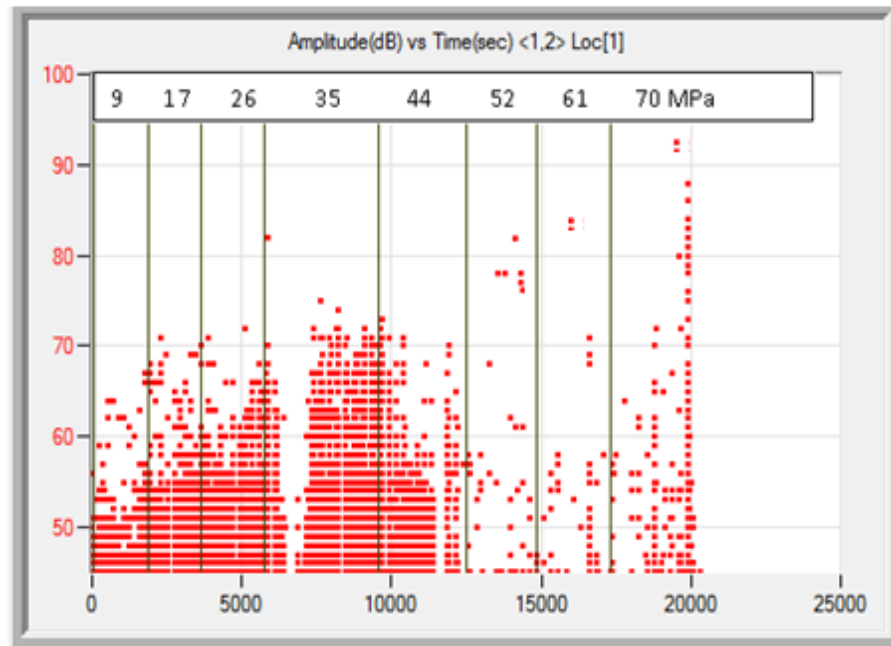
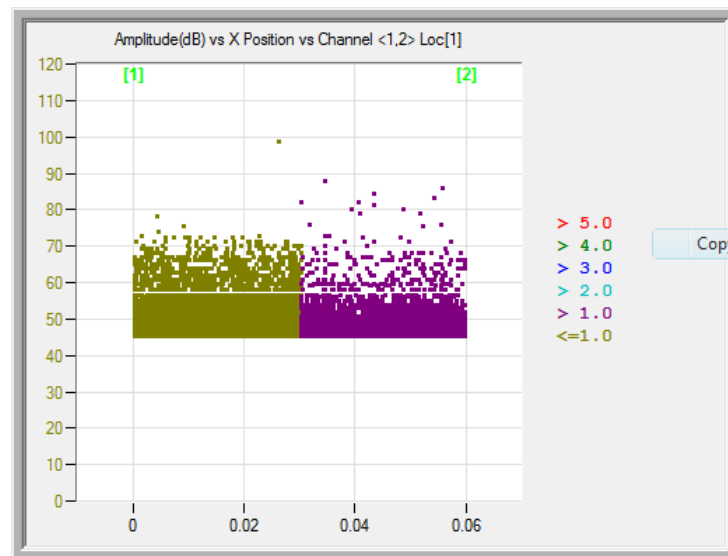
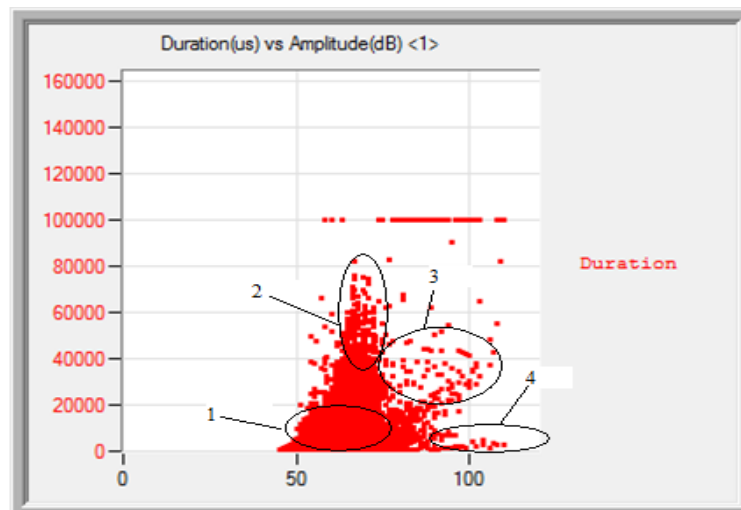


Figure 6.8. Shows the signal amplitude vs. time for the $\pm 55^\circ$ GRE pipe under pure axial loading.

Figure 6.9 shows the AE absolute dB versus position for each channel (a), and AE duration versus amplitude dB (b). Figure 6.9 (a) suggests that the failure is taking place closer to channel 2 probe. Acoustic emission with low duration events between 40db and 80db amplitude (zone 1 in Figure 6.9(b)) was due to matrix cracking. Zones 2 and 3 are intermediate and high duration events with amplitude between 50db and 90db due to delamination and debonding respectively.



(a)



(b)

Figure 6.9. AE absolute dB versus position of channel 1 and 2 (a), AE duration versus amplitude dB (b) for $\pm 55^\circ$ GRE pipes under pure axial loading.

Zone 4 is characterised by high amplitude low duration events which is associated with fibre fracture in short period of time.

Figure 6.10 shows more events occurred in the region where matrix cracks initiated and propagated and then fewer events were noted in the delamination, debonding and fibre fracture stages to indicate that the latter three sequences occurred in short period.

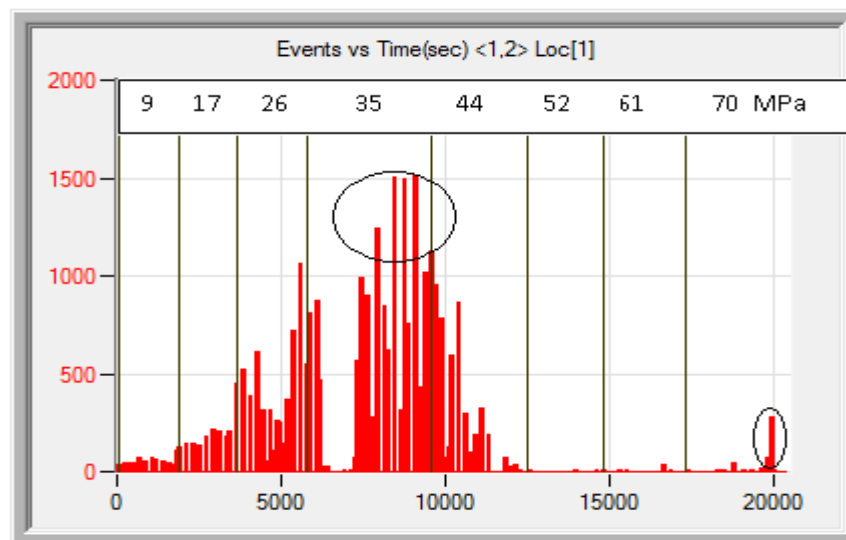


Figure 6.10. AE events vs. time for the $\pm 55^{\circ}$ GRE pipe under pure axial loading.

6.1.3 AE results for GRE pipes under pure hoop loading

A standard arrangement was prepared to conduct the UEWS test under pure hoop loading as mentioned in chapter 2. The AE equipment was attached to the pipe wall and AE signals were recorded for damage evaluation. The pipe failed at a hoop stress of about 300MPa due to buckling, which caused a stress concentration near to the end fitting. With the first cycle loading the hoop stress was 36MPa and shear stress generated along fibres. According to Puck's theory [115], the shear stress at this point would be about 20MPa, which is quite far away from the critical value of 60MPa to cause delamination; whereas transverse stress was only 10MPa which is

also below the critical transverse stress. As a result final failure was associated with the interaction between these stresses and was dominated by shear.

Figure 6.11 shows the AE signal counts versus time and wall stress for $\pm 55^\circ$ GRE pipes. AE signals started from the beginning with a random distribution, which indicates that energy was released possibly due to matrix deformation. These events appeared from the first loading and continued up to the level when buckling started to affect the bonding media. At this point the “first knee” was recognised in the absolute energy released, as demonstrated in figure 6.12. The cumulative energy then smoothly increased due to delamination and debonding at amplitudes between 50-100dB as shown in figure 6.13.

This clearly indicates that final failure was not associated with the same sequence of damage as in the cases of 2:1 biaxial loading and pure axial loading. Here complete debonding occurred at a wall stress of 250MPa and then continued until the pipe suddenly burs near to the end fittings.

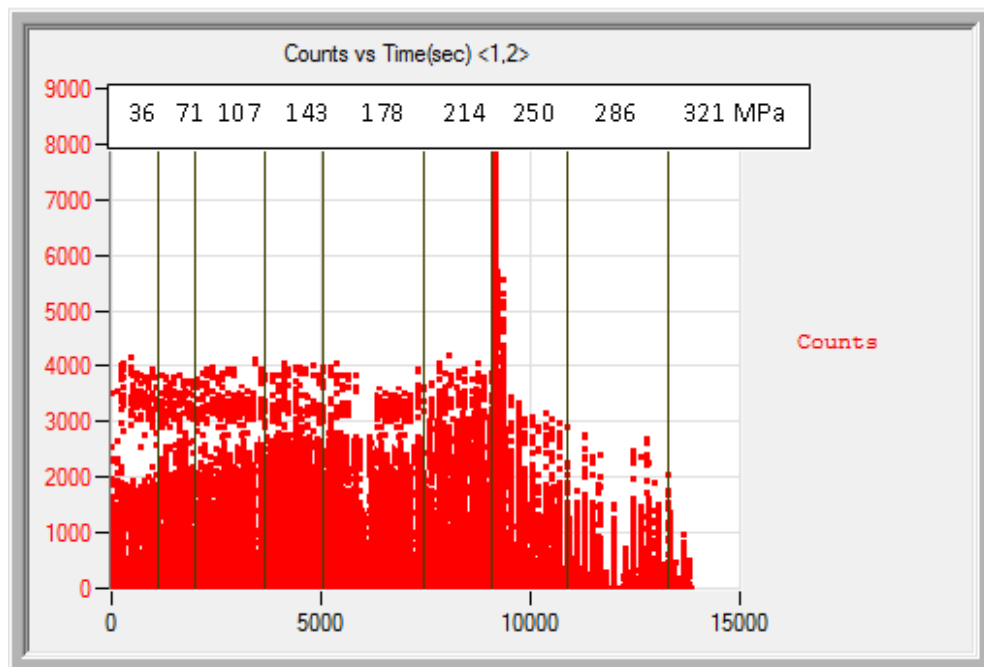


Figure 6.11. AE counts vs. time and axial stress, for $\pm 55^\circ$ GRE pipes under pure hoop loading.

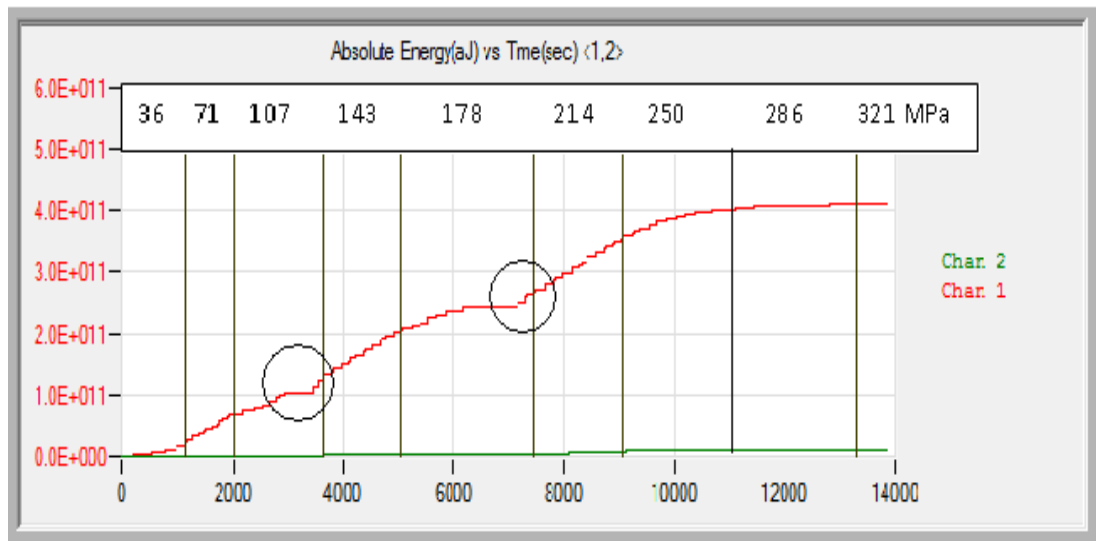


Figure 6.12. AE energy release rate vs. time and hoop stress, for $\pm 55^\circ$ GRE pipes under pure hoop ratio.

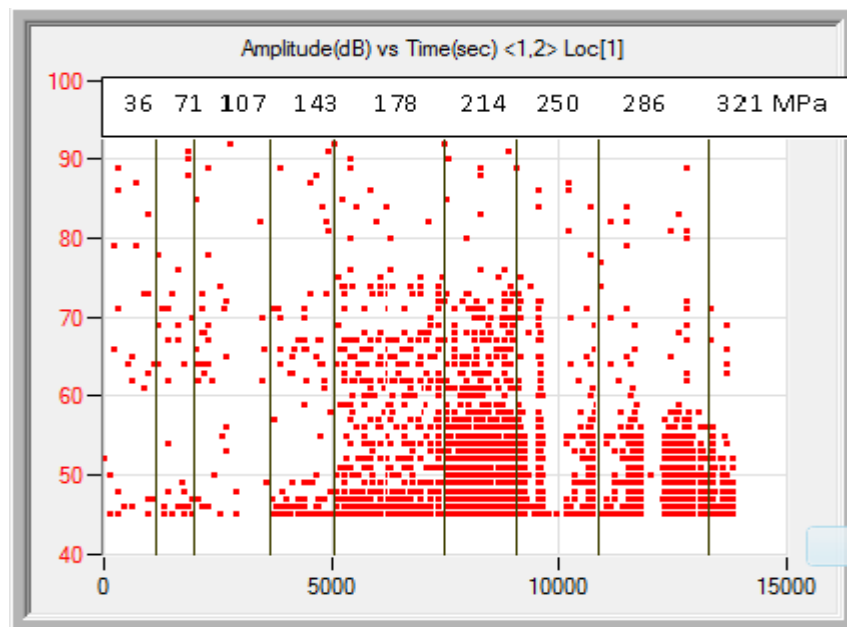
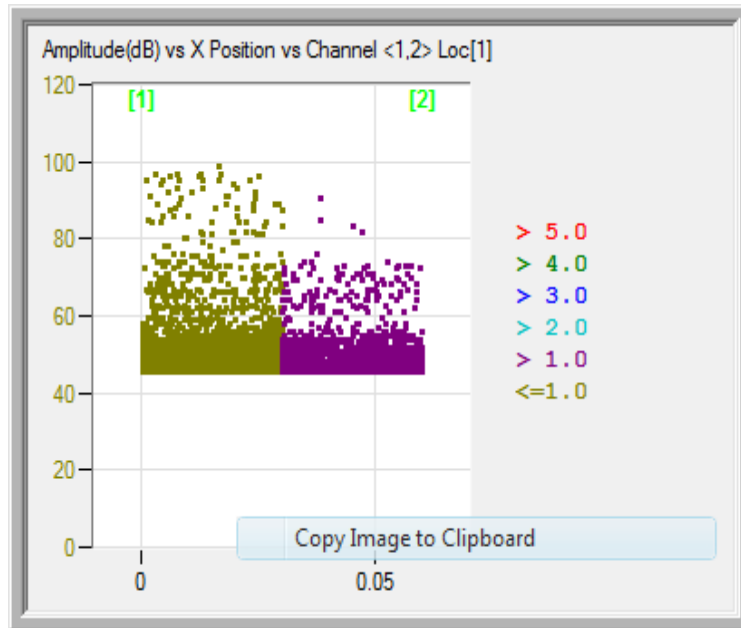


Figure 6.13. AE signal amplitude vs. time for the $\pm 55^\circ$ GRE pipe under pure hoop loading.

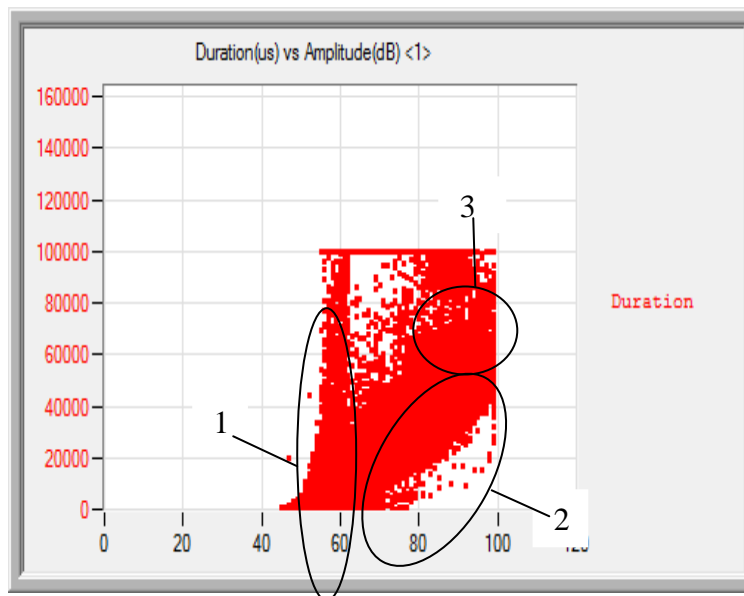
Buckling was followed by the audible sound of fibre fracture at the outer surface, particularly in areas where there was a greater stress concentration corresponding to wall stress of 250MPa. At this point the counts recorded their highest values during the test, exceeding 8000 counts, and then debonding continued smoothly due to fatigue loading which produced crumbling in the resin. Subsequently, fibres in deeper layers failed at low loads, giving rise to low amplitude AE events, and this continued until liquid found a pathway to leak through the local crack.

Figure 6.14 shows the AE amplitude versus position for each channel (a), and the AE duration versus amplitude dB (b). Figure 6.14 (a) appeared to show that the failure is taking place closer to channel 1 probe. Acoustic emission with low duration events between 40db and 60dB amplitude (zone 1 in Figure 6.14(b)) was likely due to matrix deformation. Zone 2 has acoustic emission duration events between 60dB and 100dB due to delamination and local debonding in the area where stresses were grater concentrated. High duration in zone 3 was possibly due to bursting and fibre fracture.

In figure 6.15, more events were recorded at a hoop stress of 250MPa due to debonding in the outer surface of the pipe, and then less activity appeared as the test progressed. At a hoop stress of 286MPa further events occurred due to fibre breakage as a result of high strain in the outer surface of the pipe.



(a)



(b)

Figure 6.14. AE absolute dB versus position of channel 1 and 2(a), AE duration versus amplitude dB (b) for $\pm 55^\circ$ GRE pipes under pure hoop loading.

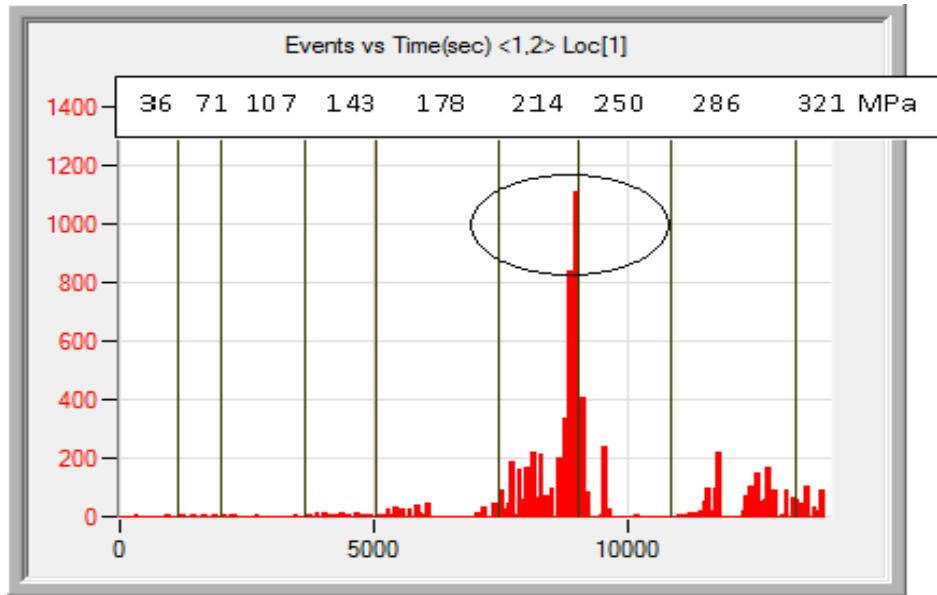


Figure 6.15. AE events vs. time for the $\pm 55^\circ$ GRE pipe under pure hoop loading.

6.2 Modelling results

6.2.1 Prediction of pipe elastic modulus

The axial and hoop modulus of the pipe can be estimated from the combination of fibre and matrix properties. The implementation of equations 4.3-4.20 (chapter 4) in Excel based on the initial values of fibre and matrix modulus was the way to work out value of each modulus. The following describe the fibre and epoxy constants that used to produce $\pm 55^\circ$ filament wound composite pipes. These were taken from FPI, Wavistrong engineering guide.

$$E_f = 72 \text{ GPa}, \quad E_m = 3.6 \text{ GPa}, \quad V_f = 0.59,$$

$$\nu_f = 0.2, \quad \nu_m = 0.4, \quad \phi = 55^\circ$$

Therefore, the elastic modulus in the fibre and transverse direction are calculated to be:

$$E_1 = 44.5 \text{ GPa}$$

$$E_2 = 14 \text{ GPa}$$

$$V_{12} = 0.282$$

$$V_{21} = 0.083$$

$$G_{12} = 4.33 \text{ GPa}$$

The hoop and elastic modulus are then determined from transformation matrix, which gives:

$$E_H = 18.5 \text{ GPa}$$

$$E_A = 12 \text{ GPa}$$

$$V_{AH} = 0.40$$

$$V_{HA} = 0.68$$

The results were then fitted with variable winding angles in order to represent their effects on the pipe properties in the axial and hoop directions. A decline in axial elastic modulus and an increase in hoop elastic modulus can be clearly observed when the winding angle deviates from 0° to 90° . Figure 6.16 shows the changes in both the axial and hoop elastic modulus with winding angle ϕ .

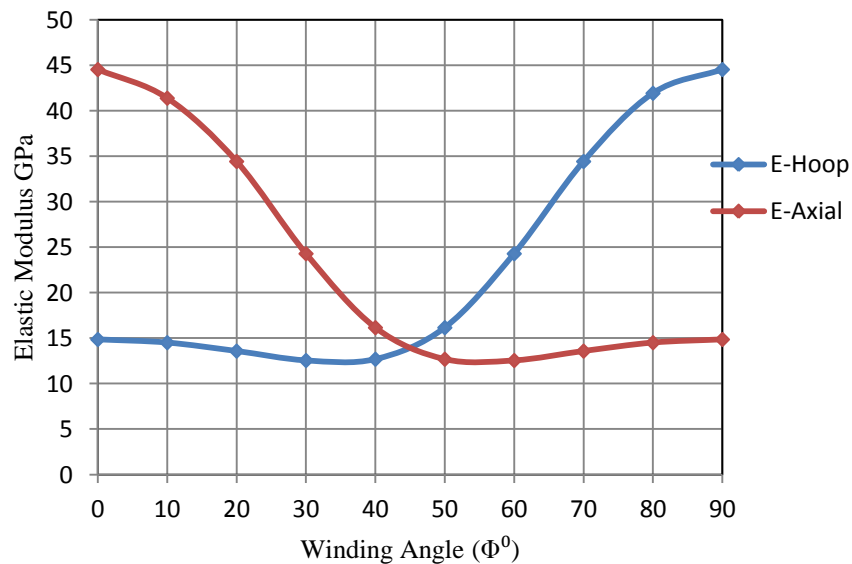


Figure 6.16. The effect of winding angle ϕ on axial and hoop elastic modulus.

From this graph it can also be noted that the values of elastic modulus in both directions have the same values at a winding angle of 45°.

6.2.2 The UEWS test based on Miner's law sum

Figure 6.17 shows the accumulation of the Miner's Law sum during the UEWS test. A comparison of the two terms in equation 4.25 (chapter 4) shows that the cyclic effect greatly exceeds the contribution from static fatigue. Indeed the curve calculated for the cyclic element alone in this case overlaps the curve obtained when considering both effects. This conclusion is not surprising when it is borne in mind that the UEWS test takes only few hours to perform, while ASTM2992b takes more than a year. This means that, if the UEWS was used for qualification purposes, supporting information would be needed about the equivalence between damage produced by cyclic or static fatigue. It is also important to note that the point at which the sum begins to differ significantly from zero, when it exceeds 1%, say, corresponds closely to the UEWS measured previously. It can therefore be argued that the UEWS test is, in effect, a confirmation of the damage growth characteristics of GRE by means of a cyclic test.

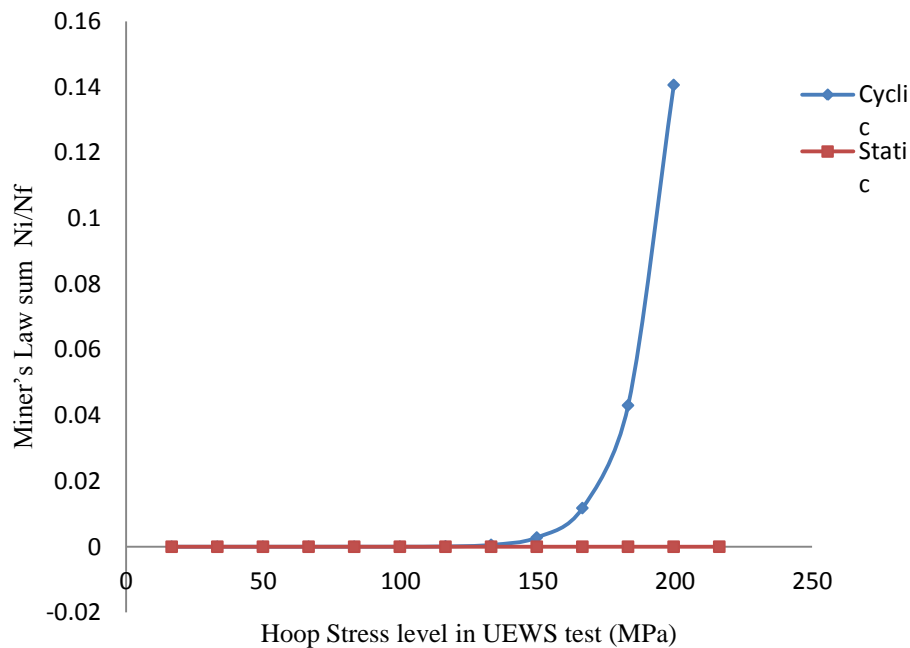


Figure 6.17. Miner's Law sum at each hoop stress level in UEWS test.

6.2.3 Effects of crack density on pipe properties

Some results are shown in figure 6.18, with the model results normalised by dividing each elastic constant by its initial non-cracked value. It can be seen that the axial Young's modulus declines most rapidly with increasing crack density, while the hoop modulus declines just a little less. The in-plane shear modulus, which might be expected to be less influenced by the presence of cracks, declines less, while the Poisson's ratio varies only a little. Weepage probably occurs at a relatively low crack density value in pipe laminates, compared with the maximum possible level, in the range 0.3-0.5. The numerical model for the data in figure 6.19 suggests that crack density is less than about 0.4, where both quantities can be described by linear approximations as in equations 4.32, 4.33 (chapter 4).

The predicted crack density of 0.4 is less than those predicted by Tao and Sun (1996) [116], but agrees with those predicted by Saied (2004) [114]. The crack density is depends on the transverse stress in the ply. After initiation cracks then propagate in terms of crack size and number, when the transverse stress exceeds the resin strength.

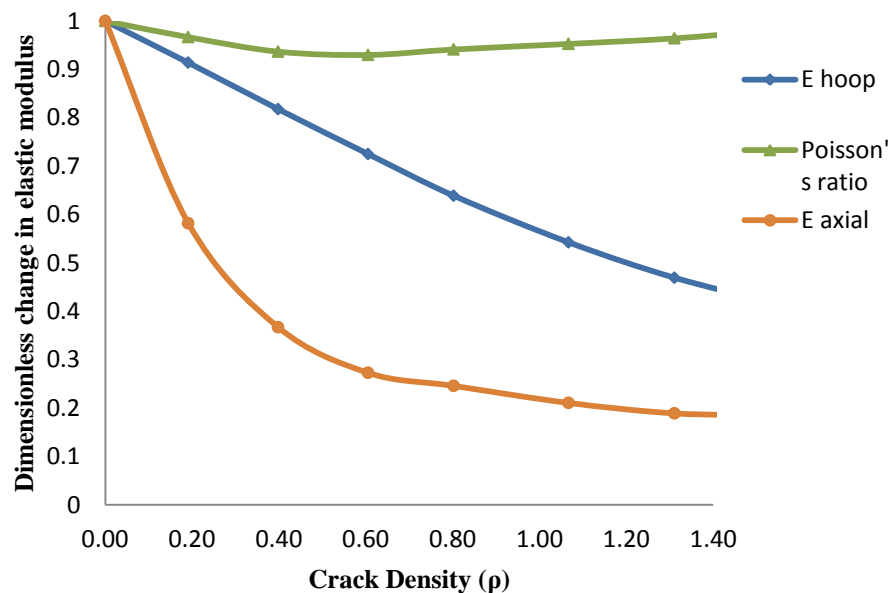


Figure 6.18. Dimensionless change in elastic constants vs. crack density for an angle ply pipe laminate, calculated from the model of Gudmundson and Zhang.

This model works in cases where axial load dominated, since the failure was clearly due to mode I (weepage). Whereas in samples under hoop dominated loads no matrix microcracks were observed and the failure occurred as a result of delamination due to stress concentration near to the pipe end. In this case the observed negative strain in the axial direction tends to close the cracks rather than propagate them.

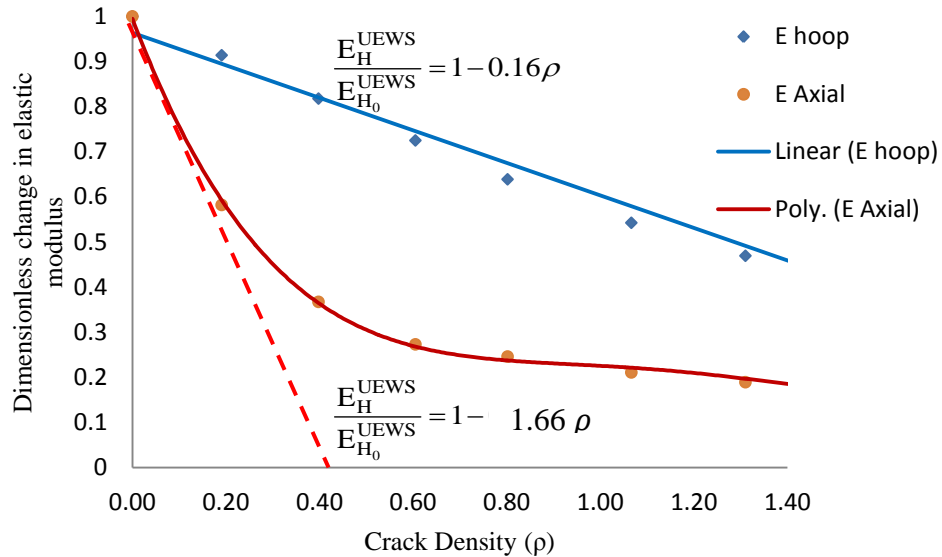


Figure 6.19. Dimensionless change in ‘hydrostatic/axial modulus’ (hoop stress divided by axial strain) and ‘hydrostatic/ hoop modulus’ (hoop stress divided by hoop strain) with increasing crack density. Calculated from the results of Gudmudson and Zhang for angle ply laminate.

Figure 6.20 shows the dimensionless change in elastic modulus as the UEWS test progressed under the 2:1 stress ratio at 20°C. A clear compatible between elastic modulus degradation and the UEWS was observed. Both axial and hoop elastic modulus declined from the original value and found compatible with the UEWS. This indicates that a serious damage of delamination started to initiate and propagate from this level, reaching the critical crack density to cause weepage at 220MPa. The graph also shows that the axial elastic modulus declines more than those in the hoop direction. At state of weepage the axial elastic modulus failed by 41% compared with virgin condition, whereas hoop elastic modulus has regression with only 17% from those in virgin condition.

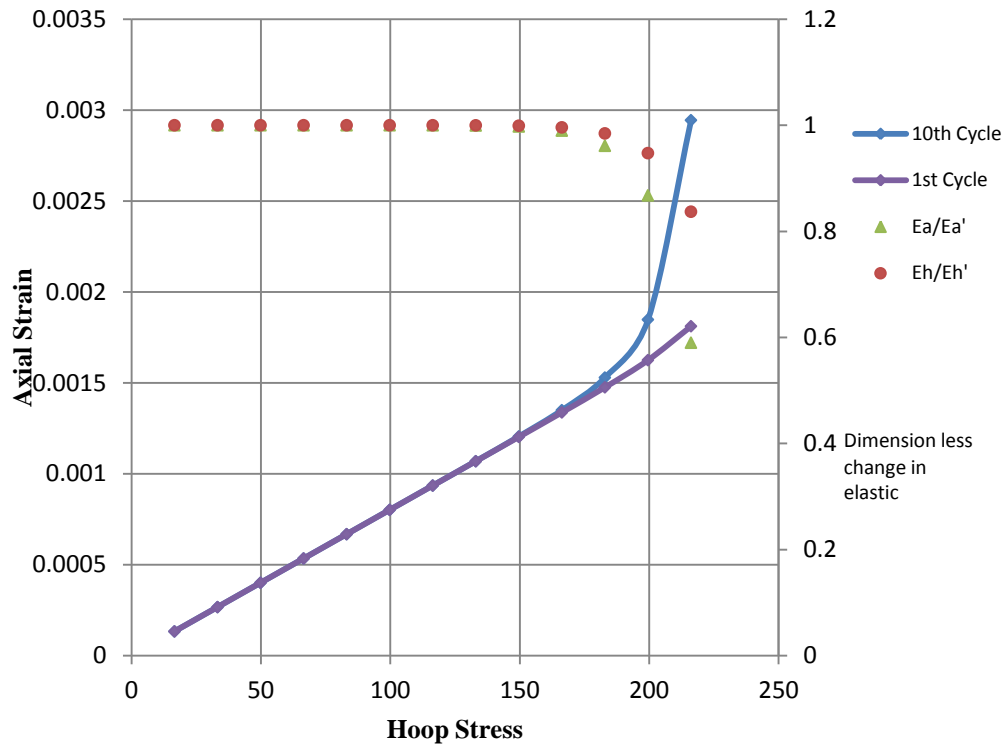


Figure 6.20. Dimension less change in elastic modulus as the UEWS test progressed under 2:1 stress ratio at room temperature.

6.2.4 Stress-strain behaviour

The stress-strain curves were predicted from the Miner's Law sum by implementing equations 4.26-4.35 (chapter 4). The predicted 1st and 10th cycle curves are initially linear and then non-linear behaviour is exhibited up to final failure. The results shown in figures 6.21, 6.22 and 6.23 for a k value of 2.5 at 20°C, 65°C and 95°C indicate that the proposed model does indeed offer the possibility of modelling changes in elastic properties in terms of both crack growth and Miner's Law. This can be seen to agree well with the experimental results.

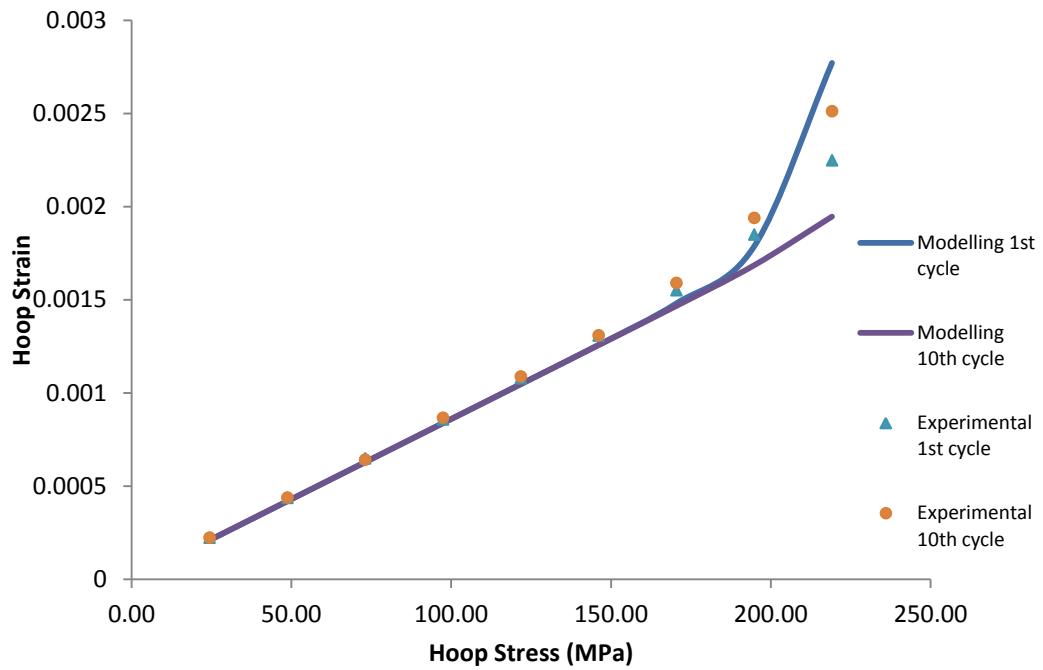


Figure 6.21. Miner's Law-based simulation of strain response in UEWS test at room temperature.

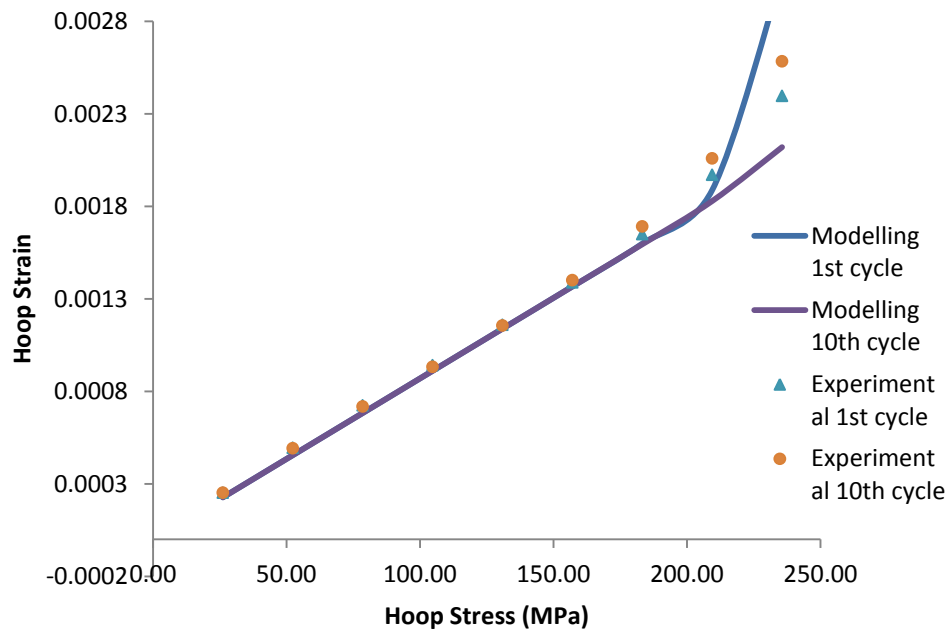


Figure 6.22. Miner's Law-based simulation of strain response in UEWS test at 65°C.

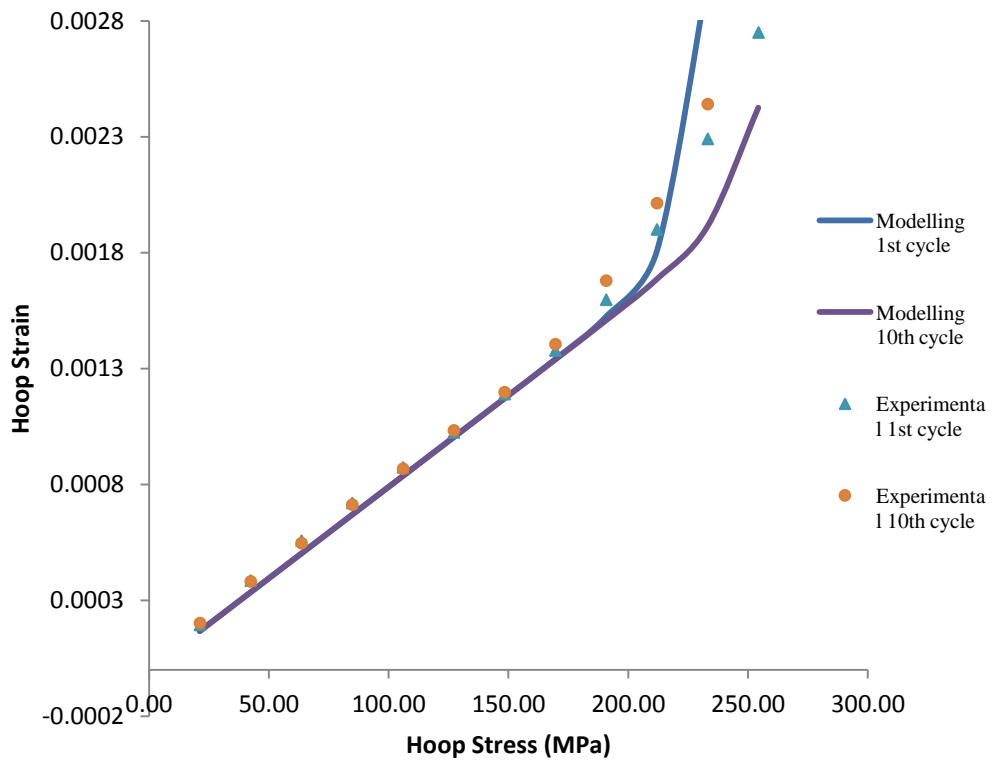


Figure 6.23. Miner's Law-based simulation of strain response in UEWS test at 95°C.

6.2.5 Modelling of the UEWS and failure envelopes

Figures 6.24, 6.25 and 6.26 shows the 'failure envelopes' produced by applying model A to the measured UEWS and failure data at different stress ratios and at room temperature, 65°C and 95°C respectively. These envelopes were modelled by the implementation of the empirical equation 4.36, which involves the interactions between σ_1 and σ_2 , and σ_2 with τ_{12} . A good agreement with the experimental data was noted over the range of load and environmental conditions.

The ratio of UEWS to failure stress has been determined in order to predict the UEWS envelope by scaling down the failure envelope. This ratio seems to be invariant for each stress condition. Table 6.1 listed UEWS points and failure stress levels as well as the UEWS to failure ratio at room temperature.

Table 6.1 listed UEWS points, failure stress levels and UEWS to failure ratio at room temperature

Stress ratio	UEWS	Failure	UEWS/Failure
1:0	95	305	0.31
4:1	160	410	0.39
2:1	180	220	0.77
1:1	75	95	0.75
0.5:1	31	40	0.73
1:0	52	72	0.7

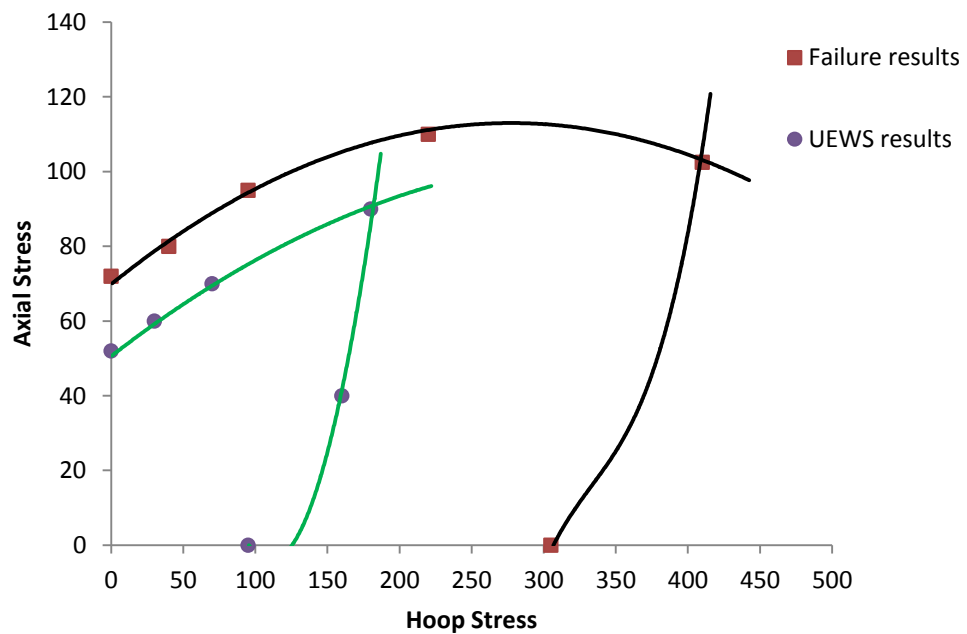


Figure 6.24. Modelling of UEWS and failure envelopes for GRE pipe, at 20°C, based on UEWS and the interactive stress criterion of equation 4.36.

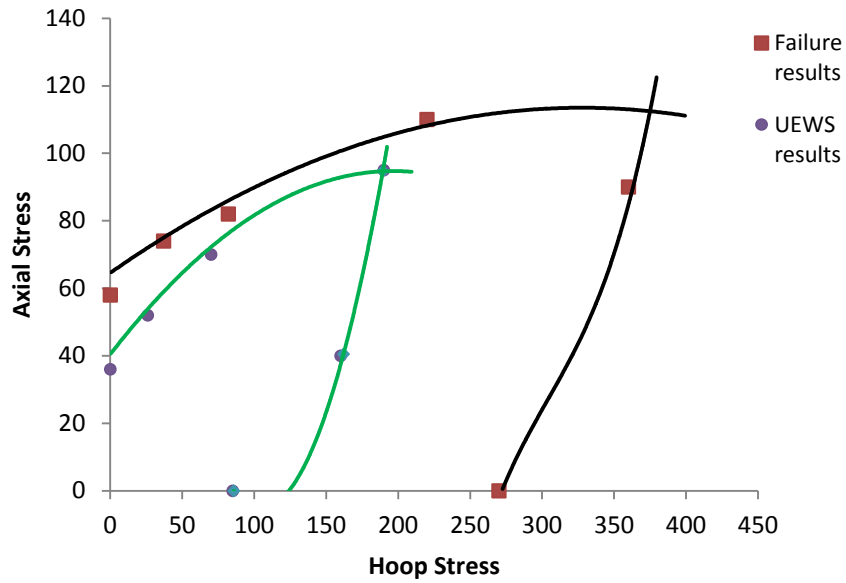


Figure 6.25. Modelling of UEWS and failure envelopes for GRE pipe, at 65°C, based on UEWS and the interactive stress criterion of equation 4.36.

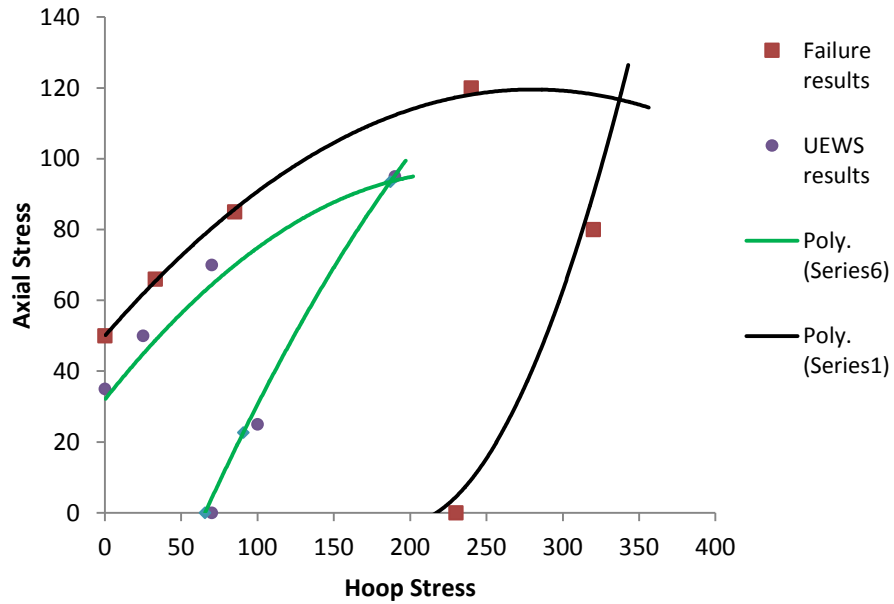


Figure 6.26. Modelling of UEWS and failure envelopes for GRE pipe, at 95°C, based on UEWS and the interactive stress criterion of equation 4.36.

Although UEWS tests were conducted by Hull (1978) [31] for $\pm 55^\circ$ GRP pipes using different material and technology, the results show good agreement with the current work in terms of ratios of UEWS to weepage stress. This ratio indeed reflects the extent of linearity in stress-strain relationships over the whole load history from zero up to final failure. This leads to the conclusion that the UEWS/failure stress ratios have approximately constant values for a given winding angle and stress ratio among pipes produced by filament wound processes.

The modelled curve fitted well with the room temperature envelopes (figure 6.24). However, the modelled curves show slight mismatch with the experimental data at 65°C and 95°C . This could be due to residual stresses from pipe manufacture and curing processes, which are not accounted for in this model. The interaction and maximum strength values of fibre and resin are listed in table 6.2:

Table 6.2. K_1, K_2 values used in the modelled envelopes for the $\pm 55^\circ$ GRE pipes.

condition	K_1	K_2	σ_1^*	σ_2^*	τ_{12}^*
25°C	0.0001505	0.000175	1000 MPa	61.7 MPa	60 MPa
65°C	0.0001147	0.000262	1000 MPa	61.7 MPa	60 MPa
95°C	0.00008	0.000328	1000 MPa	61.7 MPa	60 MPa

In model B the maximum stress criterion was used to predict the UEWS envelope by implementing equation 4.40. As mentioned in chapter 4, this criterion involves no interactions between the different modes, each of which is presented independently. Good agreement was found with the experimental data to fit the UEWS envelope, as illustrated in figure 6.27. The modelled envelope was divided into two curves. The lower curve corresponds to shear failure with hoop dominated load, and the upper curve is for where failure is governed by matrix cracking (axial dominated loading). Indeed the model fitted very well, with only a slightly deviation from the UEWS point at the 4:1 stress ratio.

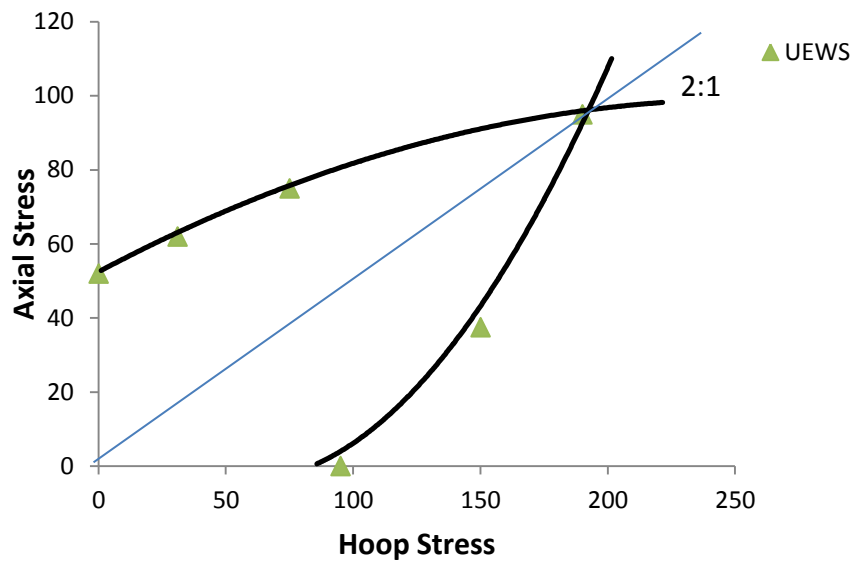


Figure 6.27 Modelling of the UEWS envelope based on maximum stress criterion

CHAPTER 7

CONCLUSIONS AND FUTURE WORK

7.1 Conclusions

Ultimate elastic wall stress tests have been conducted for the $\pm 55^\circ$ glass/fiber reinforced pipes for the purpose of meeting industrial needs. These tests enable stress-strain relationships to be studied, elastic limit envelopes established and biaxial failure envelopes defined under a variety of environmental conditions.

All the stress-strain curves were initially linear up to the UEWS point and then significant non-linear behavior occurred up to final failure. The non-linearity was strongly enhanced by matrix cracking, shearing in the glass/fiber interface and the yielding of the resin. The ratios of UEWS to weepage stress indicate the percentage of linearity during the test history from zero up to failure. The current results give the highest linearity of 75% at a 2:1 hoop to axial stress ratio and found compatible with Natting interpretation, whereas the shortest linearity was under pure hoop loading at 30%. Good agreement was achieved between the experimental and modeled results for the stress-strain curves.

The 100s axial and hoop Young's moduli for the conditioned samples under a 2:1 stress ratio were found. The hoop elastic modulus of the pipes tested showed a smooth reduction starting from 50% of UEWS condition and declining to 18% in the weeping condition. However, the axial elastic modulus has dramatically fell after the UEWS limit to be about 33% in the weeping condition.

The UEWS and failure envelopes were established for $\pm 55^\circ$ GRE pipes showing the effects of testing at elevated temperatures. The general forms of the biaxial envelopes, as might be expected, show high strength over the full range from pure

axial to pure hoop loading. Failure strengths fell as the temperature increased in all cases. A noticeable fail was recognised where hoop loading dominated, whereas only small reduction in pipe strength occurred with axial dominated loading. Nevertheless, the UEWS levels failed in most cases except in the case of the 2:1 stress ratio. At this stress ratio the UEWS at 65°C and 95°C were 5% greater than those at room temperature. This is possibly due to the pipe's ductility at elevated temperatures or the possible presence of residual stresses after manufacturing and curing processes. Good agreement between the experimental and modeled results especially at room temperature. However, slight mismatch was observed between the results at 65°C and 95°C tests, again due to the possibility of the presence of residual stress.

Four different failure modes were observed in the conducted tests. Weepage appeared as small droplets leaking through the pipe wall, and was frequently observed in pipes under hoop to axial stress ratios of 2:1, 0.5:1, and 1:1. Weepage generally occurs due to the presence of a network of transverse matrix cracks which form over time. Helical cracks are classified as mode II failure, and tend to occur along the pipe's circumference under pure axial loading. Mode III failure is termed local leakage, which occurs near to the pipe end due to the stress concentration generated from the restricted pipe ends. Finally, rupture is classified as mode IV, caused by fractures in the fibres and the complete destruction of the matrix. This type of fracture was noted near to the pipe end, where the stresses may have become concentrated.

Acoustic emission equipment was attached to the pipe wall during the UEWS tests in the cases of pure hydrostatic pressure loading and pure axial and hoop loading. The results showed agreement between the UEWS and the first detective damage obtained from the AE events and counts under pure axial loading at a wall stress of 52MPa. However, with pure hydrostatic pressure loading, damage occurred slightly before the UEWS point (180MPa) at 150MPa. In these two modes the failure sequences were started with matrix microcracking for stress releasing and then delamination occurred at stress level asymptotic to the UEWS level. Debonding and

fiber breakage appeared close to the final failure. Pipes under pure hoop loading behave differently from those mentioned above. Matrix showed significant deformation with an absent of cracking, because the negative axial strain prevents any cracks to be developed. Delamination and debonding are then occurred as a result of high strain and eventually fractures in fibres and complete destruction of the matrix took place in particular areas where stress became concentrated.

7.2 Future work

In pure hoop loading and 4:1 biaxial loading, the pipes failed due to stress concentrations from buckling and end restrictions. There would be a need to modify the testing rig so as to measure the UEWS and failure points in these load conditions. This rig should be designed to eliminate the stress concentrations generated during the UEWS tests, by either using a smaller test rig or shorten the pipe sample to avoid buckling which causes rupture.

Acoustic emission and ultrasonic tests need to be carried out along with the UEWS tests in order to detect the first damage and follow damage propagations. These tests would help to define stress levels where damages are started.

References

1. Saied, R.O., *filament wound composite tubes*. Newcastle University, 2002.
2. Garret Meijer and F. Ellyin, *A failure envelope for $\pm 60^\circ$ filament wound glass fibre reinforced epoxy tubulars*. composites part A: applied science and manufacturing, 2008. **39**: p. 555–564.
3. Nahas, M.N., Analysis of non-linear stress--strain response of laminated fibre-reinforced composites. *Fibre Science and Technology*, 1984. **20**(4): p. 297-313.
4. Sun, C.T. and J. Tao, *Prediction of failure envelopes and stress/strain behaviour of composite laminates*. *Composites Science and Technology*, 1998. **58**(7): p. 1125-1136.
5. Roberts, S.J.E., J. T. Gibson, A. G. Frost, S. R., *The Effect of Matrix Microcracks on the Stress-Strain Relationship in Fiber Composite Tubes*. *Journal of Composite Materials*, 2003. **37**(17): p. 1509-1523.
6. Wang, J. and M. Gutierrez, *Stress-strain behaviour of carbon nanotubes under cyclic loading*. *Micro & Nano Letters, IET*, 2007. **2**(4): p. 111-114.
7. Owen, M.J. and R.J. Howe, The accumulation of damage in a glass-reinforced plastic under tensile and fatigue loading. *Journal of Physics D: Applied Physics*, 1972. **5**(9): p. 1637.
8. Smith EW, P.K., Biaxial fatigue of a glass-fibre reinforced composite, Part 2, in *Biaxial and multiaxial fatigue*. EGF 3. London: Mechanical Engineering. 1989. p. 397-421.
9. Kawakami, H., T.J. Fujii, and Y. Morita, *Fatigue degradation and life prediction of glass fabric polymer composite under tension/torsion biaxial loadings*. *Journal of Reinforced Plastics and Composites*, 1996. **15**(2): p. 183-195.

10. Adden, S. and P. Horst, *Stiffness degradation under fatigue in multiaxially loaded non-crimped-fabrics*. International Journal of Fatigue, 2009. **32**(1): p. 108-122.
11. Hale, J.M.S., B. A. Speake, S. D. Gibson, A. G., *High temperature failure envelopes for thermosetting composite pipes in water*. Plastics, Rubber and Composites Processing and Applications, 2000. **29**(10): p. 539-548.
12. Standard, A.A.N., Petroleum and natural gas industries: Glass-reinforced plastics (GRP) piping, in BS EN ISO 14692-1:2002 2002., British Standards Institution: London, UK. p. 1-38.
13. Gibson, A., G., *The cost effective use of fibre reinforced composites offshore*, in *University: Newcastle 2003*, CompositeLink (Consultants) Limited Newcastle Upon Tyne.
14. Gibson, A.G., *Composite materials in the offshore industry*. Metals and materials Bury St Edmunds, 1989. **5**(10): p. 590-594.
15. Akinci, A., A. Gulec, and F. Yilmaz, *The applicability of GRP and NRP composites in rehabilitation of unpressurized pipes*. Advanced Materials Research, 2010. **83-86**: p. 563-570.
16. Hull, D., in *An Introduction to Composite Materials*. 1981, Cambridge: University of Cambridge: Cambridge, UK.
17. Agarwal, B. and J. Boutman, *Analysis and performance of fibre composites*. Second ed. Vol. 29. 1990, New York: John Wiley ISBN
18. Varma, I.K.G., V. B. Anthony, Kelly Carl, Zweben, *Thermosetting Resin-- Properties*. Comprehensive Composite Materials. 2000, Oxford: Pergamon. 1-56.
19. Materials, Resin systems for use in Fibre-Reinforced Composite Materials in http://www.azom.com/details.asp?articleid=986#_Resin_Types. available 12-05-2010, St Cross Business Park - Newport Isle of Wight PO30 5WU, UK
20. Mukhopadhyay, M., *Mechanics of Composite Materials and Structures*. . 2004., Hyderabad: Universities Press (India) Private Limited.

21. Gibson, A.G., *Review of Applications of Composite Materials in the Oil Gas Industry*, C.f.C.M. Engineering, Editor. 2000, Newcastle University.: Newcastle, UK.
22. Folkers, J.L., E Reidrich, R. S. and Fortune, M. *high performance phenolic piping for oilfield applications* in *Annual Conference 1997*. Houston, USA National Association of Corrosion Engineering
23. Bailey, J. and M. Schott, *plastic material: properties and applications*. first ed. 1982: Blackie and Son Ltd.
24. Muzzy, J.D., K. Anthony, and Z. Carl, *Thermoplastics--Properties*, in *Comprehensive Composite Materials*. 2000, Pergamon: Oxford. p. 57-76.
25. Gibson, A. and A. Fahrer, Reinforced Thermoplastic Tubes for Pressure Applications, in the eight international conference on Fibre Reinforced Composites. 2000, CompositeLink (Consultants) Limited Newcastle upon Tyne p. 201-209.
26. Gibson, A.G., K. Anthony, and Z. Carl, *Composite Materials in the Offshore Industry* *Comprehensive Composite Materials*, 2000: p. 459-478.
27. Petit, P.H. and M.E. Waddoups, *A Method of Predicting the Nonlinear Behavior of Laminated Composites*. *Journal of Composite Materials*, 1969. **3**(1): p. 2-19.
28. Hahn, H.T. and R.Y. Kim, *Swelling of composite laminates* *Advanced composite materials- Environmental effects* ed. J.R. Vinson. 1978, Newark, USA: American society for testing and materials ASTM STP658, Ed.
29. Abu-Farsakh, G.A., K.S. Numayr, and K.A. Hamad, *A micro-mechanical model for predicting the compressive strength of fibrous composite materials*. *Composites Science and Technology*, 1997. **57**(9-10): p. 1415-1422.
30. Soden, P.D., D.G. Leadbetter, P. R., and G.C. Eckold, *The strength of a filament wound composite under biaxial loading*. *Composites*, 1978. **9**(4): p. 247-250.

31. Hull, D., M.J. Legg, and B. Spencer, *Failure of glass/polyester filament wound pipe*. Composites, 1978. **9**(1): p. 17-24.
32. Soden, P., Y. Tsavalas, and M.J. Hinton, Influence of winding angle on the strength and deformation of filament-wound composite tubes subjected to uniaxial and biaxial loads. Composites Science and Technology, 1993. **46**(4): p. 363-378.
33. Kaddour, A.S., P.D. Soden, and M.J. Hinton, *Failure of ± 55 Degree Filament Wound Glass/Epoxy Composite Tubes under Biaxial Compression*. Journal of Composite Materials, 1998. **32**(18): p. 1618-1645.
34. Mistry, J., A.G. Gibson, and Y.S. Wu, *Failure of composite cylinders under combined external pressure and axial loading*. Composite Structures, 1992. **22**(4): p. 193-200.
35. Fujii, T., T. Shiina, and K. Okubo, Fatigue Notch Sensitivity of Glass Woven Fabric Composites Having a Circular Hole under Tension/Torsion Biaxial Loading. Journal of Composite Materials, 1994. **28**(3): p. 234-251.
36. Kawai, M. and H. Suda, Effects of non-negative mean stress on the off-axis fatigue behavior of unidirectional carbon/epoxy composites at room temperature. Journal of Composite Materials, 2004. **38**(10): p. 833-854.
37. Curtis, P.T. and B.B. Moore, A comparison of plain and double waisted coupons for static and tensile testing of UD GRP and CFRP, , in second international conference on composite structure. 1983, Elsevier Applied Science, London: Scotland, UK. p. 383-398.
38. Lorenzo, L. and H.T. Hahn, *Fatigue failure mechanisms in unidirectional composites*. 1987, Newyork, USA: American Society for Testing and Materials.
39. Godara, A. and D. Raabe, Influence of fiber orientation on global mechanical behavior and mesoscale strain localization in a short glass-fiber-reinforced epoxy polymer composite during tensile deformation investigated using digital image correlation. Composites Science and Technology, 2007. **67**(11-12): p. 2417-2427.

40. Foye, R.L. and Baker. Design of orthotropic laminates. in the 11th Annual AIAA structures, structural dynamics, and material 1970. Denver, Colorado, USA.
41. Owen, M.J., *Fatigue of carbon-fiber-reinforced plastics*. Fracture and fatigue. Vol. 5. 1974, New York, USA: L. J. Broutman (ed), Academic press. 341-369
42. Harris, B., *Engineering composite materials*. fatigue behaviour of fibre composites. Vol. 5. 1986, London, UK: IOM Communications.
43. Curtis, P.T., Dorey, Fatigue of composite materials and structures, in International conference on Fatigue of composite materials and structures. 1986, I. Mech. E.: London, UK. p. 297-306.
44. Fernberg, S.P. and L.A. Berglund, *Effects of glass fiber size composition (film-former type) on transverse cracking in cross-ply laminates*. composites part A: applied science and manufacturing, 2000. **31**(10): p. 1083-1090.
45. Gan, Y.X., *Effect of interface structure on mechanical properties of advanced composite materials*. International Journal of Molecular Sciences, 2009. **10**(12): p. 5115-5134.
46. Boller, K.H., Fatigue characteristics of RP laminates subjected to axial loading. Modern Plastic, 1964. **41**: p. 145-188.
47. Scholte, H.G., *Composite material, Fatigue characteristic in Maritime structure*, R.A. Sheno and J.F. Wellicome, Editors. 1993. p. 178-198.
48. Shih, G.C. and L.J. Ebert, The effect of the fiber/matrix interface on the flexural fatigue performance of unidirectional fiberglass composites. Composites Science and Technology, 1987. **28**(2): p. 137-161.
49. Curtis, P.T. An investigation of tensile fatigue behaviour of fibre carbon composite laminate, proceeding of ICCM6. in Elsevier Applied Science Publishers. 1987. London, UK: Imperial College of science and technology.

50. Sekercioglu, T., A. Gulsoz, and H. Rende, The effects of bonding clearance and interference fit on the strength of adhesively bonded cylindrical components. *Materials and Design*, 2005. **26**(4): p. 377-381.
51. El Kadi, H. and F. Ellyin, Effect of stress ratio on the fatigue of unidirectional glass fibre/epoxy composite laminae. *Composites*, 1994. **25**(10): p. 917-924.
52. Miyano, Y., M. Nakada, and M.K. McMurray, *Influence of Stress Ratio on Fatigue Behavior in the Transverse Direction of Unidirectional CFRPS*. *Journal of Composite Materials*, 1995. **29**(14): p. 1808-1822.
53. Quaresimin, M., L. Susmel, and R. Talreja, *Fatigue behaviour and life assessment of composite laminates under multiaxial loadings*. *International Journal of Fatigue*. **32**(1): p. 2-16.
54. Abd Allah, M.H., A.I. Selmy, and U.A. Khashaba, *Short communication effect of mean stress on fatigue behaviour of GFRP pultruded rod composites*. *composites part A: applied science and manufacturing*, 1997. **28**(1): p. 87-91.
55. Joon-Mo, A. and M. Shankar, Frequency Effects on Fatigue Behavior of a Silicon Carbide Fiber-Reinforced Glass#x2013;Ceramic Composite (SiC/MAS). *International Journal of Applied Ceramic Technology*, 2009. **6**(1): p. 45-52.
56. Revuelta, D. and A. Miravete, *Fatigue Damage in Composite Materials*. *International Applied Mechanics*, 2002. **38**(2): p. 121-134.
57. Hashin, Z., *Fatigue failure criteria for unidirectional fiber composites*. *Journal of Applied Mechanics, Transactions ASME*, 1981. **48**(4): p. 846-852.
58. Nairn, J.A., S. Hu, and J.S. Bark, *A critical evaluation of theories for predicting microcracking in composite laminates*. *Journal of Materials Science*, 1993. **28**(18): p. 5099-5111.
59. Aveston, J. and A. Kelly, *Theory of multiple fracture of fibrous composites*. *Journal of Materials Science*, 1973. **8**(3): p. 352-362.

60. Garrett, K.W. and J.E. Bailey, Multiple transverse fracture in 90° cross-ply laminates of a glass fibre-reinforced polyester. *Journal of Materials Science*, 1977. **12**(1): p. 157-168.
61. Jones, M.L.C. and D. Hull, *Microscopy of failure mechanisms in filament wound pipes*. *Materials Science*, 1979. **14**: p. 165-174.
62. Smith, P.A., D.G. Gilbert, and A. Poursartip, *Matrix cracking of composites inside a scanning electron microscope*. *Journal of Materials Science Letters*, 1985. **4**(7): p. 845-847.
63. Nairn, J.A., *Matrix microcracking in composites*. *Polymer Matrix Composites*. Vol. 2. 2000, Salt Lake, Utah, USA: Elsevier Science. 403–432.
64. Singh, C.V. and R. Talreja, *Evolution of ply cracks in multidirectional composite laminates*. *International Journal of Solids and Structures*, 2010. **47**(10): p. 1338-1349.
65. Rasheed, H.A. and J.L. Tassoulas, *Collapse of composite rings due to delamination buckling under external pressure*. *Journal of Engineering Mechanics*, 2002. **128**(11): p. 1174-1181.
66. Zor, M., F. Sen, and M.E. Toygar, An Investigation of Square Delamination Effects on the Buckling Behavior of Laminated Composite Plates with a Square Hole by using Three-dimensional FEM Analysis. *Journal of Reinforced Plastics and Composites*, 2005. **24**(11): p. 1119-1130.
67. Chai, H., C.D. Babcock, and W.G. Knauss, *One dimensional modelling of failure in laminated plates by delamination buckling*. *International Journal of Solids and Structures*, 1981. **17**(11): p. 1069-1083.
68. Whitcomb, J.D., Analysis of a Laminate with a Postbuckled Embedded Delamination, Including Contact Effects. *Journal of Composite Materials*, 1992. **26**(10): p. 1523-1535.
69. Aboudi, j., *Composit material series*. *Damage Mechanics of Composite Material, Interfacial Damage*, ed. R. Byron. Vol. 9. 1994, Amsterdam, The

Netherland: Center for materials, University of Delaware, Newark, Delaware, USA. 245-294.

70. Wang, J.T.-S., S.-H. Cheng, and C.-C. Lin, *Local Buckling of Delaminated Beams and Plates Using Continuous Analysis*. Journal of Composite Materials, 1995. **29**(10): p. 1374-1402.
71. Hwang, S.-F. and C.-P. Mao, The delamination buckling of single-fibre system and interply hybrid composites. Composite Structures, 1999. **46**(3): p. 279-287.
72. Ozdil, F. and L.A. Carlsson, *Characterization of Mixed Mode Delamination Growth in Glass/Epoxy Composite Cylinders*. Journal of Composite Materials, 2000. **34**(5): p. 420-441.
73. Rosenow, M.W.K., Wind angle effects in glass fibre-reinforced polyester filament wound pipes. Composites, 1984. **15**(2): p. 144-152.
74. Mertiny, P. and A. Gold, Quantification of leakage damage in high-pressure fibre-reinforced polymer composite tubular vessels. Polymer Testing, 2007. **26**(2): p. 172-179.
75. Schürhoff, J., B. Skrotzki, and G. Eggeler, Fibre breakage in short fibre reinforced metal matrix composites during creep and constant strain rate compression testing. Materials Science and Engineering A, 2004. **387-389**: p. 896-899.
76. Carroll, M. and F. Ellyin, The rate dependent behaviour of $\pm 55^{\circ}$ filament wound glass-fibre /epoxy tubes under biaxial loading. Composites science and technology, 1995. **55**: p. 391-403.
77. Hashin, Z. and A. Rotem, *A Fatigue Failure Criterion for Fiber Reinforced Materials*. Journal of Composite Materials, 1973. **7**(4): p. 448-464.
78. Frost, S.R. and A. Cervenka, Glass fibre-reinforced epoxy matrix filament-wound pipes for use in the oil industry. Composites Manufacturing, 1994. **5**(2): p. 73-81.

79. Staab, G.H., *Laminar Composites*. Lamina failure theories, ed. Butterworth and Heineman. 1999, madras, India: British library cataloguing.
80. Eckold, G.C., D. Leadbetter, and P.D. Soden, Lamination theory in the prediction of failure envelopes for filament wound materials subjected to biaxial loading. *Composites*, 1978. **9**(4): p. 243-246.
81. Hart-Smith, L.J., *Strain-based maximum-shear-stress failure criterion for fibrous composites*, in *Structural Dynamics, Materials Conference*. 1990, Collection of Technical Papers - AIAA/ASME/ASCE/AHS/ASC Structures: Long Beach, USA. p. 714-722.
82. Ramirez, G., M.D. Engelhardt, and T.J. Fowler, *On the endurance limit of fiberglass pipes using acoustic emission*. *Journal of Pressure Vessel Technology*, Transactions of the ASME, 2006. **128**(3): p. 454-461.
83. Benmedakhene, S., M. Kenane, and M.L. Benzeggagh, Initiation and growth of delamination in glass/epoxy composites subjected to static and dynamic loading by acoustic emission monitoring. *Composites Science and Technology*, 1999. **59**(2): p. 201-208.
84. Dogossy, G. and T. Czigány, Failure mode characterization in maize hull filled polyethylene composites by acoustic emission. *Polymer Testing*, 2006. **25**(3): p. 353-357.
85. Ramirez, G., M.D. Engelhardt, and T.J. Fowler, *On the Endurance Limit of Fiberglass Pipes Using Acoustic Emission*. *Journal of Pressure Vessel Technology*, 2006. **128**(3): p. 454-461.
86. Finkenstadt, V.L., C.-K. Liu, and R. Evangelista, *Poly(lactic acid) green composites using oilseed coproducts as fillers*. *Industrial Crops and Products*, 2007. **26**(1): p. 36-43.
87. Ellyin, F., Biaxial fatigue behaviour of multidirectional filament wound glass-fibre pipe. *composite science and technology*, 2001. **61**: p. 491-502.

88. Mertiny, P., F. Ellyin, and A. Hothan, An experimental investigation on the effect of multi-angle filament winding on the strength of tubular composite structures. *Composites Science and Technology*, 2004. **64**(1): p. 1-9.
89. Meijer, G. and F. Ellyin, *A failure envelope for $\pm 60^\circ$ filament wound glass fibre reinforced epoxy tubulars*. *composites part A: applied science and manufacturing*, 2008. **39**(3): p. 555-564.
90. Leijstrom, H. and M. Ifwarson. Results and experiences obtained by studsvik from long term pressure tests on plastic pipes for validation of miners rule. in *Studsvik Polymer AB*. 1998. Nykoping, Sweden.
91. Gibson, A.G., N. Dodds, and S.R. Frost, Novel approach to qualification of non-metallic pipe systems - As applied to reinforced thermoplastic pipe. *Plastics, Rubber and Composites*, 2005. **34**(7): p. 301-304.
92. Cox, H.L., *The elasticity and strength of paper and other fibrous materials*. *British Journal of Applied Physics*, 1952. **3**(3): p. 72.
93. Henaff-Gardin, C., M.C. Lafarie-Frenot, and D. Gamby, *Doubly periodic matrix cracking in composite laminates Part 1: General in-plane loading*. *Composite Structures*, 1999. **36**(1-2): p. 113-130.
94. Dharani, R. and F.S. Ji, Non-Axisymmetric Matrix Cracking and Interface Debonding with Friction in Ceramic Composites. *Applied Composite Materials*, 1998. **5**(6): p. 379-397.
95. Zhang, H. and L. Minnetyan, *Variational analysis of transverse cracking and local delamination in $[[\theta]_m/90_n]_s$ laminates*. *International Journal of Solids and Structures*, 2006. **43**(22-23): p. 7061-7081.
96. Ogi, K., S. Yashiro, and M. Takahashi, *A probabilistic static fatigue model for transverse cracking in CFRP cross-ply laminates*. *Composites Science and Technology*, 2009. **69**(3-4): p. 469-476.
97. Lee, J., D.H. Allen, and C.E. Harris, Internal State Variable Approach for Predicting Stiffness Reductions in Fibrous Laminated Composites with Matrix Cracks. *Journal of Composite Materials*, 1989. **23**(12): p. 1273-1291.

98. Schipperen, J.H.A., An anisotropic damage model for the description of transverse matrix cracking in a graphite-epoxy laminate. *Composite Structures*, 2001. **53**(3): p. 295-299.
99. Maimi, P., J.A. Mayugo, and P.P. Camanho, *A three-dimensional damage model for transversely isotropic composite laminates*. *Journal of Composite Materials*, 2008. **42**(25): p. 2717-2745.
100. Hashin, Z., *Analysis of cracked laminates: a variational approach*. *Mechanics of Materials*, 1985. **4**(2): p. 121-136.
101. Talreja and Ramesh, *Transverse cracking and stiffness reduction in composite laminates*. *Journal of Composite Materials*, 1985. **19**(4): p. 355-375.
102. Nuismer, R.J. and S.C. Tan, *Constitutive Relations of a Cracked Composite Lamina*. *Journal of Composite Materials*, 1988. **22**(4): p. 306-321.
103. Zhang, J., J. Fan, and C. Soutis, Analysis of multiple matrix cracking in $[\pm(\theta)_m/90_n]_s$ composite laminates. Part 2: Development of transverse ply cracks. *Composites*, 1992. **23**(5): p. 299-304.
104. McCartney, L.N. Stress transfer mechanics for angle-ply laminates in the 7th European Conference on Composite Materials 1996. London; UK.
105. Zhang, J., J. Fan, and K.P. Herrmann, *Delaminations induced by constrained transverse cracking in symmetric composite laminates*. *International Journal of Solids and Structures*, 1999. **36**(6): p. 813-846.
106. Adolfsson, E. and P. Gudmundson, Matrix crack induced stiffness reductions in $[(0_m/90_n/ + [\theta]_p/ - [\theta]_q)_s]_M$ composite laminates. *Composites Engineering*, 1995. **5**(1): p. 107-123.
107. Highsmith, A. and K. Reifsnider, *Internal load distribution effects during fatigue loading of composite laminates*. ASTM special technical publication 1986: p. 233–251.

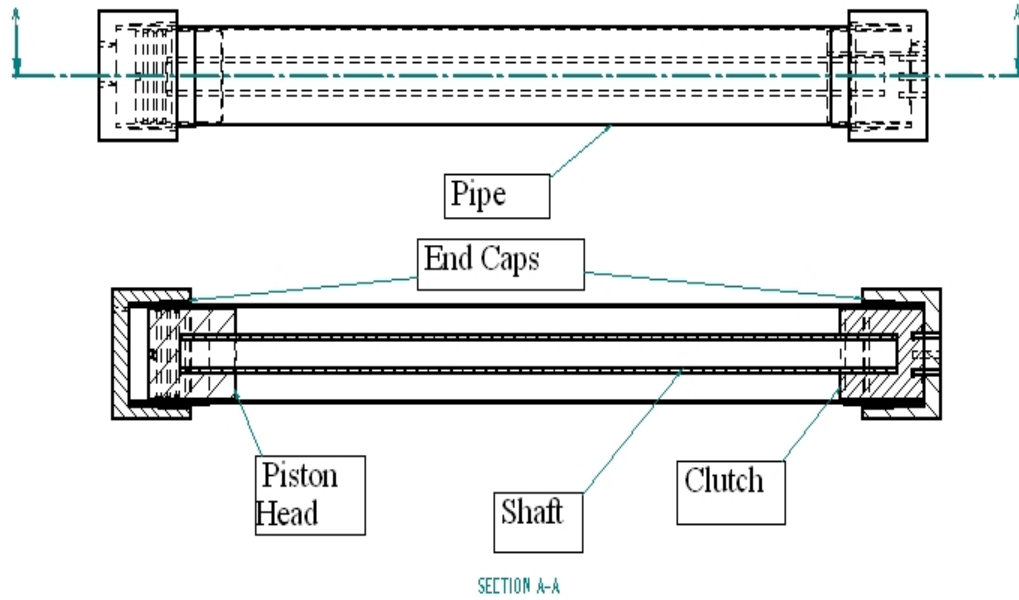
108. Kashtalyan, M. and C. Soutis, *Stiffness degradation in cross-ply laminates damaged by transverse cracking and splitting*. composites part A: applied science and manufacturing, 2000. **31**(4): p. 335-351.
109. Tounsi, A., K.H. Amara, and A. Benzair, *On the transverse cracking and stiffness degradation of aged angle-ply laminates*. Materials Letters, 2006. **60**(21-22): p. 2561-2564.
110. NDT resource center. *Introduction to Acoustic Emission Testing*. Acoustic emission equipment, 2001 [cited 2010 10-06]; http://www.ndt-ed.org/EducationResources/CommunityCollege/Other%20Methods/AE/AE_Equipment.htm].
111. Future Pipe Industries, Guideline short term testing of FRP, in Determination of the Ultimate Elastic Wall Stress of Wavistrong Pipes, K. Rookus, Editor. 1993: Arnhem, the Netherlands.
112. Gudmundson, P. and Z. Weilin, *An analytic model for thermoelastic properties of composite laminates containing transverse matrix cracks*. International Journal of Solids and Structures, 1993. **30**(23): p. 3211-3231.
113. Ellyin, F., M. Carroll, and D. Kujawski, *The behavior of multidirectional filament wound fibreglass/epoxy tubulars under biaxial loading*. Composites Part A: Applied Science and Manufacturing, 1997. **28**(9-10): p. 781-790.
114. Ramadan, O.S., Failure Envelope for Filament wound composite Tubes in Water at Elevated Temperatures, in Mechanical and system engineering. 2004, Newcastle University: Newcastle Upon Tyne. p. 180.
115. Puck, A. and W. Schneider, On failure mechanisms and failure criteria of filament-wound glass fibre/resin composites *Plastics and Polymers*, 1969. **59**: p. 33-37.
116. Tao, J.X. and C.T. Sun, *Effect of matrix cracking on stiffness of composite laminates*. Mechanics of Composite Materials and Structures, 1996. **3**(3): p. 225-239.

List of Publications and conferences

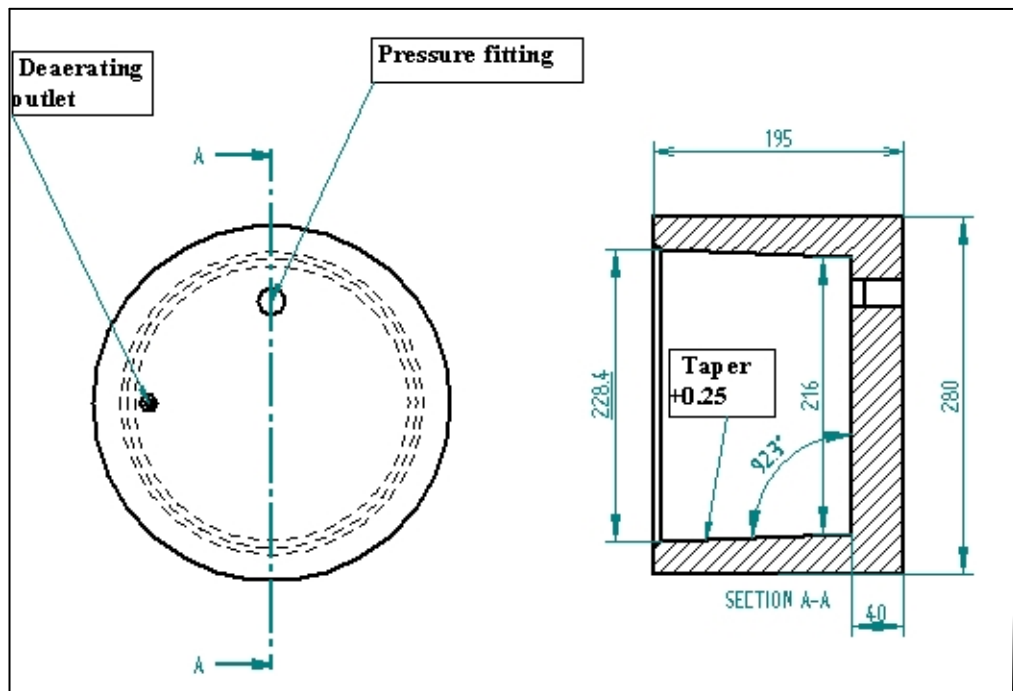
1. A.G. Gibson, M.S. Abdul Majid, T.A. Assaleh and J.M. Hale, *Qualification and Test Procedures for Fiberglass Pipe for Oil and Gas Applications*, *Plastics, Rubber and Composites*, 2010, **40**, (2), pp 80-85.
2. T.A. Assaleh, A.G. Gibson, M.S. Abdul Majid and J.M. Hale *Ultimate elastic wall stress (UEWS) test of glass fibrereinforced epoxy (GRE) pipe*, *Composites Part A* 2011.
3. A.G. Gibson, M.S. Abdul Majid, T.A. Assaleh and J.M. Hale *Qualification and Lifetime Modelling of Fiberglass Pipe*, Presented at the 13th Middle East Corrosion Conference, February 14-17, 2010, Kingdom of Bahrain.

Appendix A:

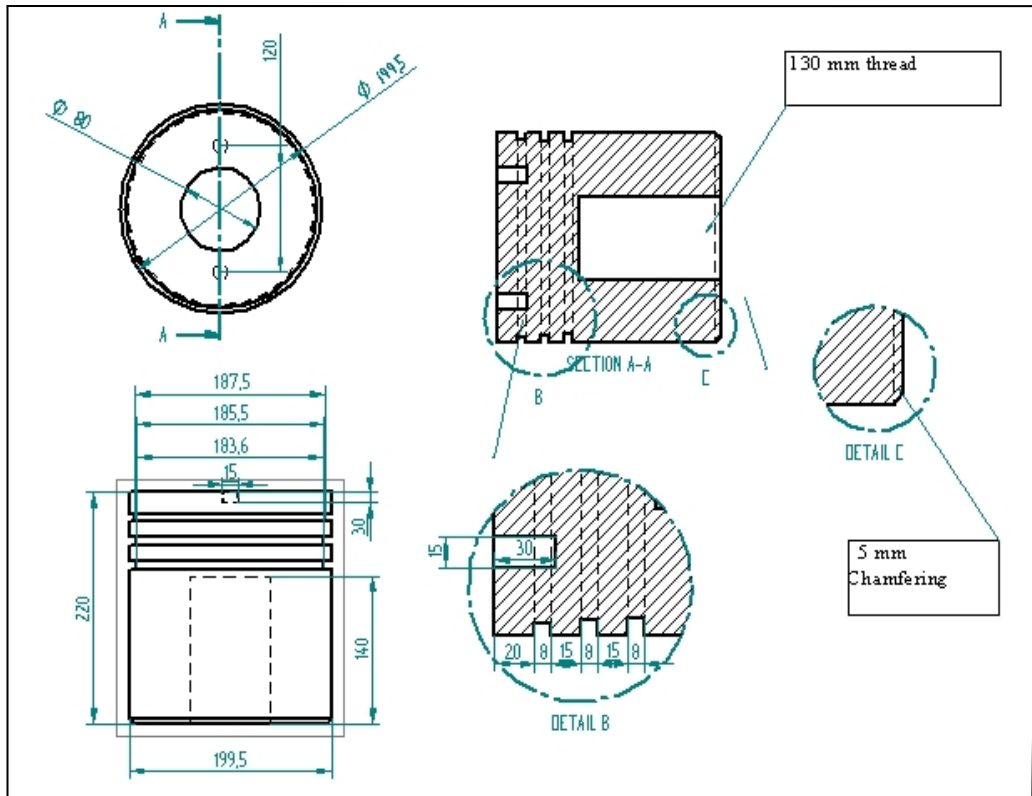
Engineering drawing of the small scale testing rig



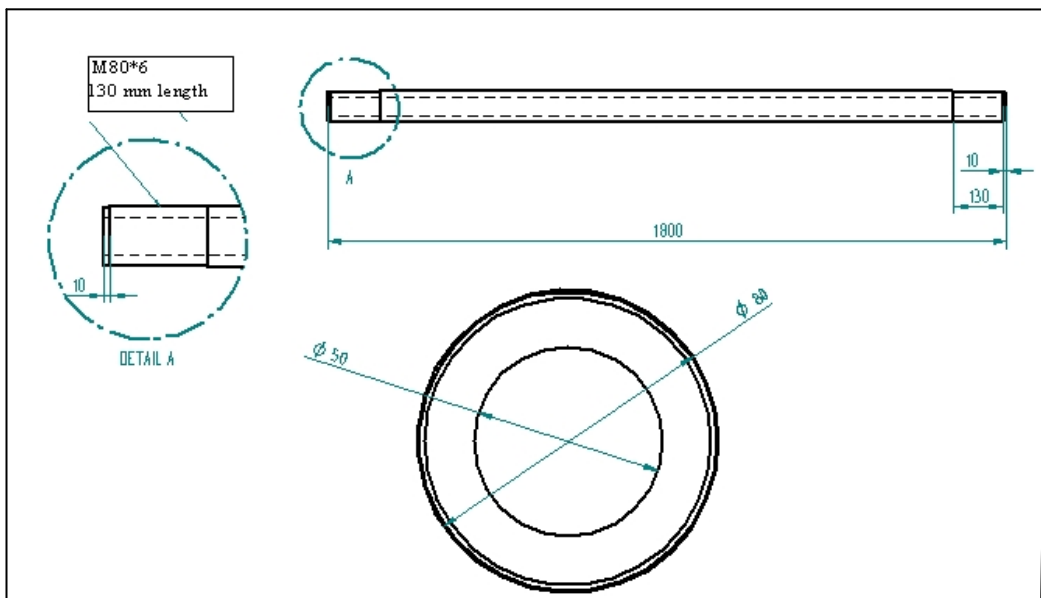
Cross section for the assembled test rig.



Cross section and front view for the adhesive end cap.



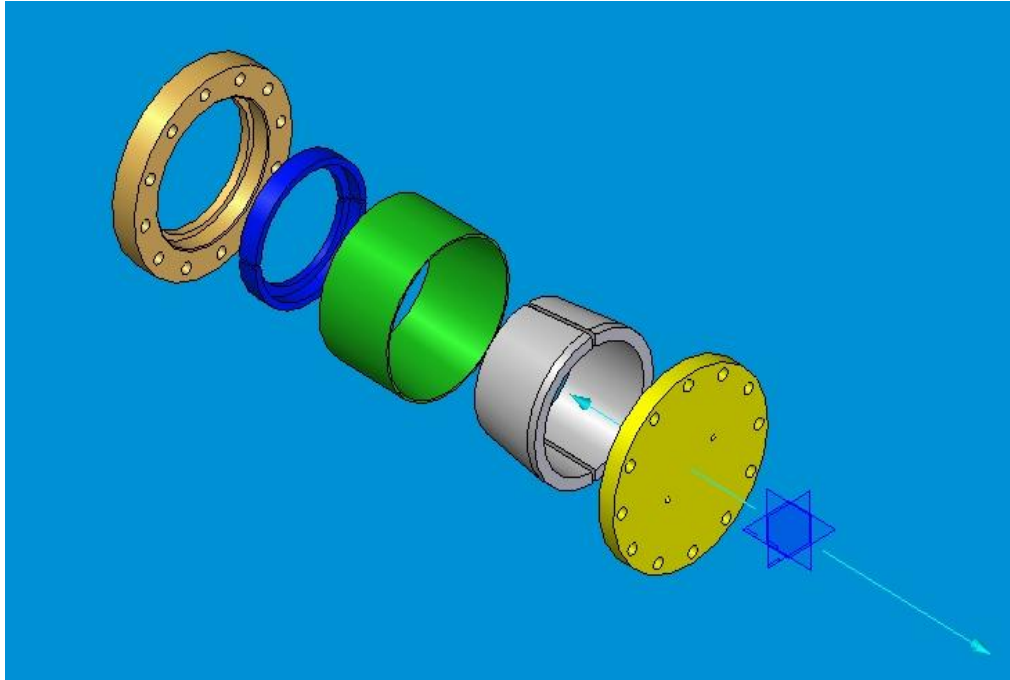
Cross section, side and front view for the rig piston.



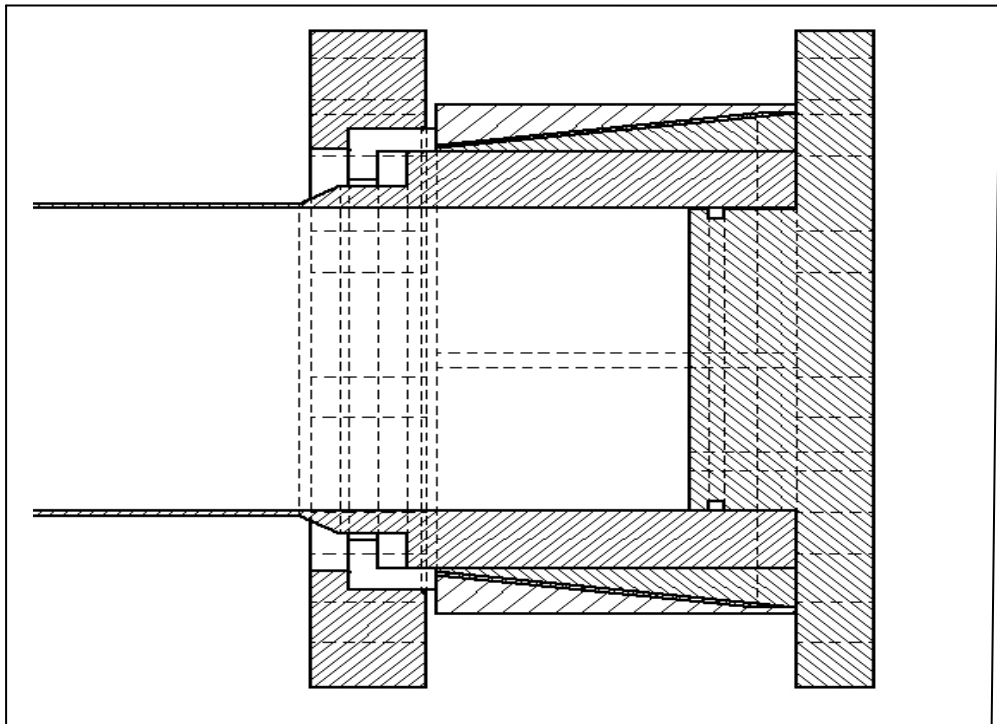
Side and front view for the rig shaft.

Appendix B:

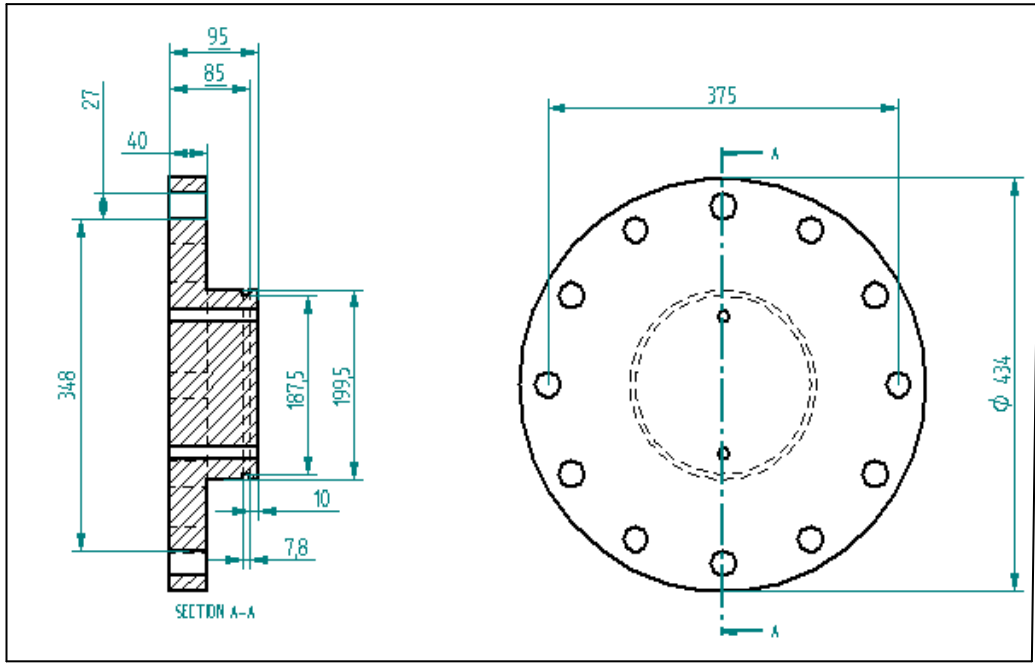
Engineering drawing of the mechanical fittings



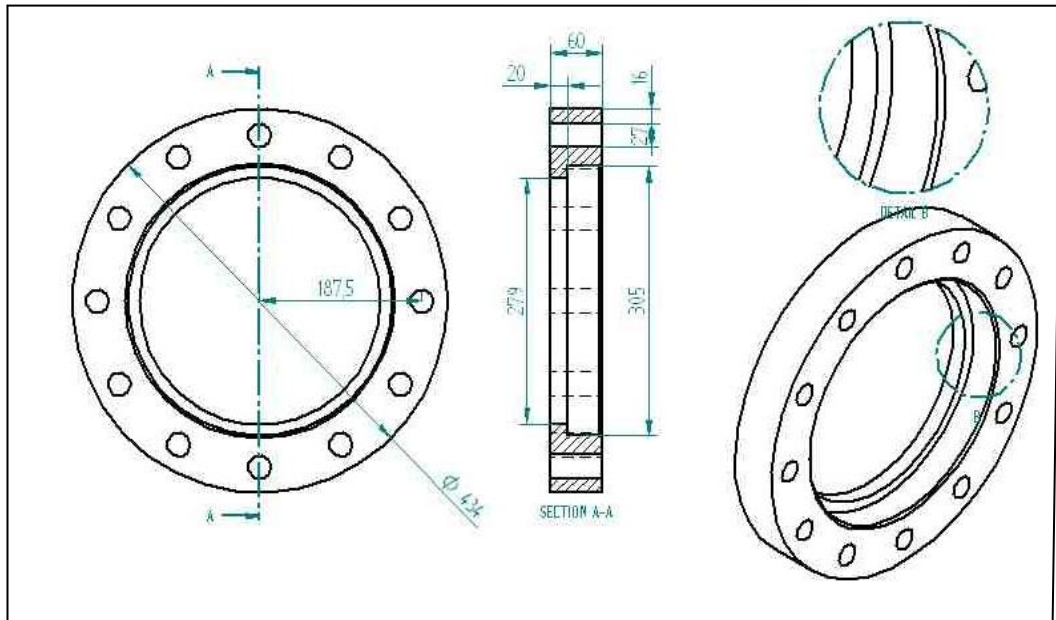
Mechanical fittings used to carry out the UEWS test at 95°C



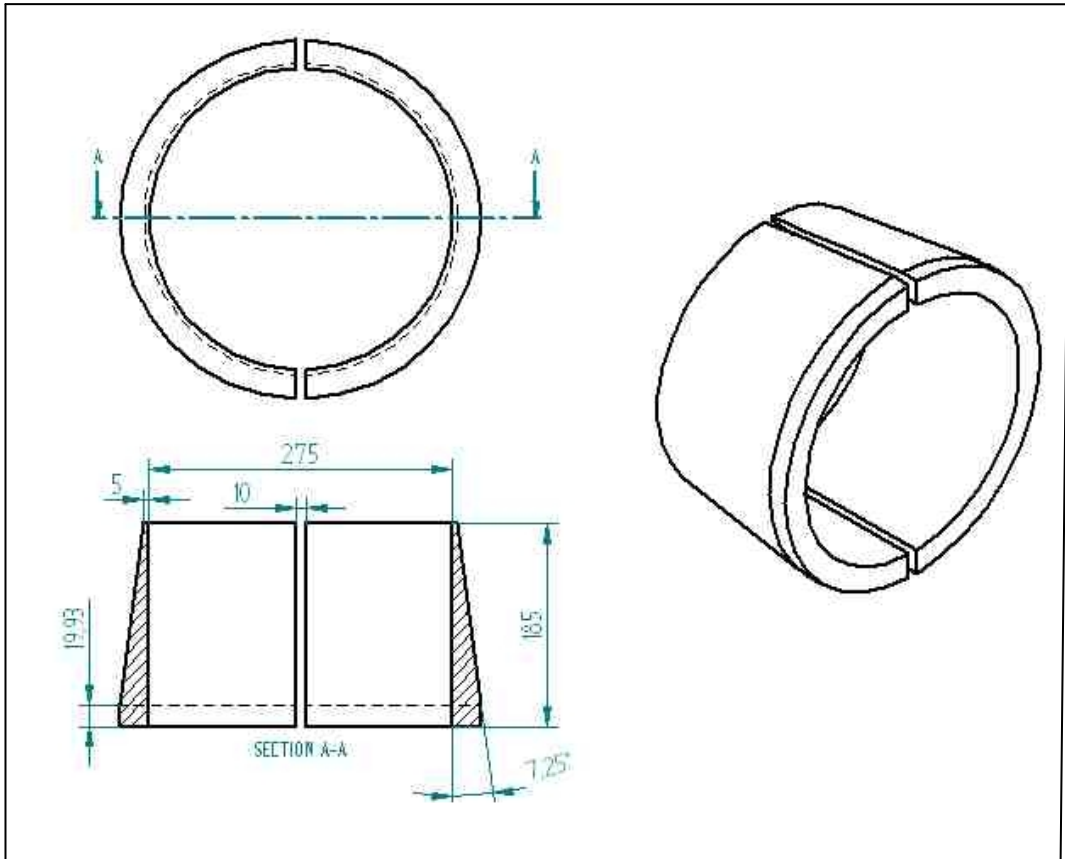
Cross section for the assembled mechanical fitting



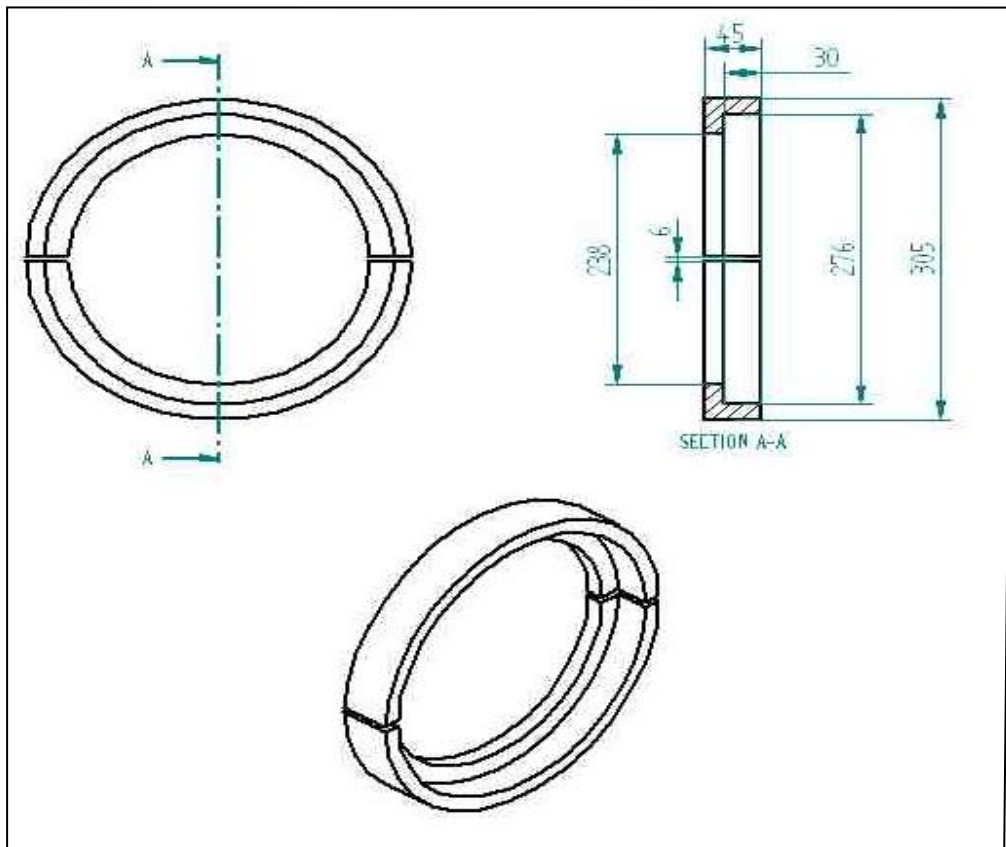
Cross section and front view for main Flange



Cross section and front view for the Loose flange



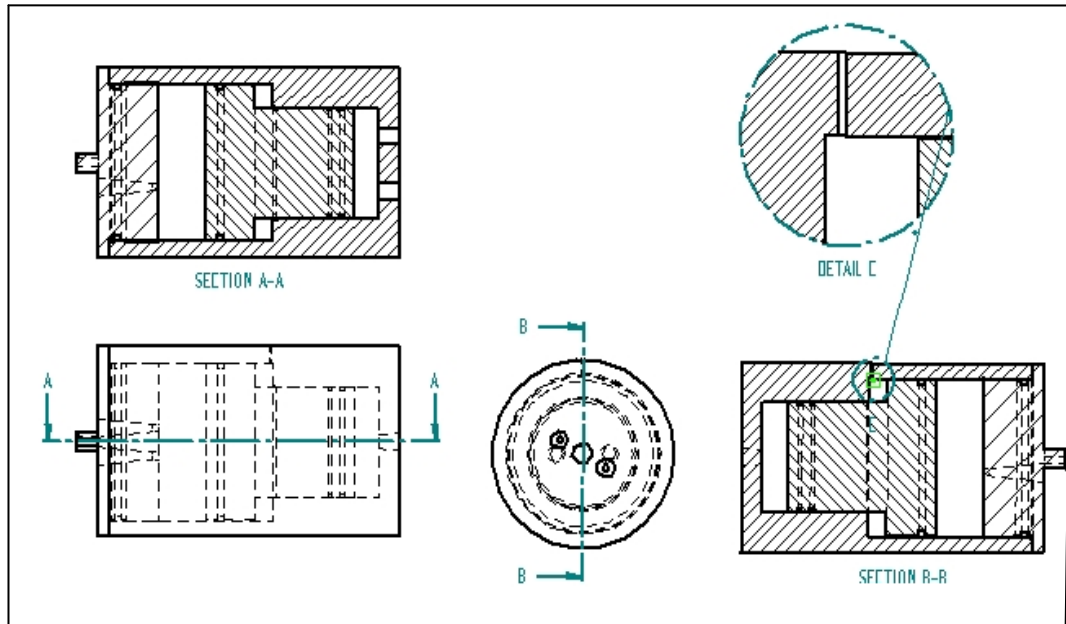
Front , cross section and isometric view for the Tapered sleeve.



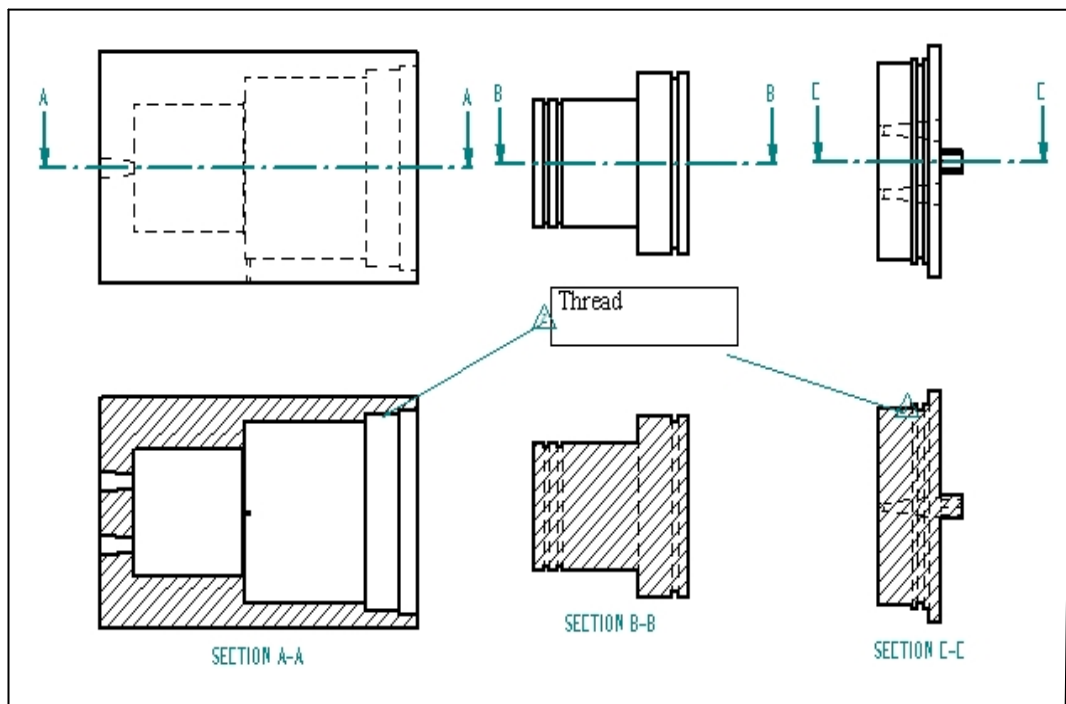
Front , section and isometric view for the Segmented ring.

Appendix C:

Engineering drawing of the pressure reducer



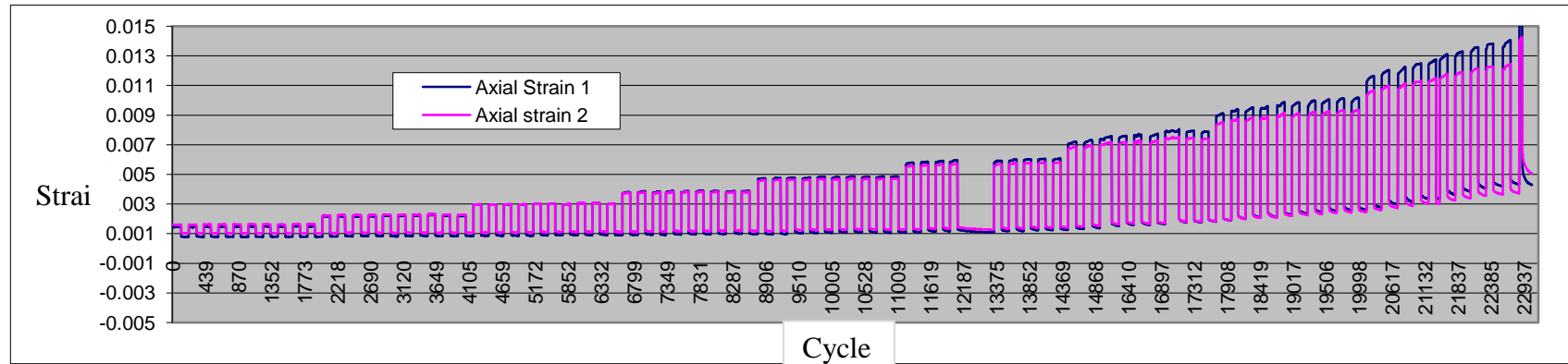
Cross section for the assembled intensivefire.



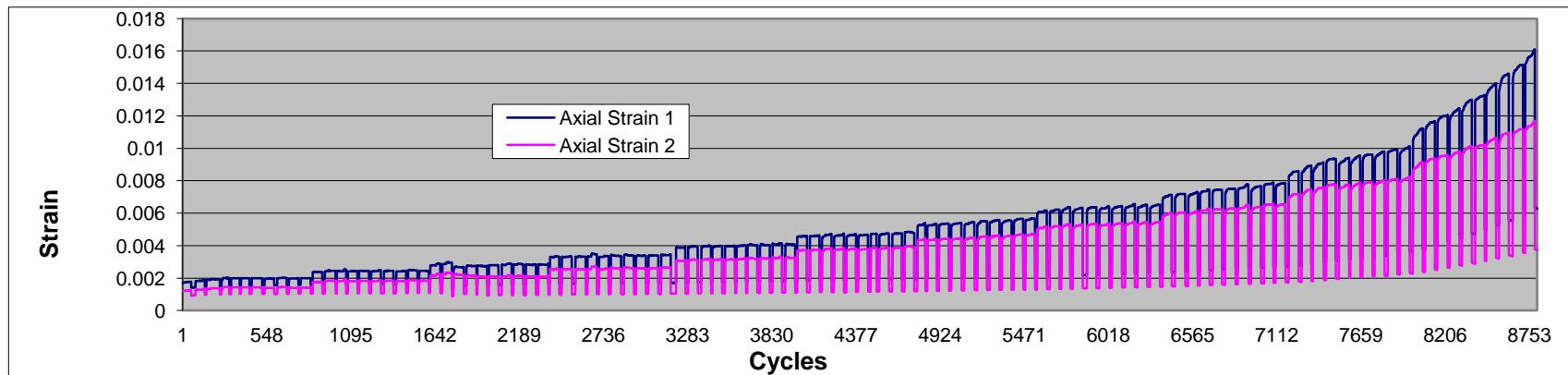
Cross section for the disassembled intensivefire.

Appendix D:

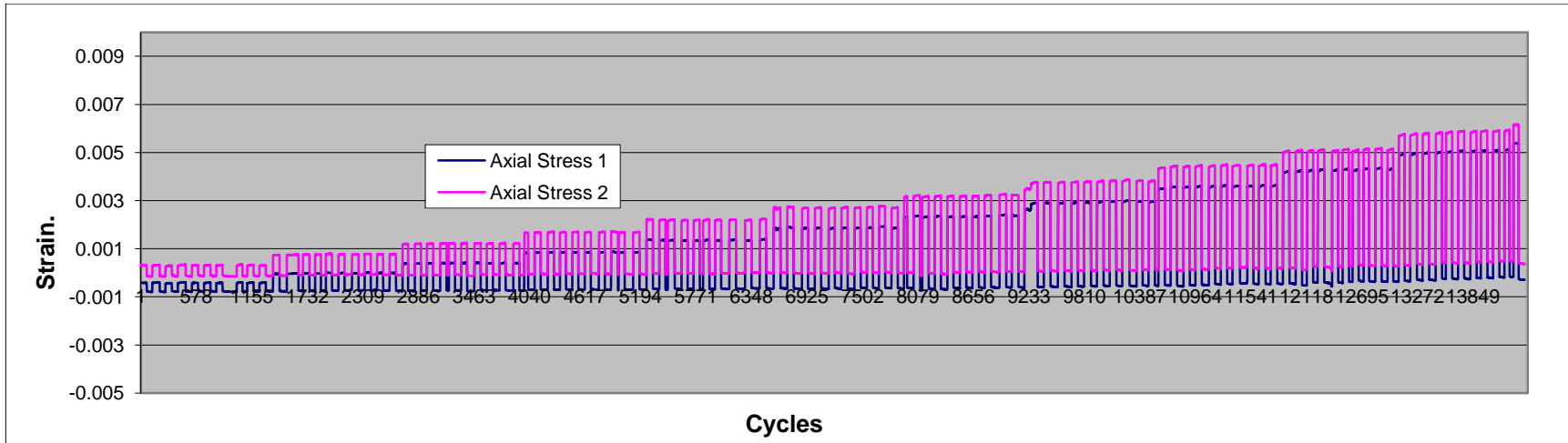
Strain plots for the $\pm 55^\circ$ GRE pipes under UEWS test



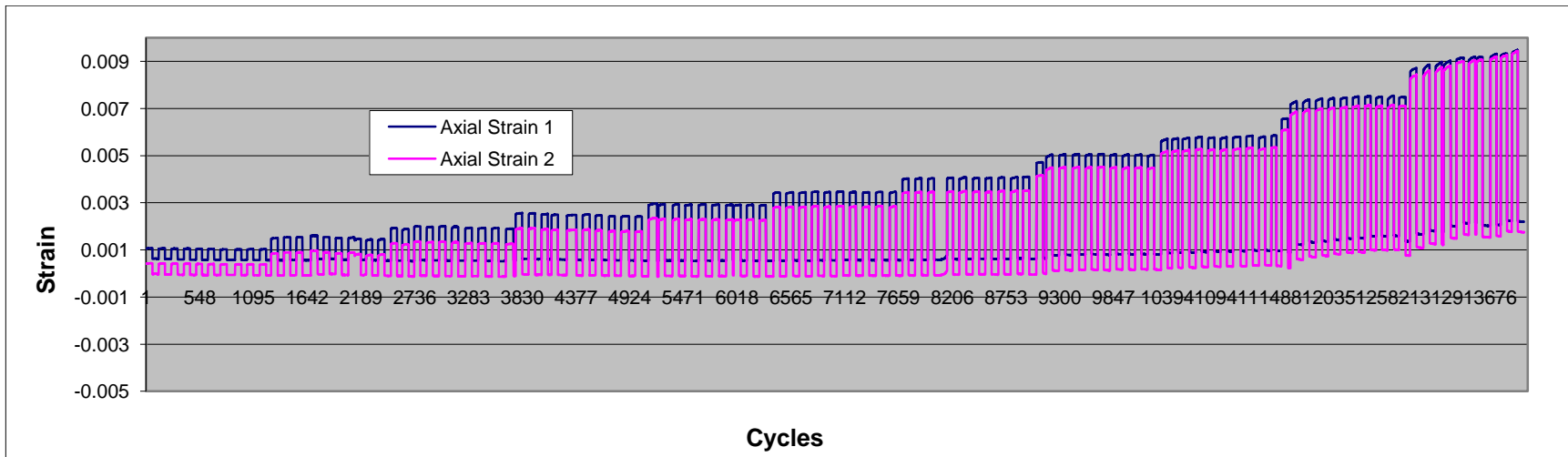
The axial strain plot during the UEWS test under pure axial loading at 65 °C.



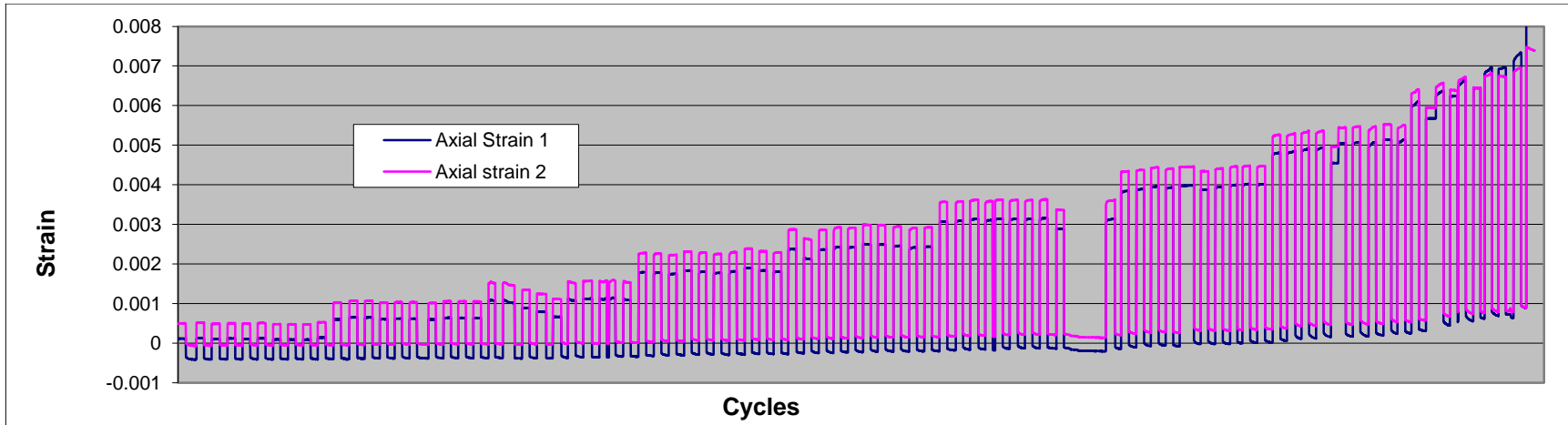
The axial strain plot during the UEWS test under pure axial loading at 95 °C.



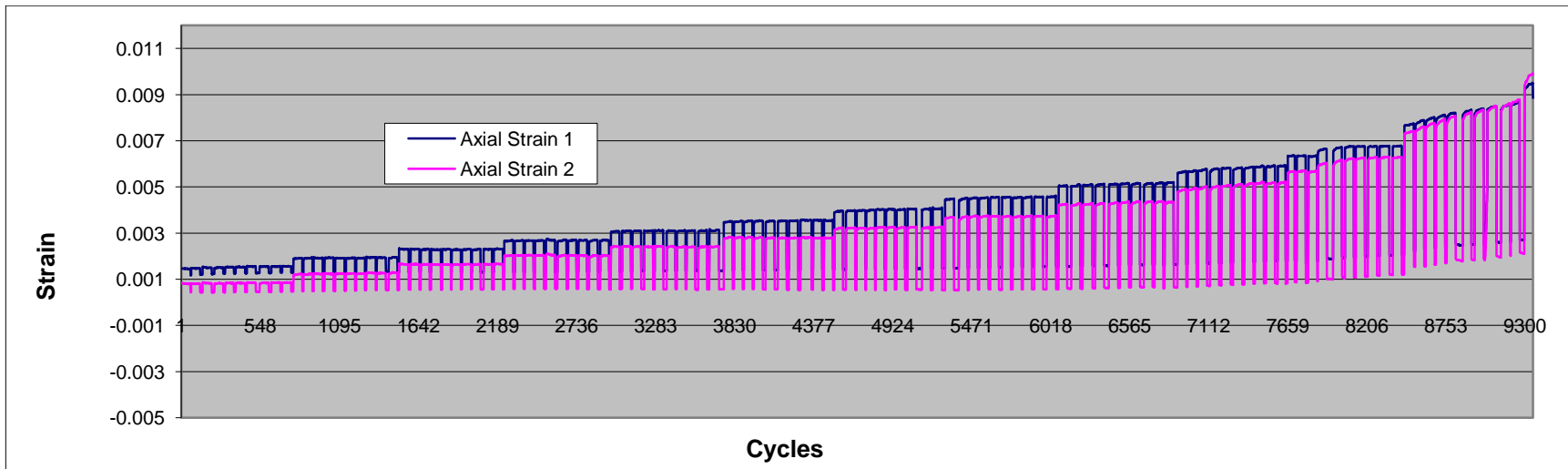
The axial strain plots during the UEWS test under a 0.5:1 hoop to axial stress ratio, at room temperature.



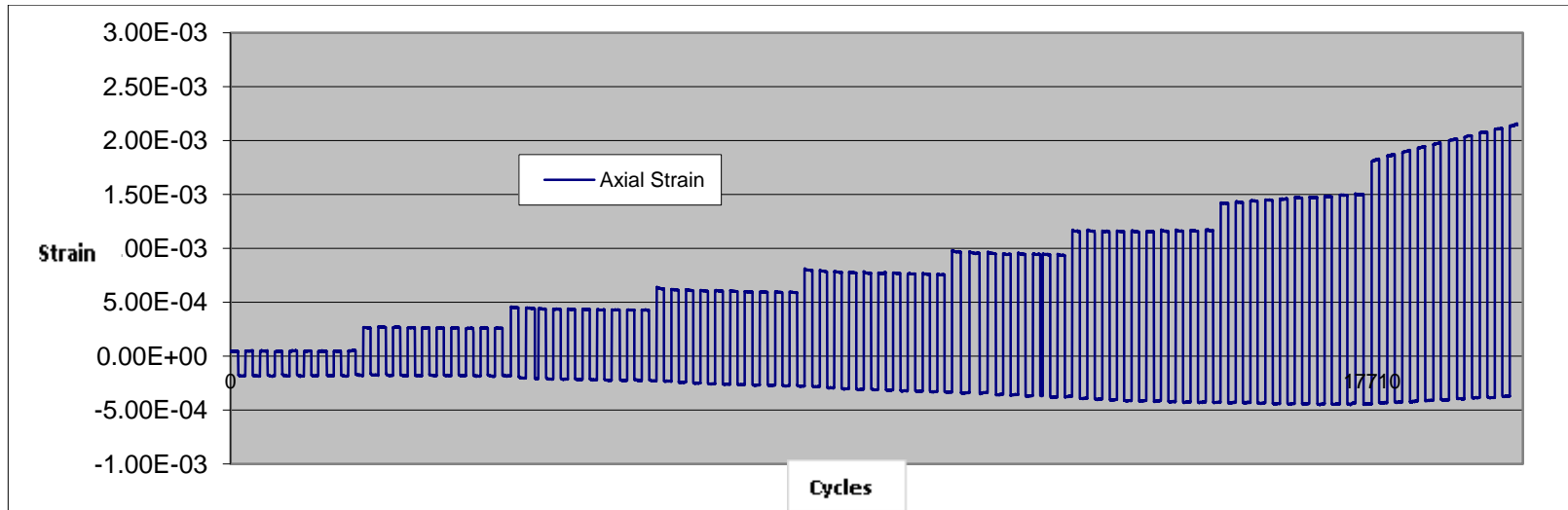
The axial strain plots during the UEWS test under a 0.5:1 hoop to axial stress ratio, at 65 °C.



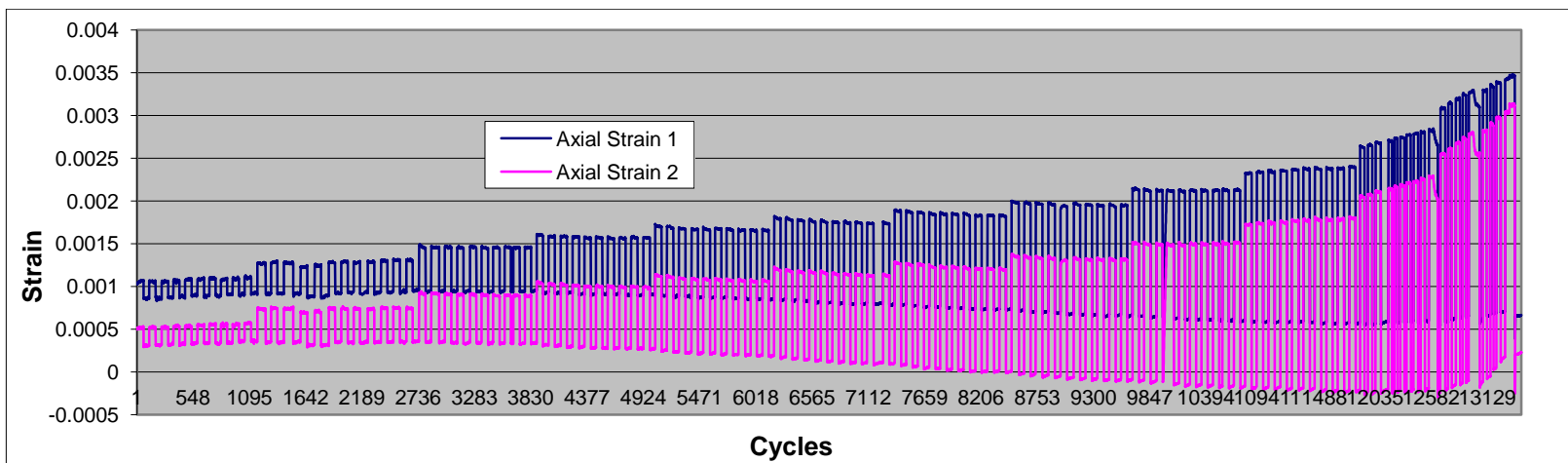
The axial strain plots during the UEWS test under a 1:1 hoop to axial stress ratio, at room temperature.



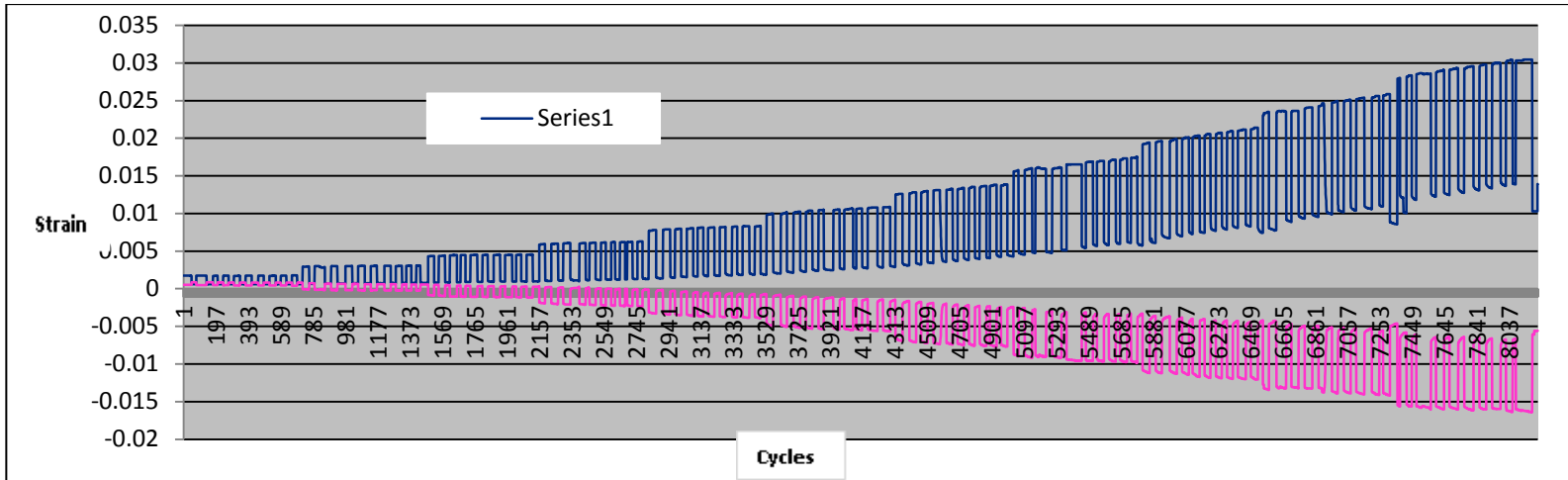
The axial strain plots during the UEWS test under a 1:1 hoop to axial stress ratio, at room temperature.



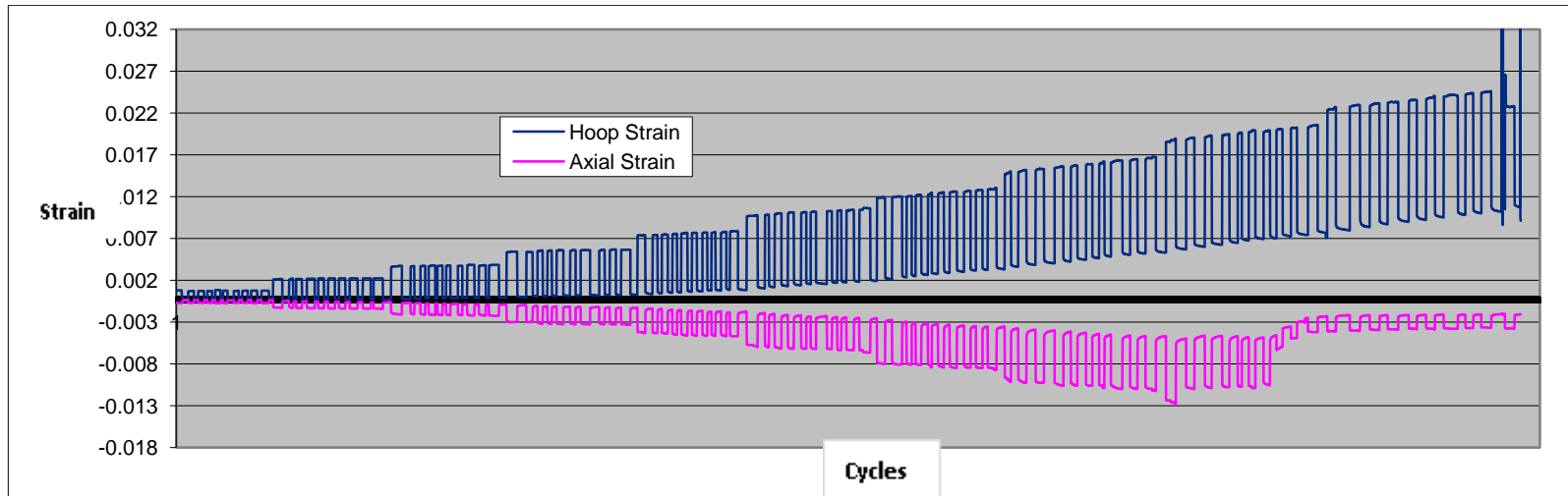
The axial strain plots during the UEWS test under a 2:1 hoop to axial stress ratio, at room temperature.



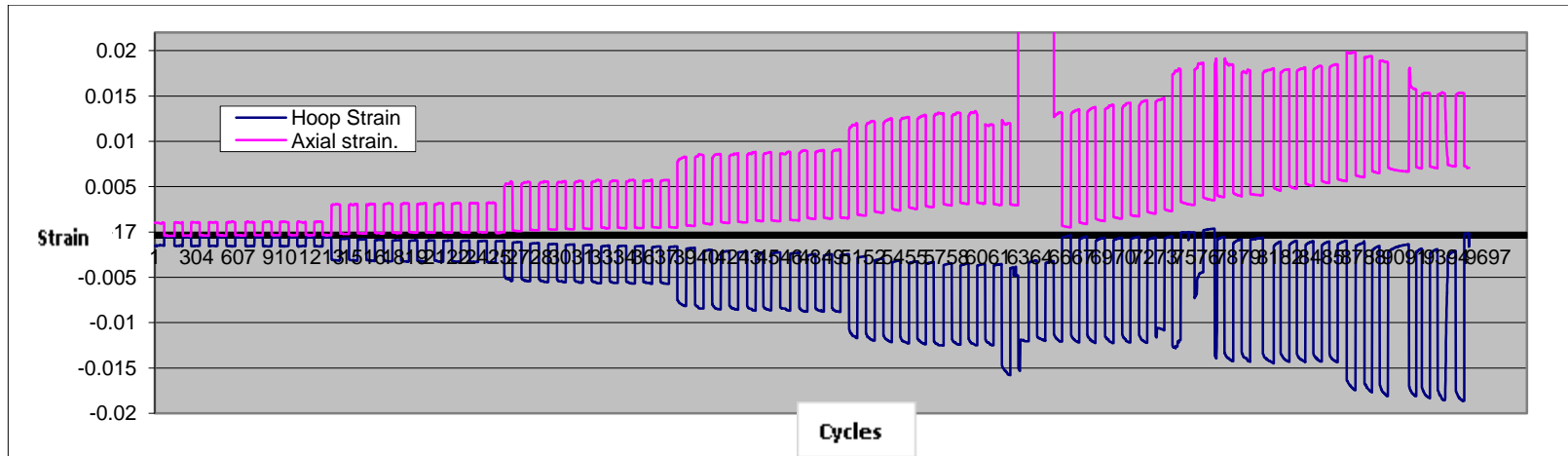
The axial strain plots during the UEWS test under a 2:1 hoop to axial stress ratio, at 95°C .



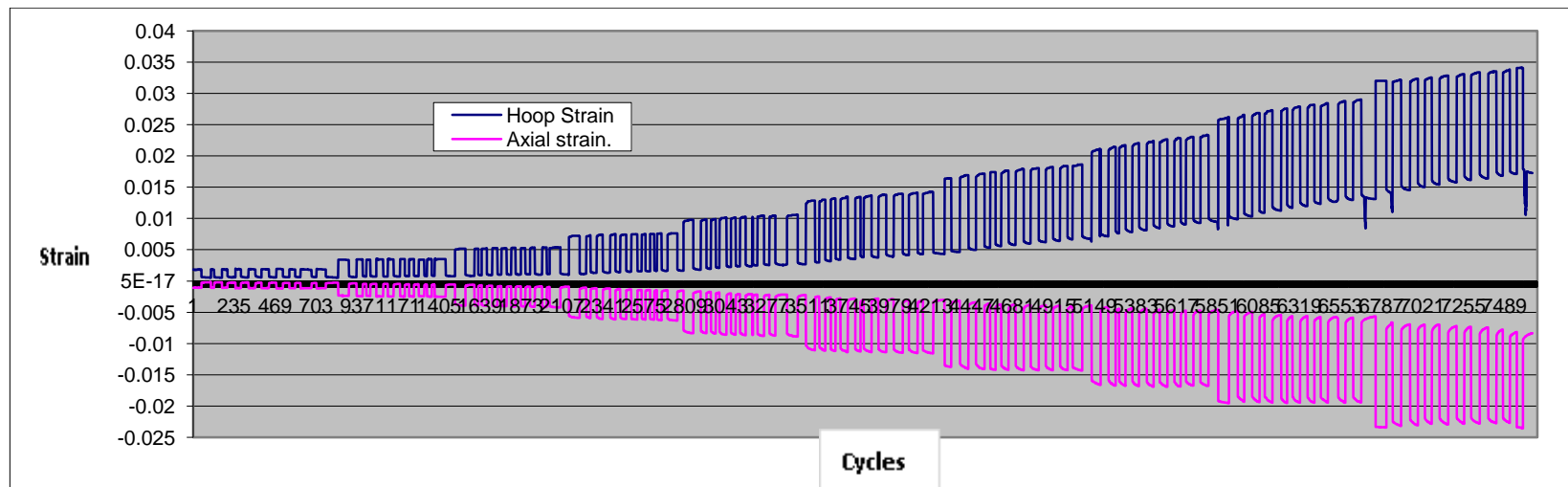
The axial and hoop strain plots during the UEWS test under a 4:1 hoop to axial stress ratio, at 95 °C.



The axial and hoop strain plots during the UEWS test under a 4:1 hoop to axial stress ratio, at 65 °C.



The axial and hoop strain plots during the UEWS test under pure hoop loading, at room temperature.



The axial and hoop strain plots during the UEWS test under pure hoop loading, at 65 °C.